Advanced Prototypes of the Aerosol Limb Imager

A dissertation submitted to the
College of Graduate and Postdoctoral Studies
in partial fulfillment of the requirements
for the degree of Doctor of Philosphy
in the Department of Physics and Engineering Physics
University of Saskatchewan
Saskatoon

By
Matthew N. Kozun

Permission to Use

In presenting this dissertation in partial fulfillment of the requirements for a Postgraduate degree from the University of Saskatchewan, I agree that the Libraries of this University may make it freely available for inspection. I further agree that permission for copying of this dissertation in any manner, in whole or in part, for scholarly purposes may be granted by the professor or professors who supervised my dissertation work or, in their absence, by the Head of the Department or the Dean of the College in which my dissertation work was done. It is understood that any copying or publication or use of this dissertation or parts thereof for financial gain shall not be allowed without my written permission. It is also understood that due recognition shall be given to me and to the University of Saskatchewan in any scholarly use which may be made of any material in my dissertation.

Requests for permission to copy or to make other uses of materials in this dissertation in whole or part should be addressed to:

Head of the Department of Physics and Engineering Physics
116 Science Place
University of Saskatchewan
Saskatoon, Saskatchewan
Canada
S7N 5E2

OR

Dean
College of Graduate and Postdoctoral Studies
University of Saskatchewan
116 Thorvaldson Building, 110 Science Place
Saskatoon, Saskatchewan S7N 5C9 Canada

Abstract

Over the past decades, the call for global monitoring of aerosol has amplified to better understand its role in climate change. The Canadian Space Agency has identified targeted program funding for mission development to address this call. The Aerosol Limb Imager, or ALI, is a candidate remote sensing instrument that will provide this monitoring.

ALI is a Canadian developed atmospheric remote sensing instrument specifically designed to be sensitive to aerosol and clouds from the mid-troposphere through the stratosphere. An orbital-based viewing platform is necessary to realize global coverage. This work presents the development of two sub-orbital prototype instruments that inform the design of a satellite instrument.

The first ALI prototype presented is a technology demonstration aimed at validating the performance of state-of-the-art optical technologies on a high-altitude balloon observatory. The instrument pairs an extended range acousto-optic tunable filter with a liquid crystal polarization rotator to capture spectrally resolved polarimetric imagery of the atmospheric limb. These technologies provide the capability to extract particle size information from the sampled radiance and to identify cloud structures. The instrument met performance expectations from a balloon platform in 2018.

The ALI elegant breadboard is the latest hardware development and is designed to measure scattered sunlight from a high-altitude aircraft. An aircraft platform offers a varying spatial scene, which is analogous to the variation observed from orbit. Along-track sampling and signal-to-noise requirements are met with a state-of-the-art large-aperture acousto-optic tunable filter. The optical design surrounding the filter is equally advanced, incorporating diamond-turned mirrors and precision optical alignment. The ALI elegant breadboard is being assembled to meet a flight opportunity on the NASA ER-2 observatory in late 2022.

The insight and experience gained through the development of these two prototypes are paramount to the design of a future satellite-based sensor. Teams from the Canadian Space Agency, a Canadian University consortium and industry partners have assembled to ensure that ALI is the right instrument to address a global need. If selected for a satellite mission, ALI will fuel new research into how aerosol shapes climate and the health of the planet.

Acknowledgements

The activities completed to write this dissertation have allowed me to travel to several traditional indigenous territories. I'd like to honour and pay respect to the indigenous ancestors and communities whose lands were occupied for this work. Most of the work was performed on Treaty 6 territory and the homeland of the Métis, and on the traditional unceded territory of the Algonquin Anishnaabeg people. Flight opportunities were realized in Treaty 9 territory and the traditional and current territory of the Arrente people.

This work was made possible through the financial support of the Canadian Space Agency's Flights and Fieldwork for the Advancement of Science and Technology funding initiative and the Space Technology Development Program, as well as through the generous support of the University of Saskatchewan.

I am lucky to have built a vast base of support from family and friends over the several years needed to complete this work. I thank them all for their endless encouragement, whether from the start of my academic career or only in the final years. I thank this group also for providing an outlet to take a break from this work to cultivate important relationships that will last a lifetime.

Finally, I wish to extend my sincerest thanks to Professor Adam Bourassa and Professor Doug Degenstein for their endless support through this work. I owe a great debt of gratitude for their insight, guidance, and mentorship through this work and most of my academic career. Paul Loewen has also played an important role by sharing his wisdom and talents with me over several years, for which I am truly grateful. I am endlessly thankful that the closure of my academic chapter has not coincided with the closure of our work relationship, and I look forward to continued collaboration with these three incredible scientists in the years to come.

For Eloise

Contents

Permission to Use i

Abstract ii

Acknowledgements iii

Contents v

List of Tables viii

List of Figures ix

List of Abbreviations xv

1 Introduction 1

2 Background 4
- 2.1 Stratospheric Aerosol . . . 4
  - 2.1.1 Transport Mechanisms . . . 5
  - 2.1.2 Stratospheric Aerosol Processes . . . 6
  - 2.1.3 Climate Impacts of Stratospheric Aerosol . . . 7
- 2.2 Instrumentation for Stratospheric Aerosol Measurement . . . 8
  - 2.2.1 In Situ Measurement . . . 9
  - 2.2.2 Lidar Instruments . . . 9
  - 2.2.3 Occultation Instruments . . . 10
  - 2.2.4 Limb Viewing Instruments . . . 12
- 2.3 Radiative Transfer and Aerosol Properties . . . 14
  - 2.3.1 Atmospheric Scattering . . . 14
  - 2.3.2 Radiative Transfer . . . 20
  - 2.3.3 Retrieval Method . . . 23
  - 2.3.4 Retrieval of Aerosol Properties . . . 25
- 2.4 Project Motivation . . . 28
- 2.5 Advanced Remote Sensing Techniques . . . 29
  - 2.5.1 Imaging Optics . . . 29
  - 2.5.2 Novel Atmospheric Spectral Filtering . . . 33
  - 2.5.3 Liquid Crystal Technology . . . 44
  - 2.5.4 ALI Version 1 . . . 46

3 Methods 48
- 3.1 High-Level Instrument Requirements . . . 48
- 3.2 Optical Design . . . 49
  - 3.2.1 Technology Trades . . . 49

3.2.2 AOTF Modelling . . . 51
3.2.3 Design Trades . . . 57
3.2.4 Optical Specification . . . 66
3.3 Opto-Mechanical Design . . . 68
3.4 Laboratory Methods . . . 70
3.4.1 Spectral Characterization . . . 71
3.4.2 Image Detector Characterization . . . 74
3.5 Pre-flight Simulation . . . 76
3.5.1 Selection of Balloon Flight Wavelength Channels . . . 77

4 A Multi-Spectral Polarimetric Imager for Atmospheric Profiling of Aerosol and Thin Cloud: Prototype Design and Sub-Orbital Performance 79
4.1 Abstract . . . 80
4.2 Introduction . . . 81
4.2.1 Stratospheric Aerosol Remote Sensing . . . 81
4.2.2 Early ALI Prototype . . . 84
4.2.3 Design Improvements . . . 85
4.2.4 Acousto-Optic Technology . . . 85
4.2.5 Liquid Crystal Polarization Rotator . . . 88
4.3 Advanced ALI Prototype . . . 89
4.3.1 Instrument Design . . . 89
4.3.2 Characterization and Calibration . . . 95
4.3.3 Instrument Simulation Model . . . 105
4.4 Stratospheric Balloon Demonstration Flight . . . 108
4.4.1 Flight Description . . . 108
4.4.2 Balloon Measurements . . . 108
4.4.3 Instrument Model Validation . . . 111
4.5 Conclusion . . . 112
4.6 Data Availability . . . 113

5 Adaptation of the Polarimetric Multi-Spectral Aerosol Limb Imager for High Altitude Aircraft and Satellite Observations 114
5.1 Abstract . . . 115
5.2 Introduction . . . 115
5.3 Instrument Design . . . 117
5.3.1 Spectral and Polarization Selection . . . 118
5.3.2 Reflective Design . . . 120
5.3.3 ALI EBB . . . 121
5.4 Instrument Performance . . . 121
5.4.1 MTF and Vertical Resolution . . . 122
5.4.2 SNR . . . 127
5.4.3 Stray Light . . . 131
5.5 Adaptation for Satellite Based Remote Sensing . . . 135
5.6 Conclusion . . . 137

6 Conclusion and Outlook **139**
6.1 Outlook Towards Orbital Operation 141

References **144**

Appendix A ALI V2 Optical Design Source Code **157**

Appendix B ALI V2 Bill of Materials **162**

List of Tables

3.1 Summary of optical layout trade off implications 59

4.1 TEAF—10-0.5-1.5-MSD-ER AOTF Properties 90
4.2 Raptor Owl 640 Detector Properties 92
4.3 Instrument Model Properties 107

5.1 List of manufacturing and build tolerances. 127

B.1 ALI V2 Bill of Materials 163

List of Figures

2.1 Viewing geometry for solar occultation measurements. The instrument makes direct line of sight measurements at different points in its orbit during a local sunrise to sample various layers of the atmosphere. 11

2.2 Viewing geometry for limb viewing measurements. The instrument field of view is centred on the sunlit portion of the atmosphere to measure sunlight that is scattered by particles in that atmosphere. Multiple scattering events are likely, including scattering from the surface of the Earth. 13

2.3 Mie scattering phase functions for three wavelengths and four particle sizes, [Mätzler, 2002]. The wavelength dependent refractive index of H_2SO_4 is used, with $m_{\lambda=1000} = 1.361 + i4.534E-7$. Radiation is incident from the left in each example, and a tendency to scatter in the forward direction (along $\theta = 0$) is observed, with a stronger response as the particle size increases. 17

2.4 Modelled sensitivity of aerosol retrieval vectors to particle size distributions. (a) Three aerosol size distributions at 22.5 km, highlighting two unimodal distributions with differing mean particle radii, and a bimodal distribution representing a post-volcanic activity atmosphere. Each size distribution generates a common retrieval vector at 750 nm. (b) Retrieval vectors as a function of wavelength for the three size distributions. Reproduced with permission of the author, [Rieger et al., 2014]. 28

2.5 Image formation of point source, P, through an ideal lens. 30

2.6 Image formation of a point source, P, through a physical lens. (a) Rays and sampled wavefronts traced from the source P to the image P'. (b) Magnified view of a single wavefront showing deviation from a spherical shape. (c) 2D spot diagram of rays traced through the lens system to a screen placed at the focus, P'. (d) Point spread function displaying energy distribution including impacts of diffraction. 33

2.7 Transfer of object modulation through an optical system. (a) Low-frequency modulation is efficiently transferred, with high contrast between bright and dark regions. The brightness in the image is shown in red. (b) High-frequency modulation is less efficiently transferred, with more energy from the bright regions registering in the dark regions in the image. The contrast between the bright and dark regions is reduced as shown in the red line. 34

2.8 Optical propagation at angle θ with respect to optical axis. (a) Intersection of orthogonal polarization states with refractive index ellipsoid. (b) Ordinary and extraordinary refractive index as a function of incidence angle with respect to the optical axis. 37

2.9 Slowness curves for shear and longitudinal acoustic waves in TeO_2. 39

2.10 Momentum matching criterion on a wave vector diagram for a non-collinear AOTF. 41

2.11 Application of an AOTF on unpolarized broadband signal. Four distinct beams exit the AOTF, identified by their polarization state and diffraction order. 42

2.12 Three thermotropic mesogen arrangements. (a) Smectic. (b) Nematic. (c) Cholesteric or twisted-nematic. [Litster and Birgeneau, 1982] 45

2.13 Optical activity within a twisted-nematic liquid crystal cell. (a) In the relaxed state, the mesogen director undergoes a 90° twist over the length of the cell. The linear polarization state of an optical wave follows the rotation. (b) The mesogen directors align to an applied electric field between the plates housing the cell, removing the optical activity and allowing the optical wave to pass through unaffected. 46

2.14 Optical layout of ALI V1. Elements 1 and 2 comprise an afocal telescope. Elements 3 and 5 are linear polarizing filters around the AOTF, Element 4. Element 6 is a singlet to focus wave fronts onto the image sensor, Element 7. 47

3.1 AOTF model geometry adapted with permission from [Zhao et al., 2014] © The Optical Society. Three optical surfaces define how an optical signal enters the AOTF, diffracts at the acoustic column (or passes through if momentum matching is not met), and then refracts out of the AOTF at a wedged interface. 52

3.2 Ray tracing phase matching condition for the second surface. Adapted with permission from [Zhao et al., 2014] © The Optical Society. 54

3.3 Overlapping wave vector surfaces for tracing acousto-optic diffraction under momentum mismatching condition. The intersection of ordinary wave vector surface and extraordinary wave vector surface translated by momentum matching acoustic wave vector is determined using numerical methods. . . . 57

3.4 Two standard methods of using an AOTF in an optical system. Ray bundle fields are differentiated by colour. (a) Confocal or telecentric layout, with focused rays reaching the AOTF. Two optical fields, identified by colour, are focused to a small region on the face of the AOTF. Note that the focal plane is commonly within the AOTF in this layout. (b) Afocal telescopic layout, with collimated rays reaching the AOTF. Two fields enter the AOTF in two distinct directions, filling the aperture of the AOTF. 58

3.5 Lateral chromatic aberration caused by telecentric AOTF layout. (a) The chromatic focal plane shift caused by AOTF crystal dispersion. (b) Simulation of image plane shift for best focus. (c) Spot size at common image focal plane. 60

3.6 Reduced spectral resolution caused by telecentric AOTF layout. (a) Diffracted wavelength described as a function of incidence angle onto AOTF. Three central wavelength tunings are displayed across ALI spectral range. (b) Comparison of telescopic (collimated input) and telecentric (focused input) spectral resolutions over ALI wavelength range. 61

3.7 Optical effects caused by noncritical phase matching in telescopic layout. (a) Distortion caused by acousto-optic interaction. The central wavelength experiences the nominal change in angle between the incident and diffracted beam, shown as a null field change. All other fields experience a differing amount of change between incidence and diffracted beams, resulting in the displayed distortion. (b) Transmission gradients occur for three sampled wavelength channels. The gradient falls out of the wavelength dependence of the AOTF transmission function. 63

3.8 Optical effects caused by the momentum matching condition in the telescopic layout. (a) Diffracted field shift as a function of incident angle and wavelength. (b) Average image shift over wavelength with respect to the 500 nm channel image shift. (c) Field-dependent magnification of the 500 nm channel. (d) Field averaged magnification over wavelength. 64

3.9 Angular broadening caused by acousto-optic image blur compared against Rayleigh criterion. 65

3.10 Input telescope design option using (a) refractive optical elements or (b) reflective optical elements. 67

3.11 Optical layout of ALI V2. Elements 3 and 4 are the afocal telescope for FOV mapping. Elements 1, 2, 5 and 6 are the LCR, LPF, AOTF and LPF respectively, providing polarization and spectral filtering. Elements 7 and 8 are fold mirrors to reduce the footprint, leading to the imaging optics described by 9. Finally, the image sensor ends the optical chain at Element 10. 69

3.12 ALI V2 opto-mechanical solution. (a) Interior opto-mechanical solution showing optics assembled on three optical breadboards, with COTS mounts for mirrors, lenses and other optical components. (b) ALI V2 optical enclosure. 71

3.13 Method for finding central diffracted wavelength from a discrete wavelength sampled spectrum. (a) Sample spectrum measured with AOTF tuning frequency f = 92 MHz. (b) Test of symmetry of central lobe. (c) Assessment of goodness-of-fit parameters to estimate central wavelength. 73

3.14 Histogram of pixel counts for a 100 ms exposure time in front of a uniform illumination source, with an average of half-well illumination. 75

3.15 Flat field calibration. (a) Uniform field illumination measurement at 1100 nm. (b) Optical footprint plot on imaging lens 1 showing signs of clipping for extreme fields. 77

3.16 Absorption cross sections of several key atmospheric species, normalized for clarity. Sampled measurement spectra for 25 selected wavelength channels are overlaid to compare measured bandpasses with expected atmospheric features. 78

4.1 Limb scatter viewing geometry. Multiple scattering events are shown with photons scattering into the FOV of the instrument [Bourassa et al., 2008b]. Adapted with permission from J Quant Spectrosc Radiat Transf. 109 (2008). Copyright 2007, Elsevier Ltd. 83

4.2 Momentum matching criterion on a wave vector diagram for a non-collinear AOTF, with axes normalized to the magnitude of the optical wave vector. The red curve shows the refractive index of the ordinary polarization state over all incident angles, and the blue curve represents that of the extraordinary state. Bragg diffraction is shown between the incident optical wave vector, $\overrightarrow{\mathbf{k}_i}$, the acoustic wave vector, $\overrightarrow{\mathbf{K}_a}$ and the diffracted optical wave vector, $\overrightarrow{\mathbf{k}_d}$. 86

4.3 AOTF diffracting unpolarized light. The broadband undiffracted beam experiences double refraction due to the crystal birefringence. Narrow band filtering produces two first order diffraction beams, paired to the two undiffracted beams. No higher diffraction orders exist due to the sinusoidal nature of the acoustic wave within the AOTF. 87

4.4 Wavelength distribution across detector in telescopic layout for filtering at 1000 nm. The marker sizes indicate the relative spectral transmission within the bandpass, dictated by momentum mismatch at these wavelengths. 91

4.5 ALI V2 instrument layout. (a) Optical layout as designed in CODE V. (b) Opto-mechanical model designed primarily with COTS components. 97

4.6 Frequency tuning curve measurements. (a) Optical layout for tuning curve measurement. (b) Sample spectra used to determine tuning curve. (c) Wavelength tuning curve as a function of applied frequency. Note the smooth joint between the two transducers at the change over frequency of 100 MHz. . . . 99

4.7 AOTF bandpass as a function of wavelength. The discontinuity at 920 nm is a result of different transducer interaction lengths. 100

4.8 Internal diffraction efficiency measurements. (a) Sample spectra showing absence of diffracted signal, described in generic pixel count digital numbers, DN. S_0 is the full 0^{th} order spectrum with the tuning frequency amplitude set to 0 W. S_P is once again the 0^{th} order spectrum but with the tuning frequency amplitude set to maximize diffraction. (b) IDE over wavelength range. . . . 102

4.9 Characterization of ALI polarization tuning. This is a full instrument characterization, including all optical elements in ALI. (a) Wavelength dependent polarization response. The spread seen in the LCR Off measurements is a result of the twisted nematic cell LCR, which is only optimized over a narrower bandwidth than the ALI spectral range. (b) Coefficients for ALI Mueller matrices. The effect of the narrow optimized bandwidth is once again seen in the variation of the g_{12} and g_{13} curves when the LCR is off. 104

4.10 Sample measurement taken from 48°41'39.8"N, 83°48'17.3"W, altitude 36.6 km, at 12:55:14 UTC on 08/26/2018 . Solar Zenith Angle = 36.8°. Wavelength channel 1025 nm, LCR off. 109

4.11 Level 1 data product from multi-spectral scan #10, Measurements taken near 48°41'39.8"N, 83°48'17.3"W, altitude 36.6 km, between 12:54:30 and 12:58:30 UTC. Solar Zenith Angle near 37° (a) LCR off. (b) LCR on. (c) Ratio of LCR off to LCR on. 110

4.12 Comparison of modelled and measured instrument response at 20 km. 112

5.1 Spectral and polarization filtering performed by the SPS subassembly. (a) SPS response with an unpowered LCR. The atmospheric linear polarization state is rotated by 90° before passing the first linear polarizer. Spectral filtering results in a second 90° rotation, so the second linear polarizer filters out the broadband signal. Originally horizontally polarized signal is filtered through the SPS. (b) SPS response with a powered LCR. The atmospheric linear polarization state passes the LCR unchanged before the first linear polarizer. Spectral filtering and the second polarizer allow originally vertically polarized signal to be filtered through the SPS. 119

5.2 Spectral and Polarization subassembly. (a) Standard view. (b) Exploded View. 120

5.3 ALI EBB Optical Layout. (a) Top view of input telescope and first periscope fold. The input aperture is in the upper left of the frame. (b). Second periscope fold, SPS and camera TMA. (c) Side view of ALI EBB showing two horizontal optical planes. (d) Isometric view of ALI EBB. Input aperture is in the center left of the frame. 122

5.4 ALI EBB Optomechanical design. (a) Input optics subassembly. (b) Periscope subassembly. (c) Camera TMA subassembly. (d) ALI EBB Assembly. Input optics chassis acts as an optical bench for the other subassemblies, including the SPS shown in Figure 5.2. Note that an additional baffle hood (not shown) is added around the periscope and SPS to shield these from the surroundings. 123

5.5 Optical modulation transfer function of nominal ALI EBB optical design. The detector cutoff spatial frequency is 33.3 cycles/mm. Solid lines represent the MTF for select fields over the FOV. 124

5.6 Limb viewing geometry. The vertical field of view has several lines of sight, based on pixel binning. Each line of sight makes a measurement at a unique tangent height. 125

5.7 Relationship between the PSF FWHM and vertical resolution in the atmospheric limb from a flight altitude of 22 km. (a) The nominal vertical resolution is displayed for various field and wavelength combinations based on the 50% encircled energy of the ALI optical design. (b) Vertical resolution calculated from 1σ tolerance analysis of encircled energy 126

5.8 STOP analysis results. (a) Finite element model of ALI EBB shows the nodal displacements under the hot operating condition of +40°C. These distortions are used to build a representative optical model. (b) Vertical resolution estimated from the hot and cold operating case optical models, using the described method to convert PSF FWHM to vertical resolution. 128

5.9 ALI EBB transmission. Spectral curves are generated using reflectance of 9 silver coated mirrors, transmission properties of polarizing filters and rotators, and diffraction efficiency of the AOTF. The mirrors have different reflection coefficients for S and P polarization states, which has a small impact on the transmission depending on the LCR state modelled. 129

5.10 Simulated signal to noise ratio for ALI EBB under two aerosol loading conditions. (a) "Clear" case with contributions from Rayleigh scattering, Ozone absorption and background aerosol levels. (b) "Signal Enhanced" case with contributions from Rayleigh scattering, Ozone absorption and aerosol loading similar to that which followed the Nabro eruption in 2011 as well as thick, low altitude cloud coverage. SNR=200 threshold is marked in thick blue. 130
5.11 Stray light PST simulation covering vertical and horizontal fields extending beyond the designed field of view with monochromatic input. We find approximately 3 orders of attenuated magnitude for in-band, in-field stray light signal, and roughly 6 orders for out-of-band, in-field stray light signal. The contributions from outside the field of view all exhibit more than 6 orders of magnitude of attenuation. 133
5.12 Mathematical model of broadband 0^{th} order stray light compared to simulated signal levels. The simulated levels have been normalized to show the rough order of magnitude of attenuation of the 0^{th} order beam that is expected to reach the detector. The minimum signal profile across all wavelength channels is calculated and reduced by a factor of 200 to simulate the SNR requirement. The 0^{th} contribution falls below this level for all tangent heights. 134
5.13 Optical design for ALI to meet requirements for orbital aerosol retrieval. This design highlights similar features to the EBB, with a telescopic input assembly, an SPS, periscope and an imaging assembly. 136

List of Abbreviations

2D	2 Dimensional
A-CCP	Aerosol and Cloud, Convection and Precipitation
ALI	Aerosol Limb Imager
ALI V1	Aerosol Limb Imager Version 1
ALI V2	Aerosol Limb Imager Version 2
ALI EBB	Aerosol Limb Imager Elegant BreadBoard
AO	Acousto-Optic
AOTF	Acousto-Optic Tunable Filter
CALIOP	Cloud-Aerosol LIdar with Orthogonal Polarization
CLAES	Cryogenic Limb Array Etalon Spectrometer
CN	Condensation Nuclei
COTS	Commercial Off The Shelf
CSA	Canadian Space Agency
EBB	Elegant BreadBoard
ESA	European Space Agency
FWHM	Full Width at Half Maximum
FOV	Field of View
GOMOS	Global Ozone Monitoring by Occulation of Stars
HALOE	HALogen Occultation Experiment
LC	Liquid Crystal
LCR	Liquid Crystal polarization Rotator
LPF	Linear Polarizing Filter
MART	Multiplicative Algebraic Reconstruction Technique
MTF	Modulation Transfer Function
NASA	National Aeronautics and Space Administration
NIR	Near Infrared
OMPS-LP	Ozone Mapping and Profiler Suite - Limb Profiler

OSIRIS	Optical Spectrograph and InfraRed Imaging System
PCW	Prospective Central Wavelength
PMT	PhotoMultiplier Tube
PSF	Point Spread Function
SAGE	Stratospheric Aerosol and Gas Experiment
SAM	Stratospheric Aerosol Measurement
SCHIAMACHY	SCanning Imaging Absorption SpectroMeter for Atmospheric CHartographY
SHOW	Spatial Heterodyne Observations of Water
SNR	Signal-to-Noise Ratio
SOFIE	Solar Occultation For Ice Experiment
SPS	Spectral and Polarization Selection
SWIR	Short-Wave Infrared
TRL	Technology Readiness Level
WOPC	Wyoming's Optical Particle Counter
UTLS	Upper Troposphere/Lower Stratosphere

Chapter 1

Introduction

The dynamics of particles in the atmosphere influence the climate experienced on Earth, the health of humans and the health of the natural environment. Particles of different types interact with solar radiation and each other through processes that seek an unreachable state of equilibrium. This balance is consistently perturbed by planetary motion, natural geological processes, and most notably in recent centuries, the activity of developing human society.

The anthropological mark on Earth is continuously spreading, from urbanization and deforestation, to the collapse of terrestrial and aquatic ecosystems, and to the loss of freshwater stores in polar latitudes [Lawrence and Vandecar, 2015, Morecroft et al., 2019, Moritz et al., 2002]. These changes continue to put pressure on inhabited regions of the planet, leading to greater demand for resources, which in turn impacts the health of the planet through negative feedback.

The overall health of the environment is increasingly being supervised through remote sensing applications. Of these applications, atmospheric monitoring offers an important tool for the indirect sampling of the composition of the atmosphere [Yang et al., 2013, Li et al., 2011, Karl et al., 2010]. The composition of essential climate variables, including carbon dioxide, methane and ozone can be inversely inferred from measurements of sunlight as it passes through the atmosphere [Buchwitz et al., 2015, Hollmann et al., 2013]. Additionally, the signatures of aerosol on solar spectral transmission play a role in understanding environmental health. Understanding the distribution and concentration of these particles helps link climate affecting interactions like cloud formation, global cooling and ozone loss [Robock and Mao, 1995, Aquila et al., 2013].

The inference of aerosol concentration and distribution is inherently complicated due to several microphysical properties of the particles. With a broad spectral signature, spe-

cialized inversion techniques are required to definitively extract these particle properties [Rieger et al., 2019, Zawada et al., 2018]. Furthermore, the fine vertical variation in aerosol distribution impacts the capability of current generation remote sensors to adequately measure stratospheric aerosol for climate modelling [Andersson et al., 2015, Boucher et al., 2013].

This work describes the development of a new atmospheric remote sensor specifically designed to perform the high-resolution monitoring of stratospheric aerosol requested by the science community. The Aerosol Limb Imager (ALI) is a passive, solid-state, polarimetric imaging spectrometer designed to measure scattered sunlight in the atmosphere. The designed viewing geometry allows for continuous atmospheric sampling from an orbital platform, aimed at providing global coverage with unprecedented temporal resolution. The implied retrieval technique builds on a legacy of Canadian-produced analytical methods, developed for the extraction of ozone concentration profiles from the Optical Spectrograph and Infrared Imaging System, and extended to additional atmospheric species like nitrogen dioxide and stratospheric aerosol. Support from the Canadian Space Agency for this instrument development represents continued efforts towards the goal of ensuring "Canada's leadership in acquiring and using space-based data to support science excellence, innovation and economic growth" [Canadian Space Agency, 2019].

The fundamental principles governing this thesis work are described in Chapter 2. A review of stratospheric aerosol properties and processes is presented, with a description of scattering and radiative transfer in the atmosphere. The current state of stratospheric aerosol monitoring is addressed, with a description of key technologies used to date. Following, a description of a novel technology is presented, describing the pairing of acousto-optic and liquid crystal technology to provide spectral and polarimetric filtering.

The key methods applied to the design and characterization of the ALI instruments are discussed in Chapter 3. Here, the high-level design requirements are established to provide a basis for the design choices made. A trade-off study is outlined to address key instrument parameters, including a justification for the technological choices and the first-order optical layout selection. A mathematical model of the acousto-optic interaction is described, which is critical for completing several of the trade-off studies. Details are then provided about the laboratory methods utilized to aid in designing and characterizing the optical unit.

The subsequent chapters of this thesis are two published manuscripts, with summaries provided to link the described topics to the broader context of this work. The first manuscript contained in Chapter 4 discusses the second prototype of ALI, featuring an extended spectral range and new dual-polarization measurement capabilities. This prototype of ALI was tested onboard a stratospheric balloon platform and presents the first documented two-dimensional spectral and polarization resolved images of the upper troposphere/lower stratosphere. This paper validates the capabilities of the technology choices for capturing the required atmospheric signals. Chapter 5 details the significant improvements achieved by adapting an orbital-based approach to instrument design for an ALI elegant breadboard. Here, custom precision optics are prescribed to meet the spatial resolution targets for ALI. Furthermore, improved throughput is achieved using a state-of-the-art large aperture acousto-optic tunable filter to reduce exposure time requirements for atmospheric measurement. This facilitates imaging from a mobile platform, nominally a high altitude aircraft like the NASA ER-2 Airborne Science Aircraft. This elegant breadboard flight campaign will simulate orbital-based measurements with spatial variation between images. The motivation of this portion of this work is to increase the technology readiness level of ALI to better demonstrate its suitability for a space flight. Finally, Chapter 6 provides conclusions for this work and a summary of necessary steps for ALI to reach the ultimate goal of orbital observation.

Chapter 2

Background

The composition of particles in the atmosphere affects the transmission of solar radiation near the Earth. Quantities and distributions of various atomic and molecular compounds influence the radiative and chemical balance in the atmosphere, which in turn influence the climate experienced on Earth. This chapter addresses details related specifically to stratospheric aerosol in the atmosphere, discussing climate effects, measurement techniques, and the impacts on the radiation balance. Finally, the use of novel optical technology for remote sensing of stratospheric aerosol is discussed.

2.1 Stratospheric Aerosol

Stratospheric aerosol is predominantly composed of aqueous sulfuric acid (H_2SO_4–H_2O), in the region 15-25 km above the earth [Junge et al., 1961]. This region was first probed in 1959, discovering that the density of particles ranging from 0.1-1.0 μm peaked at an altitude of 20 km [Junge and Manson, 1961]. This aerosol layer has been referred to as the "Junge Layer" following these findings, with its base near the tropopause.

The stable nature of the stratosphere allows for relatively long residence times of stratospheric aerosol. An inversion at the tropopause leads to increasing temperature with altitude, which prevents the thermally driven vertical transport of air parcels that is common in the troposphere. This can lead to stratospheric residence times on the order of years [Telegadas and List, 1969].

Aerosol in the Junge layer can be disturbed by natural phenomena, which dynamically change the composition of the layer. During quiescent periods, the layer is made of sulfur-bearing particles, meteoric dust and non-sulfur-bearing aerosol, but can be disturbed by

increased sulfur loading, smoke and ash. The latter constituents can enter the stratosphere during large-scale wildfire events, like those experienced in British Columbia, Canada in 2017 [Thomas et al., 2017]. Wildfires of this magnitude can lead to climate impacts comparable to that of volcanic eruptions [Bourassa et al., 2019]. Although volcanic activity has historically played the greatest role in the stratospheric aerosol dynamics, the prevalence of wildfires globally is expected to increase [Liu et al., 2010], suggesting increased interest in monitoring wildfire plumes. The following discussion will focus primarily on sulfur-based stratospheric aerosol, however.

2.1.1 Transport Mechanisms

Under typical circumstances, stratospheric aerosol precursors originate in the troposphere and are transported into the stratosphere by one of several pathways. These include quasi-isentropic transport into the extratropical lowermost stratosphere, cross-isentropic exchange into the tropical stratosphere by radiative ascent, or direct injection by overshooting convection in the tropics [Kremser et al., 2016]. All three of these mechanisms bring precursor gasses into the stratosphere at low to low-mid latitude. Although the composition and distribution are ever-changing, the previous conditions establish what is known as the background aerosol layer.

Extraordinary events can also result in increased sulfur loading in the stratosphere. The Asian monsoon anticyclone is identified as a pathway for aerosol precursors from Asia into the stratosphere [Randel et al., 2010]. This event also brings additional loading into the upper troposphere, resulting in the Asian tropopause aerosol layer [Vernier et al., 2011, Thomason and Vernier, 2013]. However, the most dynamic event that disrupts the background aerosol layer is the direct stratospheric injection of sulfur by volcanic eruptions. The convective eruption columns can lead to extremely fast conversion of sulfur dioxide (SO_2) into aerosol, which can quickly change the loading levels. Eruptions like El Chichón in 1983 and Mount Pinatubo in 1991 injected aerosol that stayed in the stratosphere for years and eventually spread over both hemispheres [Robock, 2000].

Although the stratosphere is a vertically stable region of the atmosphere, transport along latitude lines is rapid due to strong zonal winds. Altitude and latitude mixing does however

occur as a result of Brewer-Dobson circulation [Holton et al., 1995, Butchart, 2014]. This circulation pattern draws tropical stratospheric air to higher altitudes before directing it poleward. At high latitude, the circulation brings the air parcels back down to lower altitudes, causing a latitudinal distribution of tropical originating aerosol. This circulation pattern is related to the long residence times aerosol particles achieve in the stratosphere when injected in the tropics, with much shorter residence for those injected from mid-high latitudes [Holton et al., 1995].

2.1.2 Stratospheric Aerosol Processes

Macroscopic properties of the aerosol layer like the concentration and size distribution are governed by five key processes [Seinfeld and Pandis, 2006]. The formation of stratospheric aerosol is the result of *nucleation*. In the abundance of water vapour, sulfuric acid (H_2SO_4) forms aerosol through binary homogeneous nucleation [Vehkamäki et al., 2002], acting as the main source for new stratospheric aerosol. Once established, the particles may undergo condensational growth in the presence of additional H_2SO_4 and H_2O through heteromolecular *condensation* [Stauffer et al., 1973]. The particle size distribution is further influence by *coagulation*, occurring when established aerosol particles collide and form larger particles [Hamill et al., 1977]. Aerosol sinks come primarily from two processes: *sedimentation* and *evaporation*. Sedimentation occurs when particles reach low enough altitudes that they cross the tropopause and are lost due to the dynamic nature of the troposphere [Junge et al., 1961]. Conversely, evaporation occurs through the upwelling of aerosol to higher altitudes caused by Brewer-Dobson circulation, bringing the liquid particles to regions with temperatures high enough to evaporate into gas once again. These gases are circulated to high latitudes where a drop in altitude often leads to recondensation of the sulfur precursors.

Maintenance of the Junge layer must begin with sulfur-rich precursor compounds that are transported into the stratosphere. During volcanically inactive periods, the predominant precursors are carbonyl sulfide (OCS), SO_2 and H_2SO_4. Both OCS and SO_2 oxidize in the stratosphere to form H_2SO_4, which condense into aerosol in the presence of water vapour. Roughly 25% of the sulfur residing in the stratosphere is in the form of H_2SO_4–H_2O aerosol droplets [SPARC, 2006].

Sulfur and aerosol in the stratosphere play a role in the depletion of ozone in the atmosphere [Solomon, 1999]. The presence of sulfur accelerates heterogeneous chemical reactions, affecting midaltitude ozone [Fahey et al., 1993, Mills et al., 1993]. Furthermore, at high latitude, H_2SO_4–H_2O form polar stratospheric clouds. These clouds lead to chlorine activating reactions, which further deplete ozone [Solomon, 1999].

2.1.3 Climate Impacts of Stratospheric Aerosol

The presence of aerosol in the atmosphere (both tropospheric and stratospheric) disrupts and dictates the transmission of solar radiation, which in part dictates the weather that is experienced on Earth. Additionally, stratospheric aerosol can contribute to climate change. The magnitude of the climate impacts is related to the amount of scattering that occurs, which is a strong function of size distribution and concentration [Pinto et al., 1989, Lacis et al., 1992].

The most influential and direct process that stratospheric aerosol has on climate is the increase in planetary albedo as it causes an increase in radiation scattering away from the Earth. Additionally, the presence of aerosol in regions with water vapour promotes cloud formation with the aerosol acting as nucleation sites, which also increases scattering away from the Earth [Le Treut et al., 1998]. The nucleation of clouds at these altitudes impact both temperature and precipitation patterns, but hold much uncertainty in the dynamics of the interactions [Boucher et al., 2013, Zelinka et al., 2016, Zelinka et al., 2020]. Both of these processes result in a cooling effect on Earth's climate. Conversely, the aerosol layer also has the effect of scattering thermal radiation from the Earth back toward it through the greenhouse effect, causing a warming effect. Ultimately, the net radiative forcing caused by stratospheric aerosol is negative, with the cooling effects exceeding the warming one [Lacis et al., 1992, Valero and Pilewskie, 1992]. This net cooling effect is characteristic of aerosol in all regions of the atmosphere but is most notable in the stratosphere due to the long residence time in the Junge layer.

When the Junge layer is disrupted by direct injection of precursor gasses by volcanic eruptions, the size distribution of stratospheric aerosol is disrupted, leading to variations in climate [Hegerl et al., 2007]. The 1991 eruption of Mount Pinatubo is a case study that featured several notable phenomena which are key to understanding the role of stratospheric aerosol on cli-

mate. This eruption ejected ash and sulfur to altitudes of 35 km, increasing the stratospheric sulfur loading by a factor of 30-60 [Mccormick et al., 1995, Sheng et al., 2015]. The resulting aerosol was detectable until 1995, which highlights the long-lasting influence an eruption of this magnitude can have. At its peak, the net radiative forcing from the increased loading was 4 W/m^2, which is comparable to the forcing that would occur from doubling atmospheric CO_2 [Cess et al., 1993]. In the months following the eruption, temperatures near the Earth's surface dropped by 0.4°C [Thompson et al., 2009] and the net cooling exceeded anthropogenic greenhouse warming for the next 18 months [Soden et al., 2002]. Although Pinatubo is a notable example, these large-scale events only occur on average once every 30-50 years [Masson-Delmotte et al., 2013, Deligne et al., 2010]. However, smaller eruptions with higher frequency can sustain stratospheric aerosol concentration enhancements[Solomon et al., 2011].

Small volcanic events can lead to an appreciable change in surface temperature, but there remains much uncertainty related to the magnitude of radiative forcing that these events provide through scattering processes. This uncertainty stems from unknown concentration and size distribution in aerosol loading following these events, coupled with the related high-altitude cloud feedback processes. This has been speculated as a reason for discrepancies between climate models and measurements [Santer et al., 2017].

2.2 Instrumentation for Stratospheric Aerosol Measurement

The stratospheric aerosol record has been maintained through consistent measurement by a series of instruments over the past several decades. Ground-based observation with lidars starting in the 1960s has persisted through the years, but several new technologies including in situ and remote sensing instruments have evolved to provide global coverage. All the measurement methods described utilize the optical scattering properties of aerosol, which will be described in Section 2.3.

2.2.1 In Situ Measurement

The most direct method for measuring properties of stratospheric aerosol is through in situ measurements. These measurements describe the size distribution of aerosol. Three primary data sets compose much of the in situ measurement record, spanning from the mid 20^{th} century to the present. One of these sets comes from the University of Wyoming's Optical Particle Counters (WOPCs) and Condensation Nuclei (CN) counters, which are balloon-borne instruments first flown in 1971 [Deshler et al., 2019].

These WOPCs measure forward scattered signal from a broadband incandescent source at 25°, using two photomultiplier tubes (PMT) in a dark field sampling region. The symmetry of these two PMTs limits dark field noise, as a particle is only counted if each PMT is triggered. This method is sensitive to particles with radii in the range of 0.15-0.3 μm. Continued development of the WOPCs increased the measured scattering angle to 40°, which allows for measurement of particles from 0.15-10 μm. The particle concentration is determined by counting voltage pules on the PMT and converting them to a concentration based on the flow rate into the counter. The size distribution is assessed by comparing the magnitude of the voltage pulses against a calibration with known particle size and index of refraction.

During volcanically quiescent periods, particles with radii less than 0.05 μm dominate the background size distribution of stratospheric aerosol [Deshler et al., 2003]. This is below the measurement threshold of WOPCs. To extend the sampling range of WOPCs, CN counters are utilized to grow these particles to measurable sizes. The particles are exposed to a super-saturated region of ethylene glycol vapour, which condenses on the particles before entering the dark field sampling region of a WOPCs [Campbell and Deshler, 2014]. The combination of WOPC and CN measurements have offered localized long-term concentration monitoring. These have facilitated the development of an algorithm to fit particle concentration profiles to unimodal and/or bimodal lognormal size distributions [Deshler et al., 2003].

2.2.2 Lidar Instruments

Lidar measurement of stratospheric aerosol requires the use of pulsed lasers. The measurement method developed soon after this technology developed [Fiocco and Grams, 1964]. The

ground-based technique involves measuring the backscattered signal from a laser pulse directed upward from the Earth. The backscattered signal strength and the time it takes to return indicate the scattering particles in the air parcel above, with a typical vertical resolution of 75 m [Jäger, 2005].

The measured backscatter coefficient is used to infer the aerosol extinction coefficient, which is necessary for radiative transfer calculations. An extinction-to-backscatter ratio is used to map these measurements. Confirmation of this ratio relies on additional technologies, including in situ measurements [Jäger and Deshler, 2002] or remote sensing measurements [Antuña et al., 2002]. Beyond the extinction coefficient, particle size and number density information may be extracted using lasers at several wavelengths [Post, 1996]. Furthermore, sampling two crossed polarization channels of backscattered signal enables the identification of cloud structures in the optical path.

The network of ground-based lidars provides a low-cost and low-maintenance solution for long-term monitoring of aerosol. However, limited spatial coverage is available, based on the stationary nature of these observatories. Furthermore, tropospheric conditions can greatly inhibit these instruments from probing the stratosphere, depending on the optical depth of the column above the laser.

Lidar monitoring is also possible from satellite platforms, as demonstrated with the Cloud-Aerosol Lidar with Orthogonal Polarization (CALIOP) [Winker et al., 2010]. Satellite-based lidar measurement allows for global coverage while avoiding measuring through the troposphere, which may contain clouds and tropospheric aerosol. However, low signal levels require vertical and horizontal spatial averaging, and temporal averaging on the order of weeks, reducing the vertical resolution of space-based lidar to 500 m.

2.2.3 Occultation Instruments

The earliest and most implemented method for satellite-based remote sensing of stratospheric aerosol is occultation, typically solar-based. Solar occultation measurements make direct line of sight measurements of the sun through the atmosphere to assess the attenuation through its layers, shown in Figure 2.1. The native quantity measured is transmission profiles, which are used to retrieve aerosol extinction.

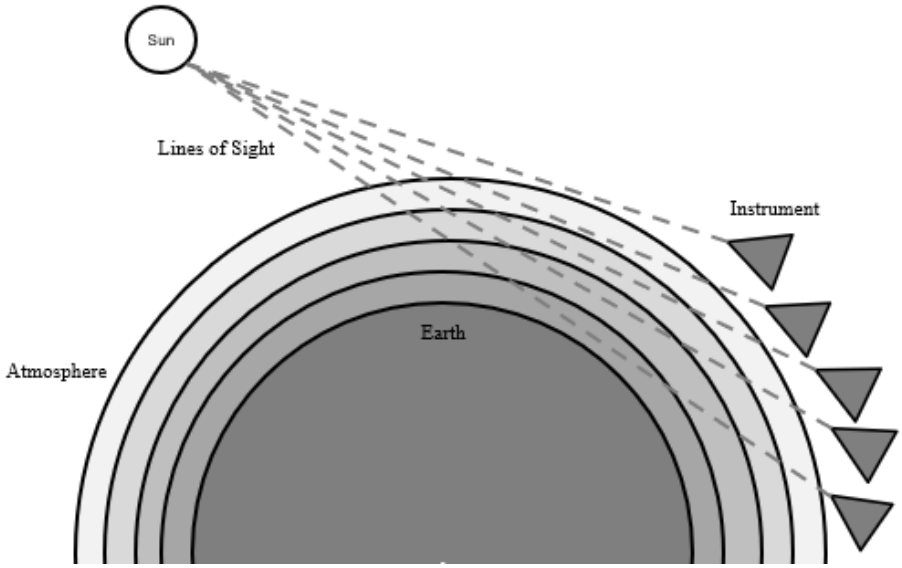

Figure 2.1: Viewing geometry for solar occultation measurements. The instrument makes direct line of sight measurements at different points in its orbit during a local sunrise to sample various layers of the atmosphere.

Solar occultation from orbit is a powerful and reliable measurement technique because each atmospheric sample collected comes with an instrument calibration sample when the instrument can view the sun from above the atmosphere. This occurs at the end of each local sunrise or the start of each sunset sample measurement. However, the requirement to sample through the atmosphere limits the number of measurements to 28-30, per day depending on season and orbit. Furthermore, the technique depends on an assumption of horizontal homogeneity along the optical path length through the atmosphere. To achieve 1 km sampling from 10 km to 40 km vertical range, this optical path length extends 1200 km.

The most notable series of instruments employing solar occultation is the Stratospheric Aerosol and Gas Experiment (SAGE). This series includes flights of the Stratospheric Aerosol Measurement II (SAM II, 1978-1993), SAGE (1979-1981), SAGE II (1984-2005), SAGE III/M3M (2002-2005) and SAGE III/ISS (2017-present), the last of which is presently operating on the International Space Station.

The SAGE progeny consists of grating spectrometers that measure spectrally resolved signal from the ultraviolet to the near-infrared region. Early generations contained individual wavelength channels, starting with four on SAGE [World Meteorological Organization, 1986]

and then seven on SAGE II [Mauldin et al., 1985]. SAGE III imposed an architecture change to implement a CCD instead of individual wavelength channels, and achieves 1-2 nm resolution from 290-1040 nm, and features a photodiode to measure 1550 nm [Cisewski et al., 2014]. The change in architecture allows SAGE III to capture additional lunar occultation measurements.

The robustness of the occultation measurement record has influenced additional instrumentation beyond the SAGE series, with novel differences for each. These instruments do not necessarily target stratospheric aerosol as their primary observable species, but often target related atmospheric species. These include the mid-wave and long-wave infrared observing Halogen Occultation Experiment (HALOE) [Russell III et al., 1993] and Cryogenic Limb Array Etalon Spectrometer (CLAES) [Roche et al., 1993], the stellar occulting Global Ozone Monitoring by Occulation of Stars (GOMOS) [Bertaux et al., 2010] and the higher altitude observing Solar Occultation For Ice Experiement (SOFIE) [Gordley et al., 2009].

2.2.4 Limb Viewing Instruments

The final commonly used method for remote stratospheric aerosol observation is by limb scattered radiation measurement. This technique orients the remote sensing instrument to observe the sunlit portion of the atmosphere, without the sun in the field of view. The geometry is captured in Figure 2.2.

This remote sensing technique offers a significant improvement in spatial sampling when compared to an occultation method because the only requirement is the observation of a sunlit portion of the atmosphere. Although select sensitivities occur for certain solar geometries, a sun-synchronous orbit can offer ample observation opportunities within a single orbit, nearing a 100% duty cycle in a near-terminator orbit.

The trade-off associated with the increased spatial sampling is that the retrieval method of atmospheric species from the limb viewing geometry is more challenging. In the case of occultation, the attenuation of light scattered out of or absorbed along the line of sight is measured, and contributions scattered into the line of sight are negligible. Conversely, in the limb viewing geometry, the measured radiance relies on these scattering events, which can occur in several scattering categories. In the simplest form, these events occur when

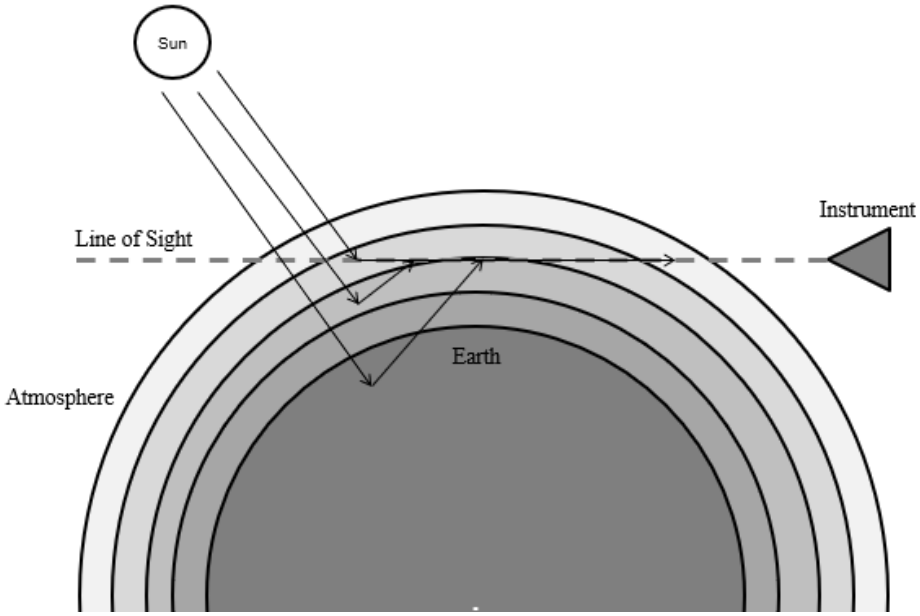

Figure 2.2: Viewing geometry for limb viewing measurements. The instrument field of view is centred on the sunlit portion of the atmosphere to measure sunlight that is scattered by particles in that atmosphere. Multiple scattering events are likely, including scattering from the surface of the Earth.

radiation is scattered off a particle directly into the line of sight of the instrument. Beyond this, reflections can occur from the surface of the Earth back into the atmosphere, where they may scatter into the line of sight. Alternatively, radiation may scatter off two or more particles in the atmosphere into the line of sight. Further combinations of these multiple scattering events are also possible, which requires a detailed radiative transfer model to perform retrieval techniques to determine the atmospheric state.

The Optical Spectrograph and InfraRed Imaging System (OSIRIS) is a limb viewing imaging spectrometer that makes Earth observations through the ultraviolet/visible/near-infrared spectrum [Llewellyn et al., 2004]. OSIRIS is a single line of sight imager with a wider horizontal field of view (FOV) than vertical. The line of sight is scanned in the atmosphere from 7-100 km and collects spectra covering 280-810 nm, achieving along-track sampling of $\sim$600 km. The scanning action occurs as the satellite platform nods during orbit, allowing vertical profile sampling. Similarly, the SCanning Imaging Absorption SpectroMeter for Atmospheric CHartographY (SCIAMACHY) is an imaging spectrometer that achieves vertical profile sampling using a scan mirror [Bovensmann et al., 1999]. The Ozone Mapping and

Profiler Suite - Limb Profiler (OMPS-LP) further improved the functionality of the limb viewing geometry by capturing three vertical profiles simultaneously via vertical slits (unlike to the horizontal slit in OSIRIS) [Flynn et al., 2006]. The vertical imaging capability through a single slit allows for rapid sampling in the along-track direction, achieving a spatial resolution of $\sim$125 km, allowing for tomographic retrieval of stratospheric aerosol [Zawada et al., 2018]. ALI is designed to measure limb scattered radiance, with the advantage of continuous vertical sampling through two-dimensional (2D) imaging.

2.3 Radiative Transfer and Aerosol Properties

The techniques described for measuring and monitoring stratospheric aerosol all require an understanding of the scattering properties of aerosol. These optical properties are fundamental to calibrating the PMTs in WOPCs, quantifying the attenuation along occultation path lengths, and modelling multiple scattering events in the atmospheric limb.

2.3.1 Atmospheric Scattering

If diffraction effects are neglected, an electromagnetic plane wave will propagate in a uniform direction, and cannot be detected from the side. Generally speaking, this occurs to sunlight as it propagates through the solar system near the Earth (at a distance far enough from the sun to behave like a plane wave rather than a spherical wave).

When radiation from the sun interacts with the densifying particle volume near the Earth's surface, the propagation is affected by the presence of atoms and molecules. This interaction, known as scattering, is characterized by the wavelength of the radiation, the size and shape of the scattering particle and the complex refractive index of the particle. Atmospheric scattering is typically characterized by elastic scattering, where little energy transfer is experienced between the electromagnetic wave and the particle. Instead, the energy is absorbed by electrons in the particle then immediately re-emitted, often in a new direction but with the same wavelength. Mie theory describes the absorption and scattering of light by spherical particles by numerically solving Maxwell's equations at a spherical boundary [Mie, 1908, Bohren and Huffman, 1998]. Here, a dimensionless size parameter is defined:

$$\alpha = \frac{\pi D_p}{\lambda}, \tag{2.1}$$

where D_p is the particle diameter and λ is the radiation wavelength. This parameter defines three dominate scattering regimes that occur in the atmosphere:

- $\alpha \ll 1$ Rayleigh scattering
- $\alpha \simeq 1$ Mie scattering
- $\alpha \gg 1$ Non-selective scattering

Each of these scattering regimes hold unique properties defining the way that the radiation is re-emitted from the particle. These properties include responses to polarization and wavelength and can result in significantly different angular distributions of emitted radiation. A scalar scattering event from a single particle is dominated by two properties: the scattering cross-section and the scattering phase function.

The likelihood that incident radiation will interact with a particle is quantified by the scattering cross section, σ. This quantity is not strictly defined by the geometric cross section of a particle, although the units are common between these two quantities. The scattering cross section may be much larger or smaller than the geometric cross section, depending on the scattering regime, and typically displays strong spectral dependence. This quantity can be conceptualized as the probability that a single particle will scatter a photon incident on a 1 cm^2 area.

The scattering phase function, P, represents the angular distribution that incident radiation may be scattered into, which is a function of scattering angle, θ, size parameter, α, and normalized refractive index, m. Here, the refractive index of the particle is normalized by the refractive index of the surrounding medium, which in the case of air is nearly 1. The scattering phase function is described as

$$P(\theta, \alpha, m) = \frac{F(\theta, \alpha, m)}{\int_0^\pi F(\theta, \alpha, m) \sin\theta d\theta}, \tag{2.2}$$

where $F(\theta, \alpha, m)$ is the intensity scattered into angle θ. The scattering phase function should therefore be interpreted as a probability distribution of a photon scattering into an infinitesimal angular range, $d\theta$, that is centered on θ. Note that the assumption of

a spherical particle means the azimuthal dependence is removed from the phase function [Seinfeld and Pandis, 2006].

The Earth's atmosphere is composed predominately of nitrogen, oxygen, argon and carbon dioxide, with trace gas species making up less than 1% of the volume of dry air. These constituents have diameters in the range of a few tenths of a nanometer, which is orders of magnitude smaller than the peak solar wavelength, near 500 nm. This leads to Rayleigh scattering, the most common process that occurs in the atmosphere. This scattering regime takes its name from Lord Rayleigh, who studied the interaction in terms of molecular oscillators [Strutt, 1871]. In this regime, a closed-form analytic solution can be found using Mie theory to describe the scattering, in terms of both the cross section and phase function.

The Rayleigh cross section is

$$\sigma_{Ray} = \left(\frac{2\pi^5 D_p^6}{\lambda^4}\right)\left|\frac{m^2-1}{m^2+2}\right|, \tag{2.3}$$

and the phase function is

$$P_{Ray}(\theta) = \left(\frac{3}{16\pi}\right)(1+\cos^2\theta). \tag{2.4}$$

This cross section reveals a λ^{-4} dependence, resulting in significantly more scattering in the blue end of the visible spectrum than in the red end. This results in the blue sky observed in Earth's atmosphere. Signal captured in remote sensing measurements of the atmosphere is dominated by this form of scattering.

The next larger category of particles is those with diameters approximately equal to the wavelength of the radiation. Stratospheric aerosol is an example of this type of scattering species in the atmosphere, with typical diameters of 0.1-1.0 μm. A closed-form solution does not exist in this regime, and a numerical solution is required consisting of Legendre polynomials and Bessel functions. Figure 2.3 shows the phase function for three near-infrared (NIR) wavelengths interacting with four spheres of H_2SO_4, each with different diameters in the Mie regime.

The smallest particle diameter in Figure 2.3 shows a phase function reminiscent of the underlying $(1+\cos^2\theta)$ shape characteristic of Rayleigh scattering. However, a larger fraction of the energy is scattered into the forward direction. As the particle size continues to increase, a larger portion of the energy is scattered in the forward direction, especially at longer

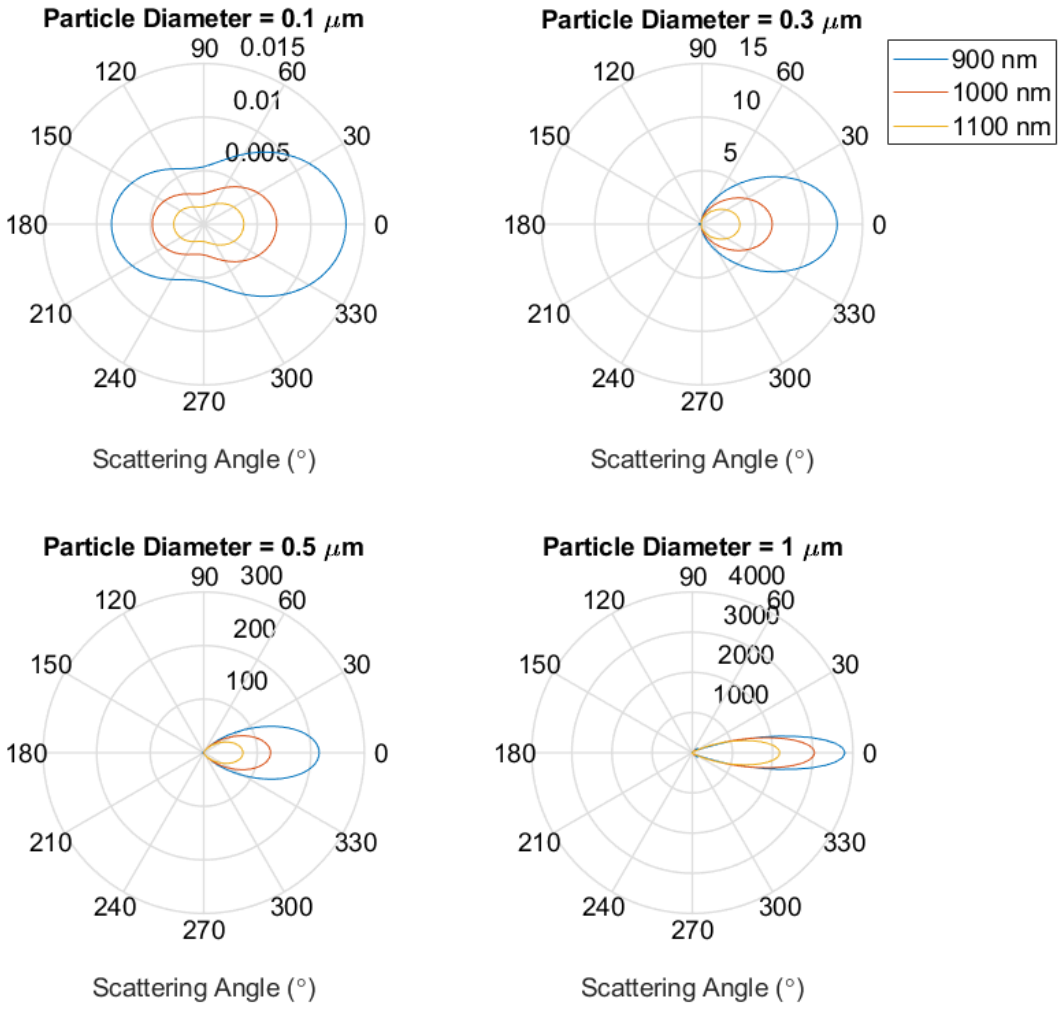

Figure 2.3: Mie scattering phase functions for three wavelengths and four particle sizes, [Mätzler, 2002]. The wavelength dependent refractive index of H_2SO_4 is used, with $m_{\lambda=1000} = 1.361 + i4.534E-7$. Radiation is incident from the left in each example, and a tendency to scatter in the forward direction (along $\theta = 0$) is observed, with a stronger response as the particle size increases.

wavelengths. This behaviour is observed when soot and ash from forest fires are present in the atmosphere, giving the sky a reddish glow.

The final elastic scattering regime occurs when the particle size parameter greatly exceeds 1. Non-selective, or geometric, scattering occurs when the particle size is much greater than the radiation wavelength. Under this condition, the macroscopic behaviours of scattering (reflection and/or refraction) dominate the interaction and the geometry of the particle becomes important. Under these conditions, the scattering phase function becomes independent of the scattering angle, polarization state or wavelength. All radiation is scattered uniformly away from the particle, as implied by the term *non-selective*. This scattering regime is characteristic of water droplets in cloud formations, which are transparent to visible wavelengths. The independence from wavelength and scattering angle causes the bright white appearance of cloud structures in the sky.

Polarized Scattering

Although sufficient for several applications, the description provided of the three primary atmospheric scattering regimes is incomplete without addressing the polarization response of these scattering scenarios. This response can be interrogated using Stokes vectors and Mueller matrices.

The four-element Stokes vector, $\mathbf{I}$, fully describes the polarization information for a select source. The vector is described as

$$\mathbf{I} = \begin{pmatrix} I \\ Q \\ U \\ V \end{pmatrix}. \tag{2.5}$$

Here, I describes the total radiance, Q represents the degree of linear polarization along the vertical/horizontal axes, U is the degree of linear polarization along the diagonal/antidiagonal axes, and V describes the degree of circular polarization.

Each scattering event imparts a polarization attribute to the scattered light. These attributes may be described by Mueller matrices acting on an incident Stokes vector, described as a scattering matrix, $\mathbf{P}(\theta)$, where the first matrix element is the phase function described

for scalar scattering. The scattering event and Stokes vector are not necessarily defined in the same coordinate frame, so rotation matrices, $\mathbf{L}(\phi)$, are required, where ϕ is the rotation angle between the two frames. The scattered Stokes vector is

$$\mathbf{I}_{scatt} = \mathbf{L}(\phi)\mathbf{P}(\theta)\mathbf{L}(-\phi)\mathbf{I}. \tag{2.6}$$

The Rayleigh-Gans approximation describes the scattering matrix for small particles ($\alpha \ll 1$) [Mishchenko et al., 2002]:

$$\mathbf{P}(\theta)_{Ray} = \frac{3}{4}\begin{bmatrix} 1+\cos^2\theta & -1+\cos^2\theta & 0 & 0 \\ -1+\cos^2\theta & 1+\cos^2\theta & 0 & 0 \\ 0 & 0 & 2\cos\theta & 0 \\ 0 & 0 & 0 & 2\cos\theta \end{bmatrix}. \tag{2.7}$$

Equation 2.7 shows that the polarization state of Rayleigh scattered light changes depending on the scattering angle. For instance, for randomly polarized incident signal ($I = 1, Q = V = C = 0$), the scattered signal will be randomly polarized for $\theta = 0$ and $\theta = 180$, but linearly polarized for $\theta = 90$ and $\theta = 270$. Also note that the total scattered radiance is characterized by a $(1 + \cos^2(\theta))$ term, as seen in Equation 2.4.

As noted previously, a closed-form solution using Mie theory does not exist to describe scattering when $\alpha \simeq 1$. Hence, a closed-form for the scattering matrix cannot be found [Bohren and Huffman, 1998]. However, for isotropic spherical particles like stratospheric aerosol, symmetry leads to matrices in the form

$$\mathbf{P}(\theta) = \begin{bmatrix} P_{11}(\theta) & P_{12}(\theta) & 0 & 0 \\ P_{12}(\theta) & P_{11}(\theta) & 0 & 0 \\ 0 & 0 & P_{33}(\theta) & P_{34}(\theta) \\ 0 & 0 & -P_{34}(\theta) & P_{33}(\theta) \end{bmatrix}. \tag{2.8}$$

A combination of the phase matrices for both Rayleigh and Mie scattering are responsible for the polarization signatures of stratospheric aerosol. The radiance from the sun is randomly polarized and is typically scattered by the Rayleigh background collection of particles. This

scattering event imparts a Rayleigh polarization feature on the scattered field. This feature is then modified by additional scattering events, like those from aerosol interactions, imparting the Mie polarization features onto the field.

The composition of particles in Earth's atmosphere affects the way that solar radiation travels through it. Macroscopically, the transmitted radiance is a function of several factors, including the number of particles, particle refractive index and path length through the atmosphere. The unique composition of trace gasses and particles impart identifiers onto the transmitted spectrum, based on unique spectral absorption and emission characteristics in their scattering cross-section. Additionally, the polarization state is influenced by particle composition. The radiative transfer equation describes how radiation interacts with the atmosphere and transmits through it. The impacts of stratospheric aerosol on this transmission can be difficult to isolate, and therefore inverse methods to retrieve aerosol properties are not straightforward. Here, the radiative transfer equation is developed, a simple but effective retrieval technique is identified, and the specific application for stratospheric aerosol is described.

2.3.2 Radiative Transfer

Spectral radiance, $I(\vec{r}, \hat{\Omega})$, describes the power measured by an optical sensor from an emitting surface area. It is described in space as a function of reference position, $\vec{r}$, and unit propagation vector, $\hat{\Omega}$, which is in the opposite direction of the sensor surface normal. The magnitude of measured radiance is derived from the radiant flux density, which is described by the optical energy, dE, per unit time, dt, per unit area, dA, that is emitted from a surface in a wavelength range from (λ,$\lambda + d\lambda$). The radiant flux density is scaled by a $1/\cos(\theta)$ factor when viewed at an angle θ from the surface normal and is measured over a small solid angle, $d\Omega$. The radiance is described by

$$I(\vec{r}, \hat{\Omega}) = \frac{dE(\vec{r})}{dt\ dA\ d\lambda\ d\Omega\ \cos(\theta)}. \tag{2.9}$$

The optical energy is described by the number of photons emitted. Therefore, the units of radiance are

$$[I(\vec{r}, \hat{\Omega})] = \frac{\text{photons}}{\text{s cm}^2\ \text{nm sterad}}. \tag{2.10}$$

For atmospheric radiative transfer, the propagation of radiance from one point to another is parameterized over an optical path, s. The transport of radiation is assumed to be in a straight line when refraction effects are negated (which is typically appropriate for Earth's atmosphere), so the point $\vec{r}$ can be described relative to an observing point, $\vec{r}_o$, as

$$\vec{r} = \vec{r}_o + \hat{\Omega}\ s. \tag{2.11}$$

Radiance may also be parameterized by the optical path as $I(s)$, rather than reference position vector and direction vectors.

As radiation propagates through a medium, it is attenuated according to the Beer-Lambert Law. Here, the radiance is attenuated over a small path length, ds, by the particle number density, n_i, and the probability of interaction, or particle cross-section, σ_i. The subscript i represents a single particle species. The change in radiance is written as

$$\frac{dI(s)}{ds} = -I(s) \sum_i n_i \sigma_i. \tag{2.12}$$

The effect of all particle species is summed. This quantity is called extinction,

$$k(s) = \sum_i n_i \sigma_i. \tag{2.13}$$

Extinction is often described in terms of scattering and absorbing components,

$$k(s) = k_{scat}(s) + k_{abs}(s). \tag{2.14}$$

A useful quantity, optical depth, may be defined over a path length with uniform extinction,

$$\tau(s) = -k(s)\ s. \tag{2.15}$$

Rearranging terms in Equation 2.12, and making substitutions for the extinction and optical depth based on definition yields,

$$\frac{dI(s)}{I(s)} = d\tau(s). \tag{2.16}$$

This differential equation may be solved to find how the radiance at a point, $I(s)$, is attenuated along the path to an observation point, $I(0)$, through the optical depth,

$$I(0) = I(s)e^{-\tau(s)}, \tag{2.17}$$

where the optical depth at the observation point is zero. This solution to the Beer-Lambert Law forms one of the primary terms in the radiative transfer equation, describing radiation losses along a path. The remaining term is responsible for describing radiation scattered into the optical path and is a function of a source term, J. The source term is once again related to extinction, however, to be a source, only the scattering component of extinction, $k_{scat}(s)$, is applicable. The addition of a source term implies that the radiance at a single point along the path may be influenced by all other points in the atmosphere. The source term, $J(s, \hat{\Omega})$, represents radiance coming from all directions scattered into the propagation direction and is written as

$$J(s, \hat{\Omega}) = \frac{k_{scatt}(s)}{k(s)} \int_{4\pi} I(s, \hat{\Omega}')\bar{p}(s, \Theta)d\Omega. \tag{2.18}$$

Here, Ω' highlights that diffuse radiance from all directions may be scattered into the propagation direction. The term $\bar{p}(s, \Theta)$ is a weighted average phase function for all scattering particles, and describes the probability of scattering per unit solid angle from direction $\hat{\Omega}'$ into $\hat{\Omega}$, with a defined scattering angle, Θ. When combining the result of the Beer-Lambert law and the effect of the source term, the radiative transfer equation is written as

$$I(0) = I(s)e^{-\tau(s)} + \int_s^0 k(s')J(s', \hat{\Omega}')e^{-\tau(s')}ds'. \tag{2.19}$$

Up to this point, the radiative transfer problem has only treated scalar radiance definitions, and ignored the polarized nature of atmospheric scattering. The vector description of the radiative transfer equation closely resembles Equations (2.18) and (2.19):

$$\mathbf{J}(s, \hat{\Omega}) = \frac{k_{scatt}(s)}{k(s)} \int_{4\pi} \mathbf{I}_{scatt}(s, \hat{\Omega}'(\theta, \phi))d\Omega, \tag{2.20}$$

$$\mathbf{I}(0) = \mathbf{I}(s)e^{-\tau(s)} + \int_s^0 k(s')\mathbf{J}(s', \hat{\Omega})e^{-\tau(s')}ds'. \tag{2.21}$$

Recall the definition of $\mathbf{I}_{scatt}$ from Equation (2.6), which contains rotation matrices, $\mathbf{L}(\pm\phi)$, a scattering matrix, $\mathbf{P}(\theta)$, and a Stokes vector, $\mathbf{I}$. $\mathbf{J}(s, \hat{\Omega})$ is now also described as a Stokes vector.

Both the scalar and vector definitions of the radiative transfer equation display the recursive nature of radiative transfer, where the integral term in the source term requires the calculation of radiance coming from an infinite number of points in an infinite number of directions, and each of these radiance calculations requires the same integral over another infinite number of directions. Each recursive step represents an additional scattering event in the atmosphere. Practically, the contribution of higher-order scattering events tails off, and fewer than 10 steps are typically required [Bourassa et al., 2008b].

The nature of Earth's atmosphere, with several particle species, relatively long path lengths, and highly variable density distribution, require specialized platforms to model the radiative transfer. SASKTRAN is one such model that solves the radiative transfer problem, which pairs well with limb viewing instruments [Bourassa et al., 2008b]. The viewing requirements for this branch of remote sensing instruments require explicit inclusion of the source term, and multiple scattering events. SASKTRAN allows for the inversion of remotely sensed observations for the retrieval of atmospheric properties in both scalar and vector definitions.

2.3.3 Retrieval Method

The problem of atmospheric modelling often comes down to an inversion problem when utilizing remote sensing measurements. In this case, the target quantities are not explicitly sampled but must be inferred from another measurable quantity. For instance, the number density of a scattering particle, like stratospheric aerosol, must be inferred from the magnitudes of spectrally sampled radiance measurements.

The SASKTRAN platform consists of three primary modules: Engine, Geometry and Atmosphere. The engine is the component that performs radiance calculations and has been under constant development since the early 1990s. Several engine options exist to calculate the radiance, including the original successive orders (SO) engine [Bourassa et al., 2008b], its successor the high resolution (HR) engine [Zawada et al., 2015], the Monte Carlo (MC) engine [Zawada et al., 2015], and others.

The geometry module is used to model the specific relation between observation positions and the sun. The geometry module established lines of sight, which represent the optical paths that the radiance propagates along towards the remote sensor. It defines angular relationships between radiance propagation vectors which are required to calculate phase function contributions, for example.

The final component, atmosphere, is the most dynamic element of SASKTRAN. This module represents the *atmospheric state* that will be modelled by the platform. This state describes the composition of the atmosphere, including which particle species are included in a simulation, how the species are distributed both vertically and horizontally, and the amount of ground reflectance (or albedo) that is simulated.

To use SASKTRAN, all three modules must be defined with a minimum set of parameters. Typically, the HR engine is defined, as it is the primary engine product. The geometry module may be defined using properties such as modified Julian date (to describe the position of the sun) and the observer position in latitude, longitude and altitude, plus the "look direction" of the observer. Finally, the atmospheric state must be assigned, which may be done with the assistance of defined climatologies. For instance, the MSIS90 climatology supports temperature and pressure identifiers, which may be used to set the number density of typical atmospheric species.

A common retrieval technique used with the SASKTRAN framework is a multiplicative algebraic reconstruction technique (MART). This technique is used to retrieve oxygen, ozone and stratospheric aerosol properties from limb scattered measurements [Degenstein et al., 2004, Degenstein et al., 2009, Bourassa et al., 2007, Bourassa et al., 2012b]. The MART defines a retrieval vector, y, which is intended to be sensitive only to the property that is targeted by the retrieval. For instance, ozone displays strong absorption in the Chappuis band (400-650 nm). Following [Degenstein et al., 2009], a retrieval vector may be defined using radiance observations at the two extremes of this band (identified as reference wavelengths), and one in the middle (identified as the absorption wavelength),

$$y^{obs} = \ln \frac{\sqrt{I(\lambda_{ref1})I(\lambda_{ref2})}}{I(\lambda_{abs})}. \tag{2.22}$$

Here, the radiance at the two reference wavelengths should not be strongly influenced by the

ozone concentration, however, an increase in ozone will lead to a radiance reduction at the absorption wavelength, thereby increasing the retrieval vector. Next, a simulated atmosphere is modeled with SASKTRAN, and a similar retrieval vector is produced from the modeled results, y^{mod}. The initial atmospheric state, x^0 will be an estimation based on a priori knowledge of the atmosphere (i.e. estimated from the MSIS90 climatology). A comparison of the two retrieval vectors will inform how the atmospheric state should be updated in the next modelling iteration. If n is the current iteration, then

$$x^{n+1} = x^n \frac{y^{obs}}{y^{mod}}. \tag{2.23}$$

The ratio of the retrieval vectors will modify the next atmospheric state to converge the observed and modelled states. Although not explicitly shown in this description, the retrieval vectors will be generated for all sampled lines of sight, and multiple retrieval vectors may be utilized. If this is the case, then a weighting function must be applied for each retrieval vector used before summing all vectors.

2.3.4 Retrieval of Aerosol Properties

Aside from special conditions such as increased loading of soot from forest fires or ash from volcanic activity, the optical properties of stratospheric aerosol lead to greater scattering than absorption. Following Equations (2.18) and (2.19), aerosol scattering is governed by the aerosol number density, phase function and scattering cross-section. An additional complicating factor is the particle size distribution. A standard unimodal lognormal particle distribution is often assumed in the form

$$\frac{dn(r)}{dr} = \frac{N}{\sqrt{2\pi}\ln(\sigma_g)r} \exp\left(- \frac{(\ln(r) - \ln(r_g))^2}{2\ln^2(\sigma_g)} \right). \tag{2.24}$$

Here, r_g is the mean particle radius, σ_g is the distribution width and N is the aerosol number density concentration. Following stratospheric disruptions like volcanic activity, bimodal lognormal size distribution assumptions may be required to account for the presence of larger particles. Recalling Figure 2.3, the size of particles in the Mie scattering regime will strongly

impact the scattering phase function. Errors in the assumed particle distribution will therefore manifest errors in the phase function.

Several retrieval methods have been developed to measure stratospheric aerosol extinction coefficient, including the OSIRIS Version 5 Data Product [Bourassa et al., 2012a]. This data product uses SASKTRAN's flagship remote sensing instrument, OSIRIS, described in Section 2.2.4. The Version 5 extinction retrieval algorithm is a modification to a previous algorithm developed by [Bourassa et al., 2007], with improvements coming from the inclusion of forward modeled calculation of the radiance of the Rayleigh atmosphere, improvements to effective albedo retrieval, and normalization of the retrieval vector to improve signal to noise. The previous algorithm defined a retrieval vector

$$y_j = \ln\left(\frac{\tilde{I}(j,\lambda_2)}{\tilde{I}(j,\lambda_1)}\right), \tag{2.25}$$

where $\tilde{I}(j,\lambda)$ represents a normalized radiance at tangent altitude j and wavelength λ [Bourassa et al., 2007]. In the published data product, $\lambda_1 = 470$ nm and $\lambda_2 = 750$ nm. The tangent altitude radiance is normalized by the radiance at a higher reference tangent altitude at the same wavelength. The tangent altitude normalization removes the need for an absolute calibration, and also reduces the sensitivity to effective albedo.

The retrieval vector is modified in Version 5 to remove sensitivity to the dominant Rayleigh scattering, particularly at low tangent altitudes. The Rayleigh contribution is simulated in an aerosol free atmosphere, then used to normalize the retrieval vector,

$$y_j = \ln\left(\frac{\tilde{I}(j,\lambda_2)}{\tilde{I}(j,\lambda_1)}\right) - \ln\left(\frac{\tilde{I}_{Ray}(j,\lambda_2)}{\tilde{I}_{Ray}(j,\lambda_1)}\right). \tag{2.26}$$

This normalization helps to linearize the retrieval vector dependence on aerosol loading. The retrieval vector is further modified to include a high altitude geometric mean normalization rather than single high altitude normalization, which improves the signal-to-noise ratio.

The limitation to this approach is that it requires an assumed particle size distribution ($r_g = 80$ nm and $\sigma_g = 1.6$ in this case) to calculate the phase function. [Rieger et al., 2014] investigate the validity of the ascribed phase functions by comparing intersecting measurements from the ascending and descending track of OSIRIS. These intersection points are

measurements of common atmospheric states with different scattering angles. Differences in the retrieved aerosol extinction indicate errors in the phase function, caused by an incorrect particle size distribution. Comparing retrieved extinction in the tropics from the ascending and descending nodes over several years highlights a systematic offset, likely pointing to an incorrect particle size distribution assumption.

[Rieger et al., 2014] further develop the retrieval technique by investigating the sensitivity of the retrieval vector to particle size. Although minimally, the 470 nm radiance is noted to be influenced by aerosol, so it is not entirely insensitive to the particle size assumptions. Therefore, the 470 nm normalization is removed from the retrieval vector.

In this 2014 study, three particle size distributions are defined that produce a common retrieval vector at 750 nm, shown in Figure 2.4a. The size distributions represent a bimodal distribution to simulate volcanic conditions, the Version 5 unimodal distribution, and a unimodal distribution with an effective radius to match the bimodal distribution. The retrieval vector is then calculated over a wider spectrum for these three distributions, displayed in Figure 2.4b. These vectors show little difference for wavelengths shorter than 800 nm, and improved particle size sensitivity at longer wavelengths, highlighted by the separation of the measurement vectors at long wavelengths. This is a key finding to identify the need for near-infrared spectral measurements to retrieve both extinction and particle size content.

Advances to the retrieval technique are under continued investigation, with improvements made to the selection of retrieval vectors as well as the inversion technique. The current Version 7 OSIRIS data product for instance utilizes a selection of wavelengths and a Levenberg-Marquardt procedure to update atmospheric state vectors, which minimizes bias due to uncertainty in particle size [Rieger et al., 2019]. This continued retrieval development has run in parallel to the development of aerosol sensing instrumentation. It has capitalized on the features of existing instruments but has also identified opportunities for improvements in the succeeding generation.

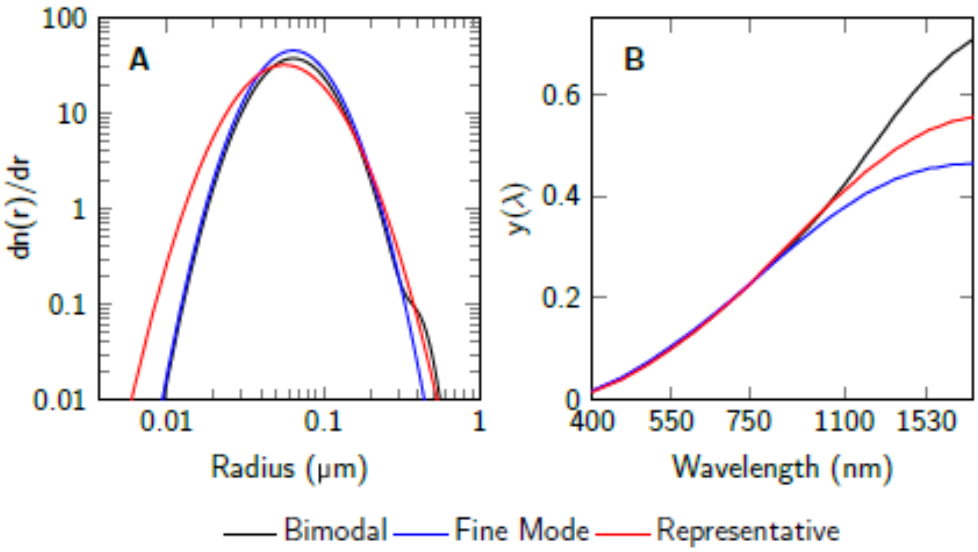

Figure 2.4: Modelled sensitivity of aerosol retrieval vectors to particle size distributions. (a) Three aerosol size distributions at 22.5 km, highlighting two unimodal distributions with differing mean particle radii, and a bimodal distribution representing a post-volcanic activity atmosphere. Each size distribution generates a common retrieval vector at 750 nm. (b) Retrieval vectors as a function of wavelength for the three size distributions. Reproduced with permission of the author, [Rieger et al., 2014].

2.4 Project Motivation

The goal of this work is to advance the design of ALI to fill the current opening in stratospheric aerosol monitoring remote sensors. This development requires the expansion of the spectral range from visible to NIR wavelengths to address the size distribution sensitivity in aerosol retrievals. Additionally, polarization sensitivity is imperative in the next generation designs for high altitude cloud identification to facilitate linking aerosol-cloud interactions.

Satellite-based instruments require several years of development from grassroots prototypes to flight-qualified operational units. Standard practices in the space sector are outlined by operating procedures, hardware development plans and review processes defined by organizations like the Canadian Space Agency (CSA), the National Aeronautics and Space Administration (NASA), the European Space Agency (ESA) and several other national organizations. One of the most concise descriptions of the hardware development plan is NASA's roadmap of Technology Readiness Levels (TRLs) [Shea, 2017]. This work is focused on im-

proving the TRL of the Aerosol Limb Imager through hardware development for sub-orbital platforms.

2.5 Advanced Remote Sensing Techniques

The several examples cited in section 2.2 have sustained a continuous stratospheric aerosol record since the 1970s, with continuous global coverage beginning with the first satellite-based remote sensors. Several of these instruments are designed specifically to target stratospheric aerosol measurements, while others have adaptable capabilities as secondary functions. The catalogue of remote sensors contains a vacancy for an instrument to capture continuous global coverage with high spatial and temporal resolution. These targets are limited by the technologies used in past and current generations of remote sensing instruments.

To fill this vacancy, a new instrument concept has been developed to specifically target some of the shortcomings of current instrumentation. The Aerosol Limb Imager began feasibility studies in the early 2010s and has continued to evolve towards a viable candidate for a satellite mission within the next 10 years. The instrument is designed to capture multispectral, 2D images of limb scattered sunlight and is the focus of the remainder of this work. Optical concepts are first discussed, addressing image formation and limitations of physical optical elements. These limitations result in degradation of image quality, which can be characterized by aberration theory and quantified by performance metrics like spot size, encircled energy and modulation transfer function. These concepts are only briefly summarized as they are well studied and documented [Born and Wolf, 2013, Hecht, 2017, Smith, 2008]. Next, acousto-optics, an electro-optical technique is examined to identify how spectrally resolved 2D images can be captured from a remote sensing platform. A discussion of a second electro-optic technique, liquid crystal polarization modulation, is also presented, followed by a discussion of the historical developments of ALI.

2.5.1 Imaging Optics

A point source, P, radiates through a uniform medium as a diverging spherical wave with maxima separated by the wavelength, shown in Figure 2.5. These maxima, or wavefronts,

are captured at a specific moment in time and drawn as thin black lines. At the interface between two media, the wave will refract according to Snell's law. An ideal lens, with a radius of curvature and an appropriately higher refractive index than the surrounding media, will refract the spherical wave at different moments in time as it propagates, forming a plane wave within the interior of the lens. As this plane wave continues to propagate rightward, it once again reaches a media interface, and the plane wave is refracted at different moments in time, forming a converging spherical wave. The point where the wavefronts converge, P', is a focused image of the point source. P and P' are optical conjugates.

The process of focusing a point source through an ideal lens can be expanded to multiple sources, each emitting a unique set of spherical wavefronts. Each source will have a single optical conjugate, related to the longitudinal and transverse position of the source with respect to the lens and its optic axis. Sources with a common longitudinal distance from the lens will ideally focus on a plane, often described as an image plane. This leads to the concept of optical image formation, in which a series of point sources from an extended object are focused through an optical system to form an image in conjugate space.

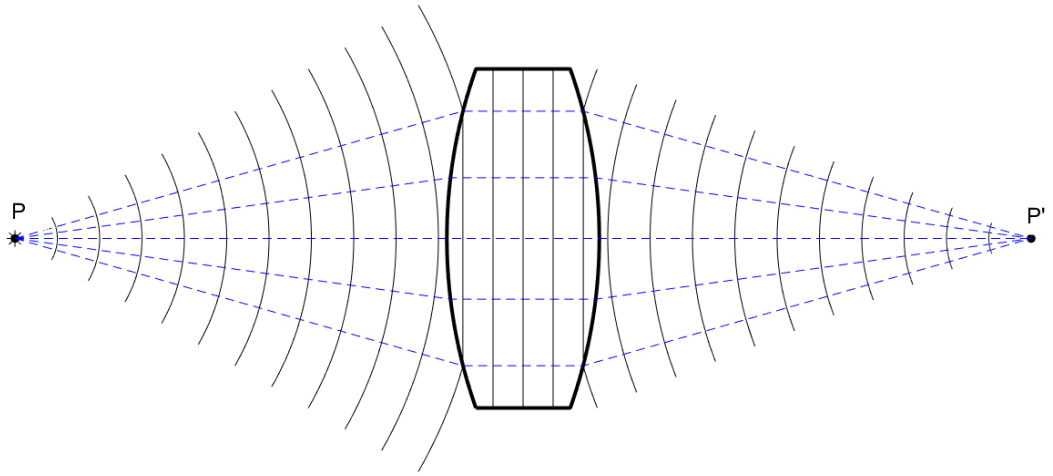

Figure 2.5: Image formation of point source, P, through an ideal lens.

A mathematical formulism for wavefront propagation in an optical system is challenging, however, it is greatly simplified by introducing the concept of optical rays. Rays are drawn perpendicular to the wavefronts, shown in blue in Figure 2.5. These rays originate and diverge from the source, P, and then converge at the focus, P'. Geometric optics is based on tracing

rays through an optical system. The technique is used for the initial layout of an optical system as well as first-order error assessment.

Physical optics impose limitations on the reshaping of wavefronts, leading to optical aberrations. Aberrations are the result of constraints in lens material selection and surface shaping. Surface shaping can also limit the performance of reflective optical elements like mirrors, which are analogous to lenses in many ways. Optical aberrations are characterized by the distance the ray is from the rotation axis of the optical element, r, and the angle at which the rays strike the surface, h. The five primary transverse aberrations, referred to as Seidel aberrations, are spherical (proportional to r^3), coma (proportional to r^2h), astigmatism (proportional to rh^2), Petzval curvature (proportional to rh^2), and distortion (proportional to h^3). Some of these Seidel aberrations also have longitudinal components with slightly different dependencies. The result of these and higher-order aberrations is the spatial broadening of energy distribution at the focus, P'. Figure 2.6a displays a geometric ray trace from a monochromatic point source, through a real lens to the focus. Select wavefronts are highlighted. Figure 2.6b shows a single wavefront with a spherical wavefront overlaid to highlight the difference in shape resulting from transmission through a physical optical element. Finally, Figure 2.6c shows the distribution of rays as observed on a screen placed at the focus of the lens from a geometric ray trace. The optical energy is distributed over a finite area rather than focused to a single point, as was described for the ideal lens case.

There are additional factors that also affect the concentration of rays at the focus. The first is diffraction caused by the physical size of the imaging optic. Diffraction is quantified by a Fourier transform related to the optical aperture and the wavelength of the source. For example, an infinite distance point source passing through a circular aperture has a well-defined diffraction limit described by the Airy disk [Airy, 1835]. In fact, diffraction occurs for an ideal lens modelled with a finite size as well. Figure 2.6d displays the point spread function (PSF) representing the physical propagation of wavefronts through a finite-sized real lens. Here, the energy distribution is shown to be similar to that in Figure 2.6c, but in this case, includes the impacts of diffraction.

The PSF is a useful analytic tool because it can be convolved with an object scene to

estimate the imaging performance of an optical system. Furthermore, it lends itself to a convenient proxy, the encircled energy, to quantify the point source image quality. The encircled energy describes the diameter of a circle that is required to capture a specified percentage of the total optical energy. For instance, a perfect Airy disk contains 83.9% of the optical energy within the central lobe of the pattern. This means the 83.9% encircled energy for an ideal lens is encircled by a diameter of $2.44\lambda \times$ f/#, where f/# is the ratio of the system focal length to pupil diameter. The encircled energy is a particularly helpful metric for assessing image quality when performing a Monte Carlo tolerance analysis to estimate the performance of an optical system with realistic manufacturing and build tolerances.

A second significant factor that limits the size of a focused spot is related to the wavelength-dependent refractive index of materials used for refractive optics. All physical sources have a finite spectral bandwidth, which will inherently focus at different distances from the lens. This leads to a wavelength-dependent broadening of the spot on a static image plane. The magnitude of this broadening, described as chromatic defocus, can be reduced through the addition of new lenses of different materials to find a balance in the spectral divergence for each lens. These chromatic effects are not seen in reflective optical systems because the laws governing reflection are achromatic.

Similar to the description for an ideal lens, the focusing of wavefronts through a physical optic can also be expanded to an extended object to form an image. Here, however, the extended point sources will each experience different amounts of optical aberration, depending on their position with respect to the lens, and therefore each features a specific PSF. A tool called the modulation transfer function (MTF) is used to quantify how the PSF redistributes energy in the image plane over an extended object. To calculate the MTF at spatial frequency f, a sinusoidal scene is imaged through the optical system, where the PSF redistributes signal from the bright part of the scene into the dark parts through a convolution. A sinusoid is selected for this metric because Fourier analysis shows that any scene can be represented by sinusoidal spatial frequencies. The MTF is calculated using the bright (I_{max}) and dark (I_{min}) parts of the image as:

$$MTF(f) = \frac{(I_{max} - I_{min})}{(I_{max} + I_{min})}. \tag{2.27}$$

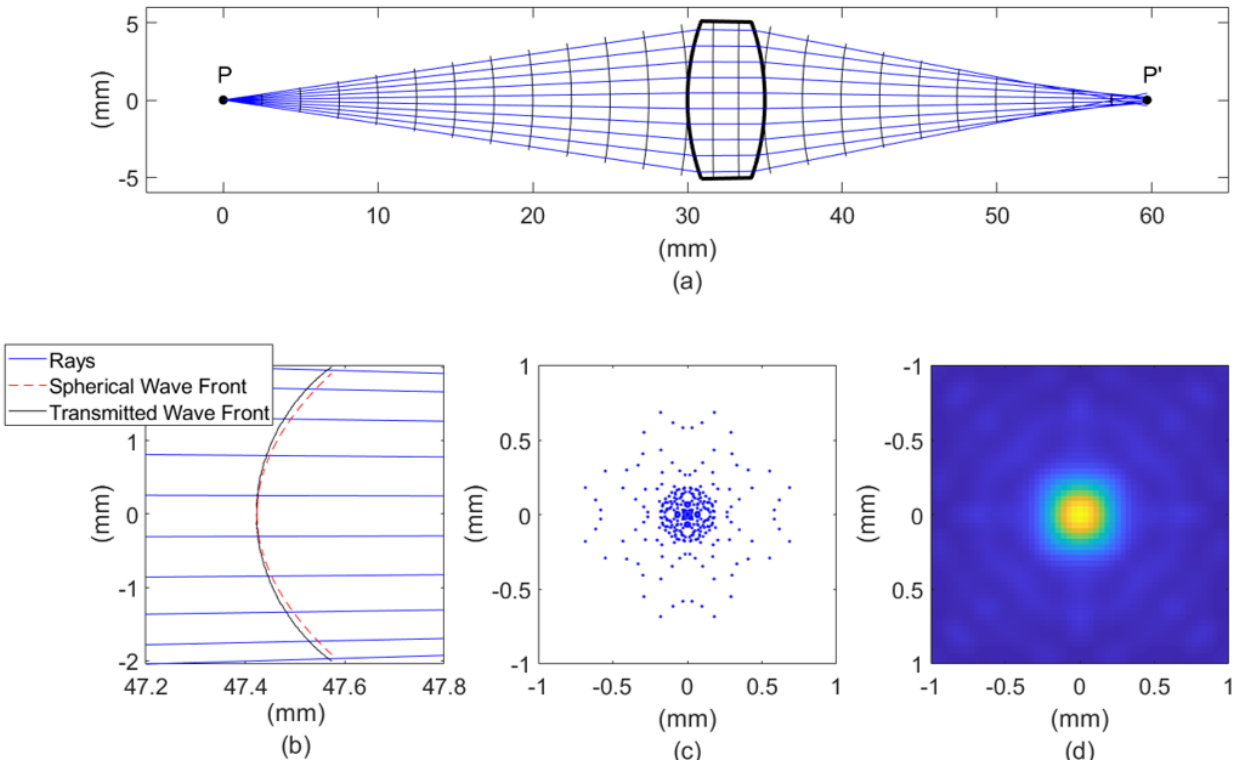

Figure 2.6: Image formation of a point source, P, through a physical lens. (a) Rays and sampled wavefronts traced from the source P to the image P'. (b) Magnified view of a single wavefront showing deviation from a spherical shape. (c) 2D spot diagram of rays traced through the lens system to a screen placed at the focus, P'. (d) Point spread function displaying energy distribution including impacts of diffraction.

Figure 2.7 shows a representation of the MTF calculation for two object scenes with differing frequencies on the left. The modulation is transferred through the optical system and captured in the image. The low-frequency modulation (Figure 2.7a) is transferred more efficiently than the high-frequency modulation (Figure 2.7b). The red lines in each plot highlight the contrast in the respective images, with greater contrast seen in the low-frequency case. Typically, contrast greater than 0.1 is required to resolve image information, but this is application-specific [Smith, 1998].

2.5.2 Novel Atmospheric Spectral Filtering

Standard spectral filtering techniques implemented in previous aerosol measurement instrumentation cannot meet the goals of ALI. Grating spectrometers restrict spatial resolution to only a single direction; transmission filters limit spectral selection flexibility and imaging

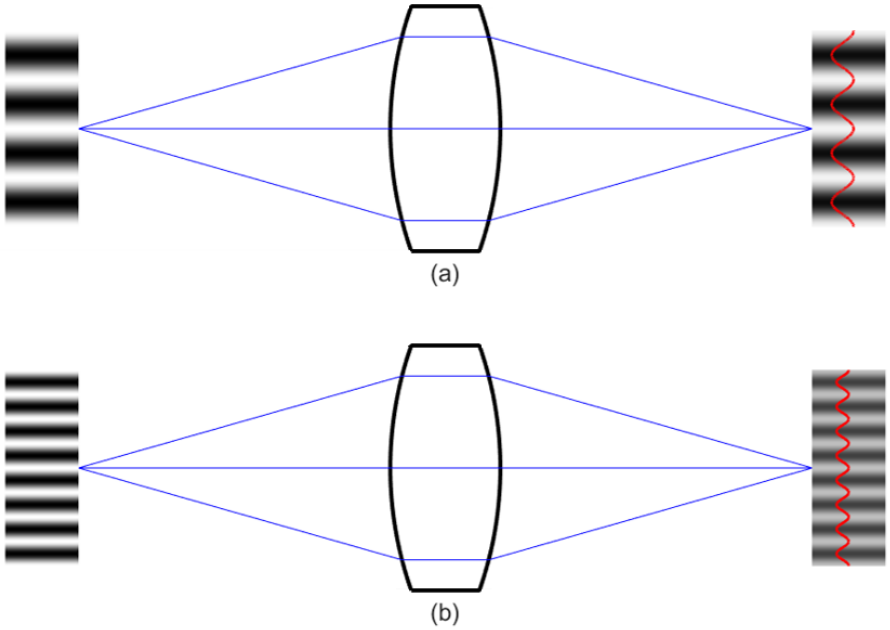

Figure 2.7: Transfer of object modulation through an optical system. (a) Low-frequency modulation is efficiently transferred, with high contrast between bright and dark regions. The brightness in the image is shown in red. (b) High-frequency modulation is less efficiently transferred, with more energy from the bright regions registering in the dark regions in the image. The contrast between the bright and dark regions is reduced as shown in the red line.

duty cycle. Here, a novel use for acousto-optic tunable filter (AOTF) technology has been identified to perform solid-state, multi-spectral imaging. The acousto-optic (AO) interaction is governed by the propagation of acoustic and optical waves through certain materials, the most effective being crystals which exhibit optical birefringence.

Optical Waves in Crystal Structures

The propagation of optical waves through birefringent crystals relies on the characteristics of the lattice structure of the atoms. This has been well characterized for several materials [Newnham, 2005]. Tellurium dioxide (TeO_2) is a common AO material with a Tetragonal 422 crystal class, which exhibits uniaxial birefringence, meaning it shows symmetry about a single rotation axis.

The optical anisotropic nature of TeO_2 arises from the electrical dipoles established within the medium, which induces a directional dependence on the electrical permitivity, ϵ. For most

materials, ϵ is a scalar value, but in this case it is a second rank tensor,

$$\boldsymbol{\epsilon} = \begin{pmatrix} \epsilon_{11} & \epsilon_{12} & \epsilon_{13} \\ \epsilon_{21} & \epsilon_{22} & \epsilon_{23} \\ \epsilon_{31} & \epsilon_{32} & \epsilon_{33} \end{pmatrix}. \tag{2.28}$$

The orientation of this tensor with respect to the crystal can be selectively chosen to eliminate all elements except for the diagonal. The tensor leads to loci of two orthogonal wave vectors, $\boldsymbol{k_o}$ and $\boldsymbol{k_e}$ [Korpel, 1996]. This is observed by starting with two of Maxwell's equations:

$$\nabla \times \boldsymbol{\mathcal{E}} = -\frac{d\boldsymbol{\mathcal{B}}}{dt}, \tag{2.29}$$

$$\nabla \times \boldsymbol{\mathcal{H}} = \frac{d\boldsymbol{\mathcal{D}}}{dt}. \tag{2.30}$$

Assuming a plane wave oscillating according to $e^{j(\omega t - \boldsymbol{k}\cdot\boldsymbol{R})}$, and recalling that $\boldsymbol{\mathcal{B}} = \mu_o \boldsymbol{\mathcal{H}}$ in material free from magnetic permeability, Equations (2.29) and (2.30) may be simplified to

$$\boldsymbol{k} \times \boldsymbol{\mathcal{E}} = \omega \mu_o \boldsymbol{\mathcal{H}} \tag{2.31}$$

and

$$\boldsymbol{k} \times \boldsymbol{\mathcal{H}} = -\omega \boldsymbol{\mathcal{D}}. \tag{2.32}$$

Eliminating $\boldsymbol{\mathcal{H}}$ and applying $\boldsymbol{a} \times (\boldsymbol{b} \times \boldsymbol{c}) = (\boldsymbol{a} \cdot \boldsymbol{c})\boldsymbol{b} - (\boldsymbol{a} \cdot \boldsymbol{b})\boldsymbol{c}$ yields:

$$(\boldsymbol{k} \cdot \boldsymbol{\mathcal{E}})\boldsymbol{k} - (\boldsymbol{k} \cdot \boldsymbol{k})\boldsymbol{\mathcal{E}} = -\omega^2 \mu_o \boldsymbol{\mathcal{D}}. \tag{2.33}$$

Recall also that $\boldsymbol{\mathcal{D}} = \boldsymbol{\epsilon}\boldsymbol{\mathcal{E}}$, where $\boldsymbol{\epsilon}$ is the tensor from Equation (2.28). The orientation of the tensor is chosen to align with the Cartesian crystal symmetry axes, resulting in

$$\boldsymbol{\epsilon} = \epsilon_0 \begin{pmatrix} n_x^2 & 0 & 0 \\ 0 & n_y^2 & 0 \\ 0 & 0 & n_z^2 \end{pmatrix}. \tag{2.34}$$

Equation (2.33) can be expressed as a set of linear equations in $\boldsymbol{\mathcal{E}}$ as

$$\begin{pmatrix} (\beta n_x^2 - k_y^2 - k_z^2) & k_x k_y & k_x k_z \\ k_x k_y & (\beta n_y^2 - k_x^2 - k_z^2) & k_y k_z \\ k_x k_z & k_y k_z & (\beta n_z^2 - k_x^2 - k_y^2) \end{pmatrix} \begin{pmatrix} E_x \\ E_y \\ E_z \end{pmatrix} = 0, \tag{2.35}$$

where

$$\beta = \mu_0 \epsilon_0 \omega^2. \tag{2.36}$$

Nontrivial solutions are found when the determinant of the 3×3 matrix equals zero, expressed as

$$\beta^2 - \beta\left(\frac{-k_x^2 - k_y^2}{n_z^2} + \frac{-k_x^2 - k_z^2}{n_y^2} + \frac{-k_y^2 - k_z^2}{n_x^2}\right) + \left(\frac{k_x^2}{n_y^2 n_z^2} + \frac{k_y^2}{n_x^2 n_z^2} + \frac{k_z^2}{n_x^2 n_y^2}\right)(k_x^2 + k_y^2 + k_z^2) = 0. \tag{2.37}$$

The uniaxial property of TeO_2 implies that the refractive indices about two of these axes are the same. Defining $n_x = n_y = n_o$ as the "ordinary" refractive index and $n_z = n_e$ as the "extraordinary" refractive index, the expression factors into

$$\left(\frac{k_x^2}{n_o^2} + \frac{k_y^2}{n_o^2} + \frac{k_z^2}{n_o^2} - \beta\right)\left(\frac{k_x^2}{n_e^2} + \frac{k_y^2}{n_e^2} + \frac{k_z^2}{n_o^2} - \beta\right) = 0. \tag{2.38}$$

Equation (2.38) is used to describe two elliptical surfaces in $\boldsymbol{k}$ space, which bound the wave vector of a specific frequency. Equating the first factor to zero traces a spherical boundary for the wave vector, regardless of the direction of $\boldsymbol{k}$. Equating the second to zero, however, traces an ellipsoid symmetric about the Z-axis. This solution space implies that any direction of propagation has two allowable wave vector solutions. The first solution is the same regardless of propagation direction, and the second varies with direction. These solutions describe the ordinary and extraordinary polarization states, respectively.

To better illustrate this point, a refractive index ellipsoid for a uniaxial material is drawn in Figure 2.8a where $n_x = n_y = n_o$ and $n_z = n_e$. A wave propagates in the YZ plane in the direction of the wave normal, s_p, at an angle, θ, with respect to the optic axis of the material (defined as the z-axis). The refractive index for this wave is defined by the intersection of the ellipsoid with a vector normal to s_p. Equation (2.38) described two solutions for $\boldsymbol{k}$, the first of which is bound by a sphere with refractive index described by n_o. This assigns the first

refractive index solution to the XY plane, shown as point "a", the ordinary refractive index. The second solution, with an orthogonal polarization to the first, intersects with the ellipsoid on an elliptical boundary which depends on θ. The second point, "b", offers the refractive index of the extraordinary polarization. A plot of the loci of the ordinary and extraordinary refractive indices as a function of angle from 0 to 2π is shown in Figure 2.8b. The ordinary refractive index, n_a, is constant with θ, but the refractive index of the extraordinary wave, n_b, varies from n_o to n_e based on the ellipse [Yariv, 1991]

$$\frac{1}{n_b(\theta)} = \frac{\cos^2(\theta)}{n_o^2} + \frac{\sin^2(\theta)}{n_e^2}. \tag{2.39}$$

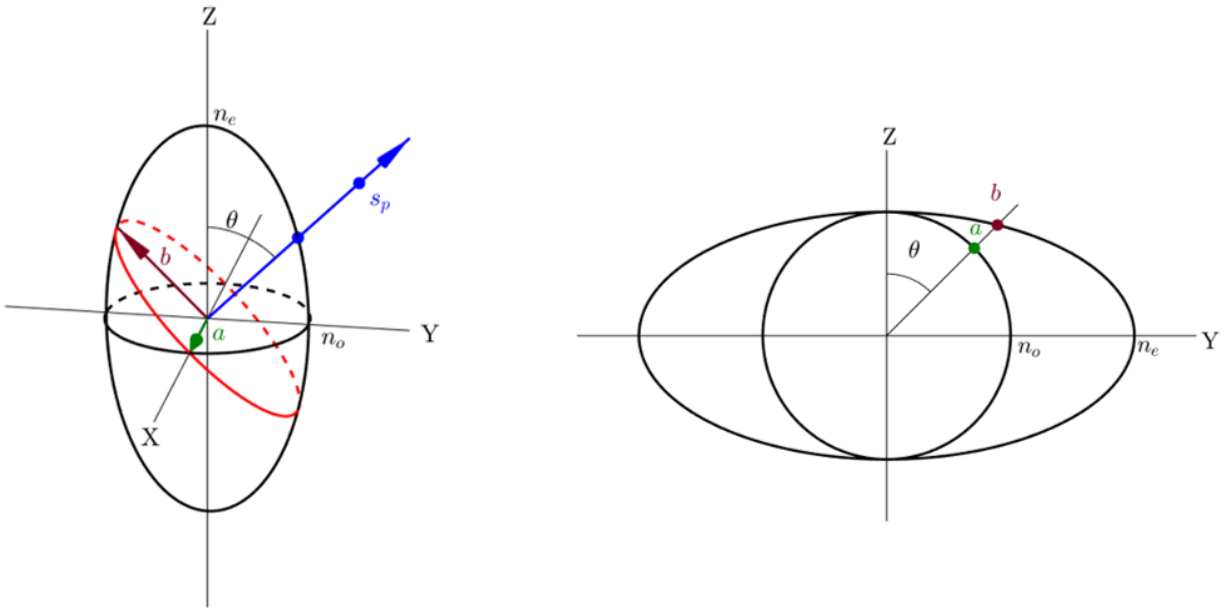

(a) **(b)**

Figure 2.8: Optical propagation at angle θ with respect to optical axis. (a) Intersection of orthogonal polarization states with refractive index ellipsoid. (b) Ordinary and extraordinary refractive index as a function of incidence angle with respect to the optical axis.

Multiplying the indices in Figure 2.8b by the magnitude of the free space wave vector will define $\boldsymbol{k_o}$ and $\boldsymbol{k_e}$. Generating similar plots for the wave vectors is essential later for illustrating the Bragg diffraction criterion that defines the AOTF interaction.

Acoustic Waves in Crystal Structures

Like optical waves, plane acoustic waves also travel through crystal structures in a manner defined by their direction with respect to the crystal structure. Here however, the primary relationship is the acoustic velocity with respect to the direction. This falls out from solutions to the Christoffel equation

$$[k^2\Gamma_{ij} - \rho\omega^2\delta_{ij}][v_j] = 0, \tag{2.40}$$

where k is the wave vector, v is the propagation speed, ρ is the material density, ω is the frequency, and Γ is the Christoffel matrix [Auld, 1990]. For a Tetragonal 422 crystal like TeO_2, this matrix is

$$\Gamma = \begin{bmatrix} c_{11}l_x^2 + c_{66}l_y^2 + c_{44}l_z^2 & (c_{12}+c_{66})l_xl_y & (c_{13}+c_{44})l_xl_z \\ (c_{12}+c_{66})l_xl_y & c_{66}l_x^2 + c_{11}l_y^2 + c_{44}l_z^2 & (c_{13}+c_{44})l_yl_z \\ (c_{13}+c_{44})l_xl_z & (c_{13}+c_{44})l_yl_z & c_{44}l_x^2 + c_{44}l_y^2 + c_{33}l_z^2 \end{bmatrix} = \begin{bmatrix} \nu & \delta & \upsilon \\ \delta & \tau & \zeta \\ \upsilon & \zeta & \gamma \end{bmatrix}. \tag{2.41}$$

Here, $l_x = k_x/k$, $l_y = k_y/k$, $l_z = k_z/k$ and c_{ij} are crystal stiffness coefficients. Non-trivial solutions to Equation (2.40) are found by setting the determinant equal to zero,

$$\begin{aligned} &[\nu(\tau\gamma - \zeta^2) + \delta(\upsilon\zeta - \delta\gamma) + \upsilon(\delta\zeta - \upsilon\tau)](k^2/\omega^2)^3... \\ &\quad + [-\nu\rho(\tau+\gamma) - \rho(\tau\gamma - \zeta^2) + \delta^2\rho + \upsilon^2\rho](k^2/\omega^2)^2... \\ &\quad\quad + [(\nu+\tau+\gamma)\rho^2](k^2/\omega^2) - \rho^3 = 0. \end{aligned} \tag{2.42}$$

Solving for k/ω, the slowness curves of a crystal can be identified. These slowness curves are the inverse of the acoustic wave velocity travelling in a specific direction, with the group velocity perpendicular to the curve. Example slowness curves for longitudinal and shear waves in the [110] [010] plane of TeO_2 are shown in Figure 2.9.

Acousto-Optic Tunable Filters

The propagation of optical and acoustic waves through materials can be exploited to control the former with the latter. This interaction was first predicted by Léon Brillouin in 1922,

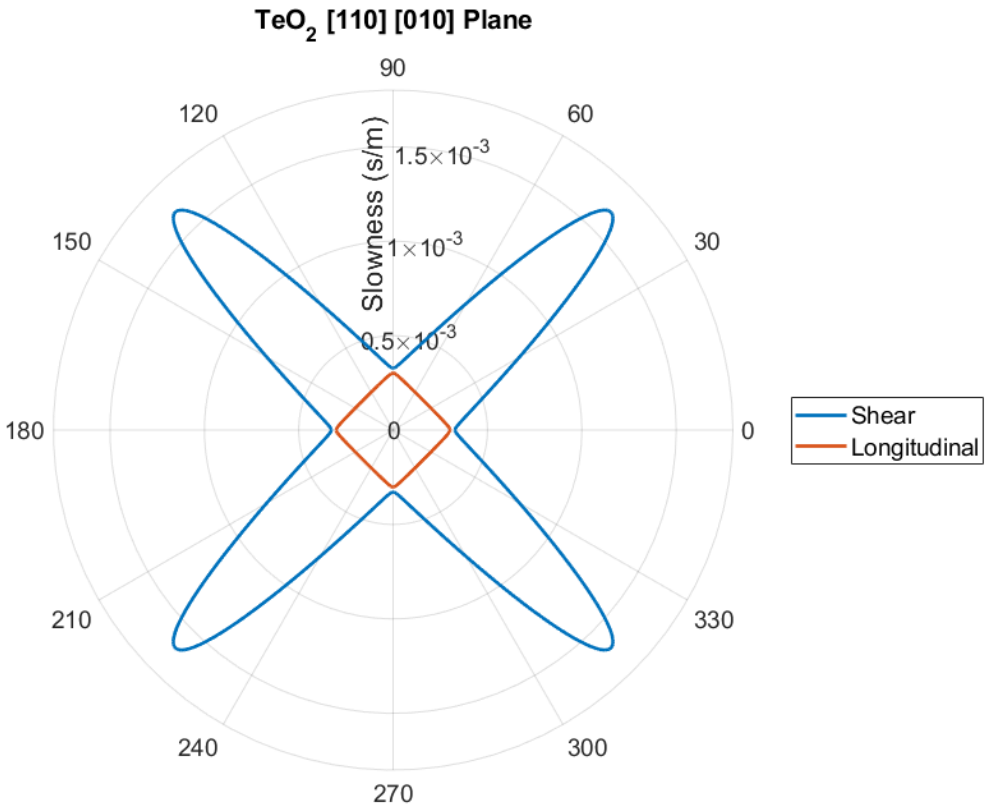

Figure 2.9: Slowness curves for shear and longitudinal acoustic waves in TeO_2.

through a demonstration of light scattering within a medium caused by an acoustic wave travelling through it [Brillouin, 1922]. Several decades later, this phenomenon was formally described as the interaction between planar sound waves and light and named the AO effect identified previously [Korpel and Poon, 1980].

The AO effect is induced in transparent materials by a periodic variation of the refractive index. This variation is introduced by the elasto-optic effect when high frequency stress causes compression and relaxation of the material [Chang, 1981]. Stress may be applied by bonding piezoelectric transducers to the material and applying a potential difference. The interaction of light with this region of periodic variation leads to AO diffraction, which is like the interaction of light with a transmission grating [Chang, 1977]. This AO diffraction was first demonstrated in a water cell in 1955, then with anisotropic materials in 1967 [Rosenthal, 1955, Dixon, 1967]. The most favourable of these materials are those with high densities and slow acoustic speeds, such as quartz (SiO_2), lithium niobate ($LiNbO_3$) and TeO_2 [Bei et al., 2004].

The Bragg diffraction criterion governing the AO interaction is based on momentum matching of incident photons from an optical wave, and phonons generated by the acoustic column. The criterion is described by

$$\overrightarrow{\boldsymbol{k}_i} \pm \overrightarrow{\boldsymbol{K}_a} = \overrightarrow{\boldsymbol{k}_d}, \tag{2.43}$$

where $\overrightarrow{\boldsymbol{k}_i}$ is the incident optical wave vector, $\overrightarrow{\boldsymbol{K}_a}$ is the acoustic wave vector and $\overrightarrow{\boldsymbol{k}_d}$ is the diffracted optical wave vector. The magnitudes of these wave vectors are

$$k_i = \frac{2\pi n_i}{\lambda_0}, \quad k_d = \frac{2\pi n_d}{\lambda_0}, \quad K_a = \frac{2\pi f}{v}. \tag{2.44}$$

Here, n_i and n_d are the refractive indices of the incident and diffracted rays, λ_0 is the central optical wavelength, f is the acoustic frequency and v is the acoustic velocity. Along with diffraction, the wave experiences a 90° rotation in linear polarization state.

The central wavelength can be tuned over a wide wavelength range by modulating the frequency of the acoustic wave inducing the AO effect. The first demonstration of this tuning behaviour was shown with collinear acoustic and optical waves [Harris and Wallace, 1969], then later with non-collinear waves [Chang, 1974]. The advantage to the non-collinear orientation is a significant increase in the acceptance angle allowing diffraction, enhanced by the birefringence of the anisotropic material [Yano and Watanabe, 1976].

The anisotropic property should be carefully examined with regard to Equation (2.43). The magnitude of the wave vectors for the incident and diffracted beams are scaled by different refractive indices, depending on the polarization state before and after the AO interaction. A ray diagram is illustrated in Figure 2.10 showing the diffraction criterion. Note that the boundary surfaces of the optical waves are derived from the refractive index surfaces in Figure 2.8b. The Poynting vectors for the incident and diffracted rays must maintain collinearity. This means that the acoustic wave vector is selected such that incident and diffracted optical wave vector surfaces lie parallel to one another [Chang, 1974]. This is highlighted by the dashed lines in Figure 2.10. The parallel tangent condition is described as noncritical phase matching, which makes the interaction relatively insensitive to the angle of incidence [Chang, 1981]. It is important to understand that both the linear polarization

state and the propagation direction of the incident ray change upon interacting with the acoustic wave. This means that the diffracted signal is identifiable and may be optically isolated based on the change of properties.

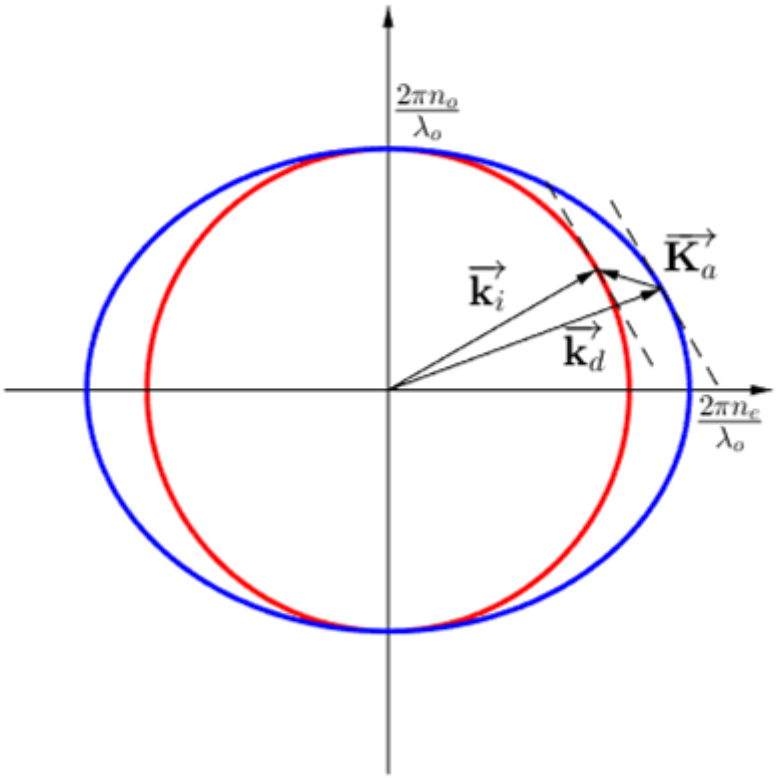

Figure 2.10: Momentum matching criterion on a wave vector diagram for a non-collinear AOTF.

The ray diagram displayed in Figure 2.10 is an example of the AO interaction for an ordinary polarized incident optical wave. Similarly, an extraordinary polarized optical wave may be incident, which would diffract into the ordinary polarization state. These two diffraction cases are referred to as the $\pm 1^{st}$ diffraction orders. Note that higher diffraction orders do not exist in AOTFs due to the sinusoidal nature of the acoustic wave (and therefore the sinusoidal refractive index modulation). For physical AOTFs, a 0^{th} diffraction order also exists, coming from the non-unit diffraction efficiency of the device. Additionally, in physical systems, the optical source is not strictly monochromatic, nor is it necessarily nearly monochromatic. In the case of a broadband source, only a narrow bandwidth near the central wavelength expe-

riences diffraction. The rays from beyond this bandwidth will transmit through, unaffected by the acoustic wave, and therefore exist as additional 0^{th} order signal. Figure 2.11 shows the nominal operation of an AOTF on an unpolarized broadband source.

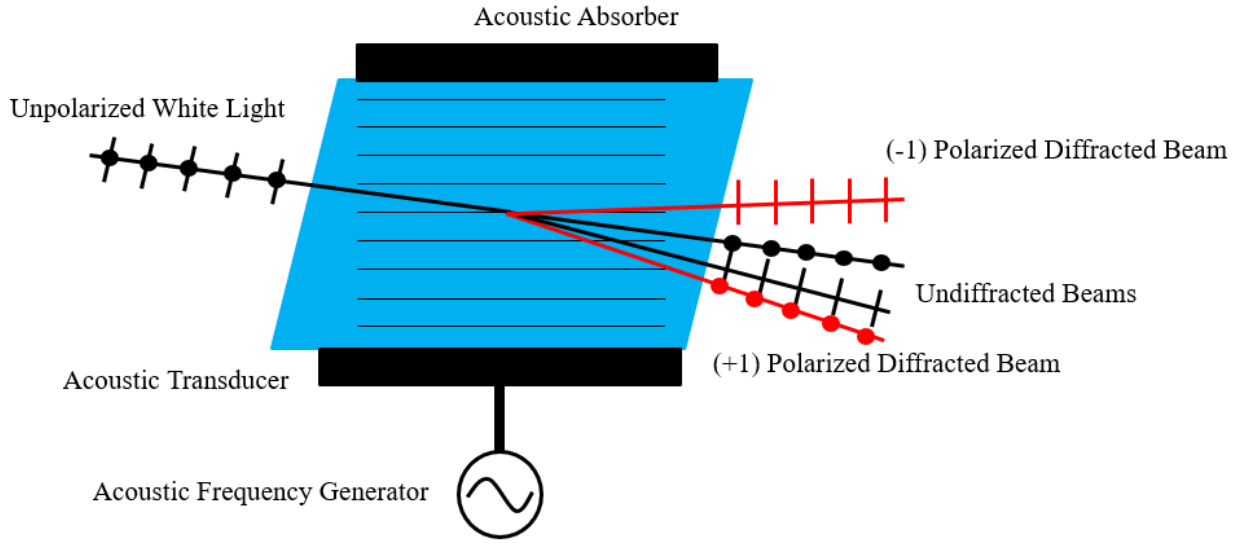

Figure 2.11: Application of an AOTF on unpolarized broadband signal. Four distinct beams exit the AOTF, identified by their polarization state and diffraction order.

The function of an AOTF on unpolarized broadband signal highlights the capability of this technology to perform spectral filtering. The narrow bandwidth experiencing the AO interaction is illustrated with red rays. The interaction occurs on both the ordinary and extraordinary polarization states of the incident signal, and the $\pm 1^{st}$ order diffracted beams diverge from one another. This leaves the 0^{th} order to propagate between these diffracted beams, but it too experiences a polarization-dependent separation based on the birefringence of the crystal.

A common method to utilize an AOTF for spectral filtering is to employ two linear polarizing filters. The first filter is placed ahead of the AOTF and is aligned such that it only transmits either the ordinary or extraordinary polarization state, as defined by the crystal orientation. This first polarizing filter eliminates one of the undiffracted beams and one of the 1^{st} order beams. The second polarizing filter is placed after the AOTF, and is cross aligned with the first. Due to the change in polarization state during the AO interaction, this second filter eliminates the second undiffracted beam, and only passes a single 1^{st} order state, thus providing narrow-band spectral filtering.

The specific properties of the narrow band filtering fall out from both the momentum matching condition for a specific crystal geometry, as well as the geometry of the transducer bonded to the crystal. Specifically, recalling the wave vector illustration in Figure 2.10, the relationship between the acoustic frequency, f_a, and the diffracted wavelength can be extracted under the assumption of small birefringence. This relationship can be approximated as

$$f_a = \left(\frac{v\Delta n}{\lambda_0}\right)\sqrt{\sin^4\theta_i + \sin^2 2\theta_i}. \tag{2.45}$$

Here, Δn is the birefringence and θ_i is the angle of the incident wave vector with respect to the optical axis [Chang, 1974]. The bandpass response is described by

$$T(\lambda_0) = T_o \mathrm{sinc}^2(\sigma L), \tag{2.46}$$

where T_o is the peak transmission, L is the interaction length and σ is the momentum mismatch parameter [Chang, 1975]. The peak transmission is a function of the AO figure of merit, M_2, and the acoustic power density, P_d, per

$$T_o = \sin^2\left(\frac{\pi}{2\lambda_0^2} M_2 P_d L^2\right)^{1/2}. \tag{2.47}$$

Finally, the full width at half maximum (FWHM) of the bandpass response can be estimated from Equation (2.46) when $\sigma L \approx 0.44$. The FWHM is

$$\Delta\lambda = \frac{0.9\lambda_0^2}{bL\sin^2\theta_o}, \tag{2.48}$$

where b is the dispersion constant [Chang, 1975]. The AOTF properties described in Equations (2.45) through (2.48) lead to trade-offs between diffraction efficiency, the bandwidth of the filtered signal, power requirements and acoustic frequency selection. It is worth noting that the sidelobes in the $sinc^2$ bandpass response may be suppressed using transducer amplitude apodization [Chang and Katzka, 1978].

2.5.3 Liquid Crystal Technology

Liquid crystals (LCs) are a classification of materials that exist in a state similar to both crystalline solids and liquid states. The classification is based primarily on the order that the molecules feature.

Classically, crystal solids are defined as either atomic solids (metals) or molecular solids (ice crystals). In the first case, the primary bonds holding the individual atomic components together are ionic or covalent. In the second case, the individual molecular components are bound by secondary bonds, which are not as strong as the ones holding the atoms together in the molecule, but still feature strong bond enthalpies. As a result, the structure of both of these crystal types is very well defined, with no degrees of freedom for either rotational or translational order. Crystals may therefore be classified based on the properties of order that they feature, such as unit cells and lattice translation vectors. Liquids on the other hand do not feature these same strong bonds between individual components and display multiple orders of freedom in both translation and rotation for the components.

Liquid crystals are composed of molecular components called mesogens with secondary bonds tying the mesogens together. They have fluidlike properties, however, the mesogens are arranged with structural order [De Gennes and Prost, 1993]. Liquid crystals are grouped into three types: thermotropic, lyotropic and polymeric. Mesogens of the first type establish their order based on the entropy of the system, ranging from the most ordered arrangements (smectic) to least ordered (nematic) as entropy increases. Once a high enough entropy is reached, the order of the mesogens breaks and the material takes on a strictly fluidlike behaviour. Thermotropic liquid crystals may also be influenced by external electromagnetic fields, which is described following.

Two types of mesogens exist, based on the structure of the molecule. These are rod-like "calamitic" mesogens, and disc-like "discotic" mesogens. The former are of current interest, specifically those which are anisotropic. These calamitic mesogens typically arrange themselves so that there exists some alignment along their long axis. The average direction of the long axis is described as a director. Three examples of mesogen arrangements are shown in Figure 2.12.

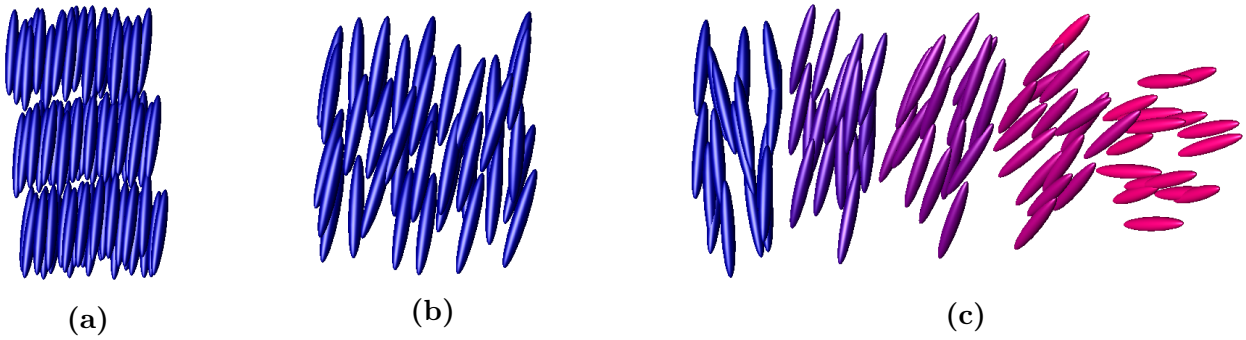

Figure 2.12: Three thermotropic mesogen arrangements. (a) Smectic. (b) Nematic. (c) Cholesteric or twisted-nematic. [Litster and Birgeneau, 1982]

The arrangement in Figure 2.12a is described as smectic. This classification contains as many as 9 subclassifications, but generally exhibit a layered translational order as well as strong rotational order exhibited by aligned directors in each layer. The nematic classification illustrated in Figure 2.12b shows a reduction in the translational order of the mesogens, with mesogens existing outside of defined layers, caused by an increase in entropy. The director however is common over the entire volume. Finally, Figure 2.12c shows the cholesteric, or twisted-nematic arrangement. Here, the mesogens once again feature a layered order, however, each layer defines a unique director, which is rotated a uniform amount with respect to the previous layer, with a pitch roughly on the order of microns [Litster and Birgeneau, 1982].

The scale of the rotating director and the anisotropic nature of twisted-nematic liquid crystals offer a desirable method for controlling or altering the polarization state of light. As described previously, the electric dipoles established within a birefringent material can influence an optical wave passing through, with distinct impacts attributed to the polarization state of the wave. In this case, the rotating director influences a rotation in the linear polarization state of light as it passes through, with a rotation angle nearly equal to the rotation of the director. This response is presented in Figure 2.13a, where liquid crystals are sandwiched between two transparent plates. Qualitatively, this optical response is very similar to that of a birefringent wave plate. However, the unique quality of these twisted-nematic liquid crystals is that the director responds to an electric field that may be applied across the cell if the two plates are transparent yet electrically conductive. This causes the directors in all layers to align such that both optical polarization states behave as ordinary

polarized waves passing through the material (the propagation direction is aligned with the optical axis of the mesogens), thus removing the optical activity displayed in the twisted state, shown in Figure 2.13b [Schadt and Helfrich, 1971].

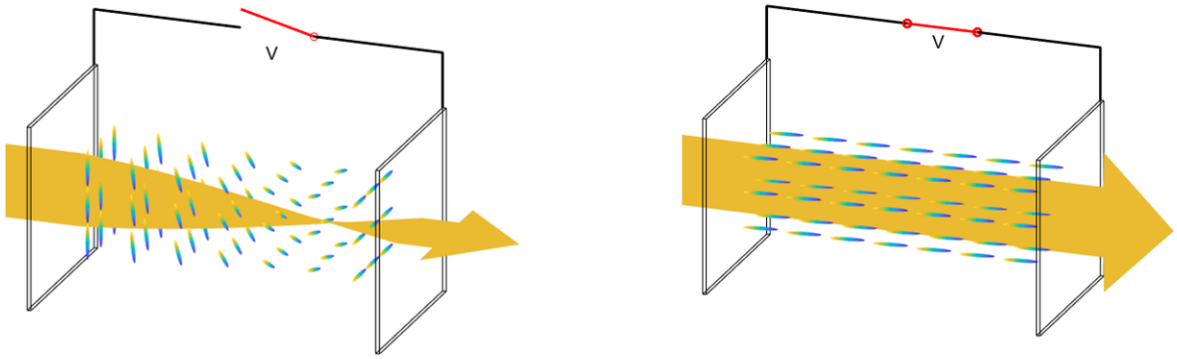

(a) **(b)**

Figure 2.13: Optical activity within a twisted-nematic liquid crystal cell. (a) In the relaxed state, the mesogen director undergoes a 90° twist over the length of the cell. The linear polarization state of an optical wave follows the rotation. (b) The mesogen directors align to an applied electric field between the plates housing the cell, removing the optical activity and allowing the optical wave to pass through unaffected.

The electro-optic element depicted in Figure 2.13 is called a Liquid Crystal polarization Rotator (LCR). As with the previously described birefringent materials used in AOTFs, the ordinary and extraordinary refractive indices of the mesogens have a wavelength dependence. This means that a specified LCR cell width can be optimized for a single monochromatic wavelength, and any additional wavelengths will experience a polarization rotation not exactly equal to 90° [Gooch and Tarry, 1974]. This results in a slightly elliptical polarization state.

2.5.4 ALI Version 1

The first generation of the ALI instrument (ALI V1) was designed and tested between 2011-2014 [Elash et al., 2016, Elash, 2016]. This instrument laid the groundwork for the developments that are discussed in this work.

ALI V1 was based on the concepts described in Sections 2.5.1 and 2.5.2. It was a multispectral imager operating over the 650-1000 nm spectral range. A transmissive optical chain

channeled scattered sunlight through an AOTF and imaged it on a charge-coupled device image sensor. The optical layout of ALI V1 is presented in Figure 2.14.

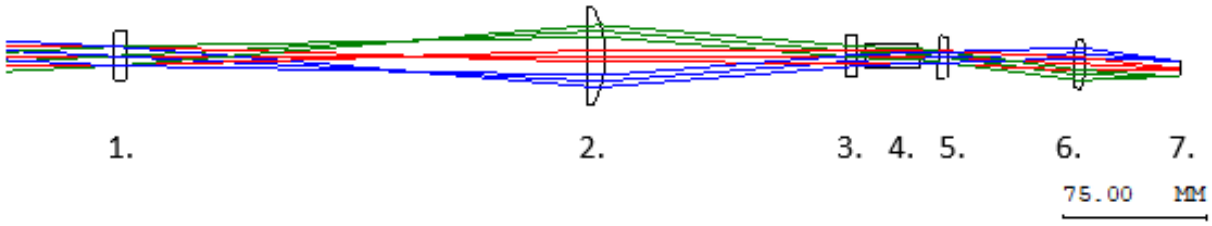

Figure 2.14: Optical layout of ALI V1. Elements 1 and 2 comprise an afocal telescope. Elements 3 and 5 are linear polarizing filters around the AOTF, Element 4. Element 6 is a singlet to focus wave fronts onto the image sensor, Element 7.

The operational performance of ALI V1 was tested on board a stabilized, high-altitude balloon platform from Timmins, Ontario in the fall of 2014. This flight represented the first demonstration of atmospheric limb scattered images captured with AOTF spectral filtering. This important proof-of-concept experiment validates the ability of this technology to capture level 0 data products for the retrieval of stratospheric aerosol properties in the upper troposphere and lower stratosphere of the atmosphere.

The following chapters describe the work completed to advance the TRL of the ALI concept. These efforts specifically focus on hardware development to improve the optical performance of ALI, tailored to several measurement platforms that progress towards the operating conditions for a satellite mission. A review of the methods used for the design and preparation for flight is presented in the following chapter.

Chapter 3

Methods

3.1 High-Level Instrument Requirements

The discussion of stratospheric aerosol remote sensors has highlighted the need for new instrumentation with long-term, global monitoring capabilities achieving high spatial and temporal resolution. The proof-of-concept demonstration of ALI V1 has positioned the instrument to fulfill this need.

The conceptual requirements for ALI are:

- Narrow band spectral filtering across the visible to near infrared spectrum.
- Polarization detection in two orthogonal linear states.
- 2 dimensional image capture with fine vertical resolution.
- Utilization of the limb viewing geometry for sub-orbital demonstration with orbital analogs.

This chapter discusses the adaptation of this concept to a realized instrument, highlighting the optical design activities and the key trade-off studies that have guided the next generations of ALI. These activities are key for both the second balloon-borne version of ALI (ALI V2) and an elegant breadboard version set to fly on a high altitude aircraft (ALI EBB). A discussion of characterization techniques is presented, motivated specifically by the preparation for the sub-orbital demonstration of ALI V2 on a high-altitude balloon platform.

3.2 Optical Design

3.2.1 Technology Trades

The conceptual instrument requirements are first addressed by selecting the appropriate technologies to best meet their needs. Each of the first three requirements leads to a unique technology selection, although the requirements themselves are not mutually exclusive. Two primary technology trade studies are summarized to justify the technologies selected for instrument realization.

Spectral Filtering

Spectral filtering may be achieved through classical optical techniques such as diffraction gratings or optical filters. The former has been demonstrated for atmospheric remote sensing in instruments like OSIRIS [Llewellyn et al., 2004] and the SAGE instruments [World Meteorological Organization, 1986, Mauldin et al., 1985]. Although this technique achieves fine spectral resolution, it does not lend itself to 2D imaging. This is because the spectral separation is achieved through an angular broadening of the optical signal, thereby washing out the spatial resolution in at least one axis.

The alternate classical approach for spectral filtering using optical filters is effectively the obverse of a diffraction grating approach. These filters are capable of operating over reasonable fields of view to maintain 2D imaging capabilities, as demonstrated on the Hubble Space Telescope [Turner-Valle et al., 2004] and for the Near Infrared Imager and Slitless Spectrograph on the James Webb Space Telescope [Doyon et al., 2012]. However, the selection of discrete filtering wavebands makes this technology rigid in terms of spectral filtering mobility. Furthermore, the use of optical filters necessarily requires a mechanism capable of moving each filter into the optical path of the instrument, impacting temporal resolution.

Acousto-optic technology, described in Section 2.5.2 strikes a balance between these two techniques. The tunable nature of AOTF devices is complimentary to continuous spectral dispersion of a grating (albeit with coarser spectral resolution) while preserving the angular registration required for 2D imaging. AOTFs are an emerging technology for several space-based

applications, including planetary and natural satellite spectroscopy [Korablev et al., 2018] and Earth observation [Dekemper et al., 2012]. Therefore, an AOTF is selected for further technology development for ALI.

Polarimetry Mechanism

The polarization effects of an AOTF must be considered when selecting a technology to capture orthogonal polarization states. Once again, classical optical techniques may be used to perform the polarization selection, however, they come at a cost for sub-orbital/orbital remote sensors.

Figure 2.11 highlighted that unpolarized signal entering into an AOTF will be diffracted into two 1^{st} orders. Theoretically, this provides the capabilities that are sought for cloud discrimination. However, the relatively high dispersion of AO materials coupled with the momentum matching criterion means that the direction of these two 1^{st} order beams will wander as the wavelength is tuned. This is an undesirable characteristic because it will significantly change the field of view captured for each tuned wavelength (both for the ALI application and several other AOTF uses). To compensate for this wander, a wedge is often cut into the exit face of the AOTF to balance the inherent dispersion and momentum matching condition. This balance can only be struck for one of the two 1^{st} order beams however and exaggerates the wander for the second. This explains the use of linear polarizing filters (LPF) that are typically placed in front of and behind an AOTF, as they act to reduce stray light passing through the optical system.

With the assumption of a LPF preceding the AOTF, a classical solution to alter the linear polarization state into the filter would be to use a set of half-wave plates. These plates rely on birefringent materials which retard the phase of the polarization state aligned to a specific crystal axis. Choosing an appropriate thickness (half of a specific wavelength), the linear polarization state of transmitted light can be rotated 90°. This rotation is specific to a single wavelength, and additional wavelengths adopt an elliptical profile unless multiple waveplates are used. To utilize this technology, a rotation mechanism is required to either rotate the wave plate about its normal axis (rotation by 45°) or to rotate the wave plate(s) into and out of the optical path. Although viable options exist for both, these impact the temporal

resolution of the instrument in much the same way optical filters would have impacted the spectral filtering design trade.

A preferable alternative to a wave plate solution is to utilize a liquid crystal polarization rotator described in Section 2.5.3. Although these too suffer from a wavelength-dependent ellipticity in the outgoing polarization state, their solid-state operation is preferable for sub-orbital platforms. They require reduced volume, mass and power when compared to a rotation mechanism, while also featuring significantly faster switching speeds. A LCR is a new addition to ALI V2 and ALI EBB as it was not used in the previous ALI V1 design.

3.2.2 AOTF Modelling

The previous chapter highlighted the theory and principles that govern the operation of an AOTF. These principles can be applied to generate a mathematical model to assess the operation of an AOTF [Zhao et al., 2014, Poon, 2006]. For this work, a model is developed based on the one presented by [Zhao et al., 2014] to aid in the design of ALI. The model uses the geometry of the AOTF crystal to assess how optical rays of various wavelengths will travel through the AOTF as it is tuned to near by central wavelengths. The geometry used for the model is described in Figure 3.1.

The formulism set out in [Zhao et al., 2014] is closely followed in this model, but deviates in the approach to handling phase-mismatching condition. An analytic solution to the phase-matching condition is determined, then a numerical method is used to assess the mismatching cases for several fields and wavelengths.

The model decomposes the function of an AOTF into three processes, described by three surfaces. This method is translatable to several ray-tracing software packages like CODE V or Zemax, as each primarily uses surface-to-surface propagation for design and analysis. The model calculates direction cosines for rays between each surface, described as (L_i, M_i, N_i), where i is the index of the previous surface. The incident ray is indexed 0. The model requires two coordinate frames, the global XYZ frame and the crystal X'Y'Z' frame.

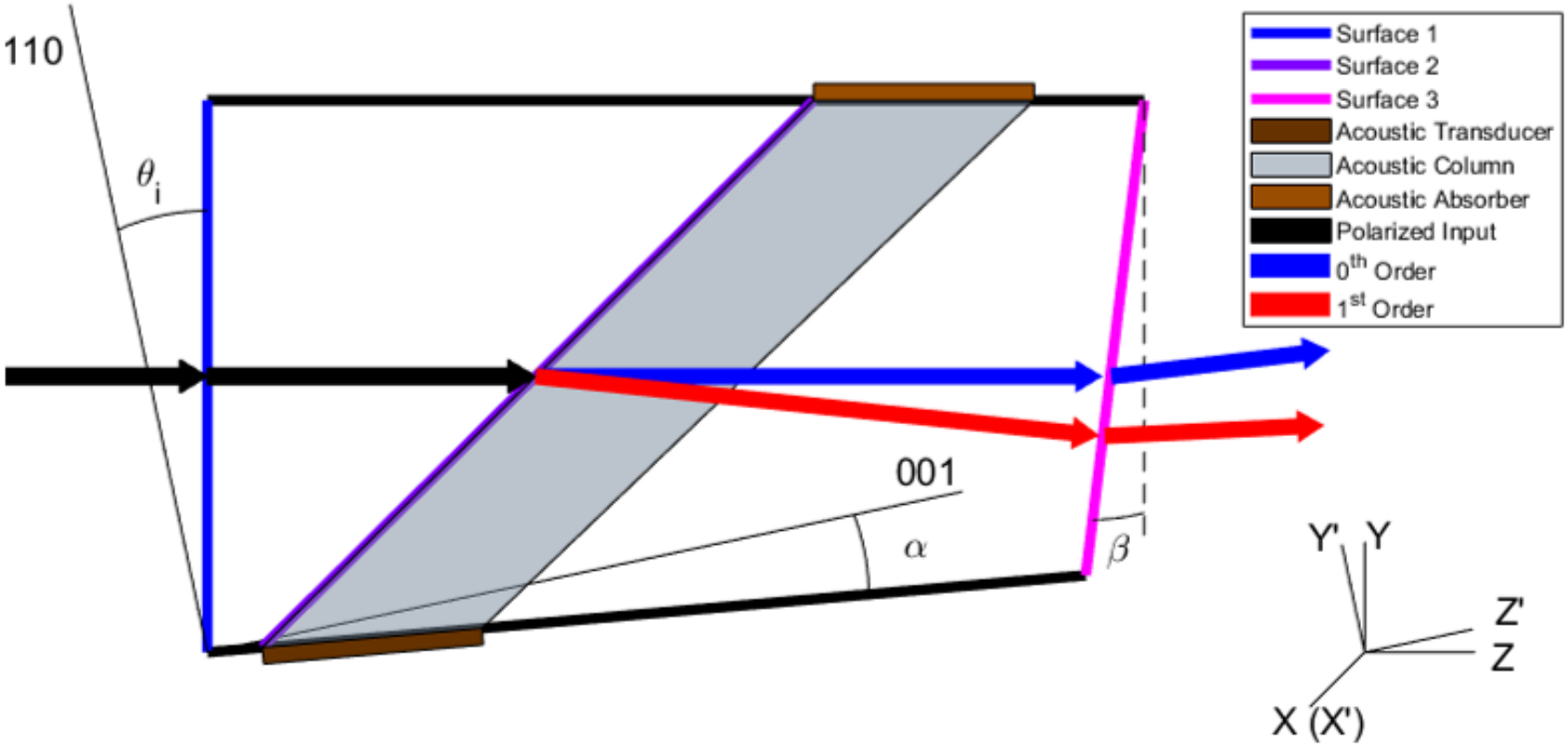

Figure 3.1: AOTF model geometry adapted with permission from [Zhao et al., 2014] © The Optical Society. Three optical surfaces define how an optical signal enters the AOTF, diffracts at the acoustic column (or passes through if momentum matching is not met), and then refracts out of the AOTF at a wedged interface.

The first surface is the interface between the surrounding medium (nominally air) and the AOTF crystal. This refractive plane scales the direction cosines of the ray by the refractive index of the crystal. This model is optimized for ordinary polarized incident rays. The ray properties following the crystal boundary are described by

$$\begin{aligned} L_1 &= \frac{L_0}{n_o}, \\ M_1 &= \frac{M_0}{n_o}, \\ N_1 &= (1 - L_1^2 - M_1^2)^{0.5}. \end{aligned} \tag{3.1}$$

The second surface is where the AO interaction is modelled and coincides with the edge of the acoustic column. At this surface, two conditions may occur. The first condition is the simple propagation of rays from outside the passband of the selected tuning frequency. The second condition models diffraction of rays within the passband. In the former case, there is no change to the direction cosines.

The diffraction condition modelled at Surface 2 solves Equation (2.43). The incident ray from Surface 1 must be rotated into the X'Y'Z' coordinate frame displayed in Figure 3.2. The coordinates of the intersection of the incident ray and the index surface, point **C**, are described by

$$\begin{aligned} x_c &= \frac{2\pi n_o}{\lambda} L_1, \\ y_c &= \frac{2\pi n_o}{\lambda} (M_1 \cos\theta_i - N_1 \sin\theta_i), \\ z_c &= \frac{2\pi n_o}{\lambda} (M_1 \sin\theta_i + N_1 \cos\theta_i). \end{aligned} \tag{3.2}$$

The acoustic vector direction cosine is found directly from the angle α between the acoustic transducer and the crystal axes. Point **D**, the intersection of the diffracted ray and the ellipsoid index surface, is found using the acoustic vector and the ellipsoid equation, thus satisfying the Bragg diffraction criterion. Although this solves for the diffracted optical wave vector, the direction of the group velocity must be determined for ray tracing. Recall that the group velocity will be normal to the ellipsoid surface, giving

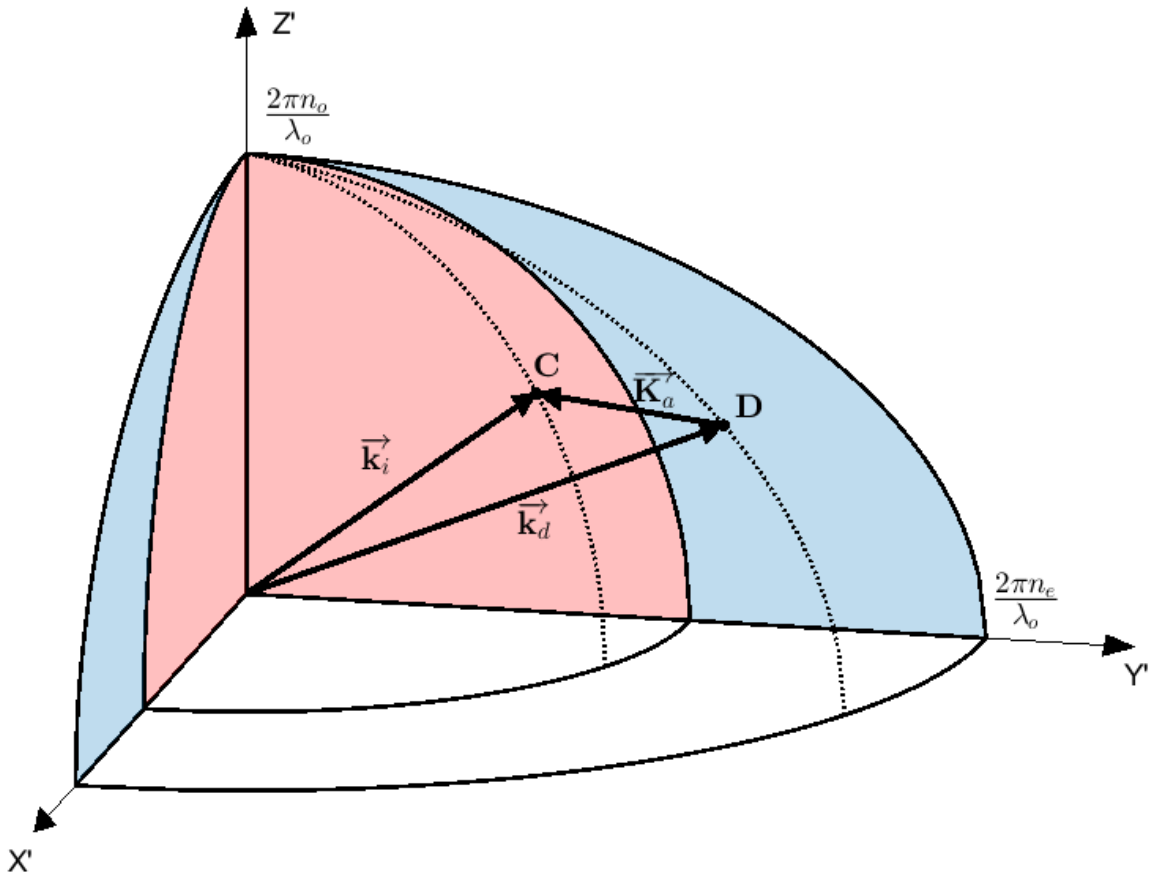

Figure 3.2: Ray tracing phase matching condition for the second surface. Adapted with permission from [Zhao et al., 2014] © The Optical Society.

$$
\begin{aligned}
L_t &= \left(\frac{n_o^4 x_D^2}{n_o^4 x_D^2 + n_o^4 y_D^2 + n_e^4 z_D^2} \right)^{0.5}, \\
M_t &= \left(\frac{n_o^4 y_D^2}{n_o^4 x_D^2 + n_o^4 y_D^2 + n_e^4 z_D^2} \right)^{0.5}, \\
N_t &= \left(\frac{n_e^4 z_D^2}{n_o^4 x_D^2 + n_o^4 y_D^2 + n_e^4 z_D^2} \right)^{0.5}.
\end{aligned} \tag{3.3}
$$

The direction cosines of the group velocity are transformed back to the global XYZ coordinate system to find the Surface 2 solution

$$
\begin{aligned}
L_2 &= L_t, \\
M_2 &= M_t \cos\theta_i + N_t \sin\theta_i, \\
N_2 &= -M_t \sin\theta_i + N_t \cos\theta_i.
\end{aligned} \tag{3.4}
$$

The third surface is another refractive interface between the AOTF crystal and the surrounding medium. Once again, two conditions may occur depending on the previous surface. If the ray propagated undiffracted, then an additional ordinary refraction event occurs, similar to Surface 1. However, under the AO diffraction condition, the polarization state of the diffracted ray has rotated 90°, leading to refraction of the extraordinary polarization state at Surface 3. Here, the phase velocity in the X'Y'Z' frame is required:

$$
\begin{aligned}
L_u &= L_2 n_e^2 P_L, \\
M_u &= (M_2 \cos\theta_i - N_2 \sin\theta_i) n_e^2 P_L, \\
N_u &= (M_2 \sin\theta_i + N_2 \cos\theta_i) n_o^2 P_L,
\end{aligned} \tag{3.5}
$$

where

$$
P_L = [L_2^2 n_e^4 + (M_2 \cos\theta_i - N_2 \sin\theta_i)^2 n_e^4 + (M_2 \sin\theta_i + N_2 \cos\theta_i)^2 n_o^4]^{-0.5}. \tag{3.6}
$$

The direction cosine of the phase velocity is used to calculate the refractive index for the specific ray direction

$$
n_e' = \left(\frac{L_u^2}{n_e^2} + \frac{M_u^2}{n_e^2} + \frac{N_u^2}{n_o^2} \right)^{-0.5}. \tag{3.7}
$$

Finally, the exiting diffracted ray is calculated by transforming back to the global coordinate frame and using Snell's law at the boundary:

$$
\begin{aligned}
L_3 &= L_u n'_e, \\
M_3 &= [M_u \cos(\theta_i + \beta) + N_u \sin(\theta_i + \beta)] n'_e \cos\beta \\
&\quad - \{1 - L_u^2 - [M_u \cos(\theta_i + \beta) + N_u \sin(\theta_i + \beta)]^2 n_e'^{\,2}\}^{0.5} \sin\beta, \\
N_3 &= [M_u \cos(\theta_i + \beta) + N_u \sin(\theta_i + \beta)] n'_e \sin\beta \\
&\quad - \{1 - L_u^2 - [M_u \cos(\theta_i + \beta) + N_u \sin(\theta_i + \beta)]^2 n_e'^{\,2}\}^{0.5} \cos\beta.
\end{aligned} \tag{3.8}
$$

The direction cosines (L_0, M_0, N_0), (L_1, M_1, N_1), (L_2, M_2, N_2), and (L_3, M_3, N_3) describe the propagation direction of the phase matched ray diffracted by an AOTF. This equation set is used both in MATLAB for numerical computing and CODE V for optical design and analysis.

As noted, the method for handling the momentum mismatching condition used in this work differs from the one described in [Zhao et al., 2014]. Here, a numerical approach is taken specifically to understand the trade-offs involved in AOTF implementation. Therefore, the momentum mismatching condition is only utilized while performing analysis with MATLAB and does not require implementation in CODE V, which would necessitate the described analytical approach.

The solution to the momentum matched condition has described the acoustic wave vector that results in AO diffraction at the desired central wavelength. To solve the mismatch condition for several directions, the extraordinary wave vector surface for nearby wavelengths is translated along the acoustic vector. This translation causes an intersection between the two wave surfaces, as highlighted in Figure 3.3. To find the intersection, cross sections parallel to the Y'/Z' plane are assessed and a binary search is used to locate the two intersection points.

The set of intersection points is first used to describe the incident ray directions that meet the momentum mismatching condition for the specific wavelength by drawing rays to the intersecting curve on the ordinary wave vector surface.

The set of all intersection points is then translated along the reverse of the acoustic wave vector and the surface tangent for each point is calculated to describe the propagation direction of the diffracted rays. The incident rays are then defined to have the same group

velocity, described as noncritical phase matching, which offsets the momentum mismatch. This describes pairs of incident and diffracted rays (and wave vectors) for a wavelength near the centrally tuned wavelength.

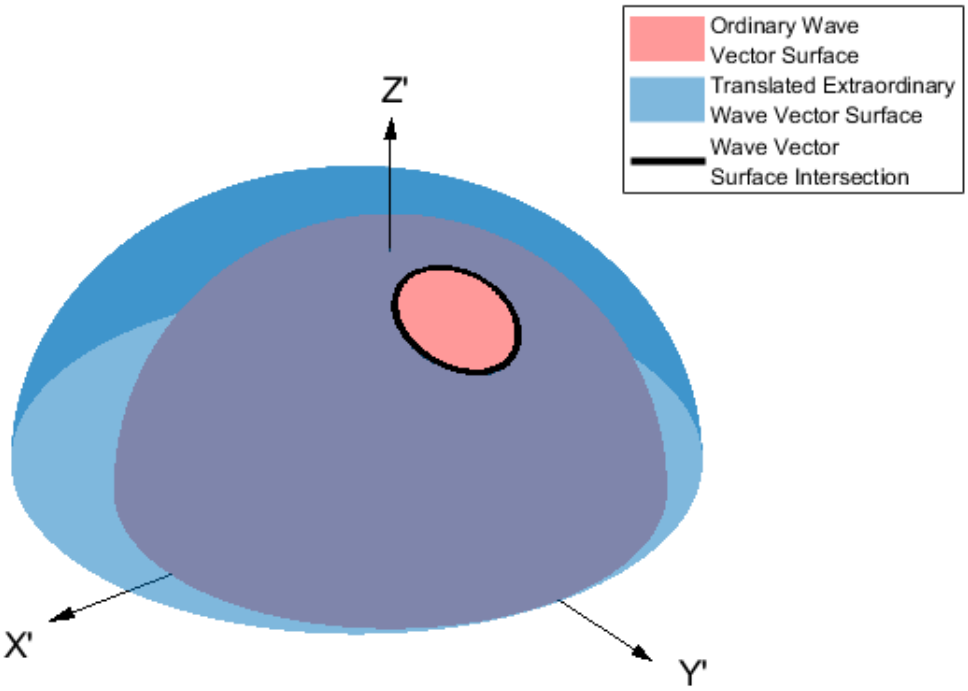

Figure 3.3: Overlapping wave vector surfaces for tracing acousto-optic diffraction under momentum mismatching condition. The intersection of ordinary wave vector surface and extraordinary wave vector surface translated by momentum matching acoustic wave vector is determined using numerical methods.

3.2.3 Design Trades

The key technologies identified in the above trades have sustained persistent technology development to improve their respective TRLs in both ALI V2 and ALI EBB. These technologies come with flexibility in their implementation, which requires additional design trade-off studies to determine the most applicable implementation for ALI. The most notable of these design trades is the use of the AOTF in either collimated or imaging space within ALI.

AOTF Optical Layout

The wide angular aperture achieved with non-collinear AOTFs allows for two primary methods of use in an optical system. The AOTF can either perform its interaction on bundles of collimated signal, filling an angular aperture or on focused bundles of signal, with an F-number paired to the AOTF acceptance angle. The two cases are shown in Figure 3.4

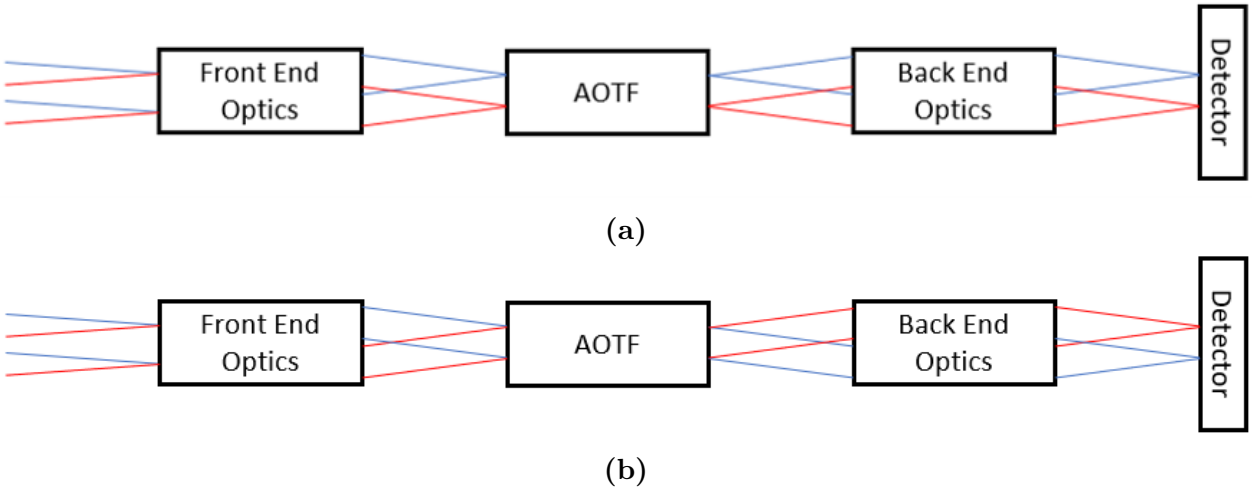

Figure 3.4: Two standard methods of using an AOTF in an optical system. Ray bundle fields are differentiated by colour. (a) Confocal or telecentric layout, with focused rays reaching the AOTF. Two optical fields, identified by colour, are focused to a small region on the face of the AOTF. Note that the focal plane is commonly within the AOTF in this layout. (b) Afocal telescopic layout, with collimated rays reaching the AOTF. Two fields enter the AOTF in two distinct directions, filling the aperture of the AOTF.

The telecentric (Figure 3.4a) and telescopic (Figure 3.4b) layout each come with unique drawbacks, which generates an important trade study to be considered. The primary disadvantages, as well as associated causes, are highlighted in Table 3.1.

The dispersion of the AOTF crystal material affects the spatial resolution of the device when used in the telecentric layout. This is described as longitudinal chromatic aberration. The refractive index of the material changes with wavelength, which changes the position of the focal plane within the AOTF, shown in Figure 3.5a. As this position changes, so too does the focus position on the image sensor following the AOTF.

The flow-down impacts of this chromatic aberration are assessed using a simple optical model with ideal lenses in front of and behind the AOTF crystal. The lens in front produces

Table 3.1: Summary of optical layout trade off implications

Cause	**Telecentric**	**Telescopic**
Dispersion in AOTF	Reduced spatial resolution	N/A
Noncritical phase matching	Reduced spectral resolution	Spectral gradient Non-uniform image illumination
Momentum matching condition	N/A	Image shift Wavelength dependent magnification
Acousto-optic blur	N/A	Reduced spatial resolution

a chromatic focal plane within the AOTF, with the 1000 nm focus located at the center of the crystal body. The second lens refocuses the 1000 nm internal focal plane onto an imaging screen. Rays of several wavelengths within the ALI spectral range are traced through this optical system, in two cases. For the first case, the image plane is moved to minimize the spot size, and this focus shift is plotted in Figure 3.5b. This plot shows that the image plane requires nearly 400 μm of range to properly focus the entire spectral range. The use of a focusing mechanism is not feasible for all systems, however. In the second case, the image plane is optimized for 1000 nm, and the resulting spot sizes of several spectral samples are plotted, shown in Figure 3.5c. There is a significant amount of defocus as the sampled wavelength moves away from 1000 nm. This defocus may be slightly reduced by optimal selection of refractive focusing optics, however, the wide wavelength range of ALI makes this challenging and likely impossible to eliminate.

Noncritical phase matching also leads to limitations of the telecentric layout. Equation (2.48) describes the bandwidth as a function of several factors, including incident angle, θ_i. The telecentric layout has a range of incident angles filling the optical aperture, thus deteriorating the spectral resolution.

The AOTF model is used to calculate the incident angles for wavelengths within the expected bandwidth at several wavelength channels across the spectral range. Three sample wavelength channels are shown in Figure 3.6a. These diffraction wavelength maps describe the relationship between the incidence angle (described horizontally and vertically along the X and Y axes) and the diffracted wavelength (described by the colour bar). A strong

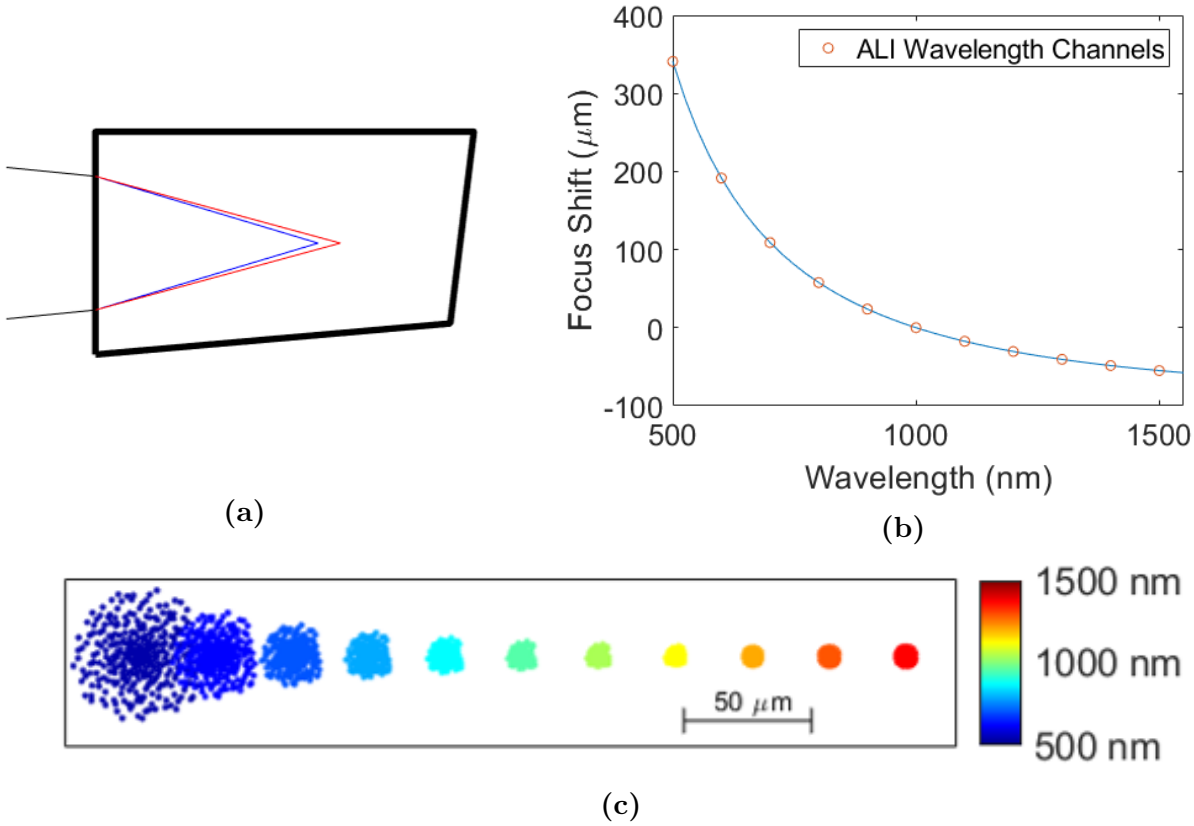

Figure 3.5: Lateral chromatic aberration caused by telecentric AOTF layout. (a) The chromatic focal plane shift caused by AOTF crystal dispersion. (b) Simulation of image plane shift for best focus. (c) Spot size at common image focal plane.

wavelength gradient is evident in the horizontal direction, with a weaker vertical structure. The bounds of these plots are set to 5° x 5° to represent the approximate full acceptance angle of a typical AOTF, which will describe the cone of fields entering the AOTF in a telecentric layout.

The maximum and minimum wavelengths that are diffracted within the cone are used to describe the "cone bandwidth". This bandwidth sets the bounds on a boxcar function in the spectral domain to convolve with measured spectral point spread functions from an AOTF. The FWHM of the convolution describes the spectral resolution of the AOTF in the telecentric layout. This telecentric bandwidth is compared against the measured bandwidth in a telescopic layout in Figure 3.6b. The spectral resolution of the telecentric layout is 3.5 to 7.0 nm wider than the telescopic layout across all channels.

The wavelength distribution over incident angle caused by noncritical phase matching

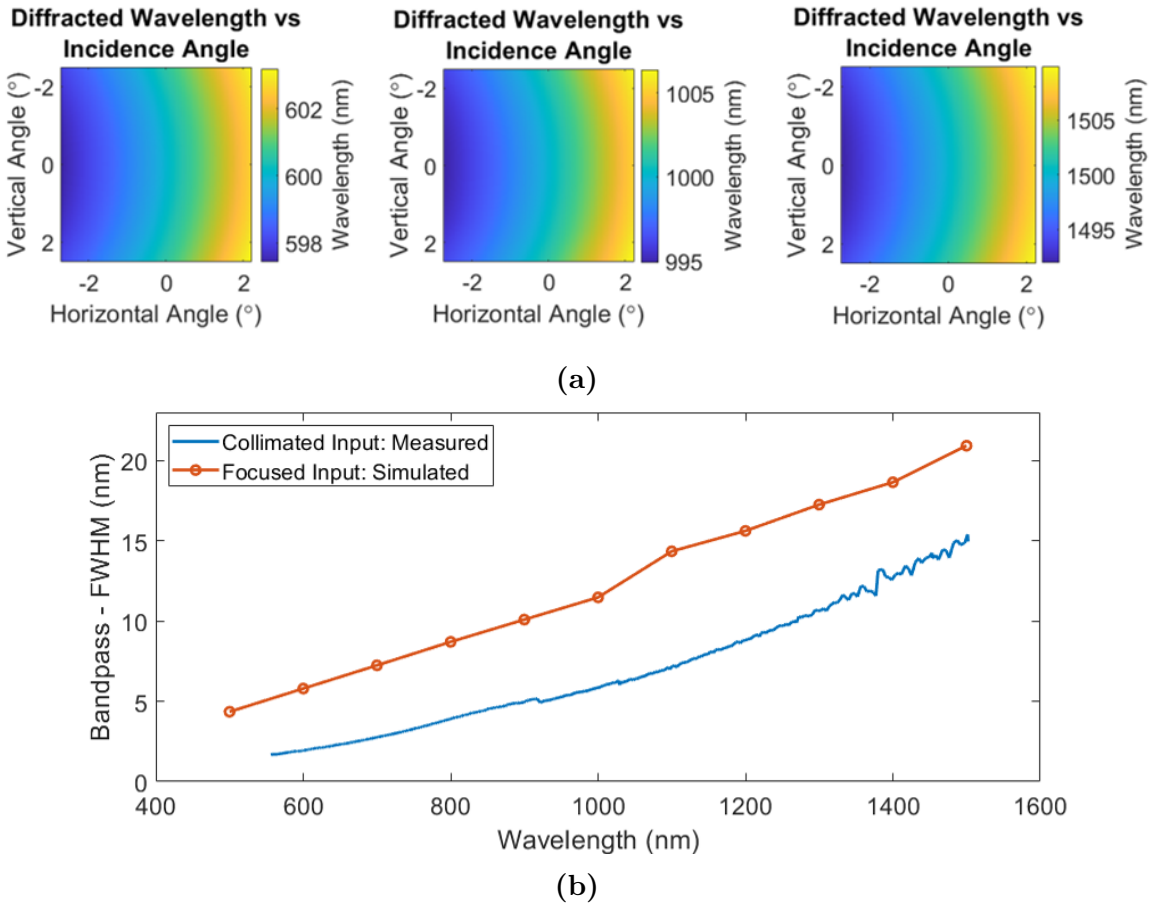

Figure 3.6: Reduced spectral resolution caused by telecentric AOTF layout. (a) Diffracted wavelength described as a function of incidence angle onto AOTF. Three central wavelength tunings are displayed across ALI spectral range. (b) Comparison of telescopic (collimated input) and telecentric (focused input) spectral resolutions over ALI wavelength range.

plays a significant role in the performance of an AOTF in the telescopic layout as well. Each field filling the AOTF will have a unique central wavelength diffracted due to changes in the incident optical wave vector directions and the common acoustic wave vector. Therefore, once the fields are imaged following the AOTF, a spectral gradient like the ones in Figure 3.6a will occur on the image sensor. Although this figure shows the diffracted wavelength as a function of incident angle, the distribution as a function of diffracted angle is similar. The difference however occurs as a result of distortion picked up through the AO interaction. The distortion for the 1000 nm wavelength channel is displayed in Figure 3.7a. Here, the difference in incident and diffracted angle with respect to the central wavelength is displayed

showing the magnitude and direction of the distortion, all as a function of incident direction and wavelength. Beyond the spectral gradient and distortion, a transmission gradient is also expected, caused by the finite bandwidth of the AOTF, described in Equation (2.46). Figure 3.7b shows that the gradient primarily affects the highest and lowest vertical incident angles in the horizontal direction that diffracts the longest wavelengths in the passband.

An additional consequence of the telescopic layout is an image shift and wavelength-dependent magnification coming from the momentum matching condition described in Equation (2.43). With a fixed acoustic angle and AO materials with strong dispersion, the diffraction angle of the on-axis ray (and all others) will necessarily change as the tuning frequency is adjusted.

In the previous case study, an assessment of the performance of individual wavelength channels in isolation was conducted to investigate optical aberrations over the field of view. Now, an inter-channel assessment will look at how differently each channel behaves with respect to one another in the telescopic layout.

The AOTF model is used to find the incident and diffracted pairs similar to the previous exercise. In this case, however, a uniform set of incident angles is tested for each wavelength (as opposed to the previous case where uniform wavelength sampling was selected over the bandpass with varying incident angles). With this simulation set, a wavelength channel comparison can be made for the diffraction angle over incidence angle, displayed in Figure 3.8a. The diffracted rays generally display a leftward shift in the chosen reference frame. The primary influence of the shift is the AO interaction, with only a small spectral variation. However, greater chromatic variance occurs from dispersion in the AOTF material. The wedge cut into the crystal is specifically designed to reduce the chromatic factor, but full spectral compensation is unachievable. Figure 3.8b quantifies the spectral image shift with respect to the 500 nm channel. Note that this channel experiences an average 2.83° angular change between the incident and diffracted rays over the field of view.

The same incident and diffracted pairs are used to assess the magnification of the diffracted rays. Here, the magnitude of the diffracted angle (less the full field of view average) is compared against the magnitude of the incident angle. Figure 3.8c shows the field response for the 500 nm channel. The largest change in magnification occurs along the vertical axis, where

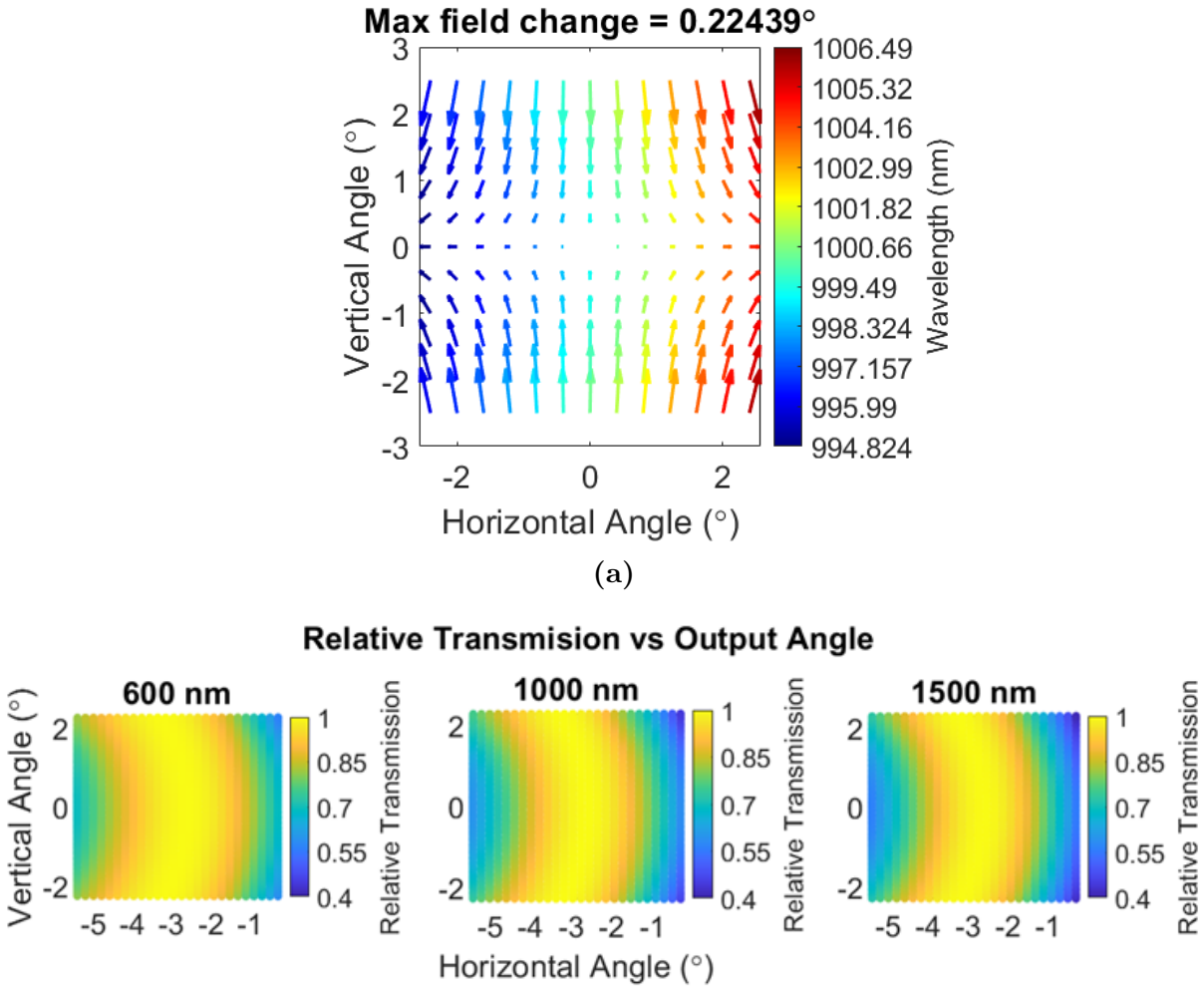

Figure 3.7: Optical effects caused by noncritical phase matching in telescopic layout. (a) Distortion caused by acousto-optic interaction. The central wavelength experiences the nominal change in angle between the incident and diffracted beam, shown as a null field change. All other fields experience a differing amount of change between incidence and diffracted beams, resulting in the displayed distortion. (b) Transmission gradients occur for three sampled wavelength channels. The gradient falls out of the wavelength dependence of the AOTF transmission function.

the diffracted angle magnitudes are smaller than the incident magnitudes. This leads to a reduction in image size along this axis. Along the horizontal axis, however, the diffracted angles are positively magnified, but by a smaller margin. The field of view averaged magnification across the spectral range is summarized in Figure 3.8d, where only a small spectral response is displayed.

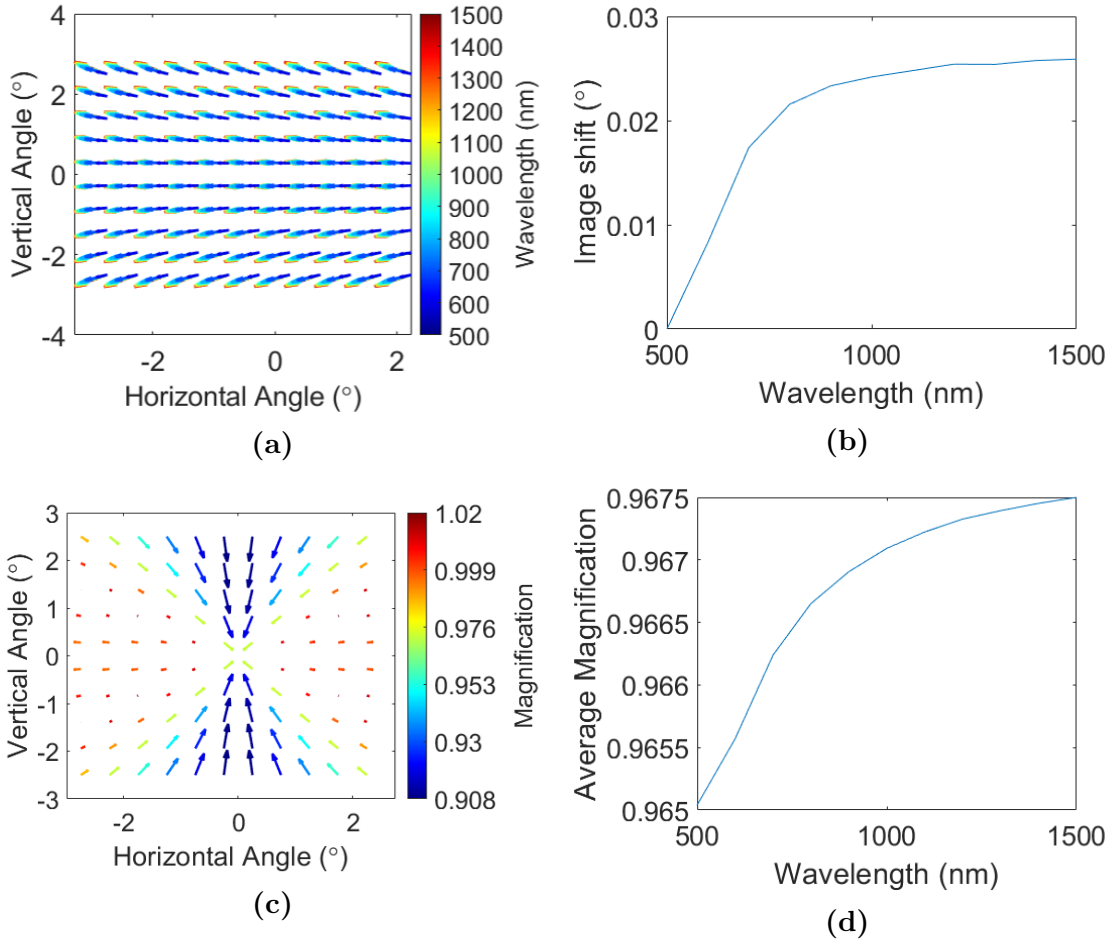

Figure 3.8: Optical effects caused by the momentum matching condition in the telescopic layout. (a) Diffracted field shift as a function of incident angle and wavelength. (b) Average image shift over wavelength with respect to the 500 nm channel image shift. (c) Field-dependent magnification of the 500 nm channel. (d) Field averaged magnification over wavelength.

The final important implication to address in the telescopic layout is the spatial broadening that occurs due to diffraction of the acoustic beam, known as acousto-optic blur. As the acoustic column travels through the AO material, it diverges due to diffraction. This acoustic diffraction is the same phenomenon that leads to the finite bandpass of the diffracted

wavelength channel [Suhre et al., 1992]. The diffraction angle broadening and bandwidth is expressed as

$$\frac{\Delta\theta_d}{\Delta\lambda} = \left(\frac{\Delta n}{n_o \lambda_o}\right)(\sin^4\theta_i + \sin^2 2\theta_i)^{0.5}. \tag{3.9}$$

The angular broadening occurs in the direction of the acoustic interaction [Zhao et al., 2017]. This angular broadening is of course tied closely to the ultimate spatial broadening that occurs upon imaging the diffracted signal. The measured bandpass displayed in Figure 3.6b is once again utilized to estimate the broadening caused by acousto-optic blur. Here, the incidence angle is $\theta_i = 29.65°$. Figure 3.9 shows that the broadening is roughly 3× larger than the Rayleigh angular resolution limit for a 10 mm diameter optic.

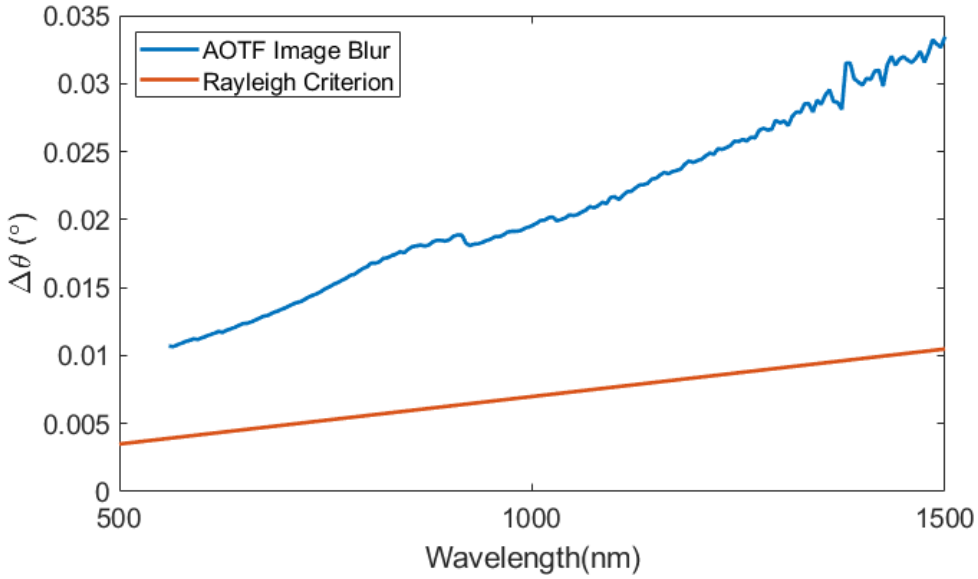

Figure 3.9: Angular broadening caused by acousto-optic image blur compared against Rayleigh criterion.

The several aberrations imparted by the two AOTF optical layouts are difficult to compare directly because there is only minor alignment of aberrations between the two design options. However, a qualitative assessment can help to delineate which aberrations will be most impactful on the image quality.

The reduced spectral resolution in the telecentric layout and the spectral gradient in the telescopic layout, both caused by noncritical phase matching, are both tolerable and can be characterized during instrument commissioning. The broad nature of aerosol scattering

implies that high spectral resolution is not a critical design driver of ALI. Similarly, the non-uniform image illumination is also manageable with appropriate flat field characterization. Similarly, the spectral image shift and magnification changes in the telescopic layout can be addressed with full-field image characterization. This leaves only the reduction in spatial resolution caused by AOTF dispersion in the telecentric case and the reduction caused by acousto-optic blur in the telescopic case. The upper hand here is given to the telescopic case because the acousto-optic blur is only unidirectional. With the appropriate orientation of the AOTF, this can be set to affect only the horizontal spatial resolution, therefore leaving the vertical resolution unaffected. This is a desirable alternative for ALI, where fine vertical resolution is required and horizontal pixel binning is anticipated. Therefore, the telescopic layout is selected for the ALI design.

3.2.4 Optical Specification

The optical design of ALI was optimized using the ray-tracing package CODE V. This software package is an industry-standard for the design and optimization of optical systems, with advanced features for beam propagation through non-sequential systems, tolerance analysis and image simulation. This tool also allows the user to define non-linear and/or user-defined behaviours to optical surfaces, providing a necessary interface to implement the AOTF model described in Section 3.2.2.

The optical design is divided into three primary subsystems: an input telescope to collect signal from the atmospheric limb and redistribute it to be accepted by the AOTF, the AOTF and polarization filtering elements, and finally an imaging system to capture the filtered signal on a sensor.

The telescopic layout chosen in the design trade requires a mapping of the instrument field of view to the acceptance angle of the AOTF. The specification for the AOTF for ALI V2 describes a $\pm 2^\circ$ acceptance angle. However, the geometry shown in Figure 2.2 requires a 6° FOV to measure from a balloon altitude of 40 km to the surface of the Earth. To achieve this mapping while preserving the etendue, an afocal telescope with $0.66\times$ angular magnification was required. Two layouts were designed, featuring either refractive or reflective optics, shown in Figure 3.10a and Figure 3.10b respectively. The qualities of these two types of

systems were weighed to determine the most appropriate choice. While the ease of alignment of the refractive elements would have been beneficial, the wide spectral range could not be easily accommodated by glass elements. The reflective solution requires tighter alignment tolerances to maintain image quality, however, the performance of reflective optics is invariant of wavelength (if we omit diffraction effects, which affect both designs). Furthermore, the reflective design offers an intermediate focus, which allows for a field stop to be installed. The reflective design was selected.

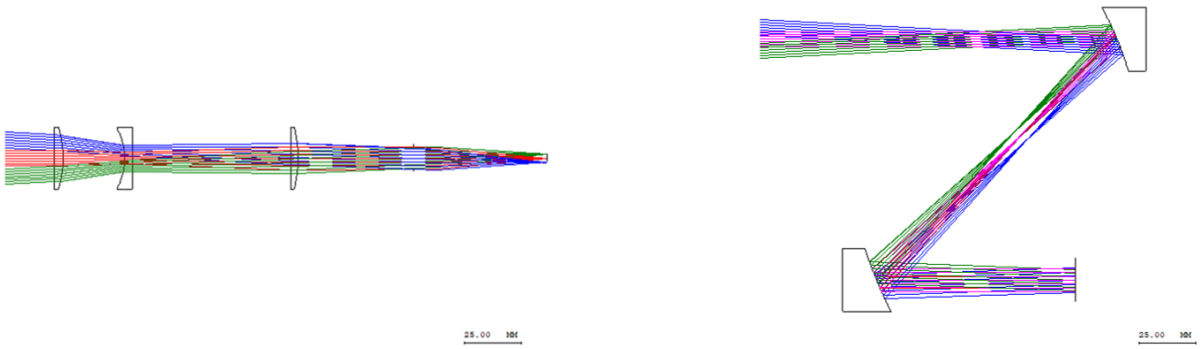

(a) **(b)**

Figure 3.10: Input telescope design option using (a) refractive optical elements or (b) reflective optical elements.

The telescope is a reflective analog to a Keplerian refractor, featuring two positive focal length elements with a separation equal to the sum of both focal lengths. The mirrors selected are off-axis parabolic mirrors with focal lengths of 50.8 mm and 76.2 mm, offering 1.5× spatial magnification (and 0.66× angular magnification). The 10 mm aperture of the AOTF was placed at the exit pupil of the telescope, allowing an instrument aperture to be defined at the start of the optical chain, facilitating the use of a baffle for out-of-field stray light suppression.

The subsystem responsible for polarization and spectral filtering is composed of the AOTF and LCR described previously, as well as a set of LPFs. The LCR came first in the chain, with its optical axis aligned at 45° with respect to the horizon. This rotated the horizontally polarized limb signal into the vertical orientation following the LCR. Following this element, the first LPF was oriented to pass vertically polarized signal, thus eliminating one of two states from propagating further along the optical path. The crystal axis of the following

AOTF was designed to diffract this vertically polarized signal. Finally, an LPF followed the AOTF to block the 0^{th} order signal that passes the AOTF.

The final subsystem is responsible for imaging the fields exiting the AOTF onto the image sensor. The sensor selected for ALI V2 was a Raptor Owl 640 Vis-InGaAs sensor, with 640 $\times$ 512 pixels and 15 μm pitch. The effective focal length to map the 4° FOV to 9.6 mm image sensor is 137 mm. Unlike the telescope subsystem, where a simple ratio of two reflective optics was required, the imaging subsystem does not have the same flexibility to use only reflective optics, specifically if choosing those that are commercial off-the-shelf (COTS) parts. Therefore, a refractive design was iterated, starting from a well-defined Cooke triplet, but deviating to allow for one plano surface on each element, thereby reducing aberration correction. A solution is optimized to utilize three COTS lenses.

The complete optical ray trace is displayed in Figure 3.11. The complete CODE V source code to generate this ray trace is found in Appendix A.

3.3 Opto-Mechanical Design

The use of COTS optical elements was a beneficial choice because there are several standard COTS mounting options for these pieces. Based on the alignment requirements, appropriate mounting solutions were found for the input telescope and back-end imaging system. The bill of materials for the ALI V2 build is provided in Appendix B.

The common optical plane for the major subassemblies provided flexibility in selecting an optical bench to base the opto-mechanical design around. Standard optical breadboards from Thorlabs, with 25 mm mounting grids were selected for their versatility and size availability. Three breadboards were selected: the first was used to mount the input telescope and spectral and polarizing filter elements, the second for the imaging system and detector, and a large breadboard to mount the first two.

The tight alignment requirements for the input telescope stems from the need to match the focus points of the two mirrors to within 100 μm. ULTIMA kinematic mounts with 3 degrees of freedom were selected to position these two mirrors, covering the tip, tilt and piston degrees. X and Y centering was achieved by adjusting the position of the second mirror

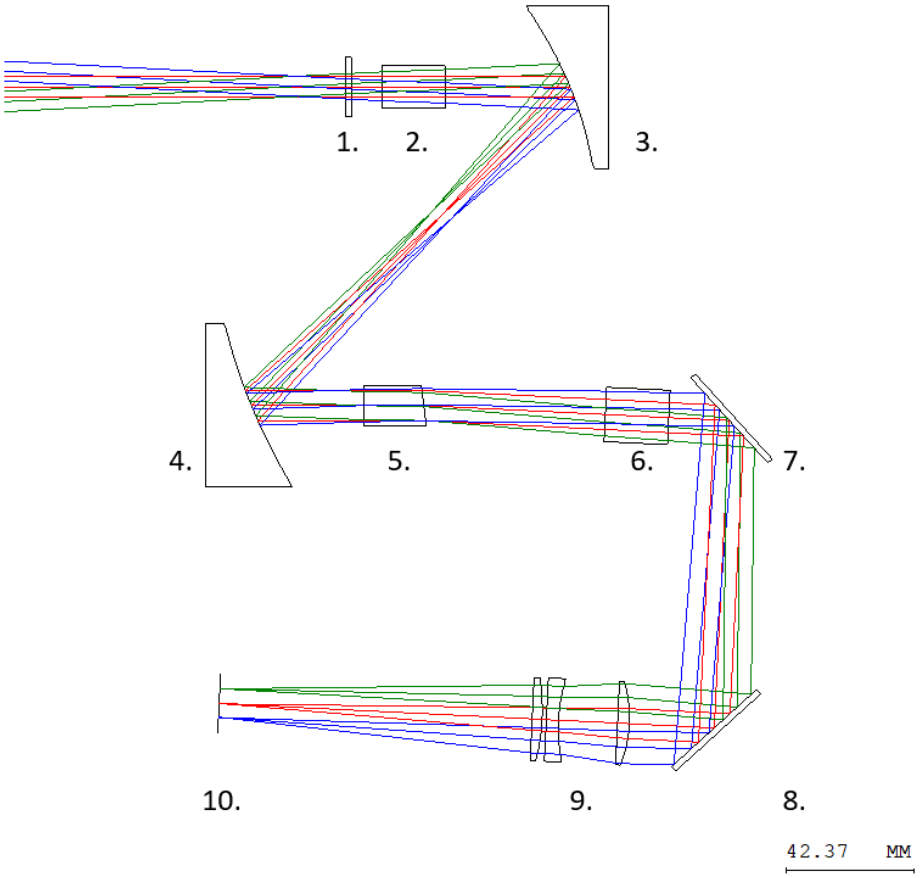

Figure 3.11: Optical layout of ALI V2. Elements 3 and 4 are the afocal telescope for FOV mapping. Elements 1, 2, 5 and 6 are the LCR, LPF, AOTF and LPF respectively, providing polarization and spectral filtering. Elements 7 and 8 are fold mirrors to reduce the footprint, leading to the imaging optics described by 9. Finally, the image sensor ends the optical chain at Element 10.

with respect to the first on the breadboard using a pedestal clamp. Finally, the clocking of the mirrors was achieved by rotating the mirror mount in the kinematic mounts. The mirrors were aligned using the two parallel laser input method [Lee, 1992].

The AOTF was installed following the input telescope on the same optical breadboard. The position of the AOTF defines the exit pupil of the telescope, which in turn defines a location for the input aperture. A stray light baffle was designed to instigate at least three reflections for out of field rays before passing the aperture. Each allowed reflection is off a diffuse black baffle vane, reducing the optical power by roughly 90% per reflection.

The LCR and input LPF were the last elements that were assembled on the first optical breadboard. These elements were housed in optical tubes from Thorlabs, with retaining

rings to secure the final aligned position. Rotational alignment was chosen to align with the AOTF crystal geometry. A diffracted signal was monitored through the AOTF as the LPF was positioned. The LCR was then oriented 45° with respect to the LPF to facilitate the 90° polarization plane rotation in its unpowered state.

The back-end imaging system following the AOTF was constructed on a second breadboard to accommodate the diffraction angle through the AOTF. The lenses for this system were once again mounted in optical tubes from Thorlabs. These tubes were threaded through their inner bore, so retaining rings could be rotated to adjust the spacing between the lenses to aid in focus alignment. Precision spacers were used between the second two lenses, and the first was positioned to achieve the best focus. The detector was mounted to the end of the optical tube. Two mounted plano mirrors were also included to fold the optical chain to reduce the overall length. Finally, the second LPF was installed and aligned to pass the diffracted signal from the AOTF. The two smaller optical breadboards were mounted on the largest and secured to achieve the best alignment between the front end and back end optics.

A light-tight enclosure was built around the optical bench to achieve signal isolation and thermal insulation. The enclosure consisted of two nested boxes, with an insulating medium filling the space between the boxes. These boxes were made of folded aluminum sheets, with thermal and electrical isolation standoffs used to separate the boxes. A thermal strap was attached to the detector to aid in thermal regulation, and several temperature sensors were secured to elements within the opto-mechanical design. Figure 3.12a shows the opto-mechanical design and Figure 3.12b displays the final enclosure of the instrument.

3.4 Laboratory Methods

Several standard optical laboratory methods and practices were used during the build and test phases of ALI V2. Furthermore, several standard optical ground support equipment (OGSE) pieces were used for these processes, including a vibration isolated optics table, a Horiba iHR320 imaging spectrometer with InGaAs and Silicon detectors, an integrating sphere, a broadband collimator, a shear plate interferometer, laser sources, spectral emission lamps, broadband lamps, optical targets, and miscellaneous optical hardware for prototyping

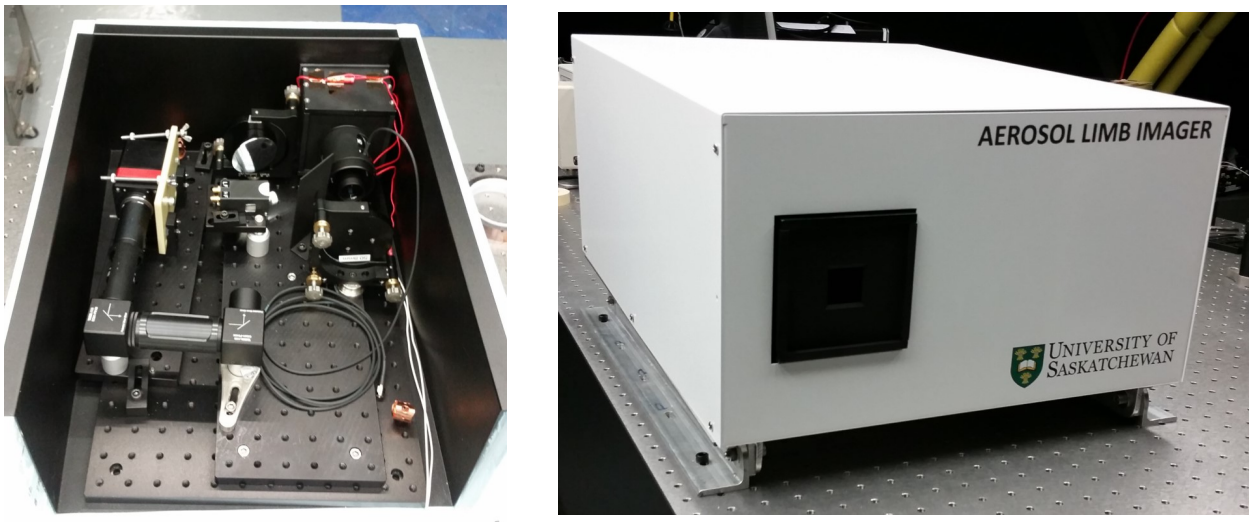

(a) (b)

Figure 3.12: ALI V2 opto-mechanical solution. (a) Interior opto-mechanical solution showing optics assembled on three optical breadboards, with COTS mounts for mirrors, lenses and other optical components. (b) ALI V2 optical enclosure.

and assembly.

A selection of methods used in the laboratory is described in further detail. These methods are unique to the technologies used in ALI and warrant further investigation beyond an understanding of standard practices.

3.4.1 Spectral Characterization

Much of the AOTF characterization was performed using a Horiba iHR320 imaging spectrometer. This metrology instrument has an adjustable slit at the focus of a parabolic collimating mirror, a programmable rotating diffraction grating, and an imaging mirror. The diffracted spectrum is imaged onto an imaging array in either one or two dimensions.

Central Wavelength Characterization

The spectrum diffracted through the AOTF in the telescopic layout was imaged onto the spectrometer slit and captured to locate the central wavelength as a function of tuning frequency.

Sidelobe suppression of the AOTF transducer, coupled with the non-ideal performance of

the acoustic source, and minor off-axis alignment of a diverging source resulted in AOTF diffracted spectra that did not display nominal sinc^2 behaviour as predicted by Equation (2.46). Typically, a blue shift occured with larger side lopes appearing on the shorter wavelength side of the central lobe. Therefore, a novel goodness-of-fit approach was adopted to identify the central diffracted wavelength of the AOTF, rather than a sinc^2 fit.

To locate the central wavelength, the relative symmetry of the central lobe was utilized. The peak wavelength sampled by the spectrometer was first identified from a measured spectrum. The spectral resolution of the spectrometer was much finer than the spectral bandpass of the AOTF, so there was little concern about identifying a peak far away from the true central lobe peak when accounting for measurement noise. An example spectrum, measured at 92 MHz is displayed in Figure 3.13a. Here, the full measured spectral sample is shown, with the central lobe highlighted and the peak sampled wavelength identified.

A window was defined around the peak sampled wavelength with 10 sampled wavelengths on either side. The size of this window changed depending on the width of the central lobe, however, a total of 21 samples was used in the 92 MHz case.

Each wavelength in this window was assessed as the "prospective central wavelength" (PCW). The central lobe was folded back onto itself about this PCW to compare the symmetry between the two sides, as shown in Figure 3.13b. A least-squares fit was applied to each set of points to establish common sampling along each side of the PCW. The cumulative difference between these two fits was archived as the goodness-of-fit parameter. The PCW nearest to the true central wavelength had the smallest goodness-of-fit parameter.

Finally, the goodness-of-fit parameters were plotted as a function of PCW in Figure 3.13c. Here, a local minimum was identified. Another least square fit was applied to each side of the minimum to find the intersection of these fits. This intersection point describes the central diffracted wavelength, λ_0.

This method was applied across all tested acoustic frequencies to determine the central wavelengths used in the frequency-wavelength tuning relation described later in Section 4.3.2

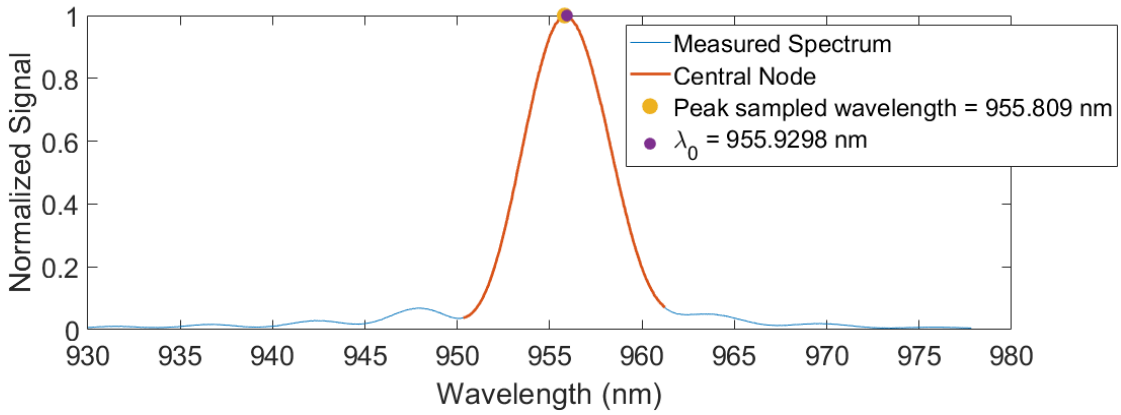

(a)

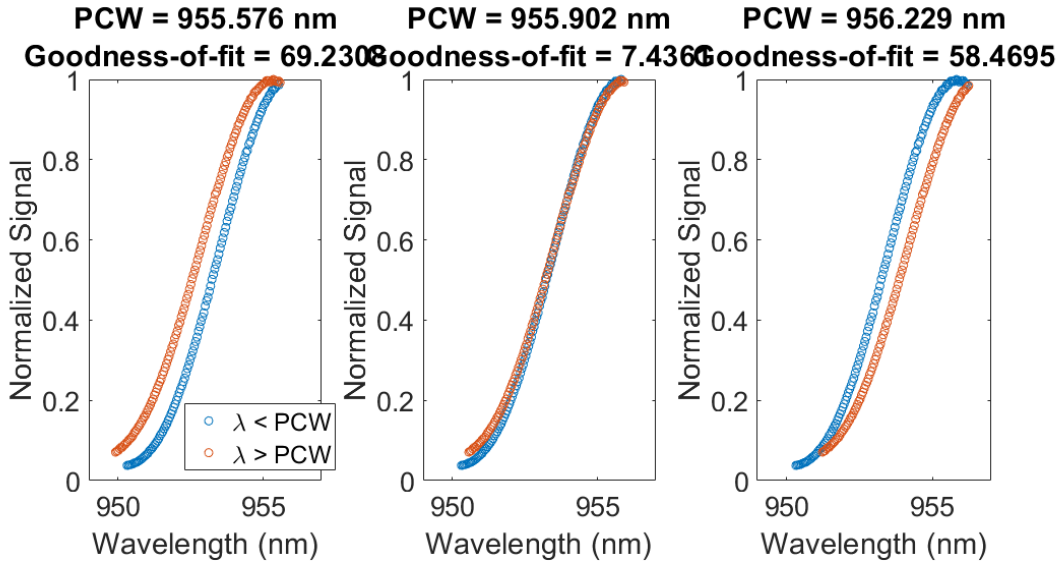

(b)

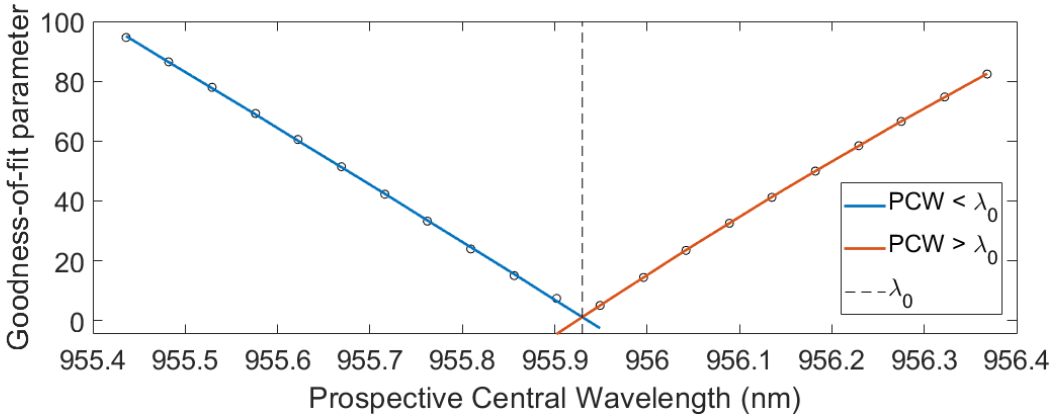

(c)

Figure 3.13: Method for finding central diffracted wavelength from a discrete wavelength sampled spectrum. (a) Sample spectrum measured with AOTF tuning frequency f = 92 MHz. (b) Test of symmetry of central lobe. (c) Assessment of goodness-of-fit parameters to estimate central wavelength.

3.4.2 Image Detector Characterization

Several characterization tests were performed to understand the performance of the detector used in ALI. These tests started with an investigation of valid detector pixels, followed by a dark current characterization and a flat field test over select wavelength channels.

Dark Current

Dark current is an intrinsic property of photosensitive devices. It is a small measure of current in each pixel, resulting from reverse saturation current and leakage current, which registers as detector counts as the image is read off of the detector. Dark current is influenced strongly by temperature because it is the result of the thermal excitation of electrons to high energy states. Longer exposure times allow more charge to build up as a result of dark current, leading to larger dark counts on the detector, even in the absence of any photons.

The dark current response of ALI was measured at various exposure times to find time-dependent masks to remove dark current from measurements. An internal thermoelectric cooler (TEC) in the ALI detector maintains a constant operating temperature for the focal plane array, which negates the need to also perform temperature-dependent calibration.

Valid Pixels

A study of valid pixels was needed to identify detector pixels that were either running hot (accumulating current too quickly and saturating prematurely) or those that were inactive or dead. Hot pixels typically showed the maximum detector count, in this case, 2^{14}, and dead pixels often to showed counts near the dark current threshold. This test was performed by placing the detector in front of a uniform source and capturing various exposure times. These images were analyzed to identify which pixels fit into the categories of hot or dead. A histogram of the pixel counts from one example image is shown in Figure 3.14. This image capture had an exposure time of 100 ms and a source radiance set to fill pixels to approximately half of the well depth. The histogram shows that 99.98% of the pixels were valid, with most of the remainder being dead pixels, and only a small portion being hot. The dead and hot pixels were excluded from all image analyses.

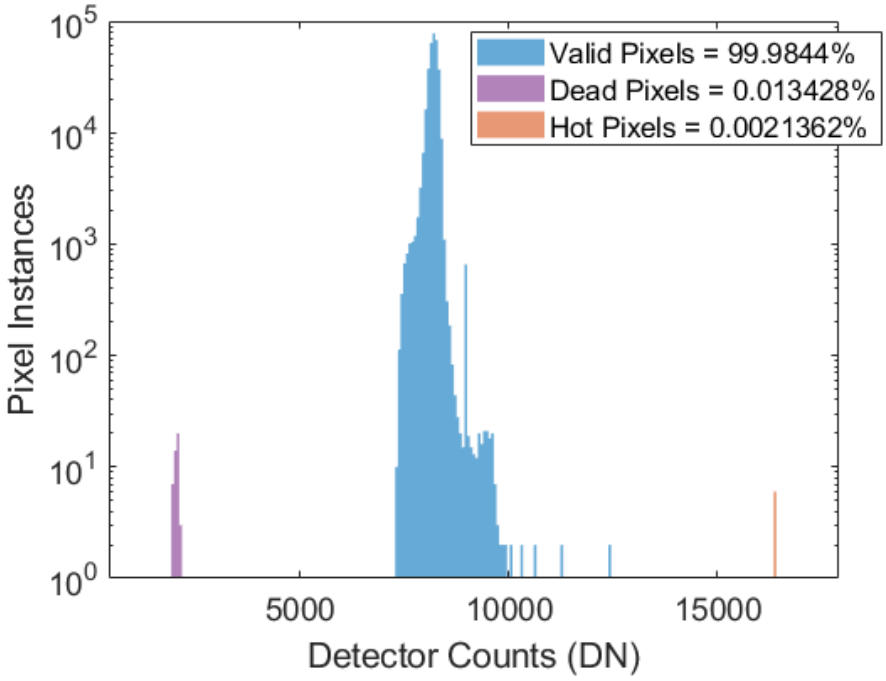

Figure 3.14: Histogram of pixel counts for a 100 ms exposure time in front of a uniform illumination source, with an average of half-well illumination.

Flat Field

The final image detector characterization performed was a flat field measurement across the spectral range. The flat field calibration was used to correct for pixel non-uniformity across the image plane. Each pixel displayed a slightly different response to uniform field illumination (highlighted by the broad valid pixel distribution in Figure 3.14). Furthermore, instrument artifacts may have also influenced illumination across the image plane. A prime example for ALI was the angular response of the AOTF, which shows degrading diffraction efficiency as the angle of incidence into the instrument increases, highlighted in Figure 3.7b.

The measurements for the flat field calibration were captured by placing ALI in front of an integrating sphere. An integrating sphere is a piece of OGSE specially designed to provide uniform illumination over all fields of view. The interior of the sphere was coated with a nearly Lambertian, white coating, which influences several diffuse scattering events. An internal source is baffled with similarly coated vanes, preventing direct illumination of the exit aperture. When used as an optical source, an integrating sphere achieves uniform illumination regardless of incidence angle, which is critical for flat field calibration.

Figure 3.15a shows an example of a flat field calibration measurement captured at 1100 nm. Under ideal imaging conditions, the entire image would show uniform illumination (with the exception of hot and dead pixels identified earlier). However, we see an illumination gradient caused primarily by the AOTF. Several measurements were made with uniform, calibrated radiance and varying exposure times to find linear equations to describe the rate of count accumulation on the detector. These rates were used to generate flat field calibration masks that may be applied to each measurement. Note that the position of the AOTF was optimized to provide the highest flat field sensitivity to the upper portion of the vertical FOV, representing higher tangent altitudes. This is the region where the signal levels are lowest, so the improved performance was useful for maximizing the signal-to-noise ratio at these altitudes.

An important instrument artifact was identified through the flat field calibration. The gradient in Figure 3.15a is also influenced by clipping at the most extreme fields. The lens diameter of the first imaging lens was selected to accommodate $\pm 3^\circ$ in either the X or Y dimension only. The error however is that the FOV is square, so the diameter should have been large enough to accommodate $\phi = \sqrt{3^{\circ 2} + 3^{\circ 2}} = 4.243^\circ$. Therefore, clipping occured, reducing signal levels in each corner of the image. This is displayed in the optical footprint plot shown in Figure 3.15b, where the shapes of the ray bundles from several fields are imposed on the clear aperture of the lens. This error was identified after the design and instrument build was completed, and could not be easily remedied. Fortuitously, this optical element is located in collimated space, so only decreased throughput was experienced, as opposed to absolute throughput loss.

3.5 Pre-flight Simulation

The SASKTRAN simulation environment was used for stratospheric balloon mission planning. A detailed instrument model was built in MATLAB to simulate the performance of ALI using spectral scenes generated using SASKTRAN. Further details on this process are described in Section 4.3.3. However, before this simulation was possible, appropriate wavelength channels had to be selected.

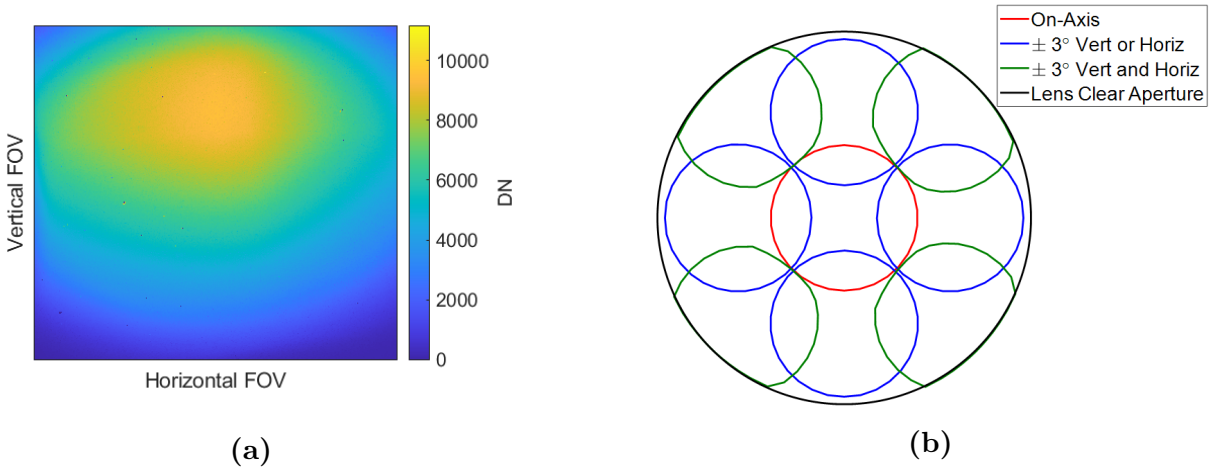

(a) **(b)**

Figure 3.15: Flat field calibration. (a) Uniform field illumination measurement at 1100 nm. (b) Optical footprint plot on imaging lens 1 showing signs of clipping for extreme fields.

3.5.1 Selection of Balloon Flight Wavelength Channels

SASKTRAN allows access to many atmospheric species climatologies to simulate the effect of unique absorption cross sections in the atmosphere. Several key species are identified that are expected to have significant spectral impacts over the spectral range of ALI. HITRAN was used to extract O_2, CO_2, CH_4, and H_2O cross sections, the Labow climatology was used for O_3 and the Burrows climatology finds the NO_2 cross sections [Gordon et al., 2017, Labow et al., 2015, Burrows et al., 1998]. These cross sections are normalized and plotted in Figure 3.16. Spectral regions with high-density cross section features were avoided when selecting the wavelength channels to measure during the ALI flight. We found specifically that NO_2 and O_3 dominate the low end of the ALI spectral region, and CH_4 and H_2O obscure regions around 1150 nm and 1400 nm. Most other regions were relatively free of strong features, so 25 spectral channels were selected, within a nominal 25 nm interval. The measured spectra for these sampled spectral channels are also highlighted in Figure 3.16.

Many additional characterization and calibration tests were performed on ALI before the flight, all further detailed in Section 4.3.2. The next chapter presents a published manuscript that provides greater detail into the ALI V2 design, characterization and flight.

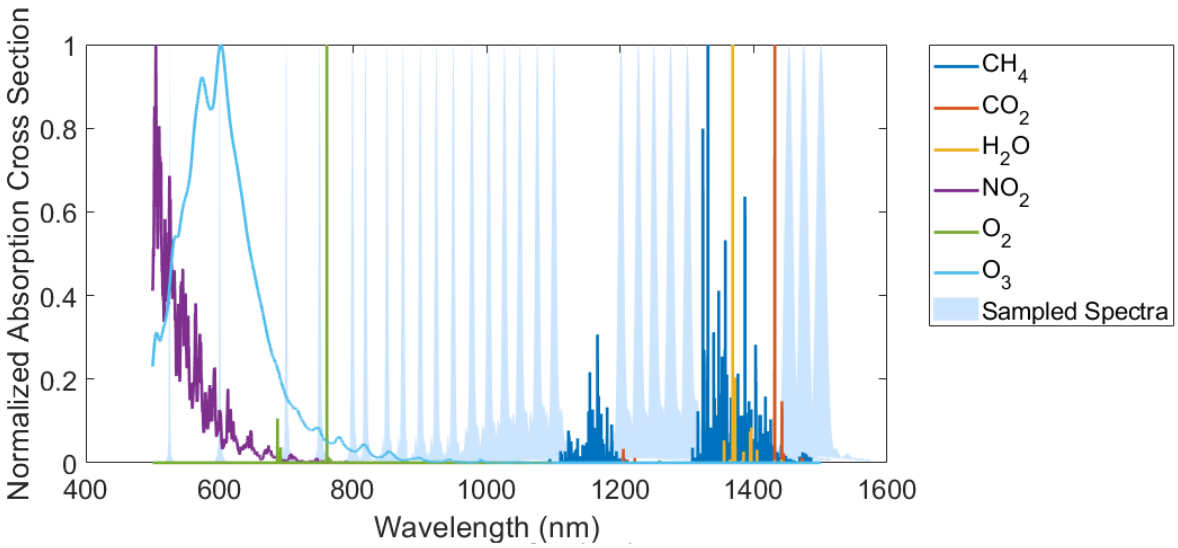

Figure 3.16: Absorption cross sections of several key atmospheric species, normalized for clarity. Sampled measurement spectra for 25 selected wavelength channels are overlaid to compare measured bandpasses with expected atmospheric features.

Chapter 4

A Multi-Spectral Polarimetric Imager for Atmospheric Profiling of Aerosol and Thin Cloud: Prototype Design and Sub-Orbital Performance

The design trades and principles described previously have been implemented to build the second generation of the ALI instrument. This manuscript provides further details into key advances made to the optical design to improve the measurement capabilities.

The attributes that set ALI V2 apart from its predecessor are a three-fold set of improvements. These include expanding the spectral measurement range, added capability to capture two nearly orthogonal polarization states and space-simulated packaging. The improved spectral range is driven by the desire to measure spectral channels longer than 1200 nm, which is critical to better understand the particle size distribution of stratospheric aerosol [Rieger et al., 2014]. This improvement is made possible by adding a second AOTF channel, in the form of a dual transducer device. Additionally, a specialized detector is selected which extends the typical short-wave infrared (SWIR) photosensitivity of InGaAs to include mid-visible wavelengths. Polarimetric measurements are facilitated by the use of a liquid crystal polarization rotator, and reflective optics are designed to reduce the instrument volume.

ALI V2 has been designed, built and tested in the Institute of Space and Atmospheric Studies optics lab and then tested from a sub-orbital platform in both Alice Springs, Australia and Timmins, Ontario. The first flight from Alice Springs experienced a critical detector power failure that prevented any measurements from being collected. However, the ther-

mal regulation system performed as expected, and the power monitoring system suggested that all other electrical components operated as expected. The secondary flight produced a novel measurement set of polarization and spectrally resolved, two-dimensional limb scattered measurements. This image set validated the pre-flight simulations with respect to optical throughput, which is a key performance indicator for the operation of ALI.

This manuscript has been published in Review of Scientific Instrument, and unless otherwise stated the version presented here is unchanged. The layout of figures and equations and the format of cross-references has been modified to match that of the overall document.

Kozun, M. N., Bourassa, A. E., Degenstein, D. A., & Loewen, P. R. (2020). A multi-spectral polarimetric imager for atmospheric profiling of aerosol and thin cloud: Prototype design and sub-orbital performance. *Rev. Sci. Instrum. 91*(10), 103106. doi:10.1063/5.0016129.

4.1 Abstract

We report on the development of a novel multi-spectral polarimetric imager for atmospheric remote sensing of aerosol and cloud properties. The instrument concept, called the Aerosol Limb Imager (ALI) is ultimately intended for satellite measurements from low Earth orbit. It utilizes a coupling of a dual transducer acousto-optic tunable filter and a liquid crystal rotator to provide dual linear polarization observations over a wide spectral range covering 600-1500 nm. In the limb, or side-viewing, geometry, these measurements provide capability to resolve vertical and horizontal distributions of aerosol and cloud properties such as extinction coefficient, optical depth, and particle distribution parameters. Here we present the design and performance of an ALI prototype. Lab characterization of the instrument is used to develop a mathematical instrument model to predict signal levels under various atmospheric conditions. Results from a sub-orbital flight of the ALI prototype on a stabilized high-altitude stratospheric balloon gondola are presented that show the first known polarimetric, multi-spectral images of the limb radiance. The signal levels obtained agree reasonably well with those predicted by the instrument model using radiative transfer calculations for typical atmospheric conditions.

4.2 Introduction

The Aerosol Limb Imager (ALI) is an atmospheric remote sensing instrument designed at the University of Saskatchewan in collaboration with the Canadian Space Agency and Honeywell Aerospace. The instrument, which is a type of multi-spectral polarimetric imager, has been developed to measure the vertical profile of atmospheric scattered sunlight to retrieve high spatial resolution stratospheric aerosol and thin cloud parameters, including extinction coefficient and particle size. This is achieved with a novel coupling of a liquid crystal polarization rotator and a large aperture acousto-optic tunable filter, which allows for rapid two dimensional imaging of multi-spectral bands at orthogonal polarization states with no moving parts. The eventual goal is the realization of the ALI instrument on a satellite platform in low Earth orbit where it will enable nearly global daily coverage of aerosol and thin cloud measurement in the upper troposphere and stratosphere. Canada has proposed ALI as a contributed instrument as a potential part of a future NASA satellite mission being currently developed by the "Aerosol, and Cloud, Convection, and Precipitation" study to fulfill recommendations from the recent "Decadal Strategy for Earth Observation from Space" [National Academies of Sciences Engineering and Medicine, 2018].

4.2.1 Stratospheric Aerosol Remote Sensing

The target geophysical parameters of the ALI instrument are vertically resolved profiles of aerosol extinction, particle size information, and thin cloud properties in the upper troposphere and stratosphere. Aerosol in the stratosphere is typically formed by the nucleation and condensation of sulphur bearing gases into liquid droplets of hydrated sulphuric acid. Due to the scattering of incoming solar radiation, the impact of aerosol in the stratosphere is a net cooling effect at the Earth's surface, with a cooling efficiency dependent upon their size distribution and concentration [Kiehl and Briegleb, 1993].

Stratospheric aerosol typically resides in a layered region 15-25 km above the surface of the Earth. Various transport mechanisms assist precursor gas molecules in crossing the tropopause where nucleation mechanisms initiate and maintain a background level aerosol concentration [Kremser et al., 2016]. However, this can be strongly perturbed by explosive

volcanic eruptions that can directly inject sulphur bearing precursor gases into the stratosphere [Robock, 2000]. Additionally, aerosol generated by intense pyro-convective forest fires is becoming increasingly important and frequent with several large events observed in recent years including in Canada in 2017 [Bourassa et al., 2019], and in Australia in 2020 [Pickrell, 2019]. The stable nature of the stratosphere allows the injected or nucleated aerosol to remain in the stratosphere for months to years, and to spread across the global atmosphere and thus impact climate [Robock, 2000]. The "persistently variable" nature of the aerosol layer [Solomon et al., 2011], and recent findings that show a potentially large impact from aerosol in the lowermost stratosphere [Andersson et al., 2015] motivate detailed global observations to further our understanding of the climate impact. Thin, high altitude cirrus are composed of water ice crystals with complex particle shapes, and have a wide range of optical depths and a high frequency of occurrence with strong seasonality. The interaction of near-by aerosol and the representation of cirrus clouds is a challenge in climate models and leads to one of the larger uncertainties in climate prediction [Patnaude and Diao, 2020].

The ALI instrument has been developed to utilize a remote sensing technique called limb scattering where spectral observations of the vertical profile of scattered sunlight are used to retrieve profiles of atmospheric composition. The Optical Spectrograph and InfraRed Imaging System (OSIRIS) was the first satellite instrument to utilize the limb scatter viewing geometry to measure aerosol in the stratosphere [Bourassa et al., 2007, Bourassa et al., 2008a]. The viewing geometry is shown in Figure 4.1. Photons scattered through interactions with molecules, aerosol and cloud particles in the atmosphere are measured by the satellite instrument and resolved spectrally. Scattering occurs either due to direct scattering from the sun into the line of sight, or through multi-scattering events. These multi-scattering events can include reflections from the surface of the Earth, and higher order scattering events in the atmosphere [Bourassa et al., 2008b]. The amount of scattering depends on the density profiles of various absorbing or scattering molecules and aerosol and cloud particles. Thus in simple terms, a measurement of scattered sunlight allows for the retrieval of these density profiles, or in the case of aerosol, the extinction coefficient profile [Bourassa et al., 2007]. Due to the increasing optical depth of the atmosphere at shorter wavelengths, the retrieval is only possible at stratospheric altitudes for wavelengths greater than 600 nm. Furthermore,

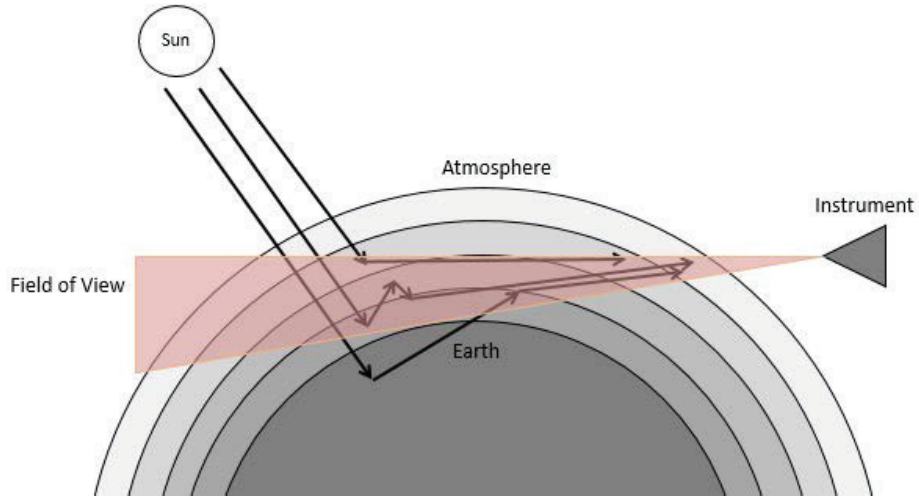

Figure 4.1: Limb scatter viewing geometry. Multiple scattering events are shown with photons scattering into the FOV of the instrument [Bourassa et al., 2008b]. Adapted with permission from J Quant Spectrosc Radiat Transf. 109 (2008). Copyright 2007, Elsevier Ltd.

measurements of wavelength channels longer than 1200 nm are required to derive information on the particle size distribution [Rieger et al., 2014, Malinina et al., 2019].

While previous and current limb scatter instruments in orbit are traditional grating or prism spectrometers [Bovensmann et al., 1999, Flynn et al., 2006], the ALI instrument is a multi-spectral imager designed specifically to optimize the aerosol measurement by taking two dimensional spatial images of the atmospheric limb with a narrow spectral passband that is successively scanned across a wide spectral range. This method is favourable because it allows for high resolution imaging to sample the fine spatial structure of aerosol in the atmosphere. The trade-off of reduced spectral sampling and resolution is justified because of the broadband nature of aerosol scattering. A second unique feature of the instrument, which does not exist in any current limb viewing satellite instrument, is the capability to explicitly measure orthogonal linear polarization (LP) states. This measurement will be used to discriminate aerosol and cloud in the measurements in a similar fashion to a lidar measurement where the radiative signature of liquid aerosol can be isolated from that of ice clouds by analysing the depolarization ratio of the backscattered signal [Winker et al., 2010].

4.2.2 Early ALI Prototype

Previous work on an early prototype of ALI was to show the proof-of-concept for the use of an imaging Acousto-Optic Tunable Filter (AOTF) to measure the signatures of stratospheric aerosol in the atmosphere in the limb scatter measurement geometry from a stratospheric balloon test platform [Elash et al., 2016]. This early prototype operated over a limited wavelength range of 650-1000 nm with a tunable bandpass no larger than 6 nm. This provided sufficient resolution to capture the characteristic broadband scattering from aerosol at selected wavelength channels that avoid contamination from molecular absorption and emission bands from trace gas species. A 6 degree square field of view provided the angular range required to image the atmospheric limb. This field of view covers a range from the horizontal at a balloon altitude of 35 km to a line-of-sight tangent to the surface of the Earth.

The version 1 prototype (ALI V1) was designed using commercial off the shelf (COTS) parts, with the acknowledgement that optical performance would not be entirely optimized (see details in [Elash et al., 2016]). The critical element in the design was the 10 mm x 10 mm imaging quality AOTF produced by Brimrose Corporation of America (model number TEAF—10-0.6-1.0-MSD). Specific parameters of this device, namely wavelength range and acceptance angle, drove the optical design. Additionally, a COTS silicon based detector was selected to align with the wavelength range of the AOTF, which also drove the optical design. The optical design consists of three singlets. The first two form an afocal telescope used to redistribute the instrument field of view into the acceptance angle of the AOTF. The final singlet is used to image the diffracted signal onto the detector. The optical design also included two orthogonally mounted broadband LP filters (pre- and post-AOTF) and a front-end baffle to help mitigate stray light.

The opto-mechanical design was also primarily based on COTS parts, with minimal custom machined parts. The optical components were mounted using an optical cage system from ThorLabs, and arranged in a linear chain on an optical rail. The footprint of ALI V1 was not a critical design driver, because the balloon platform for the experiment did not have highly limiting requirements. An insulated aluminum case was built around the optical unit, and the instrument was mounted on an aluminum base plate. A 3 degree wedge mount was

built to interface the base plate to the deck of the stratospheric balloon gondola. The wedge was required to orient the field-of-view of the instrument to the atmospheric limb between the balloon altitude and the Earth's surface.

From a stratospheric balloon flight in 2014, this prototype successfully demonstrated the capability to capture high quality spectral limb radiance images. Images were captured over 13 wavelength channels with various solar viewing geometries and show both vertical and horizontal structures in the atmosphere at the target spatial resolutions. These images were used to successfully retrieve stratospheric aerosol extinction coefficient profiles that showed reasonable agreement with nearly coincident satellite observations [Elash et al., 2016].

4.2.3 Design Improvements

In this work we further develop the ALI instrument concept as a future satellite instrument that can meet the driving scientific observation requirement for stratospheric aerosol and thin cirrus observation. Three specific improvements beyond the early prototype are highlighted in this design:

- Extension of the wavelength range to 600 - 1500 nm to provide aerosol particle size distribution information using a dual transducer AOTF; we incorporate detailed physical modelling of the AOTF filtering process in order to characterize nonidealities of the device.
- Addition of a LP selection mechanism to observe two orthogonal LP states and provide aerosol/cloud discrimination capability; we use a novel combination of a liquid crystal rotator coupled to the AOTF and characterize the performance of the system by measurement of the system Mueller matrix.
- Implementation of a folded, reflective optical design which reduces the footprint, minimizes chromatic aberration, and provides additional stray light rejection.

4.2.4 Acousto-Optic Technology

The central technology in the ALI instrument design is the AOTF. These devices provide fast wavelength tuning over a large wavelength range without the use of mechanically moving

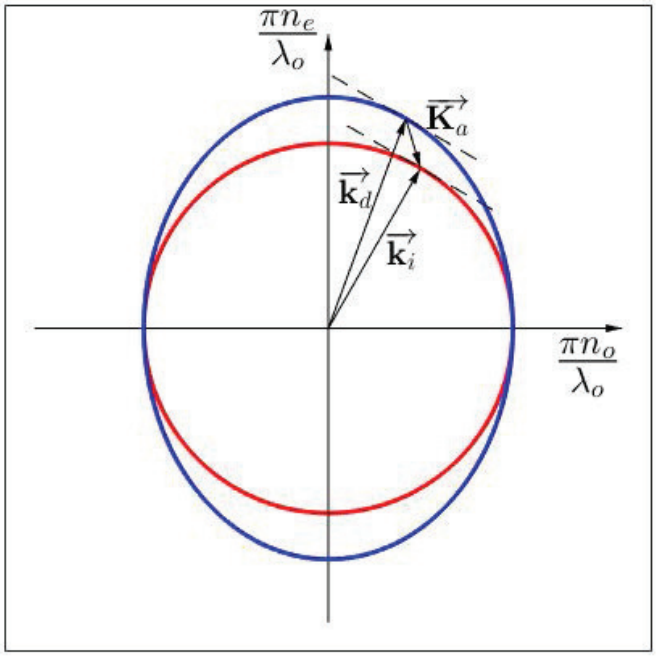

Figure 4.2: Momentum matching criterion on a wave vector diagram for a non-collinear AOTF, with axes normalized to the magnitude of the optical wave vector. The red curve shows the refractive index of the ordinary polarization state over all incident angles, and the blue curve represents that of the extraordinary state. Bragg diffraction is shown between the incident optical wave vector, $\vec{\mathbf{k}}_i$, the acoustic wave vector, $\vec{\mathbf{K}}_a$ and the diffracted optical wave vector, $\vec{\mathbf{k}}_d$.

parts. This is an advantage for satellite based instruments because it reduces the likelihood of failure due to mechanical wear. The acousto-optic (AO) effect is characterized by the Bragg diffraction criterion based on a momentum matching condition between photons and phonons. This condition is described by

$$\vec{\boldsymbol{k}}_i \pm \vec{\boldsymbol{K}}_a = \vec{\boldsymbol{k}}_d, \tag{4.1}$$

where $\vec{\boldsymbol{k}}_i$ is the incident optical wave vector, $\vec{\boldsymbol{K}}_a$ is the acoustic wave vector and $\vec{\boldsymbol{k}}_d$ is the diffracted optical wave vector. Along with diffraction, the wave may also experience retardation or a polarization rotation during the AO interaction. The momentum matching criterion for ordinary polarized incident light is displayed in Figure 4.2.

This geometry represents the non-collinear momentum matching that emerges from certain anisotropic materials [Chang, 1974]. Under Bragg diffraction, the Poynting vectors of

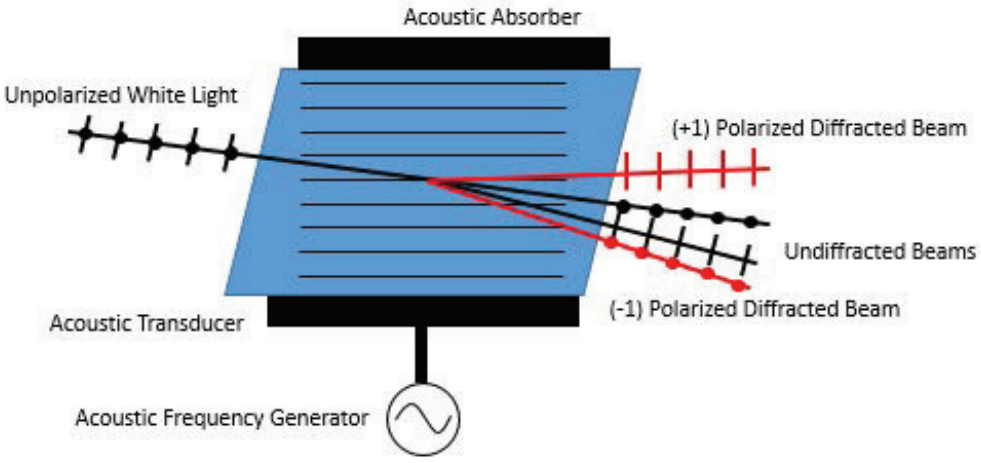

Figure 4.3: AOTF diffracting unpolarized light. The broadband undiffracted beam experiences double refraction due to the crystal birefringence. Narrow band filtering produces two first order diffraction beams, paired to the two undiffracted beams. No higher diffraction orders exist due to the sinusoidal nature of the acoustic wave within the AOTF.

the incident and diffracted rays must be parallel and are defined normal to the index curves (identified by the dashed tangent lines). The Bragg diffraction criterion dictates a number of important properties of the AOTF, including the tuning relationship between the acoustic frequency, f_a, to the optical wavelength, λ_o, the peak transmission, T_o, and the optical bandpass, $\Delta\lambda$, described in Equations (4.2) through (4.4).

$$f_a = \left(\frac{v\Delta n}{\lambda_o}\right)\sqrt{\sin^4\theta_o + \sin^2 2\theta_o}, \tag{4.2}$$

$$T_o = \sin^2\left(\frac{\pi}{2\lambda_o^2} M_2 P_d L^2\right)^{1/2}, \tag{4.3}$$

$$\Delta\lambda = \frac{0.9\lambda_o^2}{bL\sin^2\theta_o}. \tag{4.4}$$

In the previous equations, v is the acoustic speed in the material, Δn is the birefringence, λ_o is the diffracted central wavelength, θ_o is the angle of the incident wave, M_2 is the acousto-optic figure of merit, P_d is the power density, L is the interaction length and b is the dispersion constant, all described in [Chang, 1974] and [Chang, 1975].

The functionality of an AOTF is displayed in Figure 4.3 with unpolarized incident light.

An important consequence to consider with non-collinear devices is that two first diffraction orders occur, defined as $\pm 1^{st}$ order. These first order diffraction beams have opposite LP states. The undiffracted beams are denoted 0^{th} order. Note that higher diffraction orders are suppressed due to the sinusoidal nature of the acoustic wave.

4.2.5 Liquid Crystal Polarization Rotator

It has been noted earlier that linearly polarized atmospheric scattering measurements are useful for isolating clouds from stratospheric aerosol signals. The inherent LP filtering effect of a non-collinear AOTF means that a single incident LP state should be chosen for optimization. Pairing a twisted nematic liquid crystal cell with an AOTF allows for an additional LP state to be captured depending on the state of the cell. The application of a voltage across a twisted nematic cell affects the optical activity within the medium [Schadt and Helfrich, 1971]. In a relaxed state, the liquid crystals are arranged in a pattern parallel to the cell walls but with differing directions that result in a 90° twist. This twist causes the LP plane of incident light to also rotate 90°. However, when a voltage is applied across the cell, the electric field causes the liquid crystals to align with the field. Under these conditions, the polarization state of passing light is not rotated. The rotation in the relaxed state is wavelength dependent. This means that the length of the cell allows only a single wavelength to rotate by 90°, and all other wavelengths end up having an elliptical polarization state upon leaving the crystal [Gooch and Tarry, 1974]. By placing such a cell in front of an AOTF, the LP state that is incident upon the cell and nominally diffracted by the AOTF can be selected. The coupling of these two devices for multi-spectral, dual polarization measurements without moving parts is a novel application for atmospheric remote sensing from space. Although this instrumental concept has been reported in recent work [Li et al., 2015], we believe this is the first sub-orbital implementation and demonstration for atmospheric remote sensing. Implementation details are discussed in the following section.

4.3 Advanced ALI Prototype

4.3.1 Instrument Design

Extended Wavelength Range

Spectral filtering is achieved using a TEAF—10-0.5-1.5-MSD-ER AOTF from Brimrose Corporation of America. This AOTF differs from the one used in the previous ALI prototype in that it is a dual transducer AOTF operating over two frequency ranges, which provides an extended wavelength tuning range. The transducer on a typical AOTF has a limited frequency response, typically tuning over one optical octave. This dual transducer type of AOTF includes two transducers bonded to the acousto-optic crystal that are responsive over different frequency ranges, thus increasing the range of optical frequencies that will meet the diffraction criteria. The properties of this AOTF are shown in Table 4.1.

There are two methods of coupling light into an AOTF, either using a telescopic or telecentric layout. The difference between these two is that the AO interaction occurs on collimated light in the telescopic layout, or on focused light in the telecentric case. Each comes with a unique trade-off. For the telescopic case, a wavelength gradient exists over the fields diffracted by the AOTF. For the telecentric case, a chromatic defocus occurs. The impact of this is that only a single wavelength channel will be properly focused by the imaging system following the AOTF, unless active focus compensation is involved.

The telescopic layout is selected for ALI, because the spectral scattering signature of stratospheric aerosol is very broad compared to the expected field gradient. In this work we have estimated this gradient by modelling the momentum matching condition for various fields based on the crystal structure of the AOTF. The method is a modification of the approach described by [Zhao et al., 2014] for tracing rays through an AOTF. The method begins by identifying the acoustic vector for on-axis Bragg diffraction at a specific tuned wavelength, like that shown in Figure 4.2. This vector is then positioned to fit between the refractive index ellipses of the ordinary and extraordinary states of TeO_2 for wavelengths near the tuned wavelength. The position on these ellipses indicates the propagation direction of the incident and diffracted rays. By tracing the group velocity vector to the exit surface

Table 4.1: TEAF—10-0.5-1.5-MSD-ER AOTF Properties

Substrate	Tellurium Dioxide
Optical Aperture	10 mm × 10 mm
Wavelength Range	500 - 850 - 1500 nm
Spectral Resolution	1.5 nm @ 514 nm 2.2 nm @ 633 nm 7.7 nm @ 1152 nm 14.3 nm @ 1523 nm
Peak Diffraction Efficiency	20% @ 543 nm 85% @ 633 nm 72% @ 1152 nm 52% @ 1523 nm
Angular Aperture	4° - 6°
Separation Angle between 0^{th} and -1^{st} order	5.3° - 6°
Angle between input and diffracted -1^{st} order	2.6°
Max RF Power	3 W
RF Range	55 - 100 MHz 100 - 195 MHz

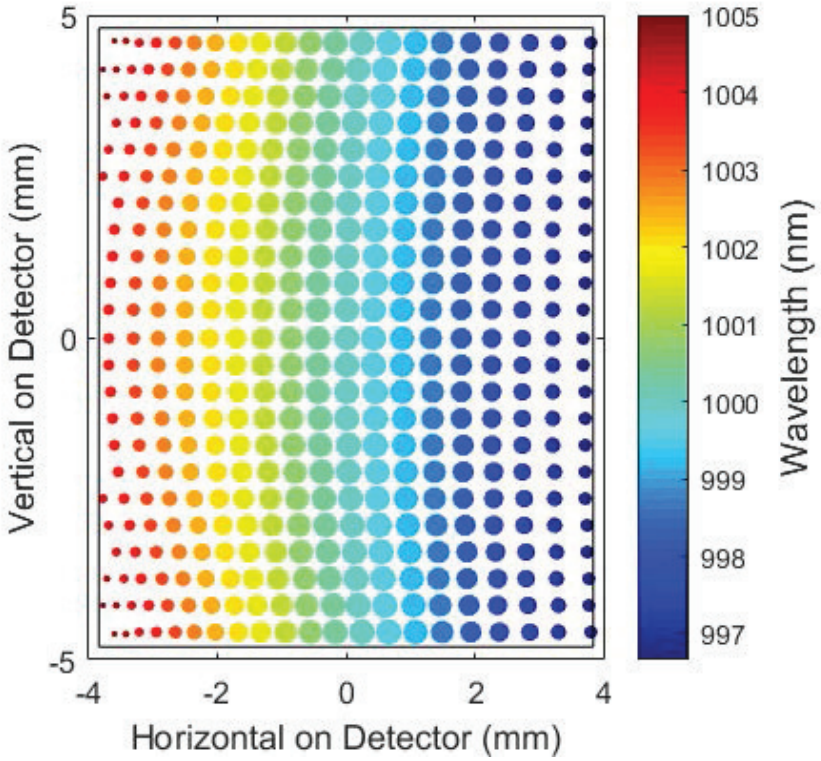

Figure 4.4: Wavelength distribution across detector in telescopic layout for filtering at 1000 nm. The marker sizes indicate the relative spectral transmission within the bandpass, dictated by momentum mismatch at these wavelengths.

of the AOTF, and applying the appropriate refraction, we can determine the propagation direction for wavelengths within the bandpass of the AOTF. Figure 4.4 shows the wavelength distribution mapped onto a 9.6 mm by 7.68 mm image plane using an ideal singlet with a 137 mm focal length. The range of wavelengths displayed is based on the bandwidth at the tuned frequency. The size of the gradient is found to be comparable to the tuned bandwidth, resulting in a negligible impact on the retrieval of aerosol and cloud information.

The extended spectral range is a challenge at the detector level as typically Si is used for visible wavelengths and InGaAs is used for near infrared beyond 1000 nm. For this design, we selected a "vis-doped" Raptor Owl 640 VIS-SWIR InGaAs detector. The spectral response of this detector is much wider than that of a standard InGaAs detector, with responsivity down to 400 nm. However, the quantum efficiency is below 50% for wavelengths shorter than 800 nm. The reduction in quantum efficiency is compensated for by a significant increase in scattered sunlight in the visible spectrum compared the near infrared. The detector

Table 4.2: Raptor Owl 640 Detector Properties

Sensor Type	InGaAs PIN-Photodiode
Active Pixels	640 × 512
Pixel Pitch	15 μm × 15 μm
Active Area	9.6 mm × 7.68 mm
Spectral Response	400 - 1700 nm
Readout Noise (RMS)	174 electrons (typical in Low Gain)
Well Depth	650,000 electrons (Low Gain)
Dark Current (e^-/pix/s)	<28,000 @ 15°C
TE Cooling	Active
Digital Output Format	14 bit Camera Link

specification is listed in Table 4.2.

Polarization Selection

The birefringent nature of the TeO_2 crystal in the AOTF results in significant angular separation between the diffraction orders once rays exit the device. Coupling this with the highly dispersive properties of the material leads to wavelength dependent beam wander if the output face of the crystal is parallel to the input. To suppress this wander, the crystal is cut with a wedge at the output face to optimize the wavelength dependent refraction, which maintains a uniform direction for one diffracted polarization state across all wavelengths. Therefore, only the signal that is linearly polarized along the ordinary axis of the crystal is uniformly transmitted through the AOTF and measured [Yano and Watanabe, 1976, Suhre and Theodore, 1996].

As shown in Figure 4.3, randomly polarized signal entering the AOTF is separated into four directions based on polarization state and wavelength. To reduce stray light contamination from the unwanted signals out of the AOTF, LP filters are placed on either side of it. Glan-Taylor type LP filters are selected for their broadband operation. The input LP filter (LPF1) is aligned such that the signal passing the element is aligned with the ordinary axis of the AOTF, thus eliminating the extraordinary polarized beam and the resulting -1^{st}

diffracted beam in Figure 4.3. This polarizer is placed early in the optical chain for two reasons: to filter the polarization state from the atmosphere prior to reflections off the telescope mirrors and to reduce the signal reaching the mirrors, which limits stray light scattering. This attenuates the signal aligned with the extraordinary axis of the crystal per the extinction ratio of the polarizer, which is on the order of 20000:1.

The output LP filter (LPF2) is aligned orthogonal to LPF1 in order to pass signal along the extraordinary axis of the AOTF, i.e. the signal diffracted by the AOTF. The undiffracted 0^{th} order signal contains most of the broadband atmospheric signal, but because this beam does not undergo the acousto-optic interaction, its polarization state is unchanged as it passes the AOTF and is significantly attenuated by LPF2. It is important to note however that the total radiance of the broadband signal is several orders of magnitude larger than the diffracted narrow band signal, so the filtering from LPF1 and LPF2 acts to bring the diffracted and undiffracted signals to comparable order.

An additional property to be exploited is the angular separation between the 0^{th} and -1^{st} orders, which is greater than 5°. The clear aperture of the output polarizer is centered about the diffracted signal, providing significant vignetting of the 0^{th} order path. Furthermore, the optical path length between the AOTF and the imaging optics is maximized using fold mirrors to increase lateral displacement between the paths and prevent the 0^{th} order path from reaching the imaging optics.

The novel dual polarization capability of this instrument capitalizes on the LP operation of the AOTF. A liquid crystal polarization state rotator (LCR) is placed ahead of LPF1 in the optical chain. The LCR acts on the polarization state of incident light by rotating it approximately 90°. This interaction has a wavelength dependence and is tuned for only a subset region of the entire instrument bandwidth, so the rotation does not perfectly reach 90° for all wavelengths.

Folded Optical Layout

A folded optical layout comes with several advantages, including reduced aberration, footprint and stray light. Two off axis parabolic mirrors are used as the front-end telescope. These mirrors reduce chromatic aberration of the input signal before the AO interaction. The use of

mirrors also reduces the footprint of the telescope, which would require a long optical chain if lenses were used.

The test environment for ALI is on the deck of a stratospheric balloon payload, imaging the atmosphere from approximately 35 km above the surface of the Earth using the limb scatter viewing geometry. Under these conditions, the full field of view from the instrument horizontal to the surface of the Earth is approximately 6°. With ALI suspended in an upper layer of the atmosphere, measurements of the radiance scattered from the volume of atmosphere in front of and below the balloon deck are captured. In the limb scatter viewing geometry, ALI measures photons that have been scattered from any point in the illuminated atmosphere within its field of view. Table 4.1 shows that the maximum acceptance cone angle of the AOTF is 4°, so the two mirrors must accommodate this angular reduction. The telescope mirrors produce an intermediate image, so a field stop is placed here to reject out of field rays. Additionally, an external baffle is designed to precede the telescope to further limit these rays from striking the first mirror to contain stray light.

The back-end imaging optics must map the acceptance angle of the AOTF to the dimensions of the detector. This requires a focal length of 137 mm on the imaging optics. A triplet is designed based loosely on the Cooke triplet format. Here refractive imaging elements are used for several reasons. The achromatic nature of the front end optics of ALI are disrupted by the AOTF, and the off the shelf availability is far greater for refractive elements. These three lenses are housed in a lens tube, following two enclosed fold mirrors to extend the optical path length following the AOTF, which allows for the residual undiffracted beam to be blocked by the lens tubes. These efforts are made to reduce the stray light reaching the detector.

Optical Design

The optical layout was designed using CODE V software. Three special user-defined surfaces are used to simulate the interaction of the AOTF, based on the method described by [Zhao et al., 2014]. The first of these surfaces is used to model refraction of the ordinary polarized beam, while setting a flag to identify rays that are entering the AOTF from outside the acceptance angle. The second simulates the AO interaction, using a list of crystallographic

properties that are described in a text file. A linked MATLAB script is used to calculate the acoustic walk-off angle and acoustic wave vector to improve the model [Poon, 2006]. Rays are finally traced to the final surface, where extraordinary refraction occurs based on the crystal geometry. Standard ray tracing algorithms are used for all other optical surfaces. All optical elements aside from the AOTF are COTS components. Figure 4.5a shows the final optical layout of ALI. The stray light baffle defines the aperture of the system, with the LCR and LPF1 immediately following. These elements select the atmospheric polarization state to be measured. Following this is the telescope, comprised of two off axis parabolic mirrors, which is used to map the instrument aperture to the AOTF aperture at the telescope exit pupil. Following the AOTF is LPF2, aligned orthogonal to the first. Two flat fold mirrors elongate the optical path length while reducing the footprint of the instrument. Finally, a triplet is used to focus the diffracted signal onto the detector. COTS opto-mechanical components are selected to hold the selected optics, shown in Figure 4.5b.

4.3.2 Characterization and Calibration

Following assembly, the instrument underwent a characterization and calibration campaign. Instrument characterization took the form of assessing the optical response of individual components and/or the optical system to electrical inputs. An example of a characterization is the frequency-wavelength tuning response to relate the input acoustic frequency to the diffracted optical wavelength channel. The characterization responses are required for development of an instrument simulation model, described later. System level calibration activities, like the flat field calibration, were also performed. These calibrations are necessary to generate Level 1 data products from the instrument measurements for aerosol property retrieval.

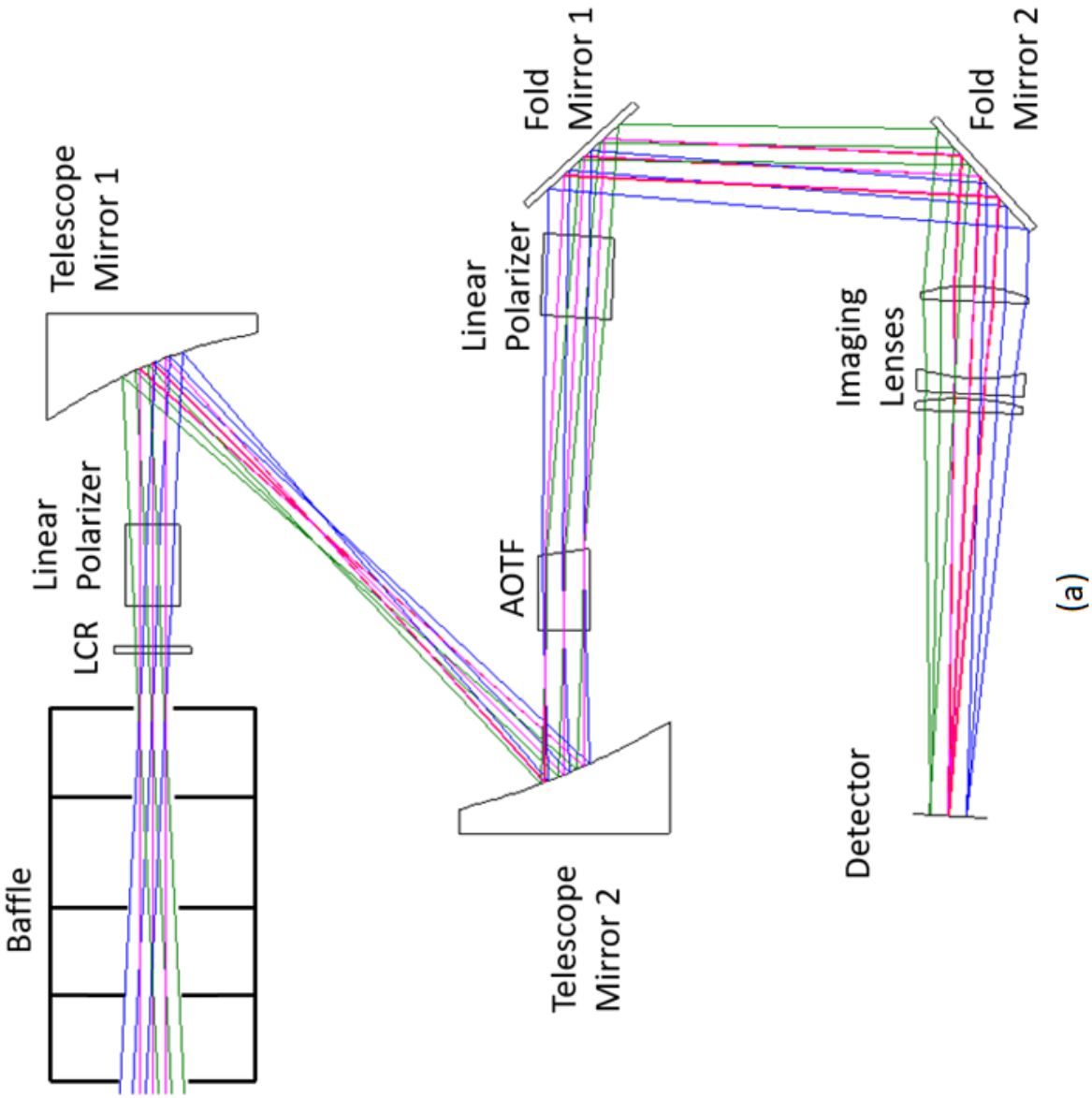
Baffle
LCR
Linear Polarizer
Telescope Mirror 1
AOTF
Linear Polarizer
Fold Mirror 1
Telescope Mirror 2
Imaging Lenses
Fold Mirror 2
Detector
(a)

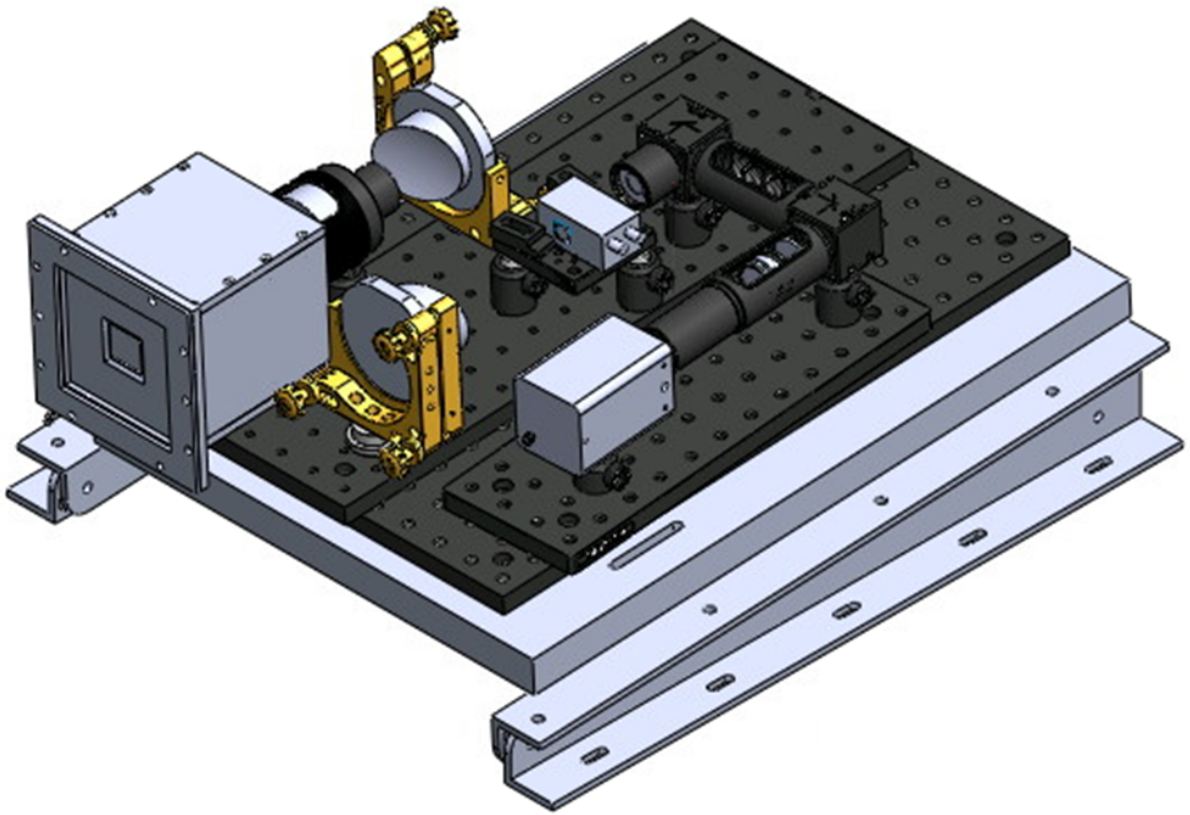

(b)

Figure 4.5: ALI V2 instrument layout. (a) Optical layout as designed in CODE V. (b) Opto-mechanical model designed primarily with COTS components.

Frequency-Wavelength Tuning

The wavelength diffracted by the AOTF is determined by the frequency of the acoustic wave propagating through the crystal in a defined direction. The relationship between the wavelength and frequency is known as the tuning curve. The tuning curve of the AOTF used in ALI is measured by scanning frequencies in 0.2 or 0.4 MHz steps across the designed frequency range of 50 - 200 MHz. The AOTF is placed between crossed polarizers, with a broadband light source with low divergence filling the aperture. The diffracted spectrum is measured with a HORIBA iHR320 spectrometer and either a CCD or InGaAs imaging array. The optical set up is shown in Figure 4.6a. Typical normalized spectra from various tuning frequencies are shown in Figure 4.6b.

The central wavelength of the diffraction peak is calculated using curve fitting to a goodness of fit parameter. The coefficients of determination for the curve fitting exceeded 0.997. Figure 4.6c shows the tuning curve for the AOTF. The inverse relationship between frequency and wavelength means the low frequency transducer diffracts wavelengths longer than 920 nm, and the high frequency transducer diffracts wavelengths below 920 nm.

Bandpass

The bandpass of the AOTF is found using the same spectra used to calculate the tuning curve. The FWHM is extracted from the normalized spectra. Figure 4.7 shows a best fit theoretical bandpass predicted by Equation (4.4) and the measured bandpass.

We see two distinct regions in the bandpass relationship, separated at 920 nm, which correspond to the two transducer frequency ranges. The difference in interaction length of the transducers leads to this step change. Differences between the measured and theoretical bandpass are within 1.5 nm, and are the result of a non-zero frequency bandwidth applied for each sample, non-zero divergence of the incident signal, and uncertainty in the AOTF geometry, each of which are not characterized in this paper. Rather, the measured bandpass is directly incorporated into the instrument simulation model described in section 2.3.

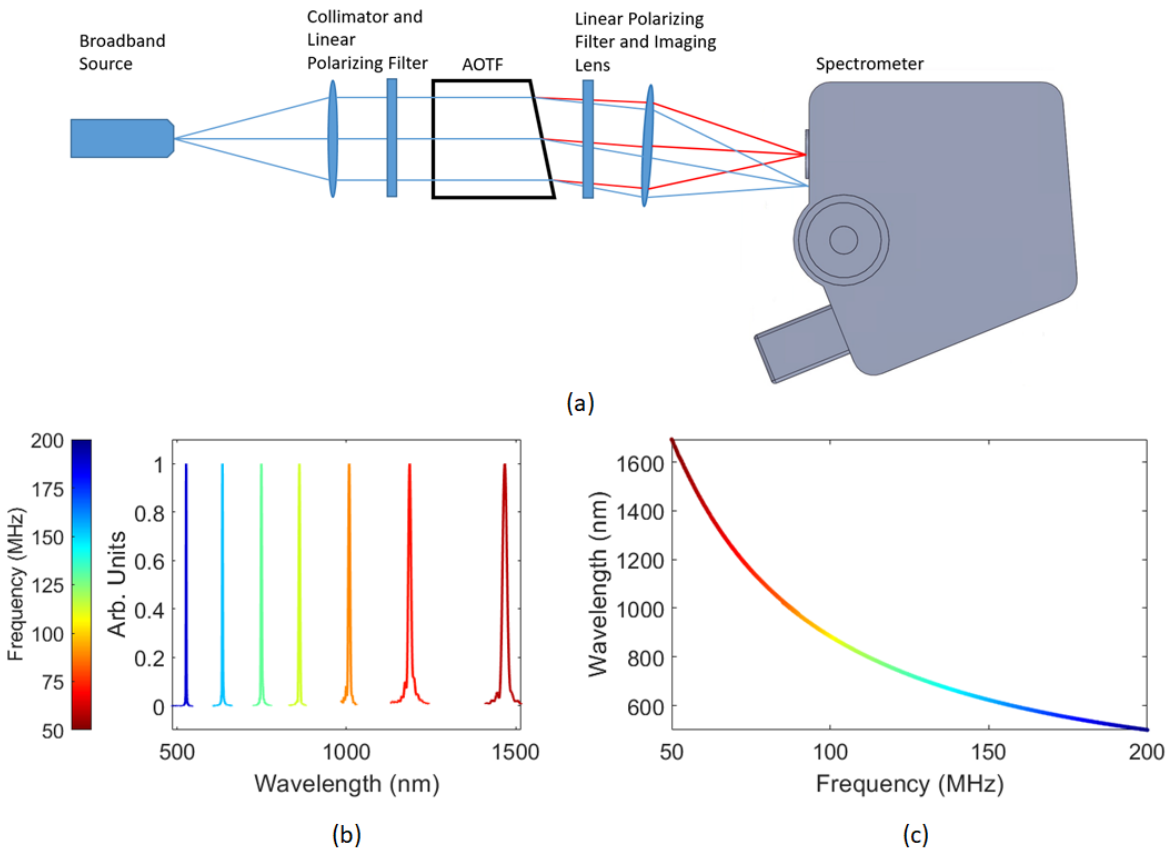

Figure 4.6: Frequency tuning curve measurements. (a) Optical layout for tuning curve measurement. (b) Sample spectra used to determine tuning curve. (c) Wavelength tuning curve as a function of applied frequency. Note the smooth joint between the two transducers at the change over frequency of 100 MHz.

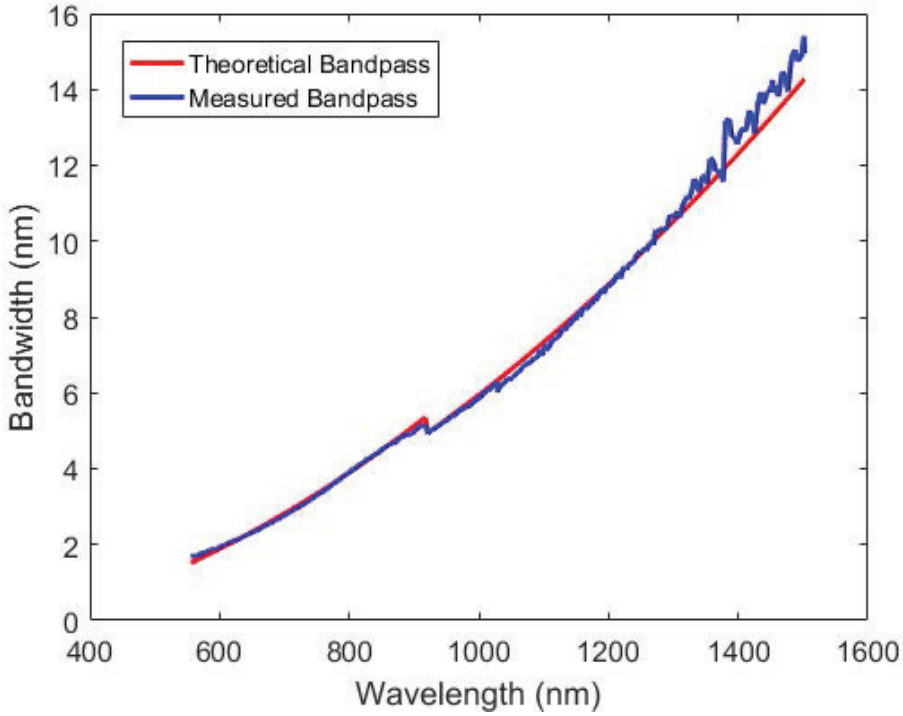

Figure 4.7: AOTF bandpass as a function of wavelength. The discontinuity at 920 nm is a result of different transducer interaction lengths.

Internal Diffraction Efficiency

The internal diffraction efficiency (IDE) of the AOTF is a measure of the fraction of passing light that is diffracted at a specific tuning frequency. It does not consider Fresnel or other losses occurring at the medium interfaces of the TeO_2 crystal. Measuring the IDE requires a similar optical set up to the one used for the tuning curve measurements, but with the AOTF rotated such that the undiffracted 0^{th} order signal passing through the AOTF is imaged onto the spectrometer entrance slit. Additionally, the polarizer following the AOTF is rotated such that it also transmits light polarized along the ordinary axis of the AOTF.

The IDE is calculated by measuring three spectra in this configuration, shown in Figure 4.8a. The first measurement made is with the source lamp turned off to capture the dark current signal on the detector. The next spectrum is the full 0^{th} order signal with the tuning frequency amplitude set to 0 W, denoted S_0. The last spectrum is the 0^{th} order signal with the tuning frequency powered to maximize diffraction, denoted S_P. This amplitude of the powered RF signal is approximately 3 W across all frequencies for this AOTF. The S_P

spectrum closely resembles the S_0 spectrum for wavelengths outside of the bandpass, and drops away within the bandpass. This is because this signal has been diffracted away from the entrance slit of the spectrometer and is no longer imaged. The dark current is subtracted from the remaining two spectra to give S_0' and S_P'. The IDE is then defined as

$$IDE(\lambda) = max\left(\frac{S_0' - S_P'}{S_0'}\right). \tag{4.5}$$

Figure 4.8b shows the IDE of the AOTF as a function of central wavelength. The sampling used for the IDE characterization is the same as that used for the tuning curves.

The IDE of the AOTF is once again a function of tuning frequency. Equation (4.3) shows that the peak transmission of the AOTF is related to the power density, which is strongly dependent upon the responsivity of the transducers to a selected frequency. The efficiency drops off significantly as we approach the extremes of the transducer responsivities. This explains the decline in IDE near 850 nm. We also note the severe drop in IDE at the far edges of the spectral range near 500 nm and 1600 nm.

Uncertainty in the IDE measurement comes from the dispersive nature of the TeO_2 crystal, as well as the variation in diffraction acceptance angle. The dispersion requires realignment of the source, collimating optics and AOTF as the wavelength is scanned, to ensure the 0^{th} order signal at the tuned central wavelength has normal incidence with the imaging optics. The non-zero divergence of the collimated input coupled with the variation in acceptance angle leads to a variation in coupling into the spectrometer over the wavelength range.

Polarization Tuning

The liquid crystal polarization rotator in ALI provides polarization selection capabilities to the instrument, but other optical elements also manipulate the polarization state being measured. These elements include the telescope and fold mirrors, the two LP filters that precede the telescope and follow the AOTF, as well as the AOTF itself. Therefore, we must characterize this manipulation in terms of Mueller matrices, which depend upon tuning frequency and LCR state. These matrices operate on the Stokes vectors describing incident light, defined as $S = \begin{bmatrix} I & Q & U & V \end{bmatrix}^T$. It is not necessary to calculate all 16 elements of the Mueller matrix for two reasons. The first is that the contribution to the total radiance from circu-

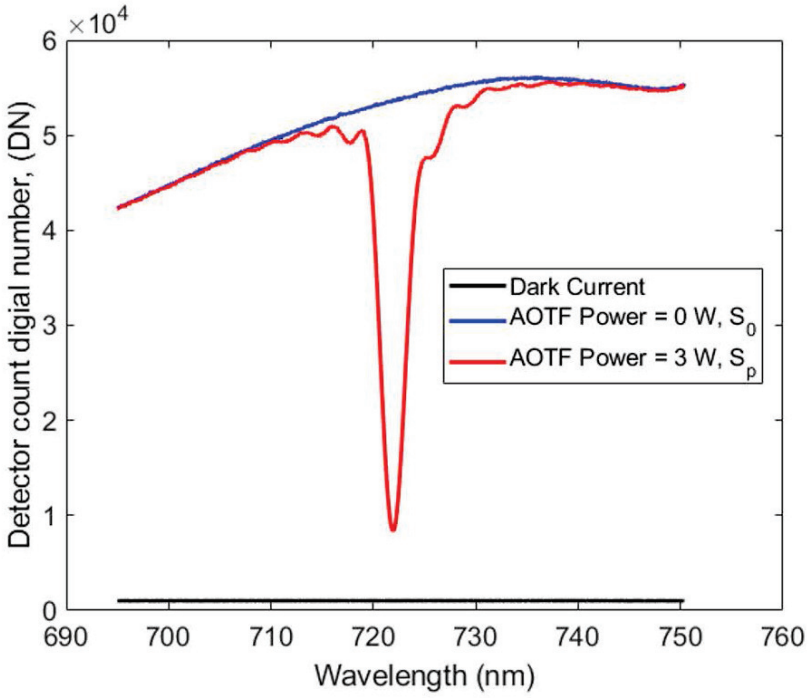

(a)

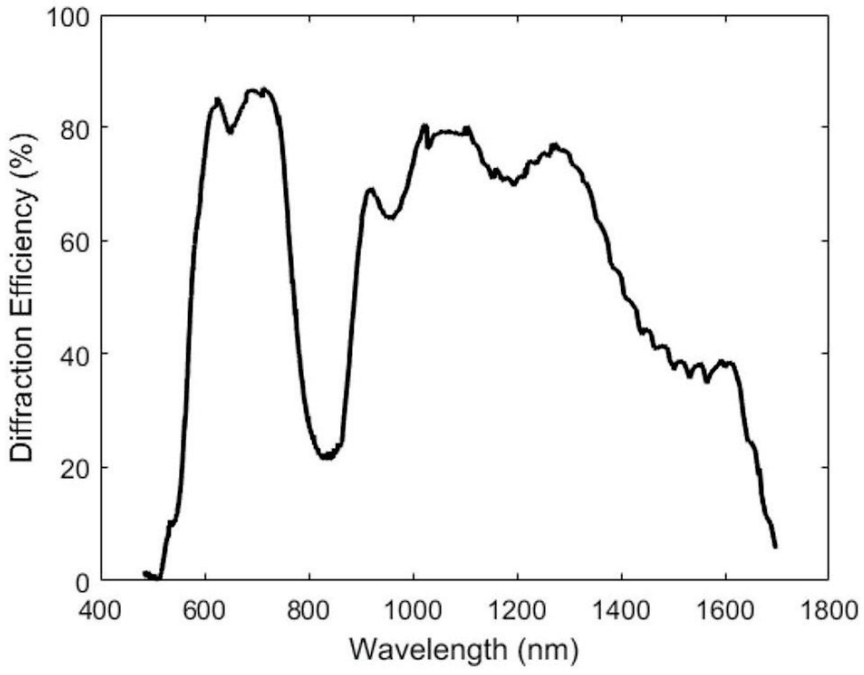

(b)

Figure 4.8: Internal diffraction efficiency measurements. (a) Sample spectra showing absence of diffracted signal, described in generic pixel count digital numbers, DN. S_0 is the full 0^{th} order spectrum with the tuning frequency amplitude set to 0 W. S_P is once again the 0^{th} order spectrum but with the tuning frequency amplitude set to maximize diffraction. (b) IDE over wavelength range.

larly polarized light is insignificant in the atmosphere. The V term is neglected in the Stokes vector, meaning the last column of the matrix is unnecessary [Hansen and Travis, 1974]. Furthermore, the detector in ALI measures the total radiance incident at the detector plane, I_{meas}, so the first three elements of the top row of the Mueller matrix are all that is required [Mclinden et al., 2011]. The measured radiance can therefore be expressed as

$$I_{meas} = f(\lambda) \begin{bmatrix} 1 & g_{12} & g_{13} \end{bmatrix} \begin{bmatrix} I_{in} & Q_{in} & U_{in} \end{bmatrix}^T, \tag{4.6}$$

where $f(\lambda)$ is the wavelength dependent transmission of the instrument that is characterized in the next subsection and g_{12} and g_{13} are the second and third elements of the top row of the system Mueller matrix. To determine the g_{12} and g_{13} parameters, a LP filter is placed at an angle α between an unpolarized broadband source and ALI. The measured signal is expressed in the form

$$I_{meas} \propto \begin{bmatrix} 1 & g_{12} & g_{13} \end{bmatrix} \begin{bmatrix} 1 & \cos 2\alpha & \sin 2\alpha \\ \cos 2\alpha & \cos^2 2\alpha & \cos 2\alpha \sin 2\alpha \\ \sin 2\alpha & \cos 2\alpha \sin 2\alpha & \sin^2 2\alpha \end{bmatrix} \begin{bmatrix} 1 \\ 0 \\ 0 \end{bmatrix} \tag{4.7a}$$

$$\propto 1 + g_{12} \cos 2\alpha + g_{13} \sin 2\alpha \tag{4.7b}$$

The 3×3 matrix in Equation (4.7a) describes the Mueller matrix of a LP filter. The constants g_{12} and g_{13} are determined by making measurements with various polarizer rotation angles, α, and using a curve fitting method to match the form of Equation (4.7b). Figure 4.9a displays normalized measurements made with an external LP filter, which have curves fitted to determine the required constants for the specific wavelength and LCR state. Figure 4.9b shows the g_{12} and g_{13} parameters for select wavelengths across the operating range. The ideal response would be that of a linear polarization in each of two orthogonal states, i.e. (g_{12}, g_{13}) equal to (1,0) for LCR Off, and equal to (-1,0) for LCR On. While this behavior is generally observed, substantial variation from the ideal case is observed for g_{13} when the LCR is off, and for g_{12} at the longest wavelengths when the LCR is off. This is due to the nature of the twisted nematic cell polarization rotator, which is optimized only for a bandwidth much narrower than our measurement range. These observations are used directly in the instrument simulation model in Section 2.4 as they are an important aspect of characterization of the response for the aerosol and cloud information retrieval.

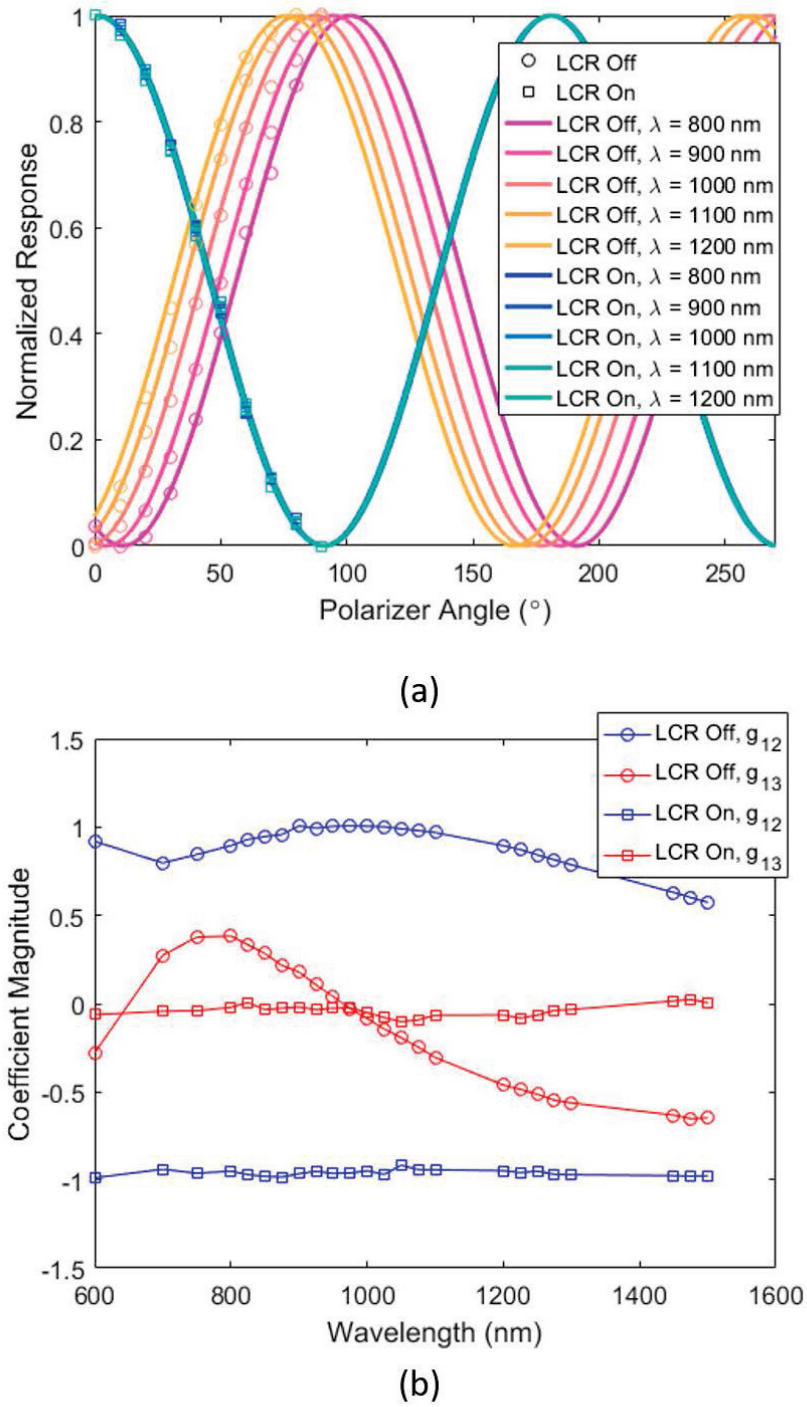

Figure 4.9: Characterization of ALI polarization tuning. This is a full instrument characterization, including all optical elements in ALI. (a) Wavelength dependent polarization response. The spread seen in the LCR Off measurements is a result of the twisted nematic cell LCR, which is only optimized over a narrower bandwidth than the ALI spectral range. (b) Coefficients for ALI Mueller matrices. The effect of the narrow optimized bandwidth is once again seen in the variation of the g_{12} and g_{13} curves when the LCR is off.

Flat Field and Absolute Calibration

A flat field calibration is performed to account for imaging sensitivity variations across the ALI field of view. Variations in sensitivity arise from several sources, including non-uniform response of the detector, variation in path length through the LCR, reduced AOTF diffraction efficiency with increasing incidence angle, and slight vignetting at the AOTF aperture from misalignment with the exit pupil of the telescope. A flat field calibration mask is applied to each pixel for each wavelength channel and LCR state. The calibration masks are measured using a calibrated broadband signal and an integrating sphere. The calibration masks then convert dark corrected pixel counts into radiance in units of $photons \cdot cm^{-2} \cdot sr^{-1} \cdot s^{-1}$.

4.3.3 Instrument Simulation Model

The performance of ALI is simulated using a mathematical instrument model developed in MATLAB. This instrument model is used to estimate the performance under a predicted test environment, and is necessary to estimate exposure times to achieve signal-to-noise ratio requirements. It can also be used as a tool to run simulation aerosol retrievals to estimate performance under various solar geometries. The model treats the instrument as a linear system, where the input, S, is a spectral radiance profile represented by Stokes vectors with units [photons $\cdot$ cm^{-2} $\cdot$ sr^{-1} $\cdot$ nm^{-1} $\cdot$ s^{-1}]. The output from the system, O, is the expected detector count digital number (DN) per second that ALI would measure in [DN$\cdot$ s^{-1}]. This model is based upon optical material properties, optical design parameters and select characterized responses described above. All parameters used in the model are wavelength dependent, and therefore we will omit explicitly describing each parameter as a function of wavelength.

The passive transmission, T_p, through the instrument is first calculated based on physical properties of the optical components. Refractive components are considered independently, and the transmission is calculated based on indices of refraction, Fresnel reflection coefficients on uncoated surfaces, and internal transmittance scaled to the center thickness of each element. Reflection coefficients are estimated for the reflecting surfaces based on the average incident angle on the element. The passive transmission is on the order of 19% - 36% over

the wavelength range.

The performance of the AOTF is simulated based on the internal diffraction efficiency measurements presented in Figure 4.8b. Similarly, the performance of the detector is simulated by the quantum efficiency, QE [$e^- \cdot photon^{-1}$], provided by the manufacturer. The performance of the detector is dominated by high responsivity in the NIR region, with reasonable performance from 600 - 900 nm. Additionally, the electron well depth in low gain is used to determine the conversion factor from electrons to DN, C_{DN}. The polarization response is modelled using the g_{12} and g_{13} parameters derived from the characterization measurements.

Specific optical design properties are also included in this model. The effective area, A_{eff}, of the aperture is calculated using the magnification of the telescope and the aperture area of the AOTF. Additionally, the instantaneous field of view is calculated based on the focal length of the imaging optics and the detector pixel size, which in turn is used to find the solid angle, SA_{pix}, each pixel sees. The final remaining parameter required by the model is the bandpass, BP, shown in Figure 4.7 as measured in the lab. The spectra used to calculate the bandpass are multiplied by a high spectral resolution input radiance spectrum and integrated over wavelength to account for the spectral resolution of the instrument. The simulation model can be summarized mathematically as,

$$O = T_p \cdot IDE \cdot QE \cdot C_{DN}^{-1} \cdot A_{eff} \cdot SA_{pix} \cdot \int BP \cdot \begin{bmatrix} 1 & g_{12} & g_{13} \end{bmatrix} S d\lambda. \tag{4.8}$$

The terms in Equation (4.8) are summarized in Table 4.3, with associated parameter value ranges. This instrument model is used to estimate exposure times based on typical input radiance profiles as calculated by the radiative transfer model SASKTRAN [Bourassa et al., 2008b]. This radiative transfer code is used to estimate solar scattering based on defined properties of a spherical atmosphere. These properties include profile distributions of atmospheric gasses, trace gasses, clouds and aerosol. The code estimates scattered radiance by tracing rays from a defined solar position into the atmosphere, and models multiple scattering and ground reflection events into a defined line of sight. Typical estimates of late summer mid-latitude atmospheric properties are used to estimate the radiance that is scattered into the ALI field of view as it measures from a 35 km balloon float altitude above Timmins, Canada in August[Hedin, 1991, Labow et al., 2015, Thomason et al., 2018].

Table 4.3: Instrument Model Properties

Symbol	Parameter	Value
T_p	Passive Transmission	$0.19 - 0.36$
IDE	Internal Diffraction Efficiency	$0.1 - 0.9$
QE	Quantum Efficiency	0.1 - 0.81 $e^{-1} \cdot photon^{-1}$
C_{DN}^{-1}	Electron to DN Conversion Factor	36.68 $e^- \cdot DN^{-1}$
A_{eff}	Effective Aperture	0.444 cm^2
SA_{pix}	Pixel Solid Angle	8.54 $\times 10^{-8}$ sr
BP	Bandpass	2 - 13 nm
S	Spectral Radiance	10^{11} - 10^{14} photons $\cdot$ $cm^{-2} \cdot sr^{-1} \cdot nm^{-1} \cdot s^{-1}$
g_{12}	Mueller matrix element	$\approx$ 1 or -1
g_{13}	Muller matrix element	-0.5 to 0.5

4.4 Stratospheric Balloon Demonstration Flight

4.4.1 Flight Description

ALI was tested in its designed environment in August, 2018 from Timmins, Canada. The instrument was carried on board the CARMEN gondola as part of a stratospheric balloon campaign led by the Canadian Space Agency and the Centre national d'etudes spatiales. The 10.5-hour flight provided 3 hours of atmospheric illumination where images were captured at stable float altitude of 37 km above the Earth. Throughout this observation period, the instrument repeatedly performed multi-spectral observation, capturing images at 24 tuned wavelength channels for both LP states. Wavelength channels were selected to avoid strong absorbing features in the atmosphere caused by trace gasses like CH_4, CO_2, H_2O, NO_2, O_2 and O_3 [Gordon et al., 2017].

4.4.2 Balloon Measurements

A full frame sample image captured during the flight is displayed in Figure 4.10. The only corrections applied to this image are the removal of dark current and the conversion from vertical pixel numbers to tangent altitudes. In this image, we observe fine cloud structure below 12 km. We also see a region of increased signal level between 12.5-25 km, which highlights the scattering due to aerosol.

The Level 0 images captured during the flight are processed using the calibrations described in the previous section. A dark current correction is first applied, then the flat field calibration masks are used to convert the detector counts into units of radiance. The field of view properties and viewing geometry are used to relate pixel rows to tangent altitudes. Finally, the center ten columns are averaged to generate Level 1 radiance profiles. Figure 4.11 shows radiance profiles captured in Scan #10 from the flight.

The behaviour of the calibrated radiance observations highlights many features that validate the performance of the instrument. We observe in the region above 12.5 km an exponential decay in radiance, corresponding to the typical atmospheric density profile. We also notice specifically at longer wavelengths, a deviation from this exponential decay occurs

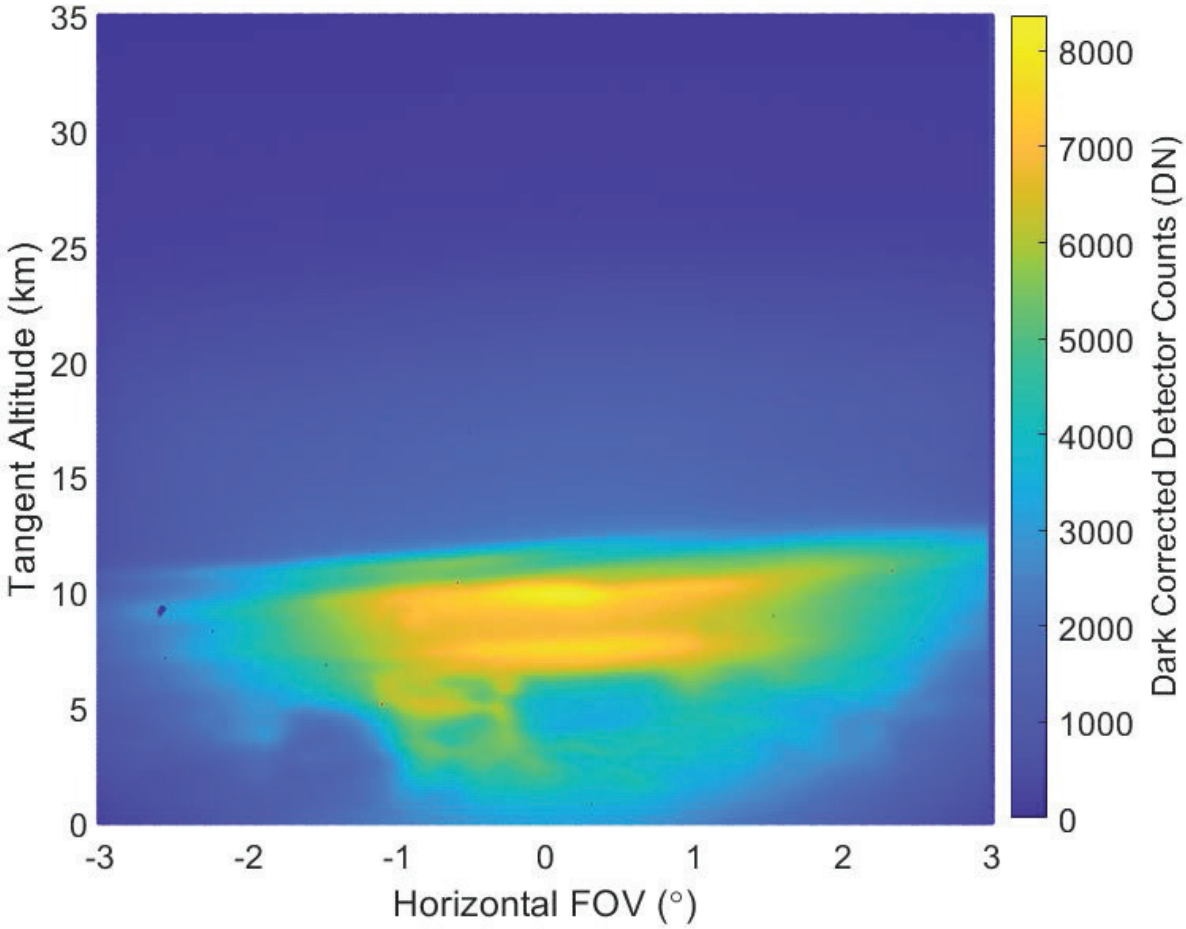

Figure 4.10: Sample measurement taken from 48°41'39.8"N, 83°48'17.3"W, altitude 36.6 km, at 12:55:14 UTC on 08/26/2018 . Solar Zenith Angle = 36.8°. Wavelength channel 1025 nm, LCR off.

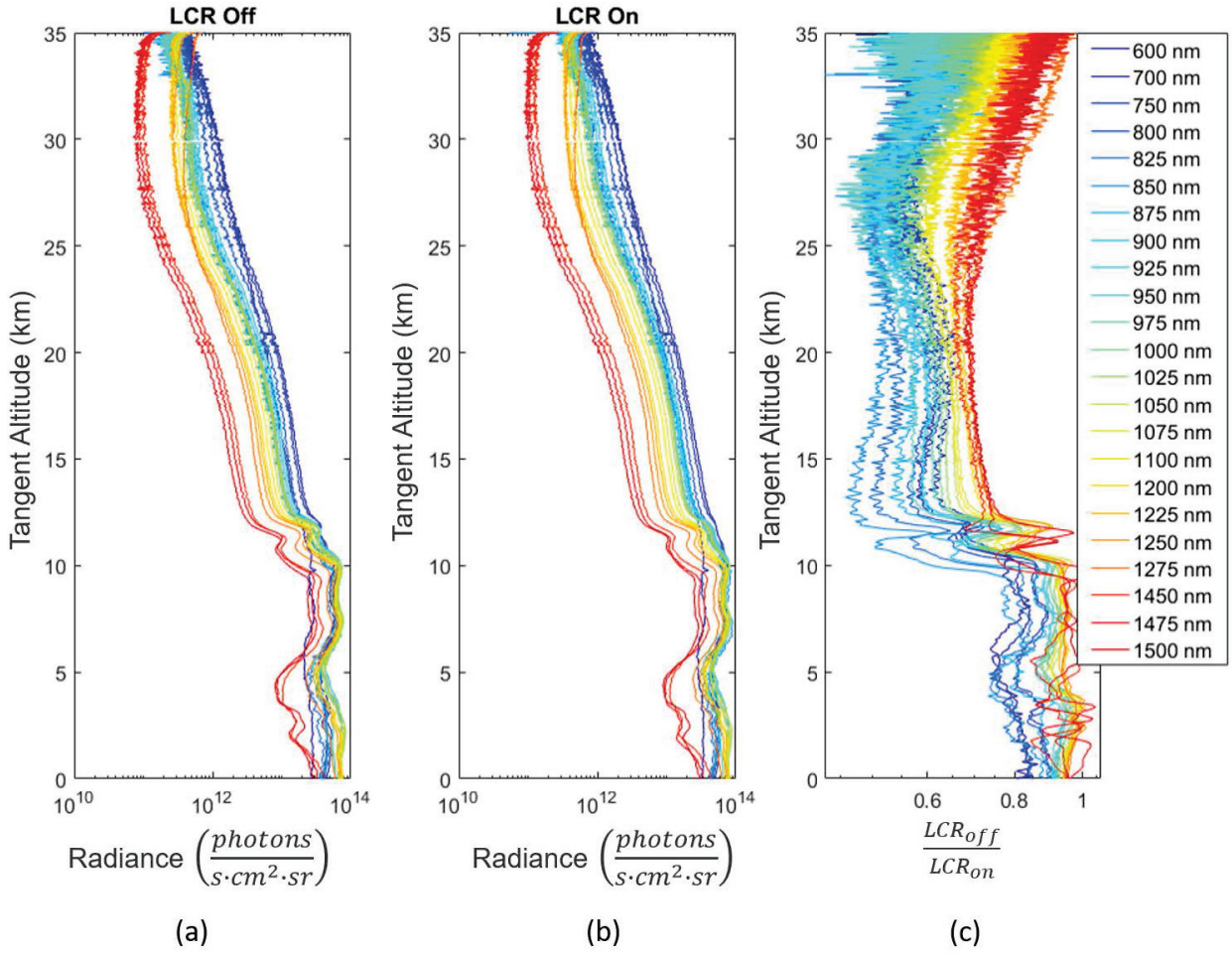

Figure 4.11: Level 1 data product from multi-spectral scan #10, Measurements taken near 48°41'39.8"N, 83°48'17.3"W, altitude 36.6 km, between 12:54:30 and 12:58:30 UTC. Solar Zenith Angle near 37° (a) LCR off. (b) LCR on. (c) Ratio of LCR off to LCR on.

between 12.5-25 km. As stated earlier, this indicates the presence of stratospheric aerosol in the sampled atmosphere. Furthermore, we see that as the channel increases, the radiance decreases. This is typical of an atmosphere exhibiting Rayleigh (molecular) and Mie (aerosol) scattering. The ratio of the two polarization states measured at each channel is shown in panel (c). We see a step change in the ratio at 12 km, corresponding to cloud coverage as we saw in Figure 4.10. Below 12 km, the ratio of the polarization states approaches 1, caused by the unpolarized nature of cirrus cloud scattering.

The slight increase in radiance at the highest measured altitudes suggests that there is some stray light contamination occurring. This issue is seen most clearly in the longer wavelength channel measurements, resulting from the wavelength dependence of Rayleigh scattering. It should however be noted that the strong increases in radiance for the 1250 nm and 1275 nm profiles are related to singlet delta oxygen emission, which peaks in a layer in the upper stratosphere [Noxon and Jones, 1962], rather than stray light.

4.4.3 Instrument Model Validation

Measurements from the balloon flight are used to validate the instrument model described previously. Aerosol concentrations are extracted from the GloSSAC climatology [Thomason et al., 2018], along with other typical atmospheric state parameters to generate polarized radiance profiles with SASKTRAN. These profiles are used to solve Equation (4.8). Figure 4.12 compares the measured and modelled instrument performance.

The modelled instrument response uses the 50^{th} percentile aerosol concentration from the GloSSAC climatology. Error bounds on the modelled response are generated using the 10^{th} and 90^{th} percentile concentrations. We find relatively good agreement between the measured response within the range of the modelled response. This is not meant to be a precise calculation as the atmospheric state is unknown; this shows that with typical atmospheric parameters, the instrument simulation model is able to quantitatively predict reasonable signal levels. As noted previously, singlet delta oxygen emission near 1270 nm results in an under predicted response for nearby channels. Additionally, we see that the 950 nm channel is impacted by H_2O absorption [Büning-Pfaue, 2003], resulting in an over prediction of the response. We also note a region of over prediction for channels below 900 nm, which is likely

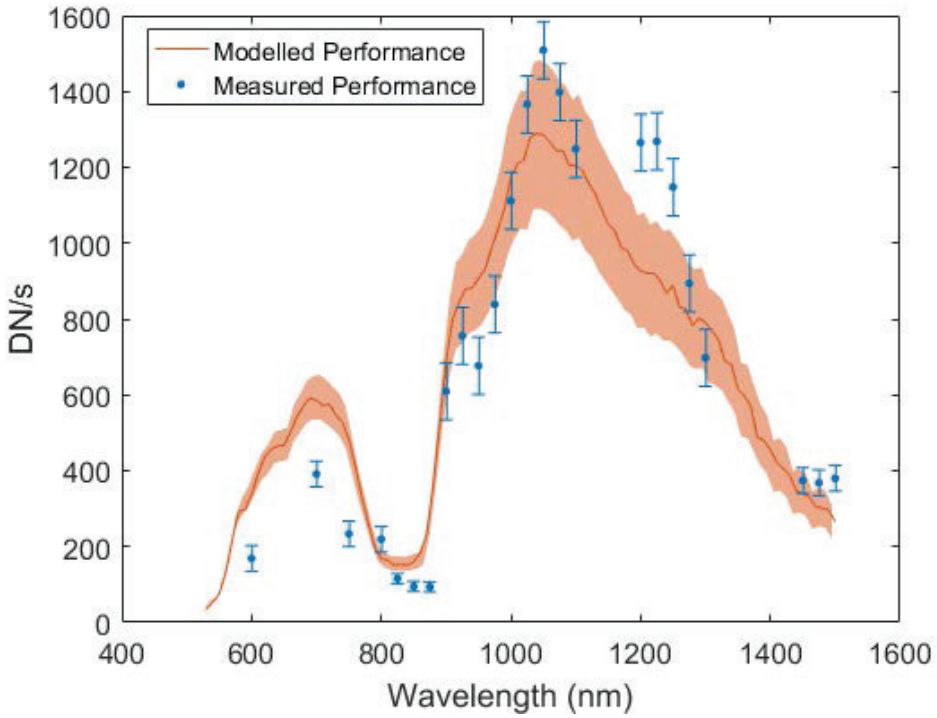

Figure 4.12: Comparison of modelled and measured instrument response at 20 km.

related to the quantum efficiency of the instrument detector.

4.5 Conclusion

A new prototype of the ALI instrument has been built and characterized. This prototype offers several improvements over its predecessor. The folded optical design reduces the overall instrument footprint, while offering improved chromatic performance. The spectral sensitivity is also greatly improved through the use of a dual channel AOTF, extending from the visible to NIR spectrum. This sensitivity to wavelength channels longer than 1200 nm will allow for greater insight into microphysics properties of aerosol distributions. Lastly, the pairing of a LCR with an AOTF offers exciting opportunities to study interactions between cloud and aerosol structures.

The advanced ALI prototype has been successfully deployed on a stratospheric balloon platform to capture multi-spectral images from a 37 km float altitude. Measurements from this flight represent some of the first spectrally resolved, polarized images in the limb viewing

geometry. Measurements of the 20 km tangent altitude have been compared against modelled results with aerosol concentrations predicted by the GloSSAC climatology to validate the predicted signal levels of the instrument.

Continued instrument development is planned to increase throughput to allow the ALI instrument to meet driving scientific requirements of resolution and signal to noise from a low Earth orbit satellite. These additional instrument studies will increase the technology readiness level of ALI for the eventual realization of orbital based remote sensing.

4.6 Data Availability

The data that support the findings of this study are available from the corresponding author upon reasonable request.

Chapter 5

Adaptation of the Polarimetric Multi-Spectral Aerosol Limb Imager for High Altitude Aircraft and Satellite Observations

The initial ALI prototypes have demonstrated the measurement of spectrally resolved two-dimensional images with fine vertical resolution using acousto-optic technology. Furthermore, pairing this technology with a liquid crystal device has added the capability to measure a second polarization state in the limb scattered viewing geometry. This manuscript furthers the ALI development to demonstrate its capabilities on a moving platform, which better simulates the ultimate orbital platform required for global monitoring.

The ALI elegant breadboard has been funded through the Space Technology Development Program from the Canadian Space Agency. Research and hardware development for this prototype is led by this work, and represents a collaborative effort between the University of Saskatchewan and Honeywell Aerospace. The instrument is designed to be flown on an aircraft, nominally NASA's ER-2 High Altitude laboratory. This platform will provide a spatially varying image scene, which is much different from the static scenes captured by the previous balloon missions. Improved spectral throughput is required to accommodate this change in the image scene, so a state-of-the-art 20 mm $\times$ 20 mm AOTF is baselined in the design. This AOTF aperture size offers a four-fold increase in throughput compared to the predecessor designs and is necessary to achieve signal-to-noise ratio and spatial sampling requirements for the mission.

The design of the ALI EBB highlights further advancement towards an orbital-based design, featuring methods and approaches typical of space instruments. These include en-

hanced thermal regulation and characterization, improved optical prescription requirements and build tolerancing and detailed stray light analysis. The manuscript concludes by detailing design modifications to make the instrument suitable for the space environment.

This manuscript has been published in Applied Optics, and unless otherwise stated the version presented here is unchanged. The layout of figures and equations and the format of cross-references has been modified to match that of the overall document.

Kozun, M. N., Bourassa, A. E., Degenstein, D. A., Haley C. S., Zheng, S. H. (2021). Adaptation of the polarimetric multi-spectral Aerosol Limb Imager for high altitude aircraft and satellite observation. *Appl. Opt. 60,* 4325-4334. doi:10.1364/AO.419249.

5.1 Abstract

An elegant breadboard prototype of the Aerosol Limb Imager (ALI) has been developed to meet key performance parameters that will meet requirements for the retrieval of aerosol from the upper troposphere and stratosphere from limb scattered sunlight radiance measurements. Similar in concept to previous high altitude balloon based generations, this instrument pairs a liquid crystal polarization rotator with an acousto-optic tunable filter to capture polarimetric multi-spectral images of the atmospheric limb. This design improves the vertical resolution, signal to noise ratio and athermalization, all of which will facilitate observation from a moving high altitude aircraft platform, which provides an analogous platform to the spatially varying measurements that would be made from a satellite. Finally, a preliminary design is presented for a satellite-based generation of ALI.

5.2 Introduction

The Aerosol Limb Imager (ALI) is a multi-spectral, dual-polarization, imaging system being developed as a future satellite instrument through a collaboration between the Canadian Space Agency, the University of Saskatchewan, and Honeywell Aerospace. This imager is used to measure the spectrum of scattered sunlight from an atmospheric limb viewing, or side-viewing, geometry. Spectrally resolved images with high vertical and horizontal spatial

resolution are obtained using an acousto-optic tunable filter (AOTF) operating over a wavelength range from 500-1500 nm. Dual linear polarization states are captured by coupling a liquid crystal polarization rotator (LCR) to the AOTF. Rapid cycling of the polarization and wavelength selection along the satellite track allows ALI to capture fine cloud structures and aerosol distributions with retrieved properties like aerosol extinction with unprecedented resolution from a passive sensor.

Recently, prototype models of the instrument concept were developed and successfully tested onboard high altitude balloon platforms. The first generation, detailed in [Elash et al., 2016], used a fully refractive design and was limited to a spectral range of 600-1000 nm and a single linear polarization state. A more advanced prototype that demonstrated the dual polarization capability and greatly extended the spectral range to 600-1500 nm is presented in [Kozun et al., 2020]. This instrument also advanced the optical design to utilize folded, reflective optics. These prototype models demonstrated the feasibility of the multi-spectral and dual polarization concept for cloud and aerosol but, by design, did not attempt to reach the signal level and image quality needed to meet scientific requirements from low Earth orbit.

In this work we present the optical design and modelled performance for an ALI instrument that is specifically motivated by compliance to scientific requirements. This optical design, which was funded through the Canadian Space Agency's Space Technology Development Program is referred to as the Elegant Bread-Board (EBB) model. As part of the program to advance the technological readiness of the instrument, the instrument is targeted for a test flight on the NASA ER-2 aircraft. The instrument will be installed in a forward facing wing pod on the aircraft to make along-track measurements. This is a similar viewing geometry that that used by the Spatial Heterodyne Observations of Water instrument flight in 2017 [Langille et al., 2019]. The satellite based requirements are mapped to requirements for the aircraft viewing geometry, which leads to an optical design unique to this platform, but not drastically different from that needed for an orbital instrument. Further, methods and procedures typical of orbital applications are implemented throughout the design and build of the instrument in anticipation of a future satellite model.

This paper describes the requirements set for the design of the ALI EBB and highlights the

key subsystems designed to meet these requirements. Special attention is given to the Spectral and Polarization Selection (SPS) subassembly. Next, an overview of the optical analysis is presented to justify the instrument performance both under nominal design conditions but also with allocations for manufacturing and build tolerances and environmental conditions. We will focus primarily on the vertical resolution and signal to noise ratio (SNR) expectations, as these are key performance indicators for this project, with attention also focused on the stray light performance. Finally, the EBB design is compared to a preliminary design for a satellite platform to highlight similarities in the design and build approach.

5.3 Instrument Design

The requirements for the ALI EBB have been substantially refined beyond those used to design the first two prototypes. Increased focus on key imaging parameters such as vertical resolution and SNR are described to meet the specific science objectives. The driving instrument design requirements are:

- Capability to measure limb radiance on the tangent of the atmospheric limb from the surface to the aircraft flight altitude.
  - Cross-track Field of View (FOV) to match the vertical FOV.
- Along-Track multi-spectral sampling every 48 seconds/every 10 km.
  - 11 horizontally polarized wavelength samples spaced evenly between 500 nm and 1500 nm.
  - 3 vertically polarized wavelength samples at 750, 1020 and 1500 nm.
  - 1 zeroth order measurement with AOTF off for stray light measurement.
- Vertical altitude resolution < 100 m.
- Signal to noise ratio of the horizontal linear polarization state > 200 over all wavelength channels.
- Boresight stability of less than 10 arcseconds over an operating temperature range of -15°C to +40°C.
- Spectral resolution of 1.2% of the central wavelength with tuning stability within one

tenth of the spectral resolution over an operating temperature range of -15°C to +40°C.

- Stray light suppression for all first-order sources to maintain SNR of > 200.

5.3.1 Spectral and Polarization Selection

ALI achieves linear polarization state dependent multi-spectral imaging by pairing an AOTF with a twisted nematic liquid crystal polarization rotator. A LCR from ArcOptix S.A. is selected for the ALI EBB. The optical activity of an LCR is controlled by applying or removing a bias voltage across the cell. In the unpowered, relaxed state, the linear polarization state of transmitted light is rotated by a nominal angle, 90° for ALI. However, when a voltage is applied, the liquid crystal molecules align with the electric field and do not affect the polarization state of the light passing through [Schadt and Helfrich, 1971]. The spectral performance of the LCR is limited in comparison to the full spectral range of ALI, with only a subset of wavelength channels being rotated by 90°. Outside of this performance range, non-ideal but characterizable polarization effects are experienced. This does not limit the performance of ALI over the wavelength range.

An AOTF is a solid-state device offering tunable narrow band wavelength filtering when the Bragg diffraction criterion is met between incident photons and tuned phonons within specific crystals. Non-collinear AOTF devices allow for acceptance angles as large as 8° with full angular separation between the diffracted and unfiltered, 0^{th} order, signals passing through. Optical birefringence of the substrate is necessary for this angular separation and facilitates a 90° rotation of the incident linear polarization state. Further details about AOTFs are found in [Chang, 1974, Chang, 1975].

The AOTF selected for the ALI EBB is a 20 mm × 20 mm TeO_2 device fabricated by Brimrose Corporation of America. The device uses a dual transducer design to provide an extended operational wavelength range. The first transducer operates from 50 MHz to 100 MHz, resulting in diffraction over the 850 nm to 1500 nm range, the second transducer responds to 100 MHz to 200 MHz, diffracting the remaining 500 nm to 850 nm range.

The LCR and AOTF are incorporated into a single subassembly to mature its design and characterization independent of the rest of the ALI EBB. This unit is called the Spectral and Polarization Selection subassembly. The SPS also contains crossed linear polarizing

filters, placed before and after the AOTF, to select only a single input polarization state and to attenuate the 0^{th} order that passes through. These are "Outrageously Wide Lambda" polarizers from Meadowlark Optics performing from 300-2700 nm. The operation of the SPS is shown in Figure 5.1. The input linear polarizer is aligned to the ordinary polarization axis of the AOTF, and the output linear polarizer is aligned with the extraordinary axis, in order to pass the spectrally filtered signal. In Figure 5.1a, the LCR is in its unpowered state, which rotates the input polarization state by 90°. This means that the signal that was horizontally polarized in the atmosphere will pass through the first linear polarizer and be spectrally filtered by the AOTF. In Figure 5.1b however, the LCR is in its powered state, so it does not affect the passing polarization state. Here, the vertically polarized component of the atmospheric signal passes through and interacts with the AOTF.

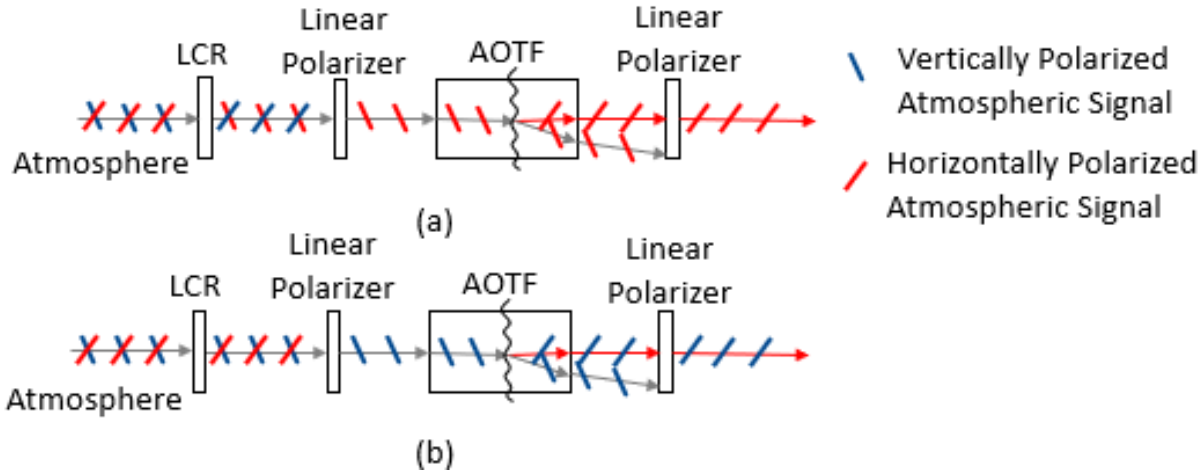

Figure 5.1: Spectral and polarization filtering performed by the SPS subassembly. (a) SPS response with an unpowered LCR. The atmospheric linear polarization state is rotated by 90° before passing the first linear polarizer. Spectral filtering results in a second 90° rotation, so the second linear polarizer filters out the broadband signal. Originally horizontally polarized signal is filtered through the SPS. (b) SPS response with a powered LCR. The atmospheric linear polarization state passes the LCR unchanged before the first linear polarizer. Spectral filtering and the second polarizer allow originally vertically polarized signal to be filtered through the SPS.

As discussed earlier, the Bragg diffraction criteria in non-collinear AOTFs is met by matching optical wave vectors in birefringent materials to an applied acoustic wave vector. The acoustic wave vector is defined by elastic properties within the medium, which are shown

to be temperature dependent [Silvestrova et al., 1987]. Temperature changes of an AOTF can therefore affect the tuning relationship between applied acoustic frequency and diffracted wavelength, as well as total diffraction efficiency [Mantsevich et al., 2015]. Therefore, the temperature of the SPS subassembly is actively maintained at approximately 22°C using a thermoelectric cooler, with feedback coming from temperature sensors placed on the SPS.

The structure of the SPS is primarily made of aluminum, with titanium flexures used for mounting to the EBB structure. An aluminum heat shunt is used to draw heat away from the SPS and EBB. The SPS subassembly design is presented in Figure 5.2.

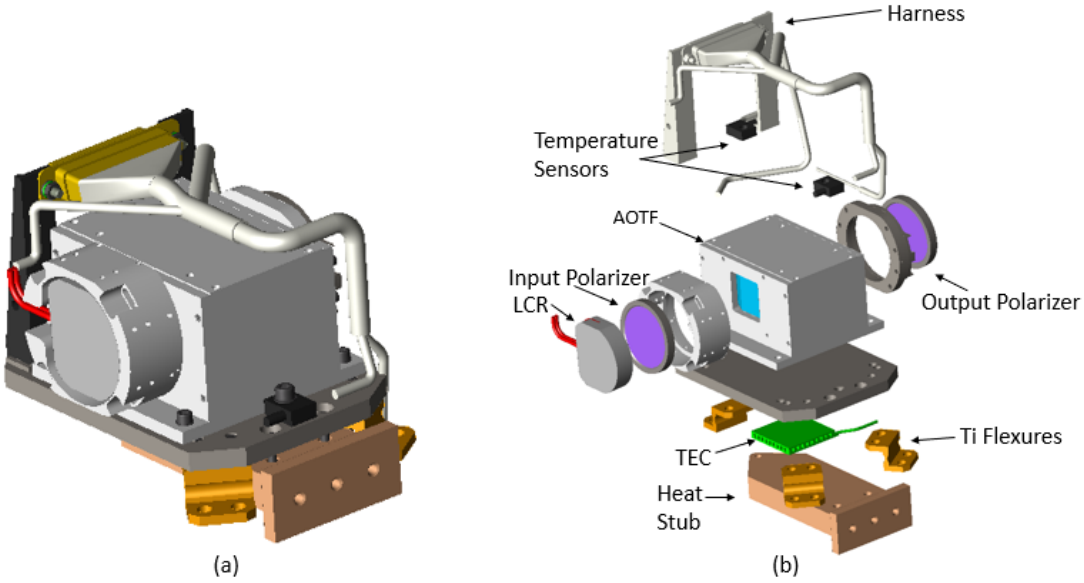

Figure 5.2: Spectral and Polarization subassembly. (a) Standard view. (b) Exploded View.

5.3.2 Reflective Design

The ALI EBB optical design is presented in Figure 5.3. All optical elements aside from the SPS are reflecting elements, primarily to achieve highly achromatic performance. The mirrors are single point diamond turned surfaces made of 6061-T651 Aluminum alloy. These mirrors provide athermal performance with low surface roughness.

The front-end telescope, shown in Figure 5.3a, is designed with two matched off-axis

parabolic mirrors and a planar fold mirror acting as a field stop at the common focus, which limits out of field stray light from propagating through the telescope. Unlike previous generations, no magnification is required from this telescope, because both the vertical FOV and the AOTF acceptance angle are 5°.

A common axis three mirror anastigmat (TMA) is used for imaging the filtered beam from the SPS, displayed in Figure 5.3b. The primary and tertiary mirrors have a common vertex, so both can be cut on the same diamond lathe configuration, aiding in alignment. This imaging system is paired to a Raptor Owl 640 camera, which incorporates a visible extended InGaAs detector with responsivity from 400–1700 nm.

A two-mirror periscope is designed to pair the input telescope to the SPS. Although this periscope provides no optical improvements, it folds the optical plane up and over itself to reduce the structural footprint, seen in Figure 5.3c. Additionally, the periscope provides compensation degrees of freedom for aligning the front and back end systems. The full optical ray trace is finally shown in Figure 5.3d.

5.3.3 ALI EBB

The opto-mechanical structure of the ALI EBB is made of 6061-T651 Aluminum alloy. The major structural components of the EBB are designed to be monolithic, to minimize structural interfaces. Conventional machining is used for all components, except for mirror interface pads which are diamond turned to reduce distortion of the mirrors upon torquing. The input telescopic optics chassis is the largest and most robust structure, and serves as an optical bench for the entire instrument. The opto-mechanical design of the ALI EBB is shown in Figure 5.4.

5.4 Instrument Performance

The performance of the ALI EBB is assessed according to several optical and mechanical criteria, related primarily to the key requirements highlighted previously.

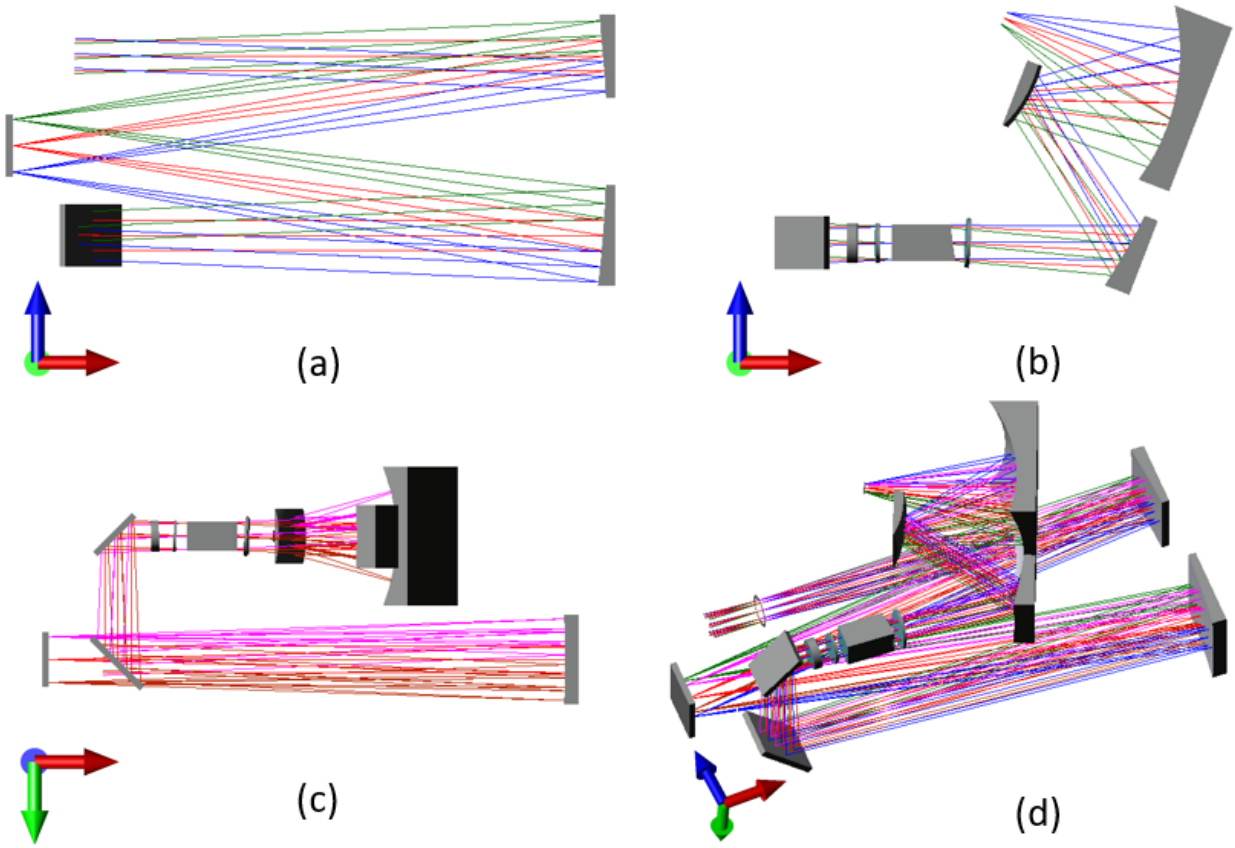

Figure 5.3: ALI EBB Optical Layout. (a) Top view of input telescope and first periscope fold. The input aperture is in the upper left of the frame. (b). Second periscope fold, SPS and camera TMA. (c) Side view of ALI EBB showing two horizontal optical planes. (d) Isometric view of ALI EBB. Input aperture is in the center left of the frame.

5.4.1 MTF and Vertical Resolution

Two key imaging performance parameters that are assessed are the modulation transfer function (MTF) and the encircled energy as it relates to resolution at the atmospheric limb.

The MTF of the ALI EBB optical design is shown in Figure 5.5. The InGaAs detector has 15 μm pixels, so the cutoff spatial frequency with dual pixel binning is 33.3 cycles/mm. Hence, we present the MTF to a maximum spatial frequency slightly above the cutoff frequency. For each wavelength, the diffraction limit is drawn with a dashed line, and the simulated MTF for various fields are shown in solid lines. The system performs near the diffraction limit over all wavelengths and fields. We also note good contrast, with an MTF greater than 0.6 for spatial frequencies up the detector cutoff.

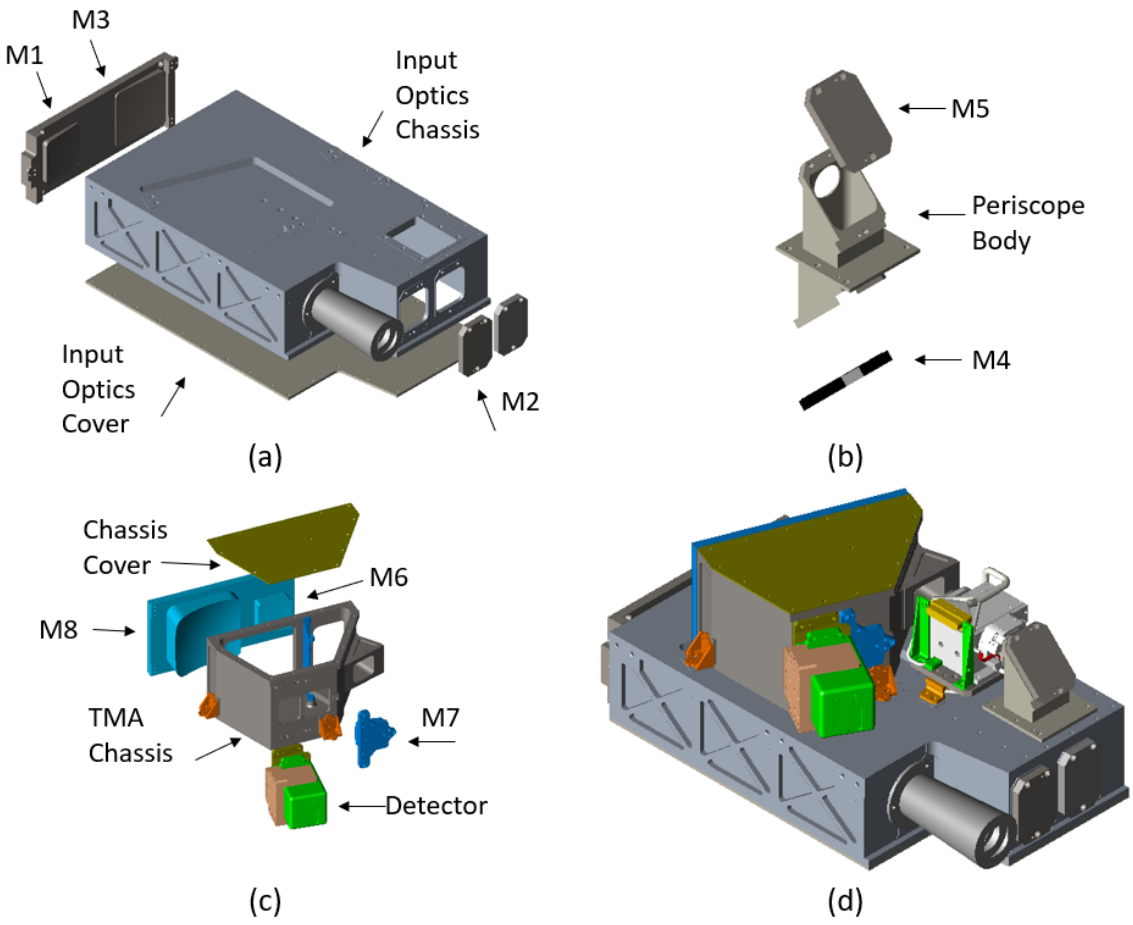

Figure 5.4: ALI EBB Optomechanical design. (a) Input optics subassembly. (b) Periscope subassembly. (c) Camera TMA subassembly. (d) ALI EBB Assembly. Input optics chassis acts as an optical bench for the other subassemblies, including the SPS shown in Figure 5.2. Note that an additional baffle hood (not shown) is added around the periscope and SPS to shield these from the surroundings.

To estimate the instantaneous vertical resolution, the spatial response of the image captured by the detector is first estimated. The point spread function (PSF) is modelled as a Gaussian with a variable full width half max (FWHM). This is convolved with a boxcar function representing a single 15 μm pixel, which describes the spatial resolution in image space.

The image space spatial resolution is next mapped into the atmospheric object space in the limb viewing geometry, shown in Figure 5.6. Assuming a 22 km flight altitude, the center of the vertical field of view strikes a tangent altitude height of 11 km at a distance of 374.9

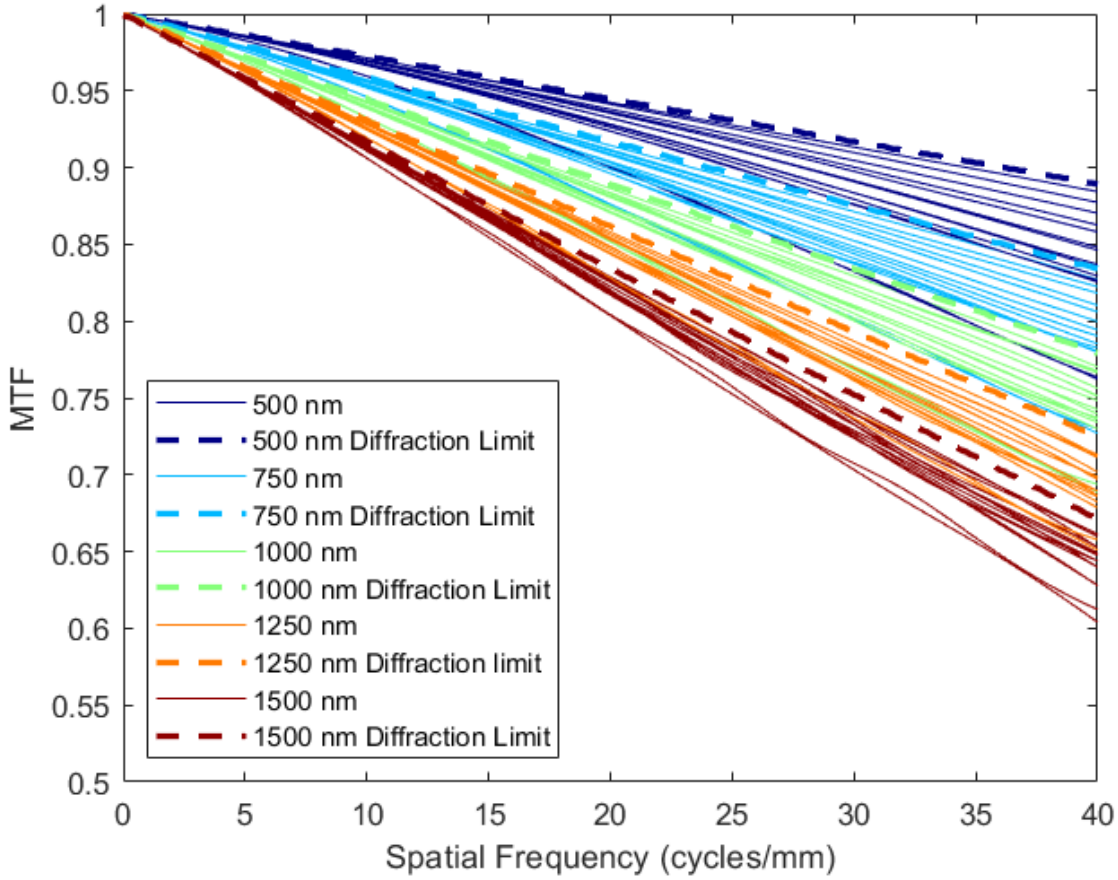

Figure 5.5: Optical modulation transfer function of nominal ALI EBB optical design. The detector cutoff spatial frequency is 33.3 cycles/mm. Solid lines represent the MTF for select fields over the FOV.

km from the instrument. At this distance, the instantaneous field of view of a pixel represents a vertical distance of 63.9 m. This scaling factor is used to map the variable image space spatial resolution into an atmospheric vertical resolution, shown as a solid line in Figure 5.7a.

To model the instrument performance, the image space spatial resolution is simulated with ray tracing software. The FWHM of the PSF is equated to the 50% encircled energy for various wavelengths and fields in the ALI optical model. The corresponding vertical resolution for sampled fields and wavelengths are highlighted in Figure 5.7a. The 50% encircled energy metric is selected because it provides the ability to compare the encircled energy between the nominal design, the thermally distorted design and the assumed as-built performance based on part manufacturing and build tolerance simulations. These three conditions all help

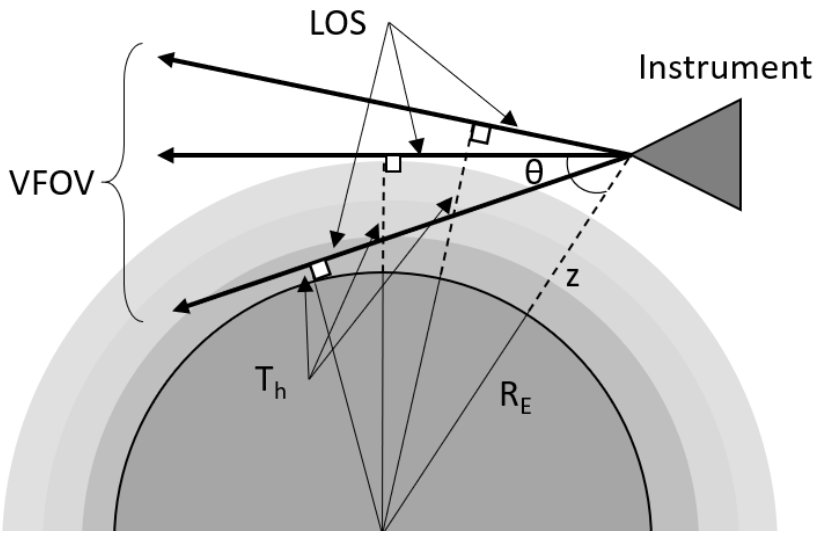

Figure 5.6: Limb viewing geometry. The vertical field of view has several lines of sight, based on pixel binning. Each line of sight makes a measurement at a unique tangent height.

estimate the expected instrument performance. The 50% encircled energy for all wavelengths and fields is below 8.5 μm for the nominal design, which translates to a vertical resolution less than 67.2 m, shown in Figure 5.7a. A tolerance analysis using manufacturing and build tolerances listed in Table 5.1 is used to calculate a 1σ change in the 50% encircled energy. The corresponding vertical resolution is shown in Figure 5.7b.

There is a significant wavelength dependence in the vertical resolution, but also a field dependence, which is less obvious in Figure 5.7b. The wavelength response is driven by diffraction effects. The field dependence is a result of the off-axis nature of the camera TMA with a gradient observed in the off-axis direction, which is particularly sensitive to tip and tilt of the camera TMA mirrors. An additional effect which impacts spatial resolution in AOTFs is image blur caused by divergence of the acoustic beam as it travels through the finite sized TeO_2 crystal [Sivanayagam and Findlay, 1984]. This divergence changes the properties of the momentum matching condition in the direction of the diffraction [Gupta and Voloshinov, 2007, Suhre and Gupta, 2005]. The diffraction direction of the AOTF has been aligned with the cross-track dimension of the atmospheric limb. The impact on the vertical resolution is shown to be minimal and therefore does not impact this analysis [Zhang et al., 2016]. The worst-case vertical resolution we expect to see at 1500 nm is 86 m,

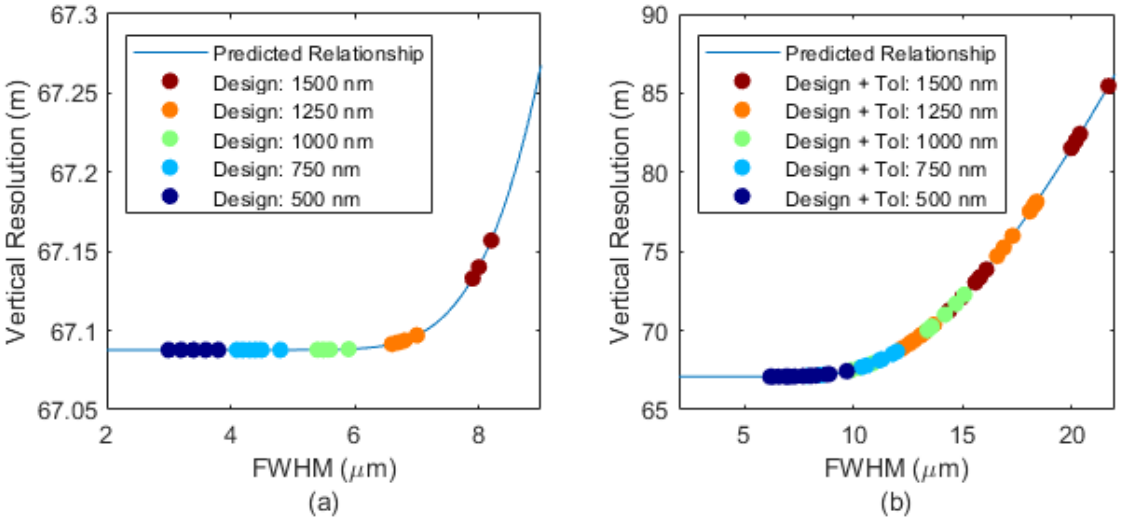

Figure 5.7: Relationship between the PSF FWHM and vertical resolution in the atmospheric limb from a flight altitude of 22 km. (a) The nominal vertical resolution is displayed for various field and wavelength combinations based on the 50% encircled energy of the ALI optical design. (b) Vertical resolution calculated from 1σ tolerance analysis of encircled energy

below the 100 m requirement.

The athermalization of the ALI EBB is tested using Structural Thermal Optical Performance (STOP) analysis. A finite element model of the ALI EBB is generated, and environmental heat loads are applied. It is assumed that the aircraft accommodation structure will maintain the operational temperature range of -15°C to +40°C. Representative heat loads are applied to the SPS and camera to induce thermal gradients to simulate operating conditions. The thermal results are mapped onto a structural node mesh to evaluate the distortions experienced by each optical element. The resulting structural distortions for the hot operating case are shown in Figure 5.8a. Finally, the nodal distortions are used to distort the optical model, and the resulting performance is evaluated. Figure 5.8b displays the vertical resolution predicted under the described thermal loading cases. When compared to Figure 5.7a, we find only a small variation in the vertical resolution under thermal loading, which validates the athermal optical design.

Table 5.1: List of manufacturing and build tolerances.

Tolerance Type	Value
Radius (mm)	0.025
Power (fringes @ 632.8 nm)	3.000
Irregularity (fringes @ 632.8 nm)	1.000
Refractive index	0.0005
Abbe number	0.005
Center thickness & airgap (mm)	0.050
Centering displacement (mm)	0.025

5.4.2 SNR

The retrieval of aerosol properties from atmospheric limb sounding images requires a signal to noise ratio of 200 or better. To validate the SNR, a mathematical model is used to estimate the performance of the instrument under variable atmospheric conditions. This model is based primarily on the optical design characteristics, theoretical diffraction efficiency of the AOTF and properties of the imaging detector. The assumptions for the SNR model are:

- f/4.35
- Theoretical optical transmission
- 15 µm pixel size
- Quantum efficiency described by Raptor Owl 640 datasheet
- Readout noise of 195 e^-
- Electronics noise of 10 e^- RMS/px
- Dark current of 100 e^-/px/s
- 14 bit analog-to-digital conversion
- Off-chip horizontal binning
- 50 ms single frame exposure time, with 11 frames co-added

The modelled optical transmission is based on standard reflectance curves for protected silver coated diamond turned aluminum mirrors, with consideration to polarization and in-

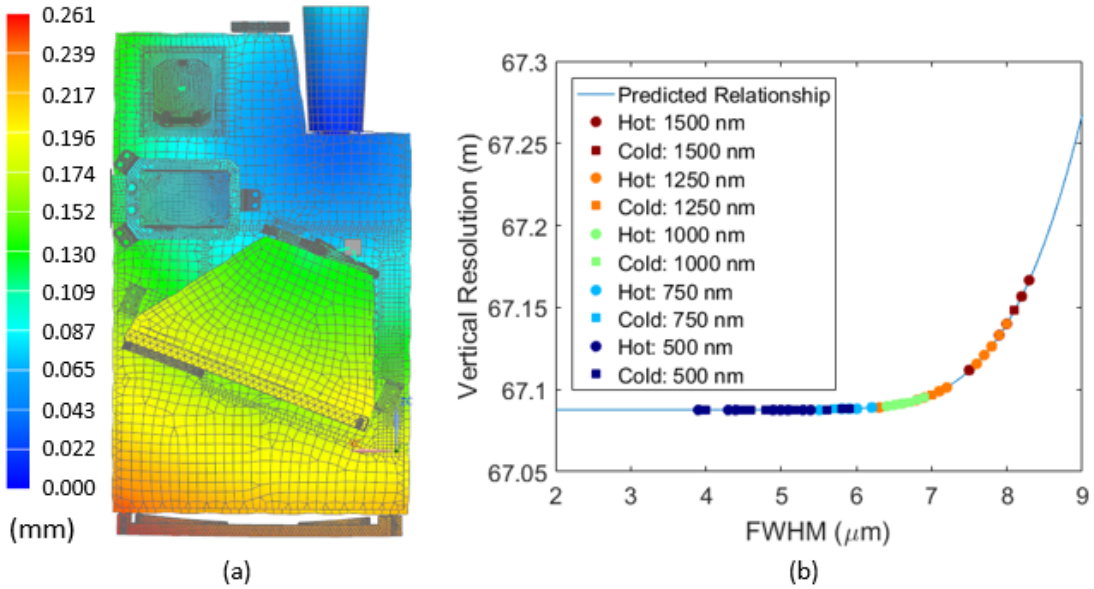

Figure 5.8: STOP analysis results. (a) Finite element model of ALI EBB shows the nodal displacements under the hot operating condition of +40°C. These distortions are used to build a representative optical model. (b) Vertical resolution estimated from the hot and cold operating case optical models, using the described method to convert PSF FWHM to vertical resolution.

cident angle. Transmission curves for the linear polarizing filters and LCR are also included, as well as the expected diffraction efficiency of the AOTF. The transmission of ALI is shown in Figure 5.9. The shape of the transmission curve is dominated by the diffraction efficiency of the dual transducer AOTF, producing a local maximum for each transducer. The diffraction efficiency drops significantly near the transducer cutoff frequency, which translates to a wavelength near 820 nm.

The optical signal is calculated in electrons for each pixel using the camera equation [Klein, 1986] and the optical system efficiency:

$$S_{px} = \frac{\pi I(\lambda) A_D \varepsilon(\lambda) \Delta\lambda(\lambda) \Delta t}{4(f/\#)^2 + 1}. \tag{5.1}$$

Here, $I(\lambda)$ is the input radiance in units of $photons/cm^2/s/sr/nm$ at the center wavelength λ. A_D is the pixel area, $\varepsilon(\lambda)$ is the optical system efficiency, which includes the transmission and detector quantum efficiency, $\Delta\lambda(\lambda)$ is the optical bandwidth of the AOTF and Δt is the exposure time.

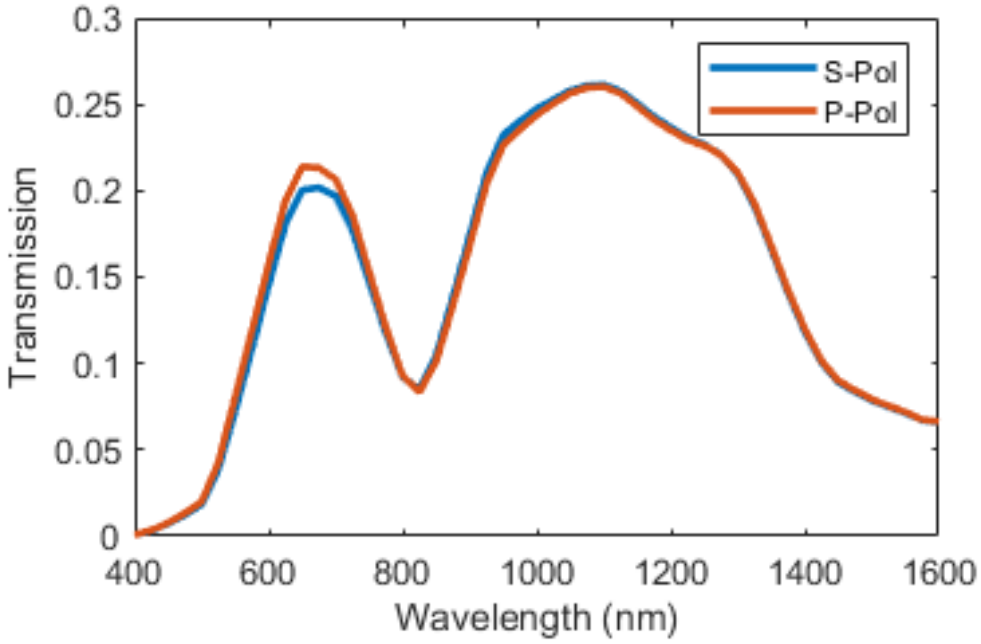

Figure 5.9: ALI EBB transmission. Spectral curves are generated using reflectance of 9 silver coated mirrors, transmission properties of polarizing filters and rotators, and diffraction efficiency of the AOTF. The mirrors have different reflection coefficients for S and P polarization states, which has a small impact on the transmission depending on the LCR state modelled.

Noise is calculated as

$$N_{px} = \sqrt{S_{px} + D_{px} + N_{ro}^2 + N_{elec}^2 + N_{dig}^2}, \tag{5.2}$$

where D_{px} is the pixel dark current, N_{ro} is the RMS readout noise, N_{elec} is the RMS electronics noise and N_{dig} is the digitization noise. The SNR is calculated as S_{px}/N_{px}. Off-chip binning modifies the SNR by the square root of the binning factor. Here, the horizontal field of view is binned into 1° bins, comprised of 102 pixels. The exposure times are set to capture 15 wavelength/polarization/calibration measurements per 10 km along track at an aircraft speed of 0.21 km/s.

The input radiance for the SNR calculation is produced by the SASKTRAN radiative transfer model [Bourassa et al., 2008b]. Two atmospheric conditions are tested, the first being a "clear" case including only effects from Rayleigh scattering, ozone and background aerosol levels, with a solar zenith angle of 60°, solar scattering angle of 90° and albedo of 0.3. The second case is a "signal enhanced" case, with aerosol loading similar to that

seen following the Nabro eruption in 2011 [Bourassa et al., 2012b], thick low altitude cloud coverage, and albedo of 1. The SNR for 14 polarization and wavelength channel pairs are shown in Figure 5.10.

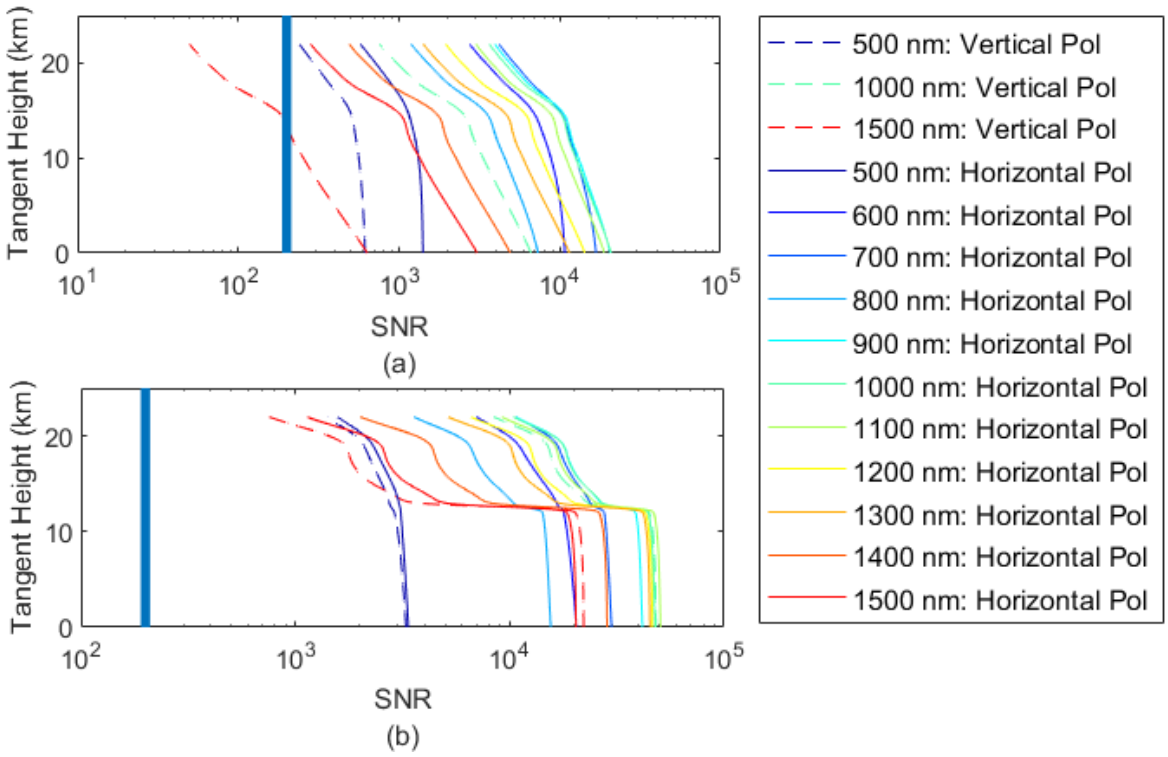

Figure 5.10: Simulated signal to noise ratio for ALI EBB under two aerosol loading conditions. (a) "Clear" case with contributions from Rayleigh scattering, Ozone absorption and background aerosol levels. (b) "Signal Enhanced" case with contributions from Rayleigh scattering, Ozone absorption and aerosol loading similar to that which followed the Nabro eruption in 2011 as well as thick, low altitude cloud coverage. SNR=200 threshold is marked in thick blue.

The SNR requirement is met for all horizontal wavelength channels except at the longest wavelength at the highest tangent heights. This suggests that vertical binning may be required in some cases in order to achieve the desired SNR. Note also that the SNR requirement only applies to the horizontal polarization state, as the vertical wavelength samples will be used for discrimination of ice clouds rather than aerosol property retrieval.

5.4.3 Stray Light

The narrow wavelength channel filtering of ALI makes it sensitive to stray light, requiring detailed stray light modelling. The stray light sources are categorized as either in-band or out-of-band based on their spectral features. The interaction at the AOTF differentiates these two sources.

The in-band contribution is diffracted through the AOTF and therefore propagates within the field of view of the detector following the SPS. This signal, referred to as the science signal, is susceptible to scattering dominated by the surface roughness and cleanliness of the optical surfaces. In this case, surface scattering from all surfaces, including those before the AOTF, are critical to monitor.

Out-of-band stray light is dominated by the 0^{th} order signal that passes through the AOTF undiffracted. This signal contains significantly more spectral bandwidth and is not affected by the diffraction efficiency of the AOTF. Although this signal is heavily attenuated by the second linear polarizer, the total integrated signal remains on a similar order of magnitude as the diffracted signal, and therefore needs to be managed appropriately within the camera TMA to reduce stray light contamination.

Two methods of stray light assessment are used. The first method is a Monte Carlo ray trace method using TracePro. This method is useful for validating stray light contributions through direct path analysis and monochromatic Point Source of Transmission (PST) analysis, as well as assessing ghosting in the SPS. The second method is a mathematical model used to simulate stray light contamination from the 0^{th} order signal passing through the SPS.

Monte Carlo Ray Trace

The structural model of the EBB shown in Figure 5.4 is imported into TracePro, where appropriate optical properties are applied to all surfaces. For the direct ray path analysis, all surfaces are either perfect specular mirrors, perfect transmitters or perfect absorbers. For the ghost analysis and PST modelling, mirror surfaces are modelled with reflectivity typical of protected silver and with reflected scattering defined by the RMS surface roughness of 9 nm. The ABg scattering model is used to define the BRDF of these surfaces. Similarly,

uncoated transmissive surfaces have transmission and reflection coefficients defined by the Fresnel equations, and scattering based on 2 nm RMS surface roughness. Non-optical surfaces have properties typical of bead-blasted black anodized aluminum [Marshall et al., 2014].

The direct ray path analysis is a reverse ray tracing technique that validates that no direct lines of sight to the detector or AOTF from outside of the field of view exist. Baffle vanes are strategically placed throughout the optical structure to limit these lines of sight, and an input baffle is included. This test validates that only fields within $\pm 2.5^\circ$ reach the input to the AOTF through the entrance aperture, and only fields within $\pm 2.5^\circ$ of the nominal diffracted beam reach the detector after propagating through the AOTF.

Ghosting analysis focuses specifically on the planar surfaces of the SPS. The broadband nature of ALI requires uncoated transmissive elements to be used. With several closely spaced flat surfaces, the likelihood of ghost production is unavoidable, however the AOTF, LCR, input polarizing filter and output polarizing filter are all tilted with respect to one another to minimize ghosts from reaching the detector from either the 0^{th} order or the science path.

PST analysis shows well behaved performance over several tested fields in the vertical and horizontal direction with respect to the boresight. Monochromatic PST tests are run for the desired science path signal, scattered science path signal and 0^{th} order scattered signal at discrete wavelengths. Figure 5.11 shows that the specular signal PST drops off beyond the designed FOV, and the scattered science path signal PST is more than 3 orders of magnitude lower than the specular signal. This scattering is dominated by the first mirror in the optical system, which may scatter light directly into the FOV of the AOTF. Finally, the 0^{th} order PST is more than 6 orders of magnitude lower than the specular science path and is dominated primarily by scattering from mirrors within the Camera TMA.

Mathematical Model

The narrow bandwidth filtering provided by the AOTF requires special attention to the broadband 0^{th} order signal that passes through the AOTF undiffracted, which is not captured in the monochromatic PST simulation presented previously. The attenuation of the two crossed polarizers in the SPS drastically reduces the 0^{th} order signal level, but the integrated spectral power is of a similar order to that of the diffracted science signal.

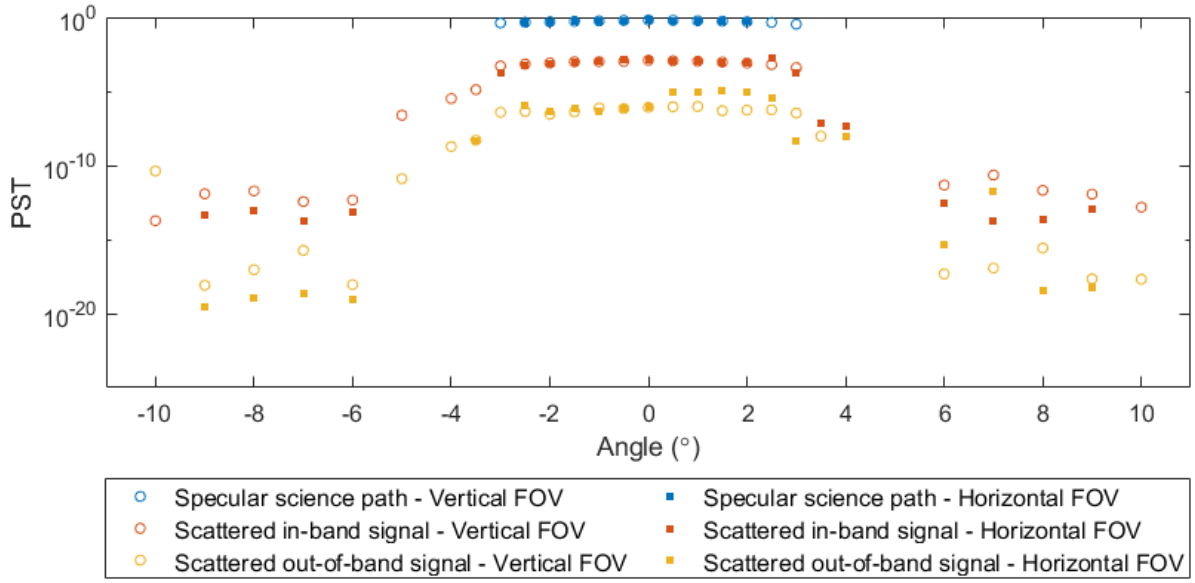

Figure 5.11: Stray light PST simulation covering vertical and horizontal fields extending beyond the designed field of view with monochromatic input. We find approximately 3 orders of attenuated magnitude for in-band, in-field stray light signal, and roughly 6 orders for out-of-band, in-field stray light signal. The contributions from outside the field of view all exhibit more than 6 orders of magnitude of attenuation.

The separation between the science path and 0^{th} order path is 6.3-7.3°. This is larger than the 5° field of view, which limits the chance of specular signal from the 0^{th} order landing on the detector. However, this signal does still have a direct view factor onto the primary camera TMA mirror, leading to three opportunities for scattering into the FOV:

1. Scattering from the primary into the detector FOV,
2. Specular reflection from the primary and scattering from the secondary into the detector FOV,
3. Specular reflections from the primary and secondary and scattering from the tertiary into the detector FOV.

The total integrated scatter (TIS) for mirror surfaces with 9 nm RMS surface roughness is used to characterize the stray light impact of each of these scattering cases. The TIS is calculated as

$$TIS(\lambda) = \left(\frac{4\pi\sigma}{\lambda}\right)^2, \tag{5.3}$$

where σ is the surface roughness. The largest TIS is 0.0512 at 500 nm.

An attenuation factor is calculated for the 0^{th} order under the three cases, using the illumination areas of the science path and 0^{th} order on each mirror in the TMA. This factor is the product of the ratios of these areas, A_{pri}, A_{sec} and A_{ter}, the solid angle of the detector at the scattering surface as a ratio of a full hemisphere, SA, and the TIS. The attenuation factors for the three scattering cases at 500 nm are 3.9×10^{-4}, 2.8×10^{-3} and 3.9×10^{-6} respectively.

To quantify the magnitude of the 0^{th} order stray light contribution, a similar model to the one described by the SNR calculation is developed to approximate relative intensities for various wavelength channels. This model uses the contrast ratios of the linear polarizers, the overall instrument transmission, and attenuation factors with wavelength dependence. Figure 5.12 shows the contribution of the 0^{th} order beam relative to the normalized expected filtered signal levels at several wavelength channels. The integrated 0^{th} order scattering levels fall below the modelled SNR requirement for all wavelength channels and tangent altitudes.

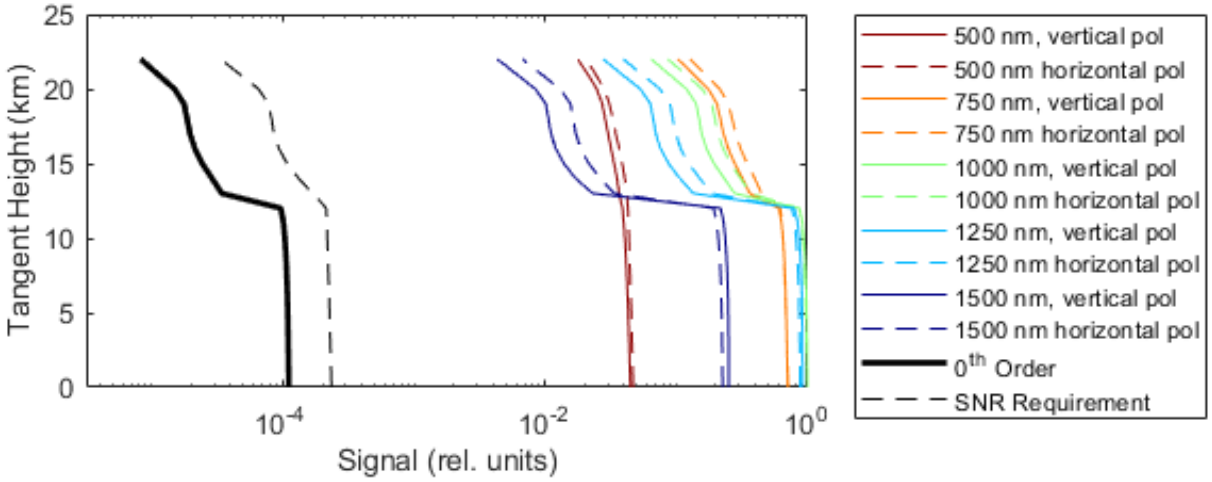

Figure 5.12: Mathematical model of broadband 0^{th} order stray light compared to simulated signal levels. The simulated levels have been normalized to show the rough order of magnitude of attenuation of the 0^{th} order beam that is expected to reach the detector. The minimum signal profile across all wavelength channels is calculated and reduced by a factor of 200 to simulate the SNR requirement. The 0^{th} contribution falls below this level for all tangent heights.

5.5 Adaptation for Satellite Based Remote Sensing

The eventual goal of the ALI instrument is to contribute to the global aerosol record from a satellite platform, with the EBB representing a necessary development model to increase the technology readiness level of the instrument. As noted, the methods and procedures for the design, build and alignment of the EBB are aligned with those required for an orbital instrument. Beyond these processes, the requirements for the ALI EBB are adapted from preliminary scientific requirements for a satellite-based ALI. The key requirements include:

- Capability to measure limb radiance on the tangent of the atmospheric limb from the surface to 40 km.
  - Cross-track FOV of 5° with a goal of 8°.
- Along-track multi-spectral sampling every 50 km with 15 wavelength/polarization channel cadence.
- Low altitude vertical resolution better than 250 m for tangent altitudes below 22 km, with a goal of better than 100 m.
- High altitude vertical resolution scaling from 250 m to a maximum of 3 km for altitudes above 22 km, with a goal of a 1 km maximum at the highest altitudes.
- Signal to Noise ratio for the horizontal linear polarization state > 200.

A fundamental difference between the EBB and satellite-based instrument is the field of view requirement. The EBB has common vertical and cross-track FOV specifications, so rotationally symmetric optics are implemented in the optical design. The vertical sampling requirements from a 600 km orbit are met with approximately 1° vertical FOV, while maintaining 5° in the cross-track direction. This requires anamorphic imaging optics paired with a high aspect ratio detector, which provides 300 km cross-track imaging at the tangent point.

An additional challenge when viewing from orbit over the larger tangent altitude range is the dynamic range required, which scales logarithmically with tangent altitude. A gradient neutral density filter is proposed with the highest optical depth targeting the lowest tangent altitudes. A preliminary layout for a satellite-based design is shown in Figure 5.13.

In the satellite layout, the two parabolic mirrors (a and d) in the telescope are offset and the fold (b) is moved away from the field stop. This has left room for a transmissive gradient

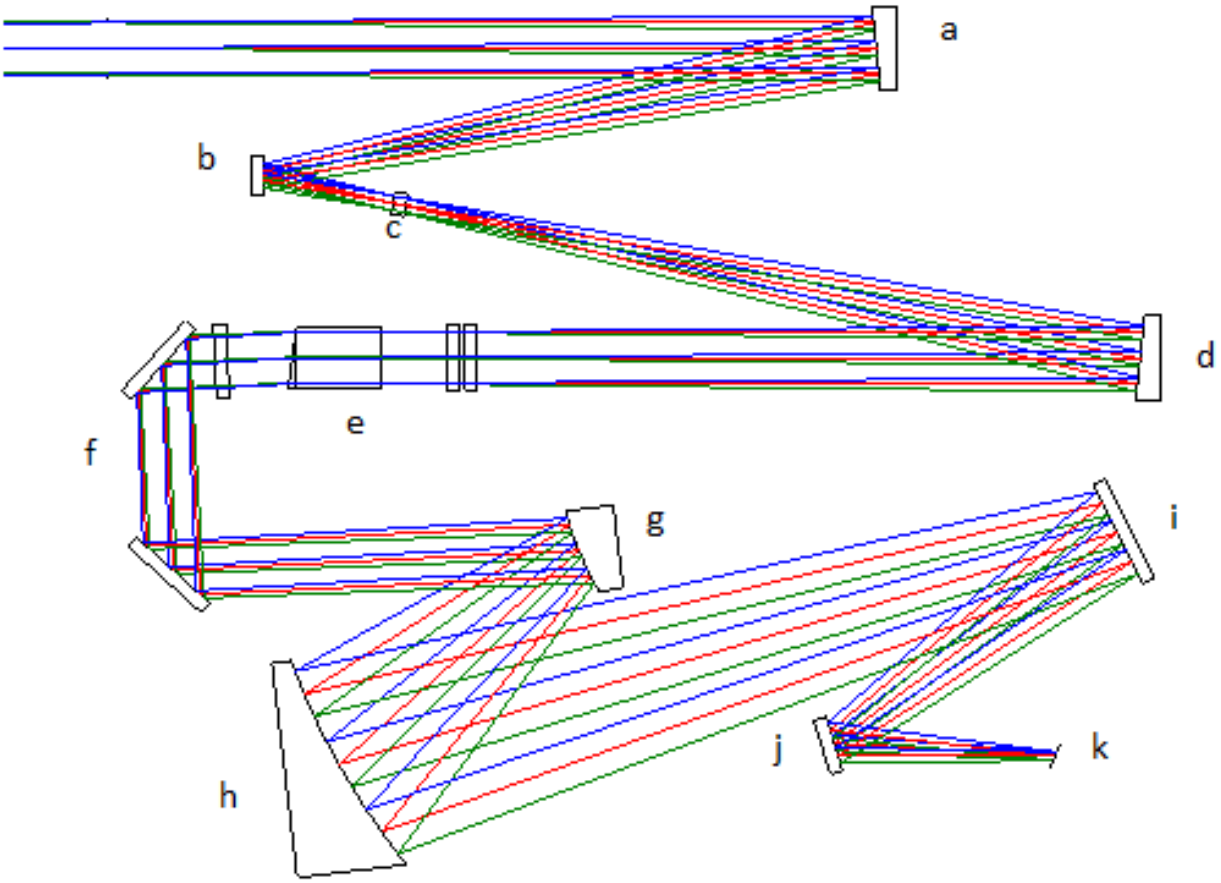

Figure 5.13: Optical design for ALI to meet requirements for orbital aerosol retrieval. This design highlights similar features to the EBB, with a telescopic input assembly, an SPS, periscope and an imaging assembly.

neutral density filter which will be mounted in a field stop (c). This stop will define the anamorphic field of view. The telescope is followed by an SPS layout once again utilizing an AOTF, LCR and linear polarizing filters (e). Here, the periscope has been rotated to keep the full optical system in a single plane (f). Finally, an anamorphic imaging assembly is designed with vertical and horizontal focal lengths of 188 mm and 141 mm respectively (g and h). Two fold mirrors (i and j) are included to optimize the detector location (k). This design is under continued development for a prospective future aerosol sensing mission.

5.6 Conclusion

The Aerosol Limb Imager has been designed as an Elegant Bread-Board to operate from a high altitude aircraft, using practices and procedures typical of an orbital mission. Building on the legacy of previous design architectures, this EBB represents an athermalized, nearly fully reflective instrument that will perform from a flight altitude of 22 km. A large aperture AOTF is paired directly with a liquid crystal polarization rotator and linear polarizing filters to comprise the spectral and polarization selection subassembly. This SPS subassembly is thermally stabilized to reduce temperature dependent wavelength drift in the spectral channel sampling.

The enlarged AOTF aperture helps boost the SNR of the ALI EBB far beyond the levels that the previous generations of the instrument achieved. At the reported levels, the system can operate from a mobile platform, which is key for assessing the distribution of aerosol and clouds over large horizontal distances. This platform provides a spatially varying scene analogous to one observed from orbit. This, combined with the large improvements in imaging capability make ALI a strong candidate to offer high quality vertical profiles, suitable for resolving fine structures in the atmosphere. Continued development and testing in a suborbital campaign will elevate the technology readiness level of ALI in order to become a viable global monitoring sensor for an upcoming satellite mission, with continued design work progressing to meet this goal.

Funding

Canadian Space Agency (9F063-140572/023/MTB, 9F063-160953/008/MTB).

Disclosures

The authors declare no conflicts of interest.

Data Availability

Data underlying the results presented in this paper are not publicly available at this time but may be obtained from the authors upon reasonable request.

Chapter 6

Conclusion and Outlook

Monitoring essential climate variables will remain an important method of surveying climate change in the coming decades. National and international organizations like the CSA, ESA and NASA have identified the value in dedicating resources to measuring these variables from remote sensing platforms, enabling the scientific community a global outlook on patterns and processes in the atmosphere. The dedication of these agencies is exemplified in the current efforts to include ALI as part of a Canadian contribution to NASA's Aerosol and Cloud, Convection and Precipitation (A-CCP) mission [National Academies of Sciences Engineering and Medicine, 2018].

ALI builds on a long legacy of atmospheric monitoring tools developed in Canada, including MOPITT, ACE-FTS, OSIRIS and more [Drummond and Mand, 1996, Bernath, 2001, Llewellyn et al., 2004]. The expertise gained through these instruments by both Canadian academic and industrial institutions facilitates the development of new ideas to meet the evolving challenges described by climate scientists. ALI specifically has grown from a laboratory prototype concept to an elegant breadboard ready to perform orbit-simulated measurement and retrievals.

The first version of ALI contributed an important proof-of-concept for using an AOTF based multi-spectral imager for limb viewing remote sensing. The work performed by [Elash et al., 2016] laid the groundwork for the instrument advancements described in this work.

The successor, ALI V2, expands the instrument capabilities in three key areas; extension of the spectral range, the addition of a second linear polarization state measurement and additional packaging flexibility through a catadioptric optical system [Kozun et al., 2020].

Expanding the spectral range ALI meets the requirement to capture the short wave in-

frared spectrum for particle size discrimination. The scattering properties of stratospheric aerosol limit the ability to extract particle size information from the visible spectrum. This means that current generation retrievals require assumptions of the particle size distribution to retrieve other aerosol properties like extinction. The retrieval vectors used in the retrieval method are shown to be sensitive to particle size for wavelengths longer than 1200 nm. Water vapour, however, influences the nearby spectral range of roughly 1350-1400 nm, meaning particle size information must be gathered from spectral channels longer than 1400 nm. This aligns well with current InGaAs sensing technology, with an upper spectral cut-off near 1700 nm. Furthermore, advances in this technology have extended the lower sensing cut-off to around 400 nm (with reduced quantum efficiency). This means that visible-extended InGaAs technology is the ideal candidate to meet the extended spectral range of ALI. Paired with this, current state-of-the-art AOTF's feature two piezo-transducers, expanding the typical diffraction range from one octave to two. ALI V2 features a spectral sensitivity range from 500-1500 nm based on the dual transducer AOTF selection.

Cloud structures in the upper troposphere and stratospheric aerosol distributions contain several similarities. Therefore, the spectral scattering structures of one may be mistaken for the other. However, the sizes of the scattering particles in clouds are much larger than visible and NIR wavelengths, leading to non-selective scattering. This scattering regime does not depend on the linear polarization of the incident radiation, which contrasts the Mie scattering regime that defines aerosol scattering. The added capability of linear polarization selection in ALI V2 allows for cloud identification in the atmospheric scene. This capability is demonstrated in the measurement set captured from the 2018 balloon campaign. This identification is fundamental for further investigation into cloud-aerosol interactions and feedbacks.

Finally, the packaging flexibility allowed for a necessary volume reduction for ALI V2. The feasibility of this instrument rests primarily on the optical performance, however, volume constraints are typically a limitation of satellite-based instrumentation. The reflective front end design and the addition of fold mirrors aided not only in the volume reduction but also in reducing chromatic aberration over the relatively large spectral range.

The flight of ALI V2 offers the first published example of spectral and polarization-resolved measurements of the atmospheric limb. The response of the instrument aligns well

with the modelled performance, validating the design process adopted for the optical system.

The ALI elegant breadboard design deviated from the previous prototypes in that a satellite-based approach was adopted. This started from the initial optical design, which utilizes optimized reflective surfaces to improve imaging performance. These surfaces are single-point diamond-turned optics made of aluminum 6061 alloy, which feature minimal surface form errors, low surface scattering, and high precision alignment interfaces. Furthermore, monolithic machined aluminum chassis are used as the opto-mechanical structure for the optics. Thermal isolation and temperature control of the spectral and polarization selection mechanism provide athermal performance over a wide operating temperature [Kozun et al., 2021].

The anticipated test environment for the ALI EBB is from a high altitude aircraft covering low to mid-latitudes. This aircraft achieves a flight altitude range of 18 km to 21 km. Although lower than the balloon platform, this test environment will offer spatially varying atmospheric scenes, which are unattainable from the balloon observatory. This spatial variation in the along-track direction will simulate the varying imagery that would be captured from a satellite platform. This demanding environment requires increased optical throughput to maintain signal-to-noise ratio requirements for aerosol property retrievals. To accommodate this, the limiting aperture of the ALI EBB has an area 4× larger than that of the predecessors. The performance models suggest that the EBB will achieve the SNR requirements over nearly all spectral channels and tangent altitudes, with post-process binning required under select circumstances.

6.1 Outlook Towards Orbital Operation

The path towards an orbital flight opportunity takes years and sometimes decades of development and prototyping before an instrument is launched into space. It relies on collaboration between academic and industry partners, and in Canada is often facilitated by the CSA. The CSA provides funding for grassroots and technology development studies, both of which have been demonstrated in the framework of ALI.

The earliest ALI prototypes were developed through the Flights and Fieldwork for the

Advancement of Science and Technology program from the CSA, to support University lead research projects to advance the capabilities and technologies of the Canadian space sector. Next, the Space Technology Development Program funded both the development of the ALI EBB and the concept design study for a preliminary layout of a satellite-based design, both presented in Chapter 5. These programs have supported the development of breakthrough technologies, and have provided opportunities to enhance technology readiness in anticipation of a future space mission.

The ALI concept has continued development beyond the work presented, in parallel streams of hardware development and scientific modelling and simulation. The hardware activities are twofold, both in further ALI EBB development for a high altitude aircraft flight, as well as a hardware feasibility study. These activities are expected to address several priorities described by Environment and Climate Change Canada and the Canadian Government and have taken place after the publication of the manuscript presented in Chapter 5.

The accommodation of the ALI EBB onto an aircraft platform is in the bidding stage at the time of writing. Upon contract award, the activity will consist of the development of the electrical and software systems to control the developed ALI EBB, as well as the mechanical accommodation of all related hardware into an ER-2 wing superpod. The intended flight campaign will also include the Spatial Heterodyne Observations of Water (SHOW) elegant breadboard, where the fields of view of the two instruments will overlap to simultaneously retrieve aerosol and water vapour content from a common atmospheric parcel. The aircraft campaign is targeted for fall 2022.

The second activity is a feasibility study of the ALI instrument for inclusion on NASA's A-CCP mission. This activity, described as a Phase 0 study, has been focused on furthering the conceptual development of ALI, as well as program planning and cost scheduling. The study has been strongly informed by the previous ALI design activities, with a focus on reducing risk and achieving technology readiness level advancement. The current Phase 0 concept has been informed by the technology challenges observed in the ALI EBB program and has notably changed the optical architecture to include two single-transducer AOTFs and both Silicon and InGaAs based detector plane arrays. These types of informed design

decisions are critical for the future success of the ALI satellite design, validating the need for the early technology development presented in this work.

The accompanying modelling and simulation work is led primarily by the ALI science team and is focused on synergies between ALI, other Canadian remote sensors, and the baseline technologies identified for the A-CCP mission. This work includes developing the ALI processing pipeline to process raw measurement data to a level 2 data product describing aerosol properties. Details from the Phase 0 concept are used for modelling the performance of this processing pipeline, and in turn, the results are used to inform trades in the Phase 0 design. Additionally, this activity targets updating the retrieval methods to incorporate short wave infrared wavelength channels for additional particle parameter sensitivity, and tomographic techniques to utilize the cross-track field of view available from ALI. The high-altitude aircraft flight described above will offer the first opportunity to test these new retrieval techniques.

The latest ALI activities have laid a framework to achieve an instrument launch in early 2029. Following a traditional multi-phase development approach accompanied by parallel technology development, a breadboard of the satellite platform design will be built and tested by early 2024 to reach TRL 4. TRL 6 and higher will be achieved with a qualification model by the end of 2026, and finally a protoflight model with be prepared for testing and flight by early 2028. The current projected budget leading up to launch is on the order of 40M CAD. Further efforts are also underway to identify cost-saving approaches utilizing a "New Space" approach of accelerated development time, reduced validation and higher risk acceptance. This secondary effort is anticipated to reduce cost by as much as 80%, and will be managed by a University-led consortium with guidance from the CSA. Regardless of the trajectory chosen, a promising future exists for ALI as it helps shape the landscape for Canada's role in global climate monitoring.

References

[Airy, 1835] Airy, G. B. (1835). On the diffraction of an object-glass with circular aperture. *Transactions of the Cambridge Philosophical Society*, 5:283.

[Andersson et al., 2015] Andersson, S. M., Martinsson, B. G., Vernier, J.-P., Friberg, J., Brenninkmeijer, C. A., Hermann, M., Van Velthoven, P. F., and Zahn, A. (2015). Significant radiative impact of volcanic aerosol in the lowermost stratosphere. *Nature communications*, 6:7692.

[Antuña et al., 2002] Antuña, J. C., Robock, A., Stenchikov, G. L., Thomason, L. W., and Barnes, J. E. (2002). Lidar validation of SAGE II aerosol measurements after the 1991 Mount Pinatubo eruption. *Journal of Geophysical Research: Atmospheres*, 107(D14).

[Aquila et al., 2013] Aquila, V., Oman, L. D., Stolarski, R., Douglass, A. R., and Newman, P. A. (2013). The response of ozone and nitrogen dioxide to the eruption of mt. pinatubo at southern and northern midlatitudes. *Journal of the Atmospheric Sciences*, 70(3):894–900.

[Auld, 1990] Auld, B. A. (1990). *Acoustic fields and waves in solids*. R.E. Krieger, Malabar, Fla., 2nd ed. edition.

[Bei et al., 2004] Bei, L., Dennis, G. I., Miller, H. M., Spaine, T. W., and Carnahan, J. W. (2004). Acousto-optic tunable filters: fundamentals and applications as applied to chemical analysis techniques. *Progress in Quantum Electronics*, 28(2):67–87.

[Bernath, 2001] Bernath, P. (2001). *Atmospheric Chemistry Experiment (ACE): An Overview*, pages 147–161. Springer Netherlands.

[Bertaux et al., 2010] Bertaux, J. L., Kyrölä, E., Fussen, D., Hauchecorne, A., Dalaudier, F., Sofieva, V., Tamminen, J., Vanhellemont, F., Fanton d'Andon, O., Barrot, G., Mangin, A., Blanot, L., Lebrun, J. C., Pérot, K., Fehr, T., Saavedra, L., Leppelmeier, G. W., and Fraisse, R. (2010). Global ozone monitoring by occultation of stars: an overview of GOMOS measurements on ENVISAT. *Atmospheric Chemistry and Physics*, 10(24):12091–12148.

[Bohren and Huffman, 1998] Bohren, C. F. and Huffman, D. R. (1998). *Absorption and scattering of light by small particles*. John Wiley & Sons, Ltd.

[Born and Wolf, 2013] Born, M. and Wolf, E. (2013). *Principles of optics: electromagnetic theory of propagation, interference and diffraction of light*. Elsevier.

[Boucher et al., 2013] Boucher, O., Randall, D., Artaxo, P., Bretherton, C., Feingold, G., Forster, P., Kerminen, V.-M., Kondo, Y., Liao, H., Lohmann, U., Rasch, P., Satheesh,

S. K., Sherwood, S., Stevens, B., and Zhang, X. Y. (2013). *Clouds and aerosols*. Cambridge University Press, Cambridge, UK.

[Bourassa et al., 2007] Bourassa, A. E., Degenstein, D. A., Gattinger, R. L., and Llewellyn, E. J. (2007). Stratospheric aerosol retrieval with optical spectrograph and infrared imaging system limb scatter measurements. *Journal of Geophysical Research: Atmospheres*, 112(D10).

[Bourassa et al., 2008a] Bourassa, A. E., Degenstein, D. A., and Llewellyn, E. J. (2008a). Retrieval of stratospheric aerosol size information from OSIRIS limb scattered sunlight spectra. *Atmospheric Chemistry and Physics*, 8(21):6375–6380.

[Bourassa et al., 2008b] Bourassa, A. E., Degenstein, D. A., and Llewellyn, E. J. (2008b). SASKTRAN: A spherical geometry radiative transfer code for efficient estimation of limb scattered sunlight. *Journal of Quantitative Spectroscopy and Radiative Transfer*, 109(1):52 – 73.

[Bourassa et al., 2012a] Bourassa, A. E., Rieger, L. A., Lloyd, N. D., and Degenstein, D. A. (2012a). Odin-OSIRIS stratospheric aerosol data product and SAGE III intercomparison. *Atmospheric Chemistry and Physics*, 12(1):605–614.

[Bourassa et al., 2019] Bourassa, A. E., Rieger, L. A., Zawada, D. J., Khaykin, S., Thomason, L. W., and Degenstein, D. A. (2019). Satellite limb observations of unprecedented forest fire aerosol in the stratosphere. *Journal of Geophysical Research: Atmospheres*, 124(16):9510–9519.

[Bourassa et al., 2012b] Bourassa, A. E., Robock, A., Randel, W. J., Deshler, T., Rieger, L. A., Lloyd, N. D., Llewellyn, E. J. T., and Degenstein, D. A. (2012b). Large volcanic aerosol load in the stratosphere linked to Asian monsoon transport. *Science*, 337(6090):78.

[Bovensmann et al., 1999] Bovensmann, H., Burrows, J. P., Buchwitz, M., Frerick, J., Noël, S., Rozanov, V. V., Chance, K. V., and Goede, A. P. H. (1999). SCIAMACHY: Mission objectives and measurement modes. *Journal of the Atmospheric Sciences*, 56(2):127–150.

[Brillouin, 1922] Brillouin, L. (1922). Diffusion de la lumière et des rayons x par un corps transparent homogène - influence de l'agitation thermique. *Ann. Phys.*, 9(17):88–122.

[Buchwitz et al., 2015] Buchwitz, M., Reuter, M., Schneising, O., Boesch, H., Guerlet, S., Dils, B., Aben, I., Armante, R., Bergamaschi, P., Blumenstock, T., et al. (2015). The greenhouse gas climate change initiative (ghg-cci): Comparison and quality assessment of near-surface-sensitive satellite-derived co2 and ch4 global data sets. *Remote Sensing of Environment*, 162:344–362.

[Büning-Pfaue, 2003] Büning-Pfaue, H. (2003). Analysis of water in food by near infrared spectroscopy. *Food Chemistry*, 82(1):107 – 115.

[Burrows et al., 1998] Burrows, J. P., Dehn, A., Deters, B., Himmelmann, S., Richter, A., Voigt, S., and Orphal, J. (1998). Atmospheric remote-sensing reference data from GOME:

Part 1. temperature-dependent absorption cross-sections of NO_2 in the 231–794 nm range. *Journal of Quantitative Spectroscopy and Radiative Transfer*, 60(6):1025–1031.

[Butchart, 2014] Butchart, N. (2014). The Brewer-Dobson circulation. *Reviews of geophysics*, 52(2):157–184.

[Campbell and Deshler, 2014] Campbell, P. and Deshler, T. (2014). Condensation nuclei measurements in the midlatitude (1982–2012) and Antarctic (1986–2010) stratosphere between 20 and 35 km. *Journal of Geophysical Research: Atmospheres*, 119(1):137–152.

[Canadian Space Agency, 2019] Canadian Space Agency (2019). Exploration, imagination, innovation: a new space strategy for Canada. Monograph. `https://www.asc-csa.gc.ca/pdf/eng/publications/space-strategy-for-canada.pdf`, Catalogue number: ST99-60/2019F-PDF.

[Cess et al., 1993] Cess, R., Zhang, M., Potter, G., Gates, W., Taylor, K., Colman, R., Fraser, J., Mcavaney, B., Dazlich, D., Randall, D., Del Genio, A., Lacis, A., Esch, M., Roeckner, E., Galin, V., Hack, J., Kiehl, J., Ingram, W., Le Treut, H., Lli, Z., Liang, X., Wang, W., and Mahfouf (1993). Uncertainities in carbon dioxide radiative forcing in atmospheric general circulation models. *Science (Washington, D.C.); (United States)*, 262(5137).

[Chang, 1974] Chang, I. C. (1974). Noncollinear acousto-optic filter with large angular aperture. *Applied Physics Letters*, 25(7):370–372.

[Chang, 1975] Chang, I. C. (1975). Analysis of the noncollinear acousto-optic filter. *Electronics Letters*, 11(25):617–618.

[Chang, 1977] Chang, I. C. (1977). Tunable acousto-optic filters: An overview. *Optical Engineering*, 16(5).

[Chang, 1981] Chang, I. C. (1981). Acousto-optic tunable filters. *Optical Engineering*, 20(6):824 – 829.

[Chang and Katzka, 1978] Chang, I. C. and Katzka, P. (1978). Tunable acousto-optical filters with apodized acoustical excitation (A). *Journal of the Optical Society of America (1917-1983)*, 68:1449.

[Cisewski et al., 2014] Cisewski, M., Zawodny, J., Gasbarre, J., Eckman, R., Topiwala, N., Rodriguez-Alvarez, O., Cheek, D., and Hall, S. (2014). The Stratospheric Aerosol and Gas Experiment (SAGE III) on the International Space Station (ISS) Mission. In *Sensors, Systems, and Next-Generation Satellites XVIII*, volume 9241, pages 59 – 65. International Society for Optics and Photonics, SPIE.

[De Gennes and Prost, 1993] De Gennes, P.-G. and Prost, J. (1993). *The physics of liquid crystals*, volume 83. Oxford university press.

[Degenstein et al., 2009] Degenstein, D. A., Bourassa, A. E., Roth, C. Z., and Llewellyn, E. J. (2009). Limb scatter ozone retrieval from 10 to 60 km using a multiplicative algebraic reconstruction technique. *Atmospheric Chemistry and Physics*, 9(17):6521–6529.

[Degenstein et al., 2004] Degenstein, D. A., Llewellyn, E. J., and Lloyd, N. D. (2004). Tomographic retrieval of the oxygen infrared atmospheric band with the OSIRIS infrared imager. *Canadian Journal of Physics*, 82(7):501–515.

[Dekemper et al., 2012] Dekemper, E., Loodts, N., Van Opstal, B., Maes, J., Vanhellemont, F., Mateshvili, N., Franssens, G., Pieroux, D., Bingen, C., Robert, C., et al. (2012). Tunable acousto-optic spectral imager for atmospheric composition measurements in the visible spectral domain. *Applied optics*, 51(25):6259–6267.

[Deligne et al., 2010] Deligne, N. I., Coles, S. G., and Sparks, R. S. J. (2010). Recurrence rates of large explosive volcanic eruptions. *Journal of Geophysical Research: Solid Earth*, 115(B6).

[Deshler et al., 2003] Deshler, T., Hervig, M. E., Hofmann, D. J., Rosen, J. M., and Liley, J. B. (2003). Thirty years of in situ stratospheric aerosol size distribution measurements from Laramie, Wyoming (41°N), using balloon-borne instruments. *Journal of Geophysical Research: Atmospheres*, 108(D5).

[Deshler et al., 2019] Deshler, T., Luo, B., Kovilakam, M., Peter, T., and Kalnajs, L. E. (2019). Retrieval of aerosol size distributions from in situ particle counter measurements: Instrument counting efficiency and comparisons with satellite measurements. *Journal of Geophysical Research: Atmospheres*, 124(9):5058–5087.

[Dixon, 1967] Dixon, R. (1967). Acoustic diffraction of light in anisotropic media. *IEEE Journal of Quantum Electronics*, 3(2):85–93.

[Doyon et al., 2012] Doyon, R., Hutchings, J. B., Beaulieu, M., Albert, L., Lafrenière, D., Willott, C., Touahri, D., Rowlands, N., Maszkiewicz, M., Fullerton, A. W., Volk, K., Martel, A. R., Chayer, P., Sivaramakrishnan, A., Abraham, R., Ferrarese, L., Jayawardhana, R., Johnstone, D., Meyer, M., Pipher, J. L., and Sawicki, M. (2012). The JWST Fine Guidance Sensor (FGS) and Near-Infrared Imager and Slitless Spectrograph (NIRISS). In *Space Telescopes and Instrumentation 2012: Optical, Infrared, and Millimeter Wave*, volume 8442, pages 1005 – 1017. International Society for Optics and Photonics, SPIE.

[Drummond and Mand, 1996] Drummond, J. R. and Mand, G. (1996). The measurements of pollution in the troposphere (mopitt) instrument: Overall performance and calibration requirements. *Journal of Atmospheric and Oceanic Technology*, 13(2):314–320.

[Elash, 2016] Elash, B. J. (2016). *The Aerosol Limb Imager*. PhD thesis, University of Saskatchewan.

[Elash et al., 2016] Elash, B. J., Bourassa, A. E., Loewen, P. R., Lloyd, N. D., and Degenstein, D. A. (2016). The aerosol limb imager: acousto-optic imaging of limb-scattered sunlight for stratospheric aerosol profiling. *Atmospheric Measurement Techniques*, 9(3):1261–1277.

[Fahey et al., 1993] Fahey, D. W., Kawa, S. R., Woodbridge, E. L., Tin, P., Wilson, J. C., Jonsson, H. H., Dye, J. E., Baumgardner, D., Borrmann, S., Toohey, D. W., Avallone,

L. M., Proffitt, M. H., Margitan, J., Loewenstein, M., Podolske, J. R., Salawitch, R. J., Wofsy, S. C., Ko, M. K. W., Anderson, D. E., Schoeber, M. R., and Chan, K. R. (1993). In situ measurements constraining the role of sulphate aerosols in mid-latitude ozone depletion. *Nature*, 363(6429):509.

[Fiocco and Grams, 1964] Fiocco, G. and Grams, G. (1964). Observations of the aerosol layer at 20 km by optical radar. *Journal of the Atmospheric Sciences*, 21(3):323–324.

[Flynn et al., 2006] Flynn, L. E., Seftor, C. J., Larsen, J. C., and Xu, P. (2006). The Ozone Mapping and Profiler Suite in *Earth Science Satellite Remote Sensing: Vol. 1: Science and Instruments*, pages 279–296. Springer Berlin Heidelberg, Berlin, Heidelberg.

[Gooch and Tarry, 1974] Gooch, C. H. and Tarry, H. A. (1974). Optical characteristics of twisted nematic liquid-crystal films. *Electronics Letters*, 10(1):2–4.

[Gordley et al., 2009] Gordley, L. L., Hervig, M. E., Fish, C., Russell, J. M., Bailey, S., Cook, J., Hansen, S., Shumway, A., Paxton, G., Deaver, L., Marshall, T., Burton, J., Magill, B., Brown, C., Thompson, E., and Kemp, J. (2009). The solar occultation for ice experiment. *Journal of Atmospheric and Solar-Terrestrial Physics*, 71(3):300–315.

[Gordon et al., 2017] Gordon, I., Rothman, L., Hill, C., Kochanov, R., Tan, Y., Bernath, P., Birk, M., Boudon, V., Campargue, A., Chance, K., Drouin, B., Flaud, J.-M., Gamache, R., Hodges, J., Jacquemart, D., Perevalov, V., Perrin, A., Shine, K., Smith, M.-A., Tennyson, J., Toon, G., Tran, H., Tyuterev, V., Barbe, A., Császár, A., Devi, V., Furtenbacher, T., Harrison, J., Hartmann, J.-M., Jolly, A., Johnson, T., Karman, T., Kleiner, I., Kyuberis, A., Loos, J., Lyulin, O., Massie, S., Mikhailenko, S., Moazzen-Ahmadi, N., Müller, H., Naumenko, O., Nikitin, A., Polyansky, O., Rey, M., Rotger, M., Sharpe, S., Sung, K., Starikova, E., Tashkun, S., Auwera, J. V., Wagner, G., Wilzewski, J., Wcisło, P., Yu, S., and Zak, E. (2017). The HITRAN2016 molecular spectroscopic database. *Journal of Quantitative Spectroscopy and Radiative Transfer*, 203:3 – 69.

[Gupta and Voloshinov, 2007] Gupta, N. and Voloshinov, V. B. (2007). Development and characterization of two-transducer imaging acousto-optic tunable filters with extended tuning range. *Appl. Opt.*, 46(7):1081–1088.

[Hamill et al., 1977] Hamill, P., Toon, O. B., and Kiang, C. S. (01 Jul. 1977). Microphysical processes affecting stratospheric aerosol particles. *Journal of Atmospheric Sciences*, 34(7):1104 – 1119.

[Hansen and Travis, 1974] Hansen, J. E. and Travis, L. D. (1974). Light scattering in planetary atmospheres. *Space Science Review*, 16:527–610.

[Harris and Wallace, 1969] Harris, S. E. and Wallace, R. W. (1969). Acousto-optic tunable filter. *Journal of the Optical Society of America*, 59(6):744.

[Hecht, 2017] Hecht, E. (2017). *Optics*. Pearson Education.

[Hedin, 1991] Hedin, A. E. (1991). Extension of the MSIS thermosphere model into the middle and lower atmosphere. *Journal of Geophysical Research: Space Physics*, 96(A2):1159–1172.

[Hegerl et al., 2007] Hegerl, G. C., Crowley, T. J., Allen, M., Hyde, W. T., Pollack, H. N., Smerdon, J., and Zorita, E. (15 Feb. 2007). Detection of human influence on a new, validated 1500-year temperature reconstruction. *Journal of Climate*, 20(4):650 – 666.

[Hollmann et al., 2013] Hollmann, R., Merchant, C. J., Saunders, R., Downy, C., Buchwitz, M., Cazenave, A., Chuvieco, E., Defourny, P., de Leeuw, G., Forsberg, R., et al. (2013). The esa climate change initiative: Satellite data records for essential climate variables. *Bulletin of the American Meteorological Society*, 94(10):1541–1552.

[Holton et al., 1995] Holton, J. R., Haynes, P. H., McIntyre, M. E., Douglass, A. R., Rood, R. B., and Pfister, L. (1995). Stratosphere-troposphere exchange. *Reviews of geophysics*, 33(4):403–439.

[Junge et al., 1961] Junge, C. E., Chagnon, C. W., and Manson, J. E. (01 Feb. 1961). Stratospheric aerosols. *Journal of Atmospheric Sciences*, 18(1):81 – 108.

[Junge and Manson, 1961] Junge, C. E. and Manson, J. E. (1961). Stratospheric aerosol studies. *Journal of Geophysical Research*, 66(7):2163–2182.

[Jäger, 2005] Jäger, H. (2005). Long-term record of lidar observations of the stratospheric aerosol layer at Garmisch-Partenkirchen. *Journal of Geophysical Research: Atmospheres*, 110(D8).

[Jäger and Deshler, 2002] Jäger, H. and Deshler, T. (2002). Lidar backscatter to extinction, mass and area conversions for stratospheric aerosols based on midlatitude balloonborne size distribution measurements. *Geophysical Research Letters*, 29(19):35–1–35–4.

[Karl et al., 2010] Karl, T., Diamond, H., Bojinski, S., Butler, J., Dolman, H., Haeberli, W., Harrison, D., Nyong, A., Rösner, S., Seiz, G., et al. (2010). Observation needs for climate information, prediction and application: Capabilities of existing and future observing systems. *Procedia Environmental Sciences*, 1:192–205.

[Kiehl and Briegleb, 1993] Kiehl, J. T. and Briegleb, B. P. (1993). The relative roles of sulfate aerosols and greenhouse gases in climate forcing. *Science*, 260(5106):311–314.

[Klein, 1986] Klein, M. V. (1986). *Optics*. Wiley, New York, second edition.

[Korablev et al., 2018] Korablev, O. I., Belyaev, D. A., Dobrolenskiy, Y. S., Trokhimovskiy, A. Y., and Kalinnikov, Y. K. (2018). Acousto-optic tunable filter spectrometers in space missions. *Appl. Opt.*, 57(10):C103–C119.

[Korpel, 1996] Korpel, A. (1996). *Acousto-optics*, volume 57. CRC Press.

[Korpel and Poon, 1980] Korpel, A. and Poon, T.-C. (1980). Explicit formalism for acousto-optic multiple plane-wave scattering. *Journal of the Optical Society of America*, 70(7):817.

[Kozun et al., 2021] Kozun, M. N., Bourassa, A. E., Degenstein, D. A., Haley, C. S., and Zheng, S. H. (2021). Adaptation of the polarimetric multi-spectral aerosol limb imager for high altitude aircraft and satellite observations. *Appl. Opt.*, 60(15):4325–4334.

[Kozun et al., 2020] Kozun, M. N., Bourassa, A. E., Degenstein, D. A., and Loewen, P. R. (2020). A multi-spectral polarimetric imager for atmospheric profiling of aerosol and thin cloud: Prototype design and sub-orbital performance. *Review of Scientific Instruments*, 91(10):103106.

[Kremser et al., 2016] Kremser, S., Thomason, L. W., von Hobe, M., Hermann, M., Deshler, T., Timmreck, C., Toohey, M., Stenke, A., Schwarz, J. P., Weigel, R., Fueglistaler, S., Prata, F. J., Vernier, J.-P., Schlager, H., Barnes, J. E., Antuña-Marrero, J.-C., Fairlie, D., Palm, M., Mahieu, E., Notholt, J., Rex, M., Bingen, C., Vanhellemont, F., Bourassa, A., Plane, J. M. C., Klocke, D., Carn, S. A., Clarisse, L., Trickl, T., Neely, R., James, A. D., Rieger, L., Wilson, J. C., and Meland, B. (2016). Stratospheric aerosol-observations, processes, and impact on climate. *Reviews of Geophysics*, 54(2):278–335.

[Labow et al., 2015] Labow, G. J., Ziemke, J. R., McPeters, R. D., Haffner, D. P., and Bhartia, P. K. (2015). A total ozone-dependent ozone profile climatology based on ozonesondes and Aura MLS data. *Journal of Geophysical Research: Atmospheres*, 120(6):2537–2545.

[Lacis et al., 1992] Lacis, A., Hansen, J., and Sato, M. (1992). Climate forcing by stratospheric aerosols. *Geophysical Research Letters*, 19(15):1607–1610.

[Langille et al., 2019] Langille, J., Letros, D., Bourassa, A., Solheim, B., Degenstein, D., Dupont, F., Zawada, D., and Lloyd, N. D. (2019). Spatial heterodyne observations of water (SHOW) from a high-altitude airplane: characterization, performance, and first results. *Atmospheric Measurement Techniques*, 12(1):431–455.

[Lawrence and Vandecar, 2015] Lawrence, D. and Vandecar, K. (2015). Effects of tropical deforestation on climate and agriculture. *Nature climate change*, 5(1):27–36.

[Le Treut et al., 1998] Le Treut, H., Forichon, M., Boucher, O., and Li, Z.-X. (1998). Sulfate aerosol indirect effect and CO_2 greenhouse forcing equilibrium response of the LMD GCM and associated cloud feedbacks. *Journal of Climate*, 11(7):1673–1684.

[Lee, 1992] Lee, Y. H. (1992). Alignment of an off-axis parabolic mirror with two parallel He-Ne laser beams. *Optical Engineering*, 31(11):2287 – 2292.

[Li et al., 2011] Li, J., Wang, M.-H., and Ho, Y.-S. (2011). Trends in research on global climate change: A science citation index expanded-based analysis. *Global and Planetary Change*, 77(1-2):13–20.

[Li et al., 2015] Li, K., Wang, Z., Yang, C.-Q., Zhang, R., Wang, Y.-L., and Song, Y.-P. (2015). A new technique of full polarization hyperspectral imaging based on acousto-optic tunable filter and liquid crystal variable retarder. *Acta Physica Sinica -Chinese Edition-*, 64.

[Litster and Birgeneau, 1982] Litster, J. D. and Birgeneau, R. J. (1982). Phases and phase transitions. *Physics Today*, 35(5):26–33.

[Liu et al., 2010] Liu, Y., Stanturf, J., and Goodrick, S. (2010). Trends in global wildfire potential in a changing climate. *Forest Ecology and Management*, 259(4):685–697.

[Llewellyn et al., 2004] Llewellyn, E. J., Lloyd, N. D., Degenstein, D. A., Gattinger, R. L., Petelina, S. V., Bourassa, A. E., Wiensz, J. T., Ivanov, E. V., McDade, I. C., Solheim, B. H., McConnell, J. C., Haley, C. S., von Savigny, C., Sioris, C. E., McLinden, C. A., Griffioen, E., Kaminski, J., Evans, W. F., Puckrin, E., Strong, K., Wehrle, V., Hum, R. H., Kendall, D. J., Matsushita, J., Murtagh, D. P., Brohede, S., Stegman, J., Witt, G., Barnes, G., Payne, W. F., Piché, L., Smith, K., Warshaw, G., Deslauniers, D. L., Marchand, P., Richardson, E. H., King, R. A., Wevers, I., McCreath, W., Kyrölä, E., Oikarinen, L., Leppelmeier, G. W., Auvinen, H., Mégie, G., Hauchecorne, A., Lefèvre, F., de La Nöe, J., Ricaud, P., Frisk, U., Sjoberg, F., von Schéele, F., and Nordh, L. (2004). The OSIRIS instrument on the odin spacecraft. *Canadian Journal of Physics*, 82(6):411–422.

[Malinina et al., 2019] Malinina, E., Rozanov, A., Rieger, L., Bourassa, A., Bovensmann, H., Burrows, J. P., and Degenstein, D. (2019). Stratospheric aerosol characteristics from space-borne observations: extinction coefficient and ångström exponent. *Atmospheric Measurement Techniques*, 12(7):3485–3502.

[Mantsevich et al., 2015] Mantsevich, S., Korablev, O., Kalinnikov, Y., Ivanov, A., and Kiselev, A. (2015). Wide-aperture TeO_2 AOTF at low temperatures: Operation and survival. *Ultrasonics*, 59:50–58.

[Marshall et al., 2014] Marshall, J. L., Williams, P., Rheault, J.-P., Prochaska, T., Allen, R. D., and DePoy, D. L. (2014). Characterization of the reflectivity of various black materials. 9147.

[Masson-Delmotte et al., 2013] Masson-Delmotte, V., Schulz, M., Abe-Ouchi, A., Beer, J., Ganopolski, J., González Rouco, J. F., Jansen, E., Lambeck, K., Luterbacher, J., Naish, T., Osborn, T., Otto-Bliesner, B., Quinn, T., Ramesh, R., Rojas, M., Shao, X., and Timmermann, A. (2013). *Information from paleoclimate archives*, pages 383–464. Cambridge University Press, Cambridge, UK.

[Mätzler, 2002] Mätzler, C. (2002). MATLAB functions for Mie scattering and absorption, Version 2.

[Mauldin et al., 1985] Mauldin, L. E. I., Zaun, N. H., Jr., M. P. M., Guy, J. H., and Vaughn, W. R. (1985). Stratospheric Aerosol And Gas Experiment II Instrument: A Functional Description. *Optical Engineering*, 24(2):307 – 312.

[Mccormick et al., 1995] Mccormick, M. P., Thomason, L. W., and Trepte, C. R. (1995). Atmospheric effects of the Mt Pinatubo eruption. *Nature*, 373(6513):399.

[Mclinden et al., 2011] Mclinden, C., McConnell, J., Strong, K., McDade, I., Gattinger, R., King, R., Solheim, B., Llewellyn, E., and Evans, W. (2011). The impact of the OSIRIS grating efficiency on radiance and trace-gas retrievals. *Canadian Journal of Physics*, 80:469–481.

[Mie, 1908] Mie, G. (1908). Contributions to the optics of turbid media, particularly of colloidal metal solutions. *Annalen der Physik, Leipzig*, 25(3):377–445.

[Mills et al., 1993] Mills, M. J., Langford, A. O., O' Leary, T. J., Arpag, K., Miller, H. L., Proffitt, M. H., Sanders, R. W., and Solomon, S. (1993). On the relationship between stratospheric aerosols and nitrogen dioxide. *Geophysical Research Letters*, 20(12):1187–1190.

[Mishchenko et al., 2002] Mishchenko, M. I., Travis, L. D., and Lacis, A. A. (2002). *Scattering, absorption, and emission of light by small particles*. Cambridge university press.

[Morecroft et al., 2019] Morecroft, M. D., Duffield, S., Harley, M., Pearce-Higgins, J. W., Stevens, N., Watts, O., and Whitaker, J. (2019). Measuring the success of climate change adaptation and mitigation in terrestrial ecosystems. *Science*, 366(6471):eaaw9256.

[Moritz et al., 2002] Moritz, R. E., Bitz, C. M., and Steig, E. J. (2002). Dynamics of recent climate change in the arctic. *Science*, 297(5586):1497–1502.

[National Academies of Sciences Engineering and Medicine, 2018] National Academies of Sciences Engineering and Medicine (2018). *Thriving on Our Changing Planet: A Decadal Strategy for Earth Observation from Space*. The National Academies Press, Washington, DC.

[Newnham, 2005] Newnham, R. E. (2005). *Properties of materials : anisotropy, symmetry, structure*. Oxford University Press, Oxford ; New York.

[Noxon and Jones, 1962] Noxon, J. F. and Jones, A. V. (1962). Observation of the (0,0) Band of the ($^1\Delta_g$ - $^3\ \Sigma\ ^-_g$) System of Oxygen in the Day and Twilight Airglow. *Nature*, 196:157–158.

[Patnaude and Diao, 2020] Patnaude, R. and Diao, M. (2020). Aerosol indirect effects on cirrus clouds based on global aircraft observations. *Geophysical Research Letters*, 47(10):e2019GL086550.

[Pickrell, 2019] Pickrell, J. (2019). Massive Australian blazes will 'reframe our understanding of bushfire'. *Science*, 366(6468):937–937.

[Pinto et al., 1989] Pinto, J. P., Turco, R. P., and Toon, O. B. (1989). Self-limiting physical and chemical effects in volcanic eruption clouds. *Journal of Geophysical Research: Atmospheres*, 94(D8):11165–11174.

[Poon, 2006] Poon, T.-C. (2006). *Engineering optics with Matlab*. World Scientific, Singapore ; Hong Kong.

[Post, 1996] Post, M. J. (1996). A graphical technique for retrieving size distribution parameters from multiple measurements: Visualization and error analysis. *Journal of Atmospheric and Oceanic Technology*, 13(4):863 – 873.

[Randel et al., 2010] Randel, W., Park, M., Emmons, L., Kinnison, D., Bernath, P., Walker, K., Boone, C., and Pumphrey, H. (2010). Asian monsoon transport of pollution to the stratosphere. *Science*, 328(5978):611–613.

[Rieger et al., 2014] Rieger, L. A., Bourassa, A. E., and Degenstein, D. A. (2014). Stratospheric aerosol particle size information in Odin-OSIRIS limb scatter spectra. *Atmospheric Measurement Techniques*, 7(2):507–522.

[Rieger et al., 2019] Rieger, L. A., Zawada, D. J., Bourassa, A. E., and Degenstein, D. A. (2019). A multiwavelength retrieval approach for improved OSIRIS aerosol extinction retrievals. *Journal of Geophysical Research: Atmospheres*, 124(13):7286–7307.

[Robock, 2000] Robock, A. (2000). Volcanic eruptions and climate. *Reviews of Geophysics*, 38(2):191–219.

[Robock and Mao, 1995] Robock, A. and Mao, J. (1995). The volcanic signal in surface temperature observations. *Journal of Climate*, 8(5):1086–1103.

[Roche et al., 1993] Roche, A. E., Kumer, J. B., Mergenthaler, J. L., Ely, G. A., Uplinger, W. G., Potter, J. F., James, T. C., and Sterritt, L. W. (1993). The cryogenic limb array etalon spectrometer (CLAES) on UARS: Experiment description and performance. *Journal of Geophysical Research: Atmospheres*, 98(D6):10763–10775.

[Rosenthal, 1955] Rosenthal, A. H. (1955). Color control by ultrasonic wave gratings. *Journal of the Optical Society of America*, 45(9):751.

[Russell III et al., 1993] Russell III, J. M., Gordley, L. L., Park, J. H., Drayson, S. R., Hesketh, W. D., Cicerone, R. J., Tuck, A. F., Frederick, J. E., Harries, J. E., and Crutzen, P. J. (1993). The halogen occultation experiment. *Journal of Geophysical Research: Atmospheres*, 98(D6):10777–10797.

[Santer et al., 2017] Santer, B. D., Fyfe, J. C., Pallotta, G., Flato, G. M., Meehl, G. A., England, M. H., Hawkins, E., Mann, M. E., Painter, J. F., Bonfils, C., Cvijanovic, I., Mears, C., Wentz, F. J., Po-Chedley, S., Fu, Q., and Zou, C.-Z. (2017). Causes of differences in model and satellite tropospheric warming rates. *Nature Geoscience*, 10(7).

[Schadt and Helfrich, 1971] Schadt, M. and Helfrich, W. (1971). Voltage-dependent optical activity of a twisted nematic liquid crystal. *Applied Physics Letters*, 18(4):127–128.

[Seinfeld and Pandis, 2006] Seinfeld, J. H. and Pandis, S. N. (2006). *Atmospheric chemistry and physics : from air pollution to climate change*, chapter 15, pages 691–719. John Wiley & Sons, Ltd, Hoboken, N.J., second edition.

[Shea, 2017] Shea, G. (2017). NASA Systems Engineering Handbook Revision 2.

[Sheng et al., 2015] Sheng, J., Weisenstein, D. K., Luo, B., Rozanov, E., Stenke, A., Anet, J., Bingemer, H., and Peter, T. (2015). Global atmospheric sulfur budget under volcanically quiescent conditions: Aerosol-chemistry-climate model predictions and validation. *Journal of Geophysical Research: Atmospheres*, 120(1):256–276.

[Silvestrova et al., 1987] Silvestrova, I. M., Pisarevskii, Y. V., Senyushenkov, P. A., Krupny, A. I., Voszka, R., Földvári, I., and Janszky, J. (1987). Temperature dependence of elastic properties of paratellurite. *physica status solidi (a)*, 101(2):437–444.

[Sivanayagam and Findlay, 1984] Sivanayagam, A. and Findlay, D. (1984). High resolution noncollinear acoustooptic filters with variable passband characteristics: design. *Appl. Opt.*, 23(24):4601–4608.

[Smith, 1998] Smith, G. H. (1998). *Practical computer-aided lens design*. Willmann-Bell, Incorporated.

[Smith, 2008] Smith, W. J. (2008). *Modern optical engineering: the design of optical systems*. McGraw-Hill Education.

[Soden et al., 2002] Soden, B. J., Wetherald, R. T., Stenchikov, G. L., and Robock, A. (2002). Global cooling after the eruption of Mount Pinatubo: a test of climate feedback by water vapor. *Science (New York, N.Y.)*, 296(5568):727.

[Solomon, 1999] Solomon, S. (1999). Stratospheric ozone depletion: A review of concepts and history. *Reviews of Geophysics*, 37(3):275–316.

[Solomon et al., 2011] Solomon, S., Daniel, J. S., Neely, R. R., Vernier, J.-P., Dutton, E. G., and Thomason, L. W. (2011). The persistently variable background stratospheric aerosol layer and global climate change. *Science*, 333(6044):866–870.

[SPARC, 2006] SPARC (2006). SPARC Assessment of Stratospheric Aerosol Properties (ASAP). Technical report, SPARC.

[Stauffer et al., 1973] Stauffer, D., Mohnen, V., and Kiang, C. (1973). Heteromolecular condensation theory applied to particle growth. *Journal of Aerosol Science*, 4(6):461–471.

[Strutt, 1871] Strutt, H. J. (1871). XV. On the light from the sky, its polarization and colour. *The London, Edinburgh, and Dublin Philosophical Magazine and Journal of Science*, 41(271):107–120.

[Suhre et al., 1992] Suhre, D. R., Gottlieb, M. S., Taylor, L. H., and Melamed, N. T. (1992). Spatial resolution of imaging noncollinear acousto-optic tunable filters. *Optical Engineering*, 31(10):2118 – 2121.

[Suhre and Gupta, 2005] Suhre, D. R. and Gupta, N. (2005). Acousto-optic tunable filter sidelobe analysis and reduction with telecentric confocal optics. *Appl. Opt.*, 44(27):5797–5801.

[Suhre and Theodore, 1996] Suhre, D. R. and Theodore, J. G. (1996). White-light imaging by use of a multiple passband acousto-optic tunable filter. *Appl. Opt.*, 35(22):4494–4501.

[Telegadas and List, 1969] Telegadas, K. and List, R. J. (1969). Are particulate radioactive tracers indicative of stratospheric motions? *Journal of Geophysical Research (1896-1977)*, 74(6):1339–1350.

[Thomas et al., 2017] Thomas, J. L., Polashenski, C. M., Soja, A. J., Marelle, L., Casey, K. A., Choi, H. D., Raut, J.-C., Wiedinmyer, C., Emmons, L. K., Fast, J. D., Pelon, J., Law, K. S., Flanner, M. G., and Dibb, J. E. (2017). Quantifying black carbon deposition over the Greenland ice sheet from forest fires in Canada. *Geophysical Research Letters*, 44(15):7965–7974.

[Thomason et al., 2018] Thomason, L. W., Ernest, N., Millán, L., Rieger, L., Bourassa, A., Vernier, J.-P., Manney, G., Luo, B., Arfeuille, F., and Peter, T. (2018). A global space-based stratospheric aerosol climatology: 1979–2016. *Earth System Science Data*, 10(1):469–492.

[Thomason and Vernier, 2013] Thomason, L. W. and Vernier, J.-P. (2013). Improved SAGE II cloud/aerosol categorization and observations of the Asian tropopause aerosol layer: 1989-2005. *Atmospheric Chemistry and Physics*, 13(9):4605–4616.

[Thompson et al., 2009] Thompson, D. W. J., Wallace, J. M., Jones, P. D., and Kennedy, J. J. (2009). Identifying signatures of natural climate variability in time series of global-mean surface temperature: Methodology and insights. *Journal of Climate*, 22(22):6120 – 6141.

[Turner-Valle et al., 2004] Turner-Valle, J. A., Sullivan, J., Mentzell, J. E., and Woodruff, R. A. (2004). Wide Field Camera 3 instrument optical design for the Hubble Space Telescope. In *Optical, Infrared, and Millimeter Space Telescopes*, volume 5487, pages 317 – 329. International Society for Optics and Photonics, SPIE.

[Valero and Pilewskie, 1992] Valero, F. P. J. and Pilewskie, P. (1992). Latitudinal survey of spectral optical depths of the Pinatubo volcanic cloud-derived particle sizes, columnar mass loadings, and effects on planetary albedo. *Geophysical Research Letters*, 19(2):163–166.

[Vehkamäki et al., 2002] Vehkamäki, H., Kulmala, M., Napari, I., Lehtinen, K. E. J., Timmreck, C., Noppel, M., and Laaksonen, A. (2002). An improved parameterization for sulfuric acid–water nucleation rates for tropospheric and stratospheric conditions. *Journal of Geophysical Research: Atmospheres*, 107(D22).

[Vernier et al., 2011] Vernier, J. Thomason, L. W., and Kar, J. (2011). CALIPSO detection of an asian tropopause aerosol layer. *Geophysical Research Letters*, 38(7):n/a–n/a.

[Winker et al., 2010] Winker, D., Pelon, J., A. Coakley Jr, J., Ackerman, S., Charlson, R., Colarco, P., Flamant, P., Fu, Q., M. Hoff, R., Kittaka, C., Kubar, T., Le Treut, H., Mccormick, M., Mégie, G., Poole, L., Powell, K., Trepte, C., Vaughan, M., and Wielicki, B. (2010). The CALIPSO mission: A global 3D view of aerosols and clouds. *Bulletin of the American Meteorological Society*, 91.

[World Meteorological Organization, 1986] World Meteorological Organization (1986). *Atmospheric Ozone, 1985: Assessment of Our Understanding of the Processes Controlling Its Present Distribution and Change*, volume 1. National Aeronautics and Space Administration.

[Yang et al., 2013] Yang, J., Gong, P., Fu, R., Zhang, M., Chen, J., Liang, S., Xu, B., Shi, J., and Dickinson, R. (2013). The role of satellite remote sensing in climate change studies. *Nature climate change*, 3(10):875–883.

[Yano and Watanabe, 1976] Yano, T. and Watanabe, A. (1976). Acoustooptic TeO_2 tunable filter using far-off-axis anisotropic Bragg diffraction. *Appl. Opt.*, 15(9):2250–2258.

[Yariv, 1991] Yariv, A. (1991). *Optical electronics*. Saunders College Publishing.

[Zawada et al., 2015] Zawada, D. J., Dueck, S. R., Rieger, L. A., Bourassa, A. E., Lloyd, N. D., and Degenstein, D. A. (2015). High-resolution and Monte Carlo additions to the SASKTRAN radiative transfer model. *Atmospheric Measurement Techniques*, 8(6):2609–2623.

[Zawada et al., 2018] Zawada, D. J., Rieger, L. A., Bourassa, A. E., and Degenstein, D. A. (2018). Tomographic retrievals of ozone with the OMPS Limb Profiler: algorithm description and preliminary results. *Atmospheric Measurement Techniques*, 11(4):2375–2393.

[Zelinka et al., 2020] Zelinka, M. D., Myers, T. A., McCoy, D. T., Po-Chedley, S., Caldwell, P. M., Ceppi, P., Klein, S. A., and Taylor, K. E. (2020). Causes of higher climate sensitivity in CMIP6 models. *Geophysical Research Letters*, 47(1):e2019GL085782.

[Zelinka et al., 2016] Zelinka, M. D., Zhou, C., and Klein, S. A. (2016). Insights from a refined decomposition of cloud feedbacks. *Geophysical Research Letters*, 43(17):9259–9269.

[Zhang et al., 2016] Zhang, R., Li, K., Chen, Y., Wang, Y., and Wang, Z. (2016). Image processing method to improve aotf spectral resolution and spatial resolution. *Journal of Modern Optics*, 63(21):2203–2210.

[Zhao et al., 2014] Zhao, H., Li, C., and Zhang, Y. (2014). Three-surface model for the ray tracing of an imaging acousto-optic tunable filter. *Applied Optics*, 53.

[Zhao et al., 2017] Zhao, H., Wang, Z., Jia, G., Zhang, Y., and Xu, Z. (2017). Chromatic aberrations correction for imaging spectrometer based on acousto-optic tunable filter with two transducers. *Opt. Express*, 25(20):23809–23825.

Chapter A

ALI V2 Optical Design Source Code

```
RDM;LEN "VERSION: 11.5  LENS VERSION: 87 Creation Date: 01-Jan-2016"
TITLE '1500'
EPD    6.666
DIM    M
WL     1500.0 1250.0 1000.0 750.0 500.0
REF    1
WIW    1 0 0 0 0
INI    '    '
XAN    0.0 0.0 0.0 3.0 -3.0
YAN    0.0 3.0 -3.0 0.0 0.0
WTF    1.0 1.0 1.0 1.0 1.0
VUX    0.0 0.0 0.0 0.0 0.0
VLX    0.0 0.0 0.0 0.0 0.0
VUY    0.0 0.0 0.0 0.0 0.0
VLY    0.0 0.0 0.0 0.0 0.0
PRV
  PWL 1500.0 1250.0 1000.0 750.0 500.0
  'TeO2_o' 2.190611109079129 2.196602667409352&
  2.20792408767 2.23378993087695&
   2.321183938029447
END
SO     0.0 0.1e14
```

```
S       0.0  75.0
S       0.0  9.999999950385273
  THC 0
S       0.0  2.0  SILICA_SPECIAL
  SLB "LCR"
  CIR 8.9
S       0.0  10.0
  SLB "LCR_out"
  CIR 8.9
S       0.0  21.0  SILICA_SPECIAL
  SLB "Gt"
  CIR 6.35
S       0.0  50.0
  SLB "GT_out"
  CIR 6.35
S       -101.6  -50.8  REFL
  SLB "M1"
  CIR 25.4
  ADY 42.08409794
  CON
  K   -1.0
  XDE 0.0; YDE -42.08409794; ZDE 0.0
  CUM 0.0; THM 4.0
S       0.0  -76.2
S       152.4  50.0  REFL
  SLB "M2"
  CIR 25.4
  ADY -63.12614691
  CON
  K   -1.0
```

```
  DAR
  XDE 0.0; YDE 0.0; ZDE 0.0
  CUM 0.0; THM 2.0
S      0.0  0.0
  STO
  XDE 0.0; YDE -63.12614691; ZDE 0.0
S      0.0  20.0  'TeO2_o'
  SLB "AOTFIn"
  REX 6.0; REY 6.0
  XDE 0.0; YDE 0.0; ZDE 0.0
S      0.0  0.0
  SLB "AOTFout"
  REX 6.0; REY 6.0
  DIF GRT
  GRO 1.0; GRS 0.014507159326053
  GRX 0.0; GRY 1.0; GRZ 0.0
  DAR
  XDE 0.0; YDE 0.0; ZDE 0.0
  ADE 7.32; BDE 0.0; CDE 0.0
S      0.0  60.0
  XDE 0.0; YDE 0.0; ZDE 0.0
  ADE -2.8; BDE 0.0; CDE 0.0
S      0.0  21.0  SILICA_SPECIAL
  SLB "GT2"
  CIR 6.35
S      0.0  20.0
  SLB "GT2out"
S      0.0  -101.6  REFL
  SLB "Fold1"
  REX 12.5; REY 17.675
```

```
  BEN
  XDE 0.0; YDE 0.0; ZDE 0.0
  ADE 45.0; BDE 0.0; CDE 0.0
  CUM 0.0; THM 2.0
S      0.0 0.0
S      0.0 28.0973 REFL
  SLB "Fold2"
  REX 12.5; REY 17.675
  BEN
  XDE 0.0; YDE 0.0; ZDE 0.0
  ADE 45.0; BDE 0.0; CDE 0.0
  CUM 0.0; THM 2.0
S      43.4 3.9 CAF2_SCHOTT
  SLB "LA5817"
  CIR 12.7
S      0.0 19.5296381641621
  SLB "L1out"
  CIR 12.7
S      -51.50000000000001 4.0 NBK7_SCHOTT
  SLB "LC1120"
  CIR 12.7
S      0.0 1.38618162709587
  SLB "L2out"
  CIR 12.7
S      65.09999999999999 3.3 CAF2_SCHOTT
  SLB "LA5012"
  CIR 12.7
S      0.0 105.179607368821
  SLB "L3out"
  CIR 12.7
```

```
SI      0.0  -1.70495816634074
  CIR  9.6
ZOO     5
ZOO     TIT
TIT     Z1  "1500"
TIT     Z2  "1250"
TIT     Z3  "1000"
TIT     Z4  "750"
TIT     Z5  "500"
ZOO     WIW W1  1  0  0  0  0
ZOO     WIW W2  0  1  0  0  0
ZOO     WIW W3  0  0  1  0  0
ZOO     WIW W4  0  0  0  1  0
ZOO     WIW W5  0  0  0  0  1
ZOO     REF  1  2  3  4  5
ZOO     GRS  S12  0.014507159326053  0.012000697388874  0.009469420336054&
 0.006887136222235  0.004165499726183
ZOO RSC  S12  100  100  100  100  100
GO
DLG     S7  0.03
DLG     S9  0.03
FRW     632.8
DER     VAL  I1  0.02295562413705749
GO
```

Chapter B
ALI V2 Bill of Materials

Table B.1: ALI V2 Bill of Materials

Assembly	**Item**	**Vendor**	**Part Number**
Instrument Top Level	Outer Enclosure	Protocase	Custom part
Instrument Top Level	Inner Enclosure	Protocase	Custom part
Instrument Top Level	Mounting Hardware	McMaster-Carr	Various
Instrument Top Level	Baffle	Department of Physics Machine Shop	Custom part
Instrument Top Level	Insulation	Lowes	96554
Instrument Top Level	Thermal Spacers	McMaster-Carr	92273A140
Instrument Top Level	Black Out Foil	Thorlabs	BKF12
Instrument Top Level	Large Optical Breadboard	Thorlabs	MB3045
Input Telescope	Mirror	Edmund Optics	69-165
Input Telescope	Mirror	Edmund Optics	69-167
Input Telescope	Mirror Adaptors	Edmund Optics	47-112
Input Telescope	Window	Thorlabs	WG12012
Input Telescope	Pedestal Base	Thorlabs	BE1/M
Input Telescope	Pedestal	Thorlabs	RS05P4M
Input Telescope	Kinematic Mount	Newport	U300-A3K
Input Telescope	Optical Breadboard	Thorlabs	MB1545/M

Assembly	**Item**	**Vendor**	**Part Number**
Spectral/ Polarization	AOTF	Brimrose Corp. of America	TEAF 10-0.5-1.5-MSD-ER
Spectral/ Polarization	Polarizer	Edmund Optics	89-548
Spectral/ Polarization	LCR	Meadowlark Optics	LTN-200-875-UNC
Spectral/ Polarization	AOTF Base Plate	Thorlabs	UBP2/M
Spectral/	Slotted Tube	Thorlabs	SM2L20C
Spectral/ Polarization	Tube Adapter	Thorlabs	SM2AD1.5 SM1A2
Spectral/ Polarization	Tube Coupler	Thorlabs	SM2T2
Imaging Channel	Lens	Thorlabs	LA5012
Imaging Channel	Lens	Thorlabs	LA5817
Imaging Channel	Lens	Thorlabs	LC1120
Imaging Channel	Detector	Raptor Photonics	OWL1.7-VS-CL-640
Imaging Channel	Garolite	McMaster Carr	9910T65
Imaging Channel	Mounting Base	Thorlabs	BA1S/M
Imaging Channel	Post Holder	Thorlabs	PH30V/M
Imaging Channel	Optical Posts	Thorlabs	TR20V/M TR30V/M
Imaging Channel	Right Angle Brackets	Thorlabs	AB90G
Imaging Channel	C Mount Adaptor	Thorlabs	SM1A9
Imaging Channel	Lens Tube	Thorlabs	SM1L10
Imaging Channel	Tube Coupler	Thorlabs	SM1T2
Imaging Channel	Slotted Tubes	Thorlabs	SM1L30C
Imaging Channel	Lens Spacer	Thorlabs	SM1S20
Imaging Channel	Fold Mirror	Thorlabs	CCM1-P01/M